Boundary Element Modelling and Full Scale Measurement of The Acoustic Performance of Outdoor Noise Barriers

A thesis submitted for the degree of Doctor of Philosophy

by

Philip Alan Morgan

Department of Mathematical Sciences, Brunel University

November 1999

Abstract

The performance of various designs of outdoor noise barrier has been investigated using numerical modelling and full scale experiments.

The numerical modelling has been performed using a two-dimensional boundary element method. The model has been extended to allow the efficient simulation of barrier arrangements on ground having two distinct impedance values and cross-sections incorporating cuttings.

It has been reported previously that the performance of a plane screen can be enhanced by adding a device to the top of the barrier to induce destructive interference. Full scale modelling and boundary element simulations have been performed on one such commercially available device. It has been shown that, taking the height increase into account, the major contribution to the improved performance is the presence of two diffracting edges rather than any interference effects generated.

It is known that the performance of a single barrier is degraded following the introduction of a barrier on the opposite side of a source. Boundary element simulations of such parallel arrangements have been performed. Modifications have been proposed to reduce the over-estimation of multiple reflections within the model, together with a method for converting predictions to the equivalent point source values. Sound absorptive, tilted and median barriers have been shown to be effective in reducing the degradation.

A multiple-edge barrier configuration is known to offer improved screening performance over a plane screen. Reported in-situ measurements have suggested the behaviour to be influenced by site geometry. Boundary element calculations have been performed to identify a more efficient variant of the device. The results suggest the addition of an inclined base panel to be most effective.

The boundary element model has been used to investigate the effect of shape and surface treatment upon railway noise barriers. The model has been adapted to allow the use of dipole sources characteristic of railway noise. The cross-section of the rolling stock has been shown to affect the performance of rigid barriers. If the upper edges are coincident, the results suggest that simple absorptive barriers provide better screening than tilted designs. The addition of multiple edges further enhances performance.

Contents

1 Introduction 1

2 The Boundary Element Method 7

2.1 The Existing Boundary Element Method 7

2.2 Modifications for the Efficient Analysis of Geometries with Two-Impedance Boundaries 20

2.2.1 Testing of the Modified Solution Procedure 23

2.2.2 Discussion of Results 25

2.2.3 Reported Applications of The Modified Solution Procedure . . 29

2.3 Modifications for the Efficient Analysis of Shallow Cuttings 31

2.3.1 The Physical Approximation 32

2.3.2 The Mathematical Formulation 34

2.3.3 Testing of the Modified Solution Procedure 48

2.4 Conclusions 67

3 Interference-Type Noise Barriers 69

3.1 A Review of Previous Work 70

3.1.1 Thnadner barriers 70

3.1.2 Rigid strip networks 75

3.1.3 Waveguide filters 78

3.1.4 The Calmzone Interference Profile 84

3.2 Full scale and computational studies of Calmzone 103

3.2.1 Full-scale Measurement and Analysis Procedures 103

3.2.2 Configuration of The Interference Device 108

3.2.3 Theoretical predictions 109
3.3 Conclusions 118

4 Parallel Barrier Arrangements **119**
4.1 A Review of Previous Work 120
4.2 Theoretical Study of Parallel Barrier Behaviour Using The Boundary Element method 121
4.2.1 Results Using Line Sources 121
4.2.2 A Modified Procedure For Simulating Parallel Barrier Arrangements 123
4.2.3 Comparison of Theoretical Results For Line Sources and Equivalent Point Sources 130
4.3 Comparison Between Theoretical and Full Scale Experimental Results 131
4.4 Conclusions 140

5 Multiple-edge Noise Barrier Profiles **142**
5.1 A Review of Previous Work 143
5.2 Optimisation of an asymmetric multiple-edge profile 149
5.2.1 The effect of simple variations on the basic profile 151
5.2.2 The effect of inclined/cranked panels 154
5.2.3 The effect of individual base-plates 157
5.2.4 The effect of a single inclined base-plate 163
5.3 Conclusions 170

6 Trackside Noise Barriers For Railways **172**
6.1 Selection of Source Characteristics 173
6.1.1 Source Position 173
6.1.2 Source Spectrum 174
6.1.3 Source Radiation Characteristics 176
6.2 Modifications Required For The Boundary Element Method 176
6.3 Method and Comparison With Other Prediction Methods 177
6.4 The Effect of Carriage Shape Upon Barrier Performance 179

6.5 The Effect of Barrier Shape Upon Screening Performance 181
6.6 Conclusions 184

7 Conclusions **186**
7.1 Recommendations For Future Work 190

References **193**

A FORTRAN BEM Model Input and Output Files **206**
A.1 The TINPUT datafile 206
A.2 The TINPUTSP file 208
A.3 The TOUTPT Output File 209

List of Tables

2.1 Calculation times for the different solution procedures 30

2.2 Predicted EOC values for the case $\beta_c \neq 0$ 47

2.3 Predicted EOC values for the case $\beta_c = 0$ 47

3.1 Thnadner barriers -Summary of experimental arrangements and measured increase in insertion loss, ΔIL, relative to specified reference barriers. 71

3.2 Summary of experimental arrangements and Insertion Losses, IL, for interference devices tested by Mizuno et al [84, 85]. 87

3.3 Summary of experimental arrangements and Insertion Losses, IL, for interference devices tested by Mizuno et al [85] and Sekiguchi et al [107]. 91

3.4 Summary of reported improvements in barrier efficiency, ΔIL, following the introduction of Calmzone to the top of a barrier. I: Measurements using train sources 98

3.5 Summary of reported improvements in barrier efficiency, ΔIL, following the introduction of Calmzone to the top of a barrier. II: Measurements using loudspeaker sources 99

3.6 Average noise levels behind barriers and reductions in average noise levels behind the barrier. 111

4.1 Comparison of insertion loss degradation (dB(A)) obtained using different methods of calculation. 123

4.2 Comparison of the improvement in insertion loss achievable through the incorporation of the box shield and/or tilted barrier surfaces in the basic parallel barrier geometry of Figure 4.1 126
4.3 Comparison of degradations in Insertion Loss, dB(A), obtained from the Boundary Element Method, with those adjusted to a point source scenario. 131
4.4 Average noise levels and relative insertion losses behind different parallel barrier options (from [120]) 137

6.1 Parameter values used in the impedance model. 178
6.2 Comparison of broad band insertion losses, dB(A). 178
6.3 Broad band insertion losses, dB(A), for various barrier configurations. 180
6.4 Comparison of average insertion losses, dB(A), for different carriage profiles. 180

List of Figures

2.1 The basic two-dimensional situation for acoustic propagation 9

2.2 Comparison of the approximations $d(\mathbf{r}, \gamma_n)$ and $e(\mathbf{r}, \gamma_n)$ with the corresponding exact values ($k = 1$, element length $= 0.1\lambda$). 14

2.3 Case of a single obstacle and the interior problem which determines uniqueness in this case 16

2.4 A sample cross-section incorporating both mutiple obstacles/barriers and closed components disconnected from the ground. 17

2.5 Typical parallel barrier arrangement 21

2.6 Approximated parallel barrier arrangement 22

2.7 Predicted insertion losses (dB) at 500 Hz (β_{c2} as for grass) 24

2.8 Predicted insertion losses (dB) at 1000 Hz (β_{c2} as for grass) 24

2.9 Plots of $|p|$ on barrier elements at 500 Hz (β_{c2} as for grass) 26

2.10 Plots of $|p|$ on barrier elements at 1000 Hz (β_{c2} as for grass) 27

2.11 Predicted insertion loss (dB(A)) for an A-weighted traffic noise spectrum (β_{c2} as for grass) 28

2.12 Predicted insertion losses (dB(A)) for an A-weighted traffic noise spectrum (Alternative ground condition) 29

2.13 Initial cross-section prior to implementation of modified solution procedure 32

2.14 The local co-ordinate system for a single barrier element 35

2.15 Comparison of the errors in $\nabla D(\mathbf{r}, \gamma_n)$ and $\nabla E(\mathbf{r}, \gamma_n)$ with the errors in $E(\mathbf{r}, \gamma_n)$ and $D(\mathbf{r}, \gamma_n)$ respectively ($k = 1.0$, element length $= 0.1\lambda$.) 40

2.16 Cross-section used to verify the accuracy of the approximations to the partial derivatives of $P_{\beta_c}(\xi, \eta)$. 45
2.17 $|p|$, $|\nabla p|$ and corresponding |error | for the case $\beta(\mathbf{r}_n) \neq 0$ 46
2.18 Cross-section used for plane wave propagation tests 48
2.19 The absolute errors in the derivatives of $\tilde{p}$ as calculated along line EH for a fully rigid cross-section 50
2.20 The absolute errors in the derivatives of $\tilde{p}$ as calculated along line AB for a cross-section with non-rigid horizontal surfaces. 51
2.21 The absolute error in p as calculated along a line of receivers lying above the top of the cutting 52
2.22 Cross-section with cutting used to test the modified solution procedure. 53
2.23 Approximation to cross-section and coordinate system used with the exisiting BEM - Cutting with horizontal floor ($\theta = 0°$). 54
2.24 Approximation to cross-section and coordinate system used with the exisiting BEM - Cutting with inclined floor ($\theta = 3.4°$). 54
2.25 Error in SPL, dB(A), for cuttings with a horizontal floor ($\theta = 0°$) . . 55
2.26 Error in SPL (dB) for cuttings with an inclined floor ($\theta = 3.4°$) . . . 56
2.27 Error in SPL, dB(A), for a fully rigid cutting with an inclined floor ($\theta = 3.4°$) 57
2.28 Error in SPL (dB) for the combined impedance cutting with a horizontal floor ($\theta = 0°$) 58
2.29 Plot of SPL values at receiver coordinates (10.0, 1.5) for the combined impedance cutting with a horizontal floor ($\theta = 0°$) 59
2.30 Plot of SPL values at receiver coordinates (10.0, 1.5) for the combined impedance cutting with a horizontal floor ($\theta = 0°$) 60
2.31 Error in SPL, dB(A), for a fully rigid cutting with an inclined floor ($\theta = 3.4°$) 61
2.32 Larger cross-sections incorporating cuttings 63
2.33 Error in SPL (dB(A)) for large cross-sections 63
2.34 Cross-section for verification of method accuracy 65

2.35 Error in SPL (dBA(A)) between modified solution procedure and coupled integral equation method. 65

3.1 Thnadner barriers as tested by Wirt [125], viewed perpendicular to the length of the barrier. 72

3.2 Splitter-type thnader arrangement (84 % open) as tested by Wirt [125]. 72

3.3 Barriers as tested by Hutchins et al [64]. 74

3.4 Prismatic array of rigid strips as tested by Amram and Stern [3]. . . . 76

3.5 Different prism arrangements as tested by Amram and Stern [3]. . . . 76

3.6 Plan view of experimental arrangement used by Amram and Stern [3] 76

3.7 Predicted insertion loss spectra for different prism arrangements as tested by Amram and Stern [3] 77

3.8 Waveguide filter as tested by Amram and Chvojka [6]. 79

3.9 A multi-polar waveguide barrier and its basic components. 80

3.10 Waveguide filters as tested by Amram and Masson [9, 79]. 83

3.11 The interference device proposed by Mizuno et al [84]. 85

3.12 The experimental arrangement and preliminary results as from Mizuno et al [84]. 86

3.13 Sound pressure level (dB) behind interference device, at receiver coordinates (3.0, 1.40), as measured by Mizuno et al [84]. 88

3.14 Insertion Loss behind interference device at receiver coordinates (3.0, 1.40) as measured by Mizuno et al [85] for varying duct width. 89

3.15 Insertion Loss at receiver coordinates (3.0, 1.40) as measured by Mizuno et al [85] for varying duct inclination. 90

3.16 Experimental arrangements used by Sekiguchi et al [107]. 94

3.17 Interference device as tested by Iida et al [65]. 96

3.18 Cross-section of the Calmzone interference device. 97

3.19 SPL for bypass of passenger train (speed = 90 km/h) at Weilheim, Germany [48]. 100

3.20 SPL for bypass of passenger train (speed = 120 km/h) at Langenlebarn, Austria [48]. 101

3.21 Plan of the TRL Noise Barrier Test Facility (NBTF). Dimensions in metres. 104
3.22 The TRL Noise Barrier Test Facility (NBTF) showing a T-profile noise barrier under test. 105
3.23 Loudspeaker noise source as used on the TRL barrier facility. 105
3.24 Normalised A-weighted one-third octave band spectrum used as the traffic noise source (normalised to zero dB). 108
3.25 A-weighted SPL plotted against average normal component of wind vector. Source position at 5.5 m in front of the barrier, microphone at 40 m behind the barrier at a height of 1.5 m. 109
3.26 The Calmzone Device mounted on a 2 m high reflective barrier at the TRL barrier facility. 110
3.27 Cross-Section through symmetrical multiple edge profile 113
3.28 Sound Pressure Levels, dB(A), obtained from full-scale measurements using the Calmzone device. 114
3.29 Predicted insertion loss spectra at a height of 1.5 m and a distance of 40 m behind the barrier, source at 5.5 m from the barrier. 115

4.1 Layout of typical parallel barrier arrangement. 122
4.2 Cross-section detailing "box-shield". 125
4.3 Possible raypaths, including those where front barrier is not visible from image source 127
4.4 Possible ray paths, including those where front barrier is visible from image source 128
4.5 Parallel barrier arrangements as tested on the Noise Barrier Test Facility. 133
4.6 Cross-section of a typical parallel barrier arrangement showing significant direct and reflected sound rays from a directional loudspeaker source, S, facing the receiver position, R. 135
4.7 Predicted sound pressure levels, dB(A), using the BEM for different parallel barrier arrangements. 139

4.8 Predicted sound pressure levels, dB(A), using the BEM for different parallel barrier arrangements. 140

5.1 Cross-section through asymmetrical RTB profile. 146

5.2 Cross-Section through symmetrical RTB profile. 147

5.3 Asymmetric multiple-edge profile as erected at site B on the M25 motorway 148

5.4 Examples of the different types of cross-section tested as part of the optimisation 150

5.5 Relative mean insertion losses, dB(A), for simple open and closed assymetric multiple-edge barrier configurations. 152

5.6 Relative insertion losses, dB(A), for simple open and closed asymmetric multiple-edge barrier configurations. 153

5.7 Relative mean insertion losses, dB(A), for assymetric multiple-edge barrier configurations - inclined panels. 155

5.8 Relative insertion losses, dB(A), for asymmetric multiple-edge barrier configurations - inclined panels. 156

5.9 Relative mean insertion losses, dB(A), for assymetric multiple-edge barrier configurations - distorted panels. 159

5.10 Relative insertion losses, dB(A), for asymmetric multiple-edge barrier configurations - distorted panels. 160

5.11 Relative mean insertion losses, dB(A), for assymetric multiple-edge barrier configurations - distorted panels No.2. 162

5.12 Relative insertion losses, dB(A), for asymmetric multiple-edge barrier configurations - distorted panels. 163

5.13 Relative mean insertion losses, dB(A), for assymetric multiple-edge barrier configurations - inclined, open baseplates. 165

5.14 Relative insertion losses, dB(A), for asymmetric multiple-edge barrier configurations - inclined, open baseplates. 166

5.15 Comparison of relative insertion loss spectra at individual receiver positions for different multiple-edge profiles 168

5.16 Comparison of relative insertion loss spectra at individual receiver positions for different multiple-edge profiles. 169

6.1 1/3 octave band A-weighted bypass spectra for different rolling stock, adjusted for measurement position at 25m from the nearside track . . 175

6.2 Basic railway cross-section 177

6.3 Cross-section for comparison of carriage shapes 181

6.4 Cross-section for comparison of barrier shapes 182

6.5 Average insertion losses, dB(A), for the barrier arrangements tested . 183

A.1 Parallel barrier arrangement defined in sample TINPUT file. 208

A.2 Sample TINPUT file 210

A.3 Sample TINPUTSP file 211

A.4 Sample TOUTPT file 212

Acknowledgements

I would particularly like to thank Dr Simon Chandler-Wilde, my supervisor, for his excellent support, encouragement and guidance over the duration of this work, his belief that I would eventually get it all finished, and for giving me the opportunity to do a PhD in the first place. I would also like to thank Dr David Hothersall and Dr Kirill Horoshenkov from the Department of Civil and Environmental Engineering, University of Bradford, for their support and assistance whilst I was both a PhD student in the Department and a Research Assistant in the Acoustics Group.

I would like to thank the staff of the Noise and Vibration Group at the Transport Research Laboratory, particularly Dr Greg Watts and Nigel Godfrey for their advice and assistance with the experiments on the Barrier Test Facility, and Steve Phillips and Greg Harris for their patience and understanding as I've tried to balance my PhD with the demands of starting a new job.

A very special thank you must go to my family, particularly my mother and step-father, for their unwavering support, encouragement and understanding. Words cannot express how grateful I am to you for always being there - I couldn't have got this far without you.

I would also like to thank Marcus Ludwig, Chris Ross, Simon Trasler, Andrew Peplow, Donanld Crombie and all my other friends and colleagues in academia and business for their help and assistance throughout my research.

Finally, I would like to thank EPSRC and the Transport Research Laboratory for financially supporting this work.

To Mum

Chapter 1

Introduction

With the increasing volumes of traffic present on major road systems and the introduction of faster trains on mainline rail networks, the problem of environmental noise generated by road/rail transport is becoming more significant. The abatement of such noise can be achieved, with varying degrees of success, using any of three principal measures. These are treatment directly at the source position, treatment at the locations where the noise levels are identified as being a nuisance or unacceptable, and modification of the propagation path between the source and receiver.

Various methods can be adopted for reducing the noise directly at source. Engine noise can be substantially reduced through modifications to the exhaust systems, transmission etc, e.g. [112], or by enclosing the engine. For road traffic at speeds above 60 km/h "rolling noise", i.e. noise generated by the interaction between the tyre and road surface, becomes the dominant source component. Several studies, e.g. [41], have reported on the effects of modifications to the tyres, whilst porous road surfaces [93, 94, 28] have been shown to be effective at reducing rolling noise by allowing the dissipation of trapped air in the tread grooves of the tyre. However, the modification of existing vehicles is unlikely in the absence of mandatory measures, and porous road surfaces are not widely used. Reducing vehicle speeds is a further option, although more applicable to urban areas, through the introduction of traffic

calming measures, although this can generate problems in other areas such as air pollution from increased exhaust emissions etc. Similarly, wheel/rail interaction is a dominant component of railway noise. Reduction through modifications to the wheels and rails, e.g. [51], or the use of bogie shrouds [67] have been previously reported. At speeds above 250 – 300 km/h, aerodynamic noise has been identified as becoming a significant component, although the problem is not treated easily.

Treatment directly at the receiver is more difficult to achieve, especially since noise reduction is rarely required over a very small area. Within dwellings, the introduction of sound insulation to air gaps, doors and windows is the most frequently applied solution. However such measures can be costly to implement and there is no reduction of noise levels outside the dwelling.

Modification of the propagation path can be considered in several ways. In the development of new road/rail schemes, space permitting, increased source/receiver separation can be introduced. Attenuation through enhancement of the ground effect is a further possibility. However, the introduction/improvement of abatement measures is frequently necessary to provide screening from existing sources. Consequently, the most common means of modifying the propagation path is through the introduction of barriers and screens, the most effective placement being as close to the source(s) as possible.

Developments in materials and surface treatments continue to improve the screening potential of plane vertical barriers. This is particularly important in cases where reflected sound is propagated back in the direction of the receiver position, e.g. parallel barriers on either side of the track/carriageway, or in the presence of high-sided vehicles. However attenuation requirements are not the sole factor determining barrier design. Planning restrictions, visual preferences and structural performance all influence the chosen form of the structure. The requirement for improved screening with minimal height increase has led to the investigation and development of designs other than plane screens, including tilted barriers, e.g. [83, 59, 109], capped

barriers, e.g. [47, 58], interference devices, e.g. [65, 122], multiple-edge barriers, e.g. [25, 26, 121] and other novel designs, e.g. [98, 80, 2].

It has therefore become increasingly important that accurate design tools are available for the design/development of noise barriers. The techniques available include experimental scale modelling, full scale modelling, and theoretical prediction methods.

Most of the theoretical methods which have been developed are semi-empirical and based on ray tracing and geometrical acoustics. Two of the most influential studies were those of Maekawa [77] and Kurze and Anderson [73]. These predicted the insertion loss of a reflecting knife-edge screen based on the Fresnel number, $N = 2\delta/\lambda$, where δ is the path difference between the direct wave and that diffracted over the top of the barrier, and λ is the wavelength of the incident sound wave. The methods have been applied to predict the insertion loss of a rigid vertical screen on the ground, and form the basis for the treatment of barriers in variation prediction methods including the standard UK prediction methods for road traffic and railway noise [32, 33, 34]. They have also been extended to cope with diffraction from reflecting wedges [78]. However these methods only predict the amplitude of the diffracted sound field. Other work, e.g. [68, 43], has been reported using geometrical diffraction theory to predict the effects of different barriers, which allows approximation of both the phase and amplitude of the diffracted sound. Comparisons of the different methods have been reported by Isei et al [66] and Nicolas et al [95]. In addition, the use of approximations of spherical wave reflection coefficients have been reported, e.g. see [30, 104, 40], to allow for the inclusion of reflections from the ground and barrier surfaces of finite impedance.

The application of the boundary element method to outdoor sound propagation was first reported by Daumas [29] for predicting the acoustic field around vertical screens on a flat rigid ground surface. The application of the technique to barriers of arbitrary cross-section and more complicated absorptive treatment was introduced

by Seznec [108] and developed in [13, 16, 57]. It is the flexibility of the method with regards to these characteristics which provides the main advantage over geometrical techniques based upon diffraction. With continuing developments in computer technology the method is becoming increasingly cost effective, particularly relative to either full-scale or scale model experiments. As with the theoretical approaches mentioned above, modelling is largely restricted to propagation in homogeneous atmospheres although recent attempts have been made to overcome this [76, 75] . The method is best adapted to modelling situations where the ground is basically flat and homogeneous with little deviation other than for noise barriers and/or strips of different ground type, each of relatively short surface length.

Scale model experiments have been widely reported in the development of more efficient barrier designs, e.g. [82, 64, 80]. However full scale measurements are the most effective means of evaluating barrier performance. Full scale in-situ tests , e.g. [46, 121, 21], are preferable since the impact of specific physical and environmental factors upon the behaviour of a barrier can be directly observed. The high cost of barrier construction/modification and the need to account for any variability in traffic flow and therefore source strength mean that short term studies investigating different barrier designs are impractical. An alternative is full scale testing on a purpose-built test facility as in [118, 119, 120, 122]. In such circumstances test conditions are far more controlled, particularly with regards to the source, and shorter barrier lengths can be tested, reducing costs. Such an approach is much better suited for short term investigations.

In this thesis a study is presented of the performance of different types of noise barrier which can be used for the abatement of noise from roads and railways. Both theoretical and full scale measurement techniques have been used to assess the efficiency of different configurations.

The theoretical results presented in the thesis have largely been obtained through

the application of the two-dimensional boundary element numerical method developed in [13, 16, 57]. The mathematics of the method, together with the inherent advantages and disadvantages are discussed. The method has been applied in the form of a computer model, the operation of which is discussed. Two significant modifications of the existing method are presented and assessed. The first improves the computational efficiency of the method for the study of cross-sections in which the noise barrier or barriers sit on flat ground consisting of ground of two distinct impedance values, whilst maintaining accuracy of solution. The second modification allows for the efficient modelling of cross-sections incorporating a cutting, using an extension of ideas from the first modification. Comparisons with results obtained using equivalent cross-sections and the standard 2-D method are made and discussed. An application of the first of these modifications to the study of the combined effect of noise barriers and porous road surfaces has been reported elsewhere [124, 123].

One means which has been proposed for improving the screening performance of a plane screen with minimal increase in height is through the addition of an "interference device" at the top of the barrier. Such a device allows sound propagation by some path in addition to that of diffraction directly over the top of the barrier, hopefully creating, by means of a difference in phase, destructive interference between the two paths. A review of previous work is presented. Full scale testing and boundary element simulations are used to assess the performance of one such device, which is commercially available and used extensively for noise abatement on Japanese railways. The construction of the device is such that the increased attenuation may not be attributable solely to interference effects. Various tests have been conducted to identify the relative contribution of the attenuation modes.

The 2-D boundary element method has been used to study the efficiency of parallel barrier arrangements, for the case of a single barrier on either side of the carriageway. A brief review of previous work is presented. To improve the agreement between the theoretical and measured results, a modification is presented to the way in which the method is implemented by reducing the number of multiple reflections

between barrier surfaces. A technique for adapting the 2D line source results to their point source equivalents is proposed for simple cases. A comparison of these numerical predictions, for both the original and modified cases, is made with results obtained using the standard UK road traffic noise prediction method. Discrepancies between theoretical predictions and the results of a previous full-scale experimental study [120] are discussed, including the effect of introducing low barriers to the central reservation.

A multiple edge noise barrier profile has been developed which offers an improvement in barrier screening without any increase in height [25, 26]. Full scale in-situ tests of this profile have been previously conducted [121] under a range of different physical conditions. These tests and the corresponding conclusions are summarised. In response to the conclusions reached, theoretical simulations using the 2-D boundary element method have been carried out with the aim of identifying the optimum profile of the device. The logic behind the optimisation and results are presented and discussed, together with the implications for the use of multiple edge barrier configurations in real situations.

Noise nuisance from railways has become a major concern particularly near lines which carry heavy traffic at high speeds. A study is presented of the performance of various trackside noise barriers for railways, determined using the boundary element method. The basic method described in Chapter 2 uses monopole sources and has been adapted to allow the sources to exhibit dipole-type radiation characteristics. A comparison of boundary element predictions is made with results obtained using the standard UK prediction method. The effect of the profile of the rolling stock on barrier efficiency is examined, together with the effect of changing the shape of the noise barrier whilst fixing the position of the upper edge relative to the structure gauge.

Parts of this thesis have been previously published in conference proceedings and scientific journals [87, 88, 122, 89, 90, 91, 124].

Chapter 2

The Boundary Element Method

As observed in Chapter 1, the theoretical results presented in this thesis have largely been obtained using the 2-D boundary element method. The application of the method to the study of noise barriers on level ground has been well documented in previous studies [13, 16, 57, 58, 26]. In all instances, the method has been applied in the form of a computer model. In this chapter the theory behind the boundary element method is outlined, together with an explanation of the operation of the computer program. It is observed that in certain instances, the method is inefficient in terms of the computation time required. Modifications are presented which are intended to overcome this problem for two types of cross-section whilst maintaining numerical accuracy; these cross-sections are those in which the noise barrier(s) sit on flat ground comprised of ground of two distinct impedance values or where the noise source is located in a cutting. Comparisons with the existing boundary element method are presented and discrepancies between the two discussed.

2.1 The Existing Boundary Element Method

The following simple situation is used as the basis of the method:

The system is constrained to a two-dimensional geometry by assuming that all geometrical and acoustical properties in the z-direction are constant. Within this system, a mono-frequency source is positioned at some point in a homogeneous medium which lies above a locally reacting homogeneous boundary (of normalised

surface admittance β_c). The medium is assumed to be at rest in the absence of any sound waves. The equivalent three-dimensional source is therefore defined as a coherent line source of infinite length and parallel to the z-axis.

Such a source would not occur in outdoor sound propagation; in this situation the problem would be based around one or more point sources. In the case of road/rail traffic, noise is received from many sources moving along the carriageway/track and can reasonably be approximated by an incoherent line source of sound. However results from the numerical method can be related to practical measurements. Predictions of excess attenuation and insertion loss agree very well with analytical solutions [57] and measurements using a point source for both scale model [16, 24, 26] and full scale experiments [118, 122]. Further, comparisons between predicted results and full scale measurements are presented in Chapters 3-5 and a method of converting the two-dimensional boundary element results to the equivalent point source values is detailed in Chapter 4. The point source is located on the axis of the line source and in the same vertical plane as the receiver, perpendicular to the barrier. Scale model tests [72] have indicated that sound pressure levels measured behind a barrier for an incoherent line source compare favourably with values calculated for an array of point sources (using the method of Maekawa [77]). It was also observed that although the attenuation of an incoherent line source by a barrier is 3-5 dB less than Maekawa's predictions for a point source at normal incidence, the relative screening efficiency of barriers for such sources is similar.

Although the boundary element method can be extended to three-dimensions [99, 37], the two-dimensional approach is less computationally expensive.

An obstacle (in this case, a noise barrier) lies on the plane. It is assumed that the axis of the barrier is parallel to the axis of the source and that the barrier is of infinite length and has uniform cross-section and surface treatment along that length. This system is shown diagrammatically in Figure 2.1. D denotes the region of propagation which lies entirely in the upper half-plane, ∂D is the boundary (ground surface) which lies on the line $y = 0$ and γ denotes the barrier surface. It should be noted that part or all of γ may lie in the ground surface, and that γ need not be connected.

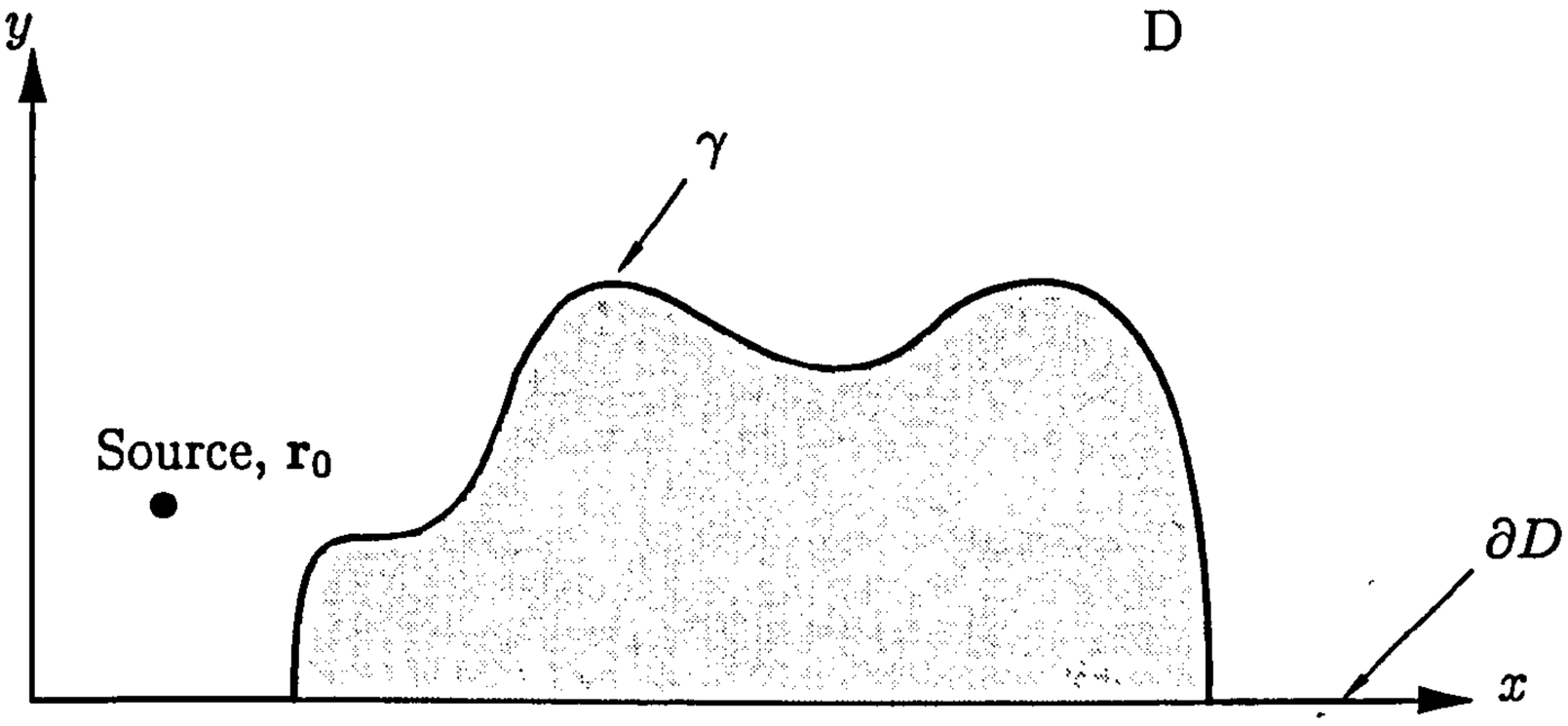

Figure 2.1: The basic two-dimensional situation for acoustic propagation

Let $p(\mathbf{r}, \mathbf{r}_0)$ denote the acoustic pressure at an arbitrary point $\mathbf{r} = (x, y)$ in the medium due to a source at $\mathbf{r}_0 = (x_0, y_0)$. As with the boundary, the barrier surface is assumed to be locally reacting, with $\beta(\mathbf{r}_s)$ the normalized surface admittance at the point $\mathbf{r}_s = (x_s, y_s)$ on γ, defined by

$$\beta(\mathbf{r}_s) = \frac{\rho c}{Z(\mathbf{r}_s)} \tag{2.1}$$

where ρc (ρ is the density and c is the sound speed) is the acoustic impedance of the medium and $Z(\mathbf{r}_s)$ is the acoustic impedance of the surface at $\mathbf{r}_s$, i.e. the ratio between the acoustic pressure and the normal fluid velocity at point $\mathbf{r}_s$ on the surface. For these conditions $p(\mathbf{r}, \mathbf{r}_0)$ satisfies the following boundary value problem (BVP) in $\overline{D} := D \cup \partial D$,

1. the Helmholtz equation,

$$(\nabla^2 + k^2)p(\mathbf{r}, \mathbf{r}_0) = \delta(\mathbf{r} - \mathbf{r}_0), \quad \mathbf{r} \in D; \tag{2.2}$$

2. the impedance boundary condition

$$\frac{\partial p(\mathbf{r}, \mathbf{r}_0)}{\partial n(\mathbf{r})} = ik\beta(\mathbf{r})p(\mathbf{r}, \mathbf{r}_0), \quad \mathbf{r} \in \partial D, \tag{2.3}$$

with $\beta(\mathbf{r}) = \beta_c, \mathbf{r} \in \partial D \setminus \gamma$;

3. the Sommerfeld radiation conditions

$$\begin{aligned} \frac{\partial p(\mathbf{r},\mathbf{r}_0)}{\partial r} - ikp(\mathbf{r},\mathbf{r}_0) &= o(r^{-\frac{1}{2}}), \\ p(\mathbf{r},\mathbf{r}_0) &= O(r^{-\frac{1}{2}}), \end{aligned} \tag{2.4}$$

as $r \to \infty$.

In the above equations, k is the wavenumber, $r := |\mathbf{r}|$ and $\partial/\partial n(\mathbf{r})$ is the partial derivative in the direction of the normal at $\mathbf{r}$ on ∂D directed out of D. In addition, the normalised surface admittance β is assumed to satisfy either that $\beta(\mathbf{r}) = 0$ (rigid boundary) or that $\Re\{\beta(\mathbf{r})\} > 0$ (absorbing boundary), for all $\mathbf{r} \in \partial D$.

It can be shown using Green's first theorem that the BVP has, at most, one solution [14].

To use a boundary element method (BEM), the problem must be reformulated as a boundary integral equation (BIE). This requires a fundamental solution of the Helmholtz equation which also satisfies the Sommerfeld radiation conditions. The simplest fundamental solution is the free field Green's function defined by the equation

$$G_f(\mathbf{r},\mathbf{r}_0) := -\frac{i}{4}H_0^{(1)}(k|\mathbf{r}-\mathbf{r}_0|), \tag{2.5}$$

where $H_0^{(1)}$ is the Hankel function of the first kind of order zero. For reasons that will become clear it is preferable to use the Green's function for the upper half-plane $y > 0$ with homogeneous impedance boundary condition on $y = 0$ with constant admittance β_c. Let $G_{\beta_c}(\mathbf{r},\mathbf{r}_0)$ denote this Green's function, i.e. G_{β_c} is the solution to the above boundary value problem, (2.2, 2.3, 2.4), in the case when no barrier is present, ∂D coincides with $y = 0$, and $\beta \equiv \beta_c$.

From [45], $G_{\beta_c}(\mathbf{r},\mathbf{r}_0)$ can be expressed in the form

$$G_{\beta_c}(\mathbf{r},\mathbf{r}_0) = G_f(\mathbf{r},\mathbf{r}_0) + G_f(\mathbf{r},\mathbf{r}_0') + P_{\beta_c}(\mathbf{r},\mathbf{r}_0), \tag{2.6}$$

where $G_f(\mathbf{r},\mathbf{r}_0)$ is the direct wave contribution, $G_f(\mathbf{r},\mathbf{r}_0')$ is the reflected wave contribution (where $\mathbf{r}_0' = (x_0, -y_0)$ is the image of the source in the half plane) and

$P_{\beta_c}(\mathbf{r}, \mathbf{r}_0)$ is the correction factor for an impedance boundary, defined such that for all $\mathbf{r}, \mathbf{r}_0 \in \overline{D}$,

$$P_{\beta_c}(\mathbf{r}, \mathbf{r}_0) = \hat{P}_{\beta_c}(k(x - x_0), k(y + y_0)) \tag{2.7}$$

where, for $\xi \in \mathbb{R}$, $y \geq 0$,

$$\hat{P}_{\beta_c}(\xi, \eta) = \frac{i\beta_c}{2\pi} \int_{-\infty}^{+\infty} \frac{\exp(i(\eta(1-s^2)^{\frac{1}{2}} - \xi s))}{(1-s^2)^{\frac{1}{2}}((1-s^2)^{\frac{1}{2}} + \beta_c)} ds, \tag{2.8}$$

and

$$\Re\left\{(1-s^2)^{\frac{1}{2}}\right\} \quad \& \quad \Im\left\{(1-s^2)^{\frac{1}{2}}\right\} \geq 0.$$

The efficiency of the BEM depends upon the efficient calculation of $G_{\beta_c}(\mathbf{r}, \mathbf{r}_0)$. Efficient polynomial approximations to the Hankel function $H_0^{(1)}$ are given in [1] and efficient, accurate approximations for $P_{\beta_c}(\mathbf{r}, \mathbf{r}_0)$ given in [17].

By applying Green's second theorem to the functions $G_{\beta_c}(., \mathbf{r})$ and $p(., \mathbf{r}_0)$ it can be shown [14] that $p(\mathbf{r}, \mathbf{r}_0)$ satisfies the following boundary integral equation

$$\varepsilon(\mathbf{r})p(\mathbf{r}, \mathbf{r}_0) = G_{\beta_c}(\mathbf{r}, \mathbf{r}_0) + \int_\gamma \left(\frac{\partial G_{\beta_c}(\mathbf{r}_s, \mathbf{r})}{\partial n(\mathbf{r}_s)} - ik\beta(\mathbf{r}_s) G_{\beta_c}(\mathbf{r}_s, \mathbf{r}) \right) p(\mathbf{r}_s, \mathbf{r}_0) ds(\mathbf{r}_s), \tag{2.9}$$

where $ds(\mathbf{r}_s)$ denotes the arc length of an element on γ at $\mathbf{r} = (x_s, y_s)$, and $\varepsilon(\mathbf{r}) = 1$ when $\mathbf{r}$ lies anywhere in D except on the barrier surface γ; $\varepsilon(\mathbf{r}) = \frac{1}{2}$ if $\mathbf{r}$ is at some point on γ which is not a corner point; $\varepsilon(\mathbf{r}) = \Omega/(2\pi)$, if $\mathbf{r} = (x, y)$ is a corner point on γ where $y > 0$, where Ω is the angle in the medium subtended by two tangents to the boundary at $\mathbf{r}$; $\varepsilon(\mathbf{r}) = \Omega/\pi$ if $\mathbf{r} = (x, 0)$ is a corner point on the ground surface; $\varepsilon(\mathbf{r}) = 1$ if $\mathbf{r} = (x, 0)$ is on the ground surface but not a corner.

Note that (2.9) expresses the pressure at any arbitrary receiver in the region D solely in terms of the pressure on γ. To solve (2.9) numerically a boundary element collocation method can be used as follows.

First γ is approximated as a polygonal arc consisting of N straight line segments, $\gamma_1, \gamma_2, \ldots, \gamma_N$. Denoting the midpoint and length of each boundary element as $\mathbf{r}_n =$

(x_n, y_n) and h_n respectively, (2.9) can be approximated by

$$\begin{aligned}\varepsilon(\mathbf{r})p(\mathbf{r},\mathbf{r}_0) &\approx G_{\beta_c}(\mathbf{r}_0,\mathbf{r}) + \sum_{n=1}^{N}\int_{\gamma_n}\left\{\frac{\partial G_{\beta_c}(\mathbf{r}_s,\mathbf{r})}{\partial n(\mathbf{r}_s)}\right. \\ &\qquad \left. -ik\beta(\mathbf{r}_s)G_{\beta_c}(\mathbf{r}_s,\mathbf{r})\right\} p(\mathbf{r}_s,\mathbf{r}_0)ds(\mathbf{r}_s) \\ &\approx G_{\beta_c}(\mathbf{r}_0,\mathbf{r}) + \sum_{n=1}^{N}\left\{B(\mathbf{r},\gamma_n) - ik\beta(\mathbf{r}_n)C(\mathbf{r},\gamma_n)\right\} p(\mathbf{r}_n,\mathbf{r}_0) \\ &\qquad \mathbf{r}\in D\cup\partial D, \quad \mathbf{r}_0\in D, \end{aligned} \tag{2.10}$$

where the integral expressions

$$C(\mathbf{r},\gamma_n) := \int_{\gamma_n} G_{\beta_c}(\mathbf{r}_s,\mathbf{r})ds(\mathbf{r}_s) \tag{2.11}$$

$$B(\mathbf{r},\gamma_n) := \int_{\gamma_n} \frac{\partial G_{\beta_c}(\mathbf{r}_s,\mathbf{r})}{\partial n(\mathbf{r}_s)}ds(\mathbf{r}_s) \tag{2.12}$$

are so-called single- and double-layer potentials respectively. Noting (2.6) we can write

$$C(\mathbf{r},\gamma_n) = E(\mathbf{r},\gamma_n) + E(\mathbf{r},\gamma_n') + C_p(\mathbf{r},\gamma_n), \tag{2.13}$$

$$B(\mathbf{r},\gamma_n) = D(\mathbf{r},\gamma_n) + D(\mathbf{r},\gamma_n') + B_p(\mathbf{r},\gamma_n), \tag{2.14}$$

where, for a given straight line arc Γ and $\mathbf{r}\in\mathbb{R}^2$,

$$D(\mathbf{r},\Gamma) := \int_{\Gamma} \frac{\partial G_f(\mathbf{r},\mathbf{r}_s)}{\partial n(\mathbf{r}_s)}ds(\mathbf{r}_s), \tag{2.15}$$

$$E(\mathbf{r},\Gamma) := \int_{\Gamma} G_f(\mathbf{r},\mathbf{r}_s)ds(\mathbf{r}_s), \tag{2.16}$$

while

$$B_p(\mathbf{r},\gamma_n) := \int_{\gamma_n} \frac{\partial P_{\beta_c}(\mathbf{r},\mathbf{r}_s)}{\partial n(\mathbf{r}_s)}ds(\mathbf{r}_s), \tag{2.17}$$

$$C_p(\mathbf{r},\gamma_n) := \int_{\gamma_n} P_{\beta_c}(\mathbf{r},\mathbf{r}_s)ds(\mathbf{r}_s). \tag{2.18}$$

Before numerical implementation we replace the single- and double-layer potentials C and B in (2.10) by approximations c and b respectively, where [16]

$$c(\mathbf{r},\gamma_n) := e(\mathbf{r},\gamma_n) + e(\mathbf{r},\gamma_n') + c_p(\mathbf{r},\gamma_n), \tag{2.19}$$

$$b(\mathbf{r},\gamma_n) := d(\mathbf{r},\gamma_n) + d(\mathbf{r},\gamma_n') + b_p(\mathbf{r},\gamma_n). \tag{2.20}$$

Here d and e denote accurate product midpoint rule approximations to D and E, defined in (3.9) of [16] and (4.1.13) of [15] respectively, and b_p and c_p are approximations to B_p and C_p respectively. Except in the exceptional case when $\mathbf{r} = (x, y) = \mathbf{r}_n$ with $y = 0$, we approximate, as in [16], $C_p(\mathbf{r}, \gamma_n)$ by the midpoint rule, i.e.

$$c_p(\mathbf{r}, \gamma_n) := h_n P_{\beta_c}(\mathbf{r}, \mathbf{r}_n), \tag{2.21}$$

and, noting that from Theorem 8 in [17]

$$\frac{\partial}{\partial y_s} P_{\beta_c}(\mathbf{r}, \mathbf{r}_s) = -ik\beta_c P_{\beta_c}(\mathbf{r}, \mathbf{r}_s) - 2ik\beta_c G_f(\mathbf{r}, \mathbf{r}'_s), \tag{2.22}$$

approximate

$$\begin{aligned} B_p(\mathbf{r}, \gamma_n) &= \int_{\gamma_n} \left\{ n_x(\mathbf{r}_s) \frac{\partial P_{\beta_c}(\mathbf{r}, \mathbf{r}_s)}{\partial x_s} + n_y(\mathbf{r}_s) \frac{\partial P_{\beta_c}(\mathbf{r}, \mathbf{r}_s)}{\partial y_s} \right\} ds(\mathbf{r}_s) \\ &= n_x(\mathbf{r}_n) \int_{\gamma_n} \frac{\partial P_{\beta_c}(\mathbf{r}, \mathbf{r}_s)}{\partial x_s} ds(\mathbf{r}_s) \\ &\qquad -ik\beta_c n_y(\mathbf{r}_n) \left[C_p(\mathbf{r}, \mathbf{r}_n) + 2E(\mathbf{r}, \gamma'_n) \right] \end{aligned} \tag{2.23}$$

by

$$\begin{aligned} b_p(\mathbf{r}, \gamma_n) &:= h_n n_x(\mathbf{r}_n) \left. \frac{\partial P_{\beta_c}(\mathbf{r}, \mathbf{r}_s)}{\partial x_s} \right|_{\mathbf{r}_s = \mathbf{r}_n} \\ &\qquad -ik\beta_c n_y(\mathbf{r}_n) \left[2e(\mathbf{r}, \gamma'_n) + c_p(\mathbf{r}, \gamma_n) \right]. \end{aligned} \tag{2.24}$$

Chandler-Wilde et al [16] use the approximation (2.21) also in the case when $\mathbf{r} = \mathbf{r}_n$ and $y = 0$. In the work here reported we use in this case the more accurate trapezium rule approximation

$$c_p(\mathbf{r}, \gamma_n) := \frac{h_n}{2} \left\{ P_{\beta_c} \left[\left(\frac{h_n}{2}, 0 \right), (0, 0) \right] + P_{\beta_c} \left[(0, 0), (0, 0) \right] \right\}. \tag{2.25}$$

Figure 2.2 compares the accuracy of the approximations for $e(\mathbf{r}, \gamma_n)$ and $d(\mathbf{r}, \gamma_n)$ with the exact values of the respective integrals for the case of a single element and either a local or distant receiver. The accuracy of these approximations is discussed in more detail in Section 2.3.2.

Therefore, to obtain the approximate solution p_N, we solve the following equation:

$$\epsilon(\mathbf{r}) p_N(\mathbf{r}, \mathbf{r}_0) = G_{\beta_c}(\mathbf{r}_0, \mathbf{r}) + \sum_{n=1}^{N} \left\{ b(\mathbf{r}, \gamma_n) - ik\beta(\mathbf{r}_n) c(\mathbf{r}, \gamma_n) \right\} p_N(\mathbf{r}_n, \mathbf{r}_0). \tag{2.26}$$

a) Near receiver (0.1λ from midpoint of element)

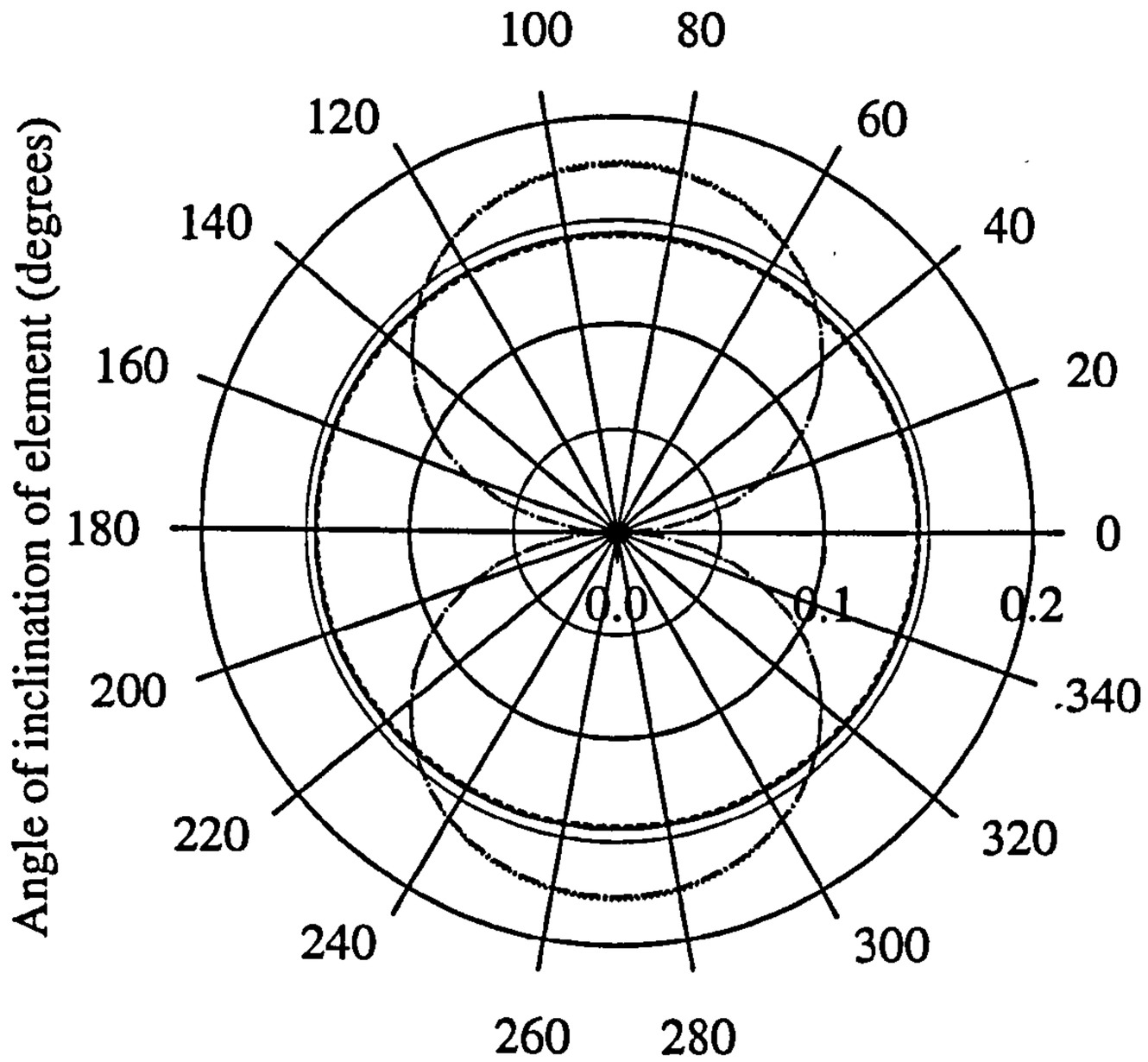

b) Distant receiver (20λ from midpoint of element)

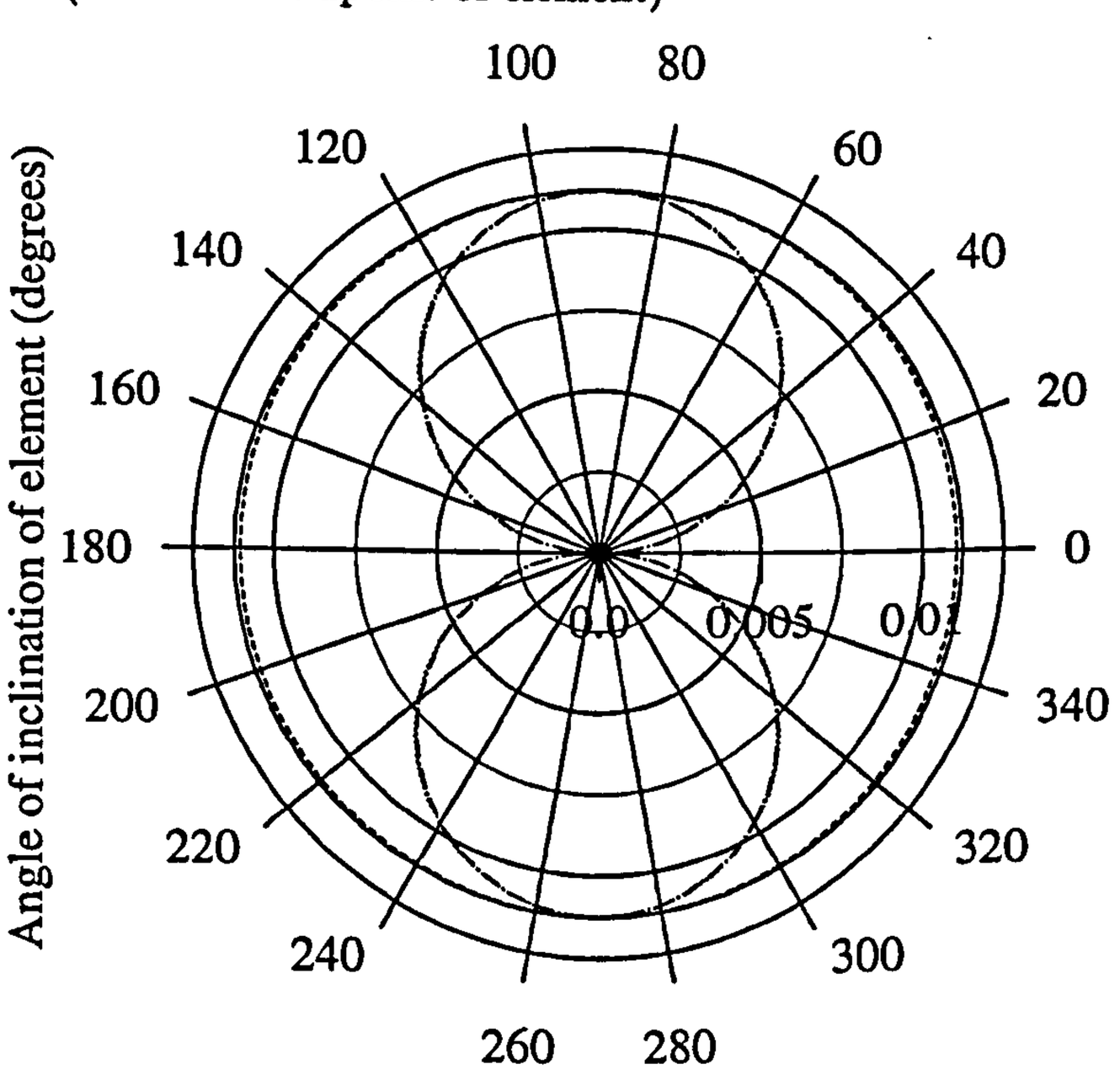

Figure 2.2: Comparison of the approximations $d(\mathbf{r}, \gamma_n)$ and $e(\mathbf{r}, \gamma_n)$ with the corresponding exact values ($k = 1$, element length $= 0.1\lambda$); ——, approximation to $|e(\mathbf{r}, \gamma_n)|$; - - - -, exact value of $|e(\mathbf{r}, \gamma_n)|$; ·····, approximation to $|d(\mathbf{r}, \gamma_n)|$; — · —, exact value of $|d(\mathbf{r}, \gamma_n)|$. The angle of inclination is the angle between the line of the element and that from receiver to element midpoint.

This expresses p_N at an arbitrary receiver position, $\mathbf{r} \in D \cup \partial D$, in terms of the values of p_N at the midpoints of the N elements. To determine these N values, we set $\mathbf{r} = \mathbf{r}_n, n = 1, 2, \ldots, N$, in (2.26) which results in a system of N linear equations with unknowns $p_N(\mathbf{r}_n, \mathbf{r}_0), n = 1, 2, \ldots, N$, i.e.

$$\sum_{n=1}^{N} a_{mn} p_N(\mathbf{r}_n, \mathbf{r}_0) = G_{\beta_c}(\mathbf{r}_0, \mathbf{r}_m), \quad m = 1, 2, \ldots, N, \tag{2.27}$$

where

$$a_{mn} = \frac{1}{2}\delta_{mn} - b(\mathbf{r}_m, \gamma_n) + ik\beta(\mathbf{r}_n)c(\mathbf{r}, \gamma_n), \quad m, n = 1, 2, \ldots, N. \tag{2.28}$$

In later calculations, the values for the normalised surface admittance of the impedance boundary, β_c, and the barrier surface, $\beta(\mathbf{r}_s)$, are calculated using the model of Delany and Bazley [31] or that of Attenborough [10, 11]. Specifically, each barrier and ground surface is assumed to have the admittance of a rigidly backed porous layer of depth D, with Z_b and k_b, the impedance and complex wavenumber of the porous layer, as given in [31] as a function of frequency/flow resistivity or in [10, 11, 18] as a function of frequency/flow resistivity, porosity, tortuosity and pore shape factor.

By calculating the attenuation for 3 different cases, namely in free-field, due to the presence of the ground only and due to the combined presence of ground and barrier, and applying these results to a source spectrum which is characteristic of road/rail traffic, broad-band sound pressure levels (SPL) and insertion losses (IL) can be determined. Insertion loss is defined as the reduction in SPL following the introduction of the barrier(s), i.e., at the particular frequency corresponding to the wavenumber k,

$$IL = -20 \log_{10} \left| \frac{p(\mathbf{r}, \mathbf{r}_0)}{G_{\beta_c}(\mathbf{r}, \mathbf{r}_0)} \right| dB. \tag{2.29}$$

The source spectra used in this thesis are A-weighted, i.e. a standard bias has been applied to the SPL spectrum of the source to account for the sensitivity of the human ear.

The boundary element method has distinct advantages and disadvantages when applied to the study of acoustic performance:

1. The method is largely restricted to modelling the propagation of sound in a homogeneous atmosphere, i.e. wind and temperature effects cannot be incorporated (though see [76, 75] for recent attempts to overcome these limitations) - this means that for sensible comparisons with results from the method, outdoor measurements must be taken under these conditions or suitably adjusted to these conditions.

2. While the method is able to handle cross-sections of arbitrary shape and impedance, the two-dimensional nature prevents the study of cases where the profile or surface properties vary along the longitudinal axis of the barrier, i.e. in the z direction.

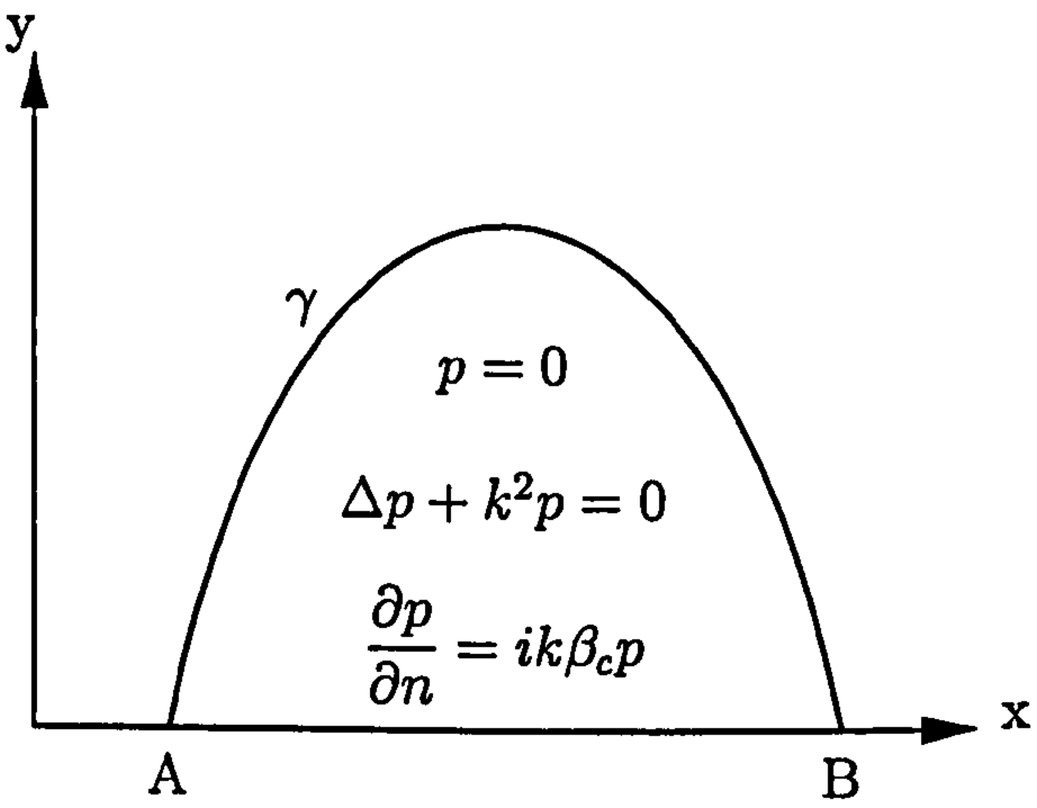

Figure 2.3: Case of a single obstacle and the interior problem which determines uniqueness in this case

3. The basic Helmholtz integral equation, (2.9), suffers from the problem that there may exist wavenumbers k at which it has more than one solution. Consider the situation shown in Figure 2.3 in which the boundary is flat, except for a single obstacle/barrier bounded by the arc γ. In this case the integral equation has more than one solution if and only if the problem in the bounded region under the obstacle shown in Figure 2.3 has a resonant mode [16]. This interior problem consists of the boundary condition $p = 0$ on γ and the impedance condition $\partial p/\partial n = ik\beta_c p$ on that part of the line $y = 0$ inside the obstacle. If $\Re\beta_c > 0$ (the ground is absorbing) then the interior has no resonant modes. If the barrier is on rigid ground ($\beta_c = 0$) then the interior

problem has resonant modes at an unbounded infinite sequence of positive wavenumbers, called the *irregular wavenumbers* for the integral equation. The corresponding frequencies are called *eigenfrequencies.*

For a simple rectangular cross-section of height H and width B, the wavenumbers which correspond to the eigenfrequencies are given by the formula

$$k = \sqrt{\left[\frac{n\pi}{B}\right]^2 + \left[\frac{1}{H}\left(m\pi + \frac{\pi}{2}\right)\right]^2} \quad \begin{cases} m = 0, 1, 2, \ldots \\ n = 1, 2, 3, \ldots \end{cases} \tag{2.30}$$

Clearly as H and B increase, the number of possible eigenfrequencies within a given frequency range increases, the first possible eigenfrequency occurring earlier than previously. If there is more than one obstacle/barrier, as shown in Figure 2.4, then there is an infinite sequence of irregular wavenumbers associated with each obstacle and if there are components of γ which are closed curves, disconnected from the ground (Figure 2.4), then there are irregular wavenumbers associated with each component, these being the resonant modes for the Helmholtz equation in the component with boundary condition $p = 0$.

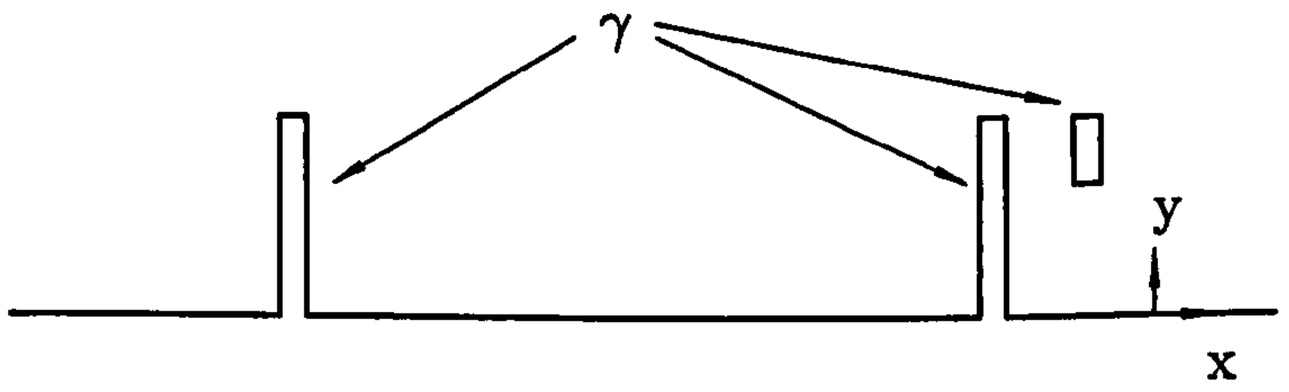

Figure 2.4: A sample cross-section incorporating both multiple obstacles/barriers and closed components disconnected from the ground. The ground surfaces are assumed to have the same constant admittance, $\beta_c = 0$.

4. The numerical method necessitates that the element size used for the discretization be small in comparison to the wavelength of the source, resulting in greater computational expense as both the frequency and the size of γ increases. Calculation of the Green's function is more complex when the ground plane is non-rigid because of the presence of the $P_{\beta_c}(\mathbf{r}, \mathbf{r}_0)$ term in (2.6). This further increases the computation time.

5. The formulation is such that for geometries incorporating thin sections the method generates inaccurate results [14]. This occurs because in the limit

of zero thickness, the matrix $[a_{mn}]$ in (2.28) contains more unknowns than equations and becomes singular - for small thicknesses the equations on opposing sides of the barrier will be almost identical so that the matrix is near to singular.

6. The function $G_{\beta_c}(\mathbf{r}, \mathbf{r}_0)$ is defined only for $\mathbf{r}$ and $\mathbf{r}_0$ in the upper half-plane, so that all surfaces must lie on or above a fixed horizontal datum, defined by the line $y = 0$. The ground surface, if flat, is usually taken to be coincident with this line, provided that the whole region of propagation and all scattering surfaces thereby lie in the upper half-plane $y \geq 0$. The numerical method requires that surfaces be discretized where either $y > 0$ (Γ_2) or $y = 0$ and $\beta \neq \beta_c$ (a barrier surface, Γ_1, in the ground but of different impedance). Therefore modelling geometries where $\gamma = \Gamma_1 \cup \Gamma_2$ is large in comparison to the wavelength of the source proves highly computationally expensive. Such cross-sections occur in cases incorporating cuttings, where the cutting floor lies below the level of the exterior ground plane, or in cases involving ground of variable acoustic type, eg. a roadway with grassland on either side. The efficiency of the method in these situations can be improved slightly with careful choice of the impedance boundary condition in relation to surface size.

7. That 2-D boundary element results can be related to practical measurements was discussed earlier in this chapter. Duhamel [37] has shown in the development of an efficient 3-D boundary element method that for several different barrier configurations, the EA values predicted by the 2-D BEM agree well with those using the 3-D method for a point source in the case of source/receiver arrangements both in and above a rigid ground plane. SPL results obtained using a 3-D BEM for the case of a T-profile barrier and a point source above a finite impedance ground [38] have been shown to give good agreement with experimental measurements, the errors being for the most part of the order of 1 dB.

The boundary element method as described in this section has been converted

into a FORTRAN computer program, to allow ease of application. The boundary element results presented in this and the remaining chapters have been obtained using this computer program. The cross-section under examination, comprising the ground plane, ∂D, the obstacle(s)/noise barrier(s), γ, and the source and receiver positions, is defined in a datafile, TINPUT, providing one input to the program. A further datafile, TINPUTSP, is required which contains details of the source spectra to be used and the element sizes at each frequency to be used in the discretization of γ. Examples of these datafiles are presented in Appendix A. The computer program runs as follows (assuming $NFREQ$ frequencies in the source spectrum, and NR receiver positions):

1. The geometrical and spectral data is read into the computer model, and the cross-section converted to dimensionless co-ordinates using the wavenumber $k_{f(i)}$ at each frequency $f(i), i = 1, 2, \ldots, NFREQ$.

2. Calculations are then performed at each frequency as follows:

   2.1. The admittance of each straight line component on γ is calculated and the corresponding admittance on each boundary element determined. The admittance of the ground plane, β_c, is also calculated.

   2.2. The pressures on γ are then calculated, solving the integral equation (2.9) in its approximate form (2.26). This is achieved by calculating the coefficient matrix $[a_{mn}]$ of (2.28) and the right-hand side vector G_{β_c} of (2.27), and then solving the linear system of equations (2.27).

   2.3. Then at each receiver position, $\mathbf{r}(j), j = 1, 2, \ldots, NR$:

      2.3.1. The total acoustic pressure is determined for three cases,

         a) in free-field, using (2.5),

         b) in the absence of the barrier but with the ground present, using (2.6), and

         c) in the presence of both the ground and barrier, using (2.6) and adding the correction for the barrier (the summation from (2.10) determined by a quadrature over the barrier surface)

2.3.2. For the same three cases, the attenuation relative to free-field at 1 m is calculated

2.3.3. Application of the spectral data to these values provides the sound pressure level (SPL), excess attenuation (EA) and insertion loss (IL) results for frequency $f(i)$ and receiver $r(j)$. The broadband results are also calculated.

The modifications studied in this thesis which are described in the following sections are aimed at minimising the effects of some of the reported weaknesses, and have been incorporated into the computer model. The 2-D method described is currently being adapted by the author to model a 3-D incoherent line source, rather than a coherent line source, but at the cost of greatly increased computation time.

2.2 Modifications for the Efficient Analysis of Geometries with Two-Impedance Boundaries

Consider the parallel barrier arrangement shown in Figure 2.5 which is a typical cross-section for a simulation of noise propagation from a vehicle source above a motorway with noise barriers on either side of the carriageway. The roadway is of admittance β_{c1}. Assuming that the ground is homogeneous beyond the barriers and of the same admittance β_{c2} on both sides of the road, the boundary element method described in the previous section can be applied. Indeed, the pressure satisfies the integral equation (2.9) with $\gamma = \Gamma_1 \cup \Gamma_2$ the part of the cross-section $ABCDEFGH$, consisting of the road surface (Γ_1) and the barrier on each side of the road (Γ_2).

However, numerical solution is expensive; the whole of γ must be discretized into elements which are small in comparison to the wavelength. For example, at 1000 Hz (wavelength $\lambda = 0.34$ m) with 5 elements per wavelength, for the geometry in Figure 2.5 the number of elements required on the barriers is $N_1 = 120$ and on the road surface $N_2 = 500$, in total $N = N_1 + N_2 = 620$. To solve the linear system (2.27), the $N \times N$ coefficient matrix must first be constructed, requiring N^2 calculations of G_{β_c}. The solution procedure itself requires $O(N^3)$ floating point operations.

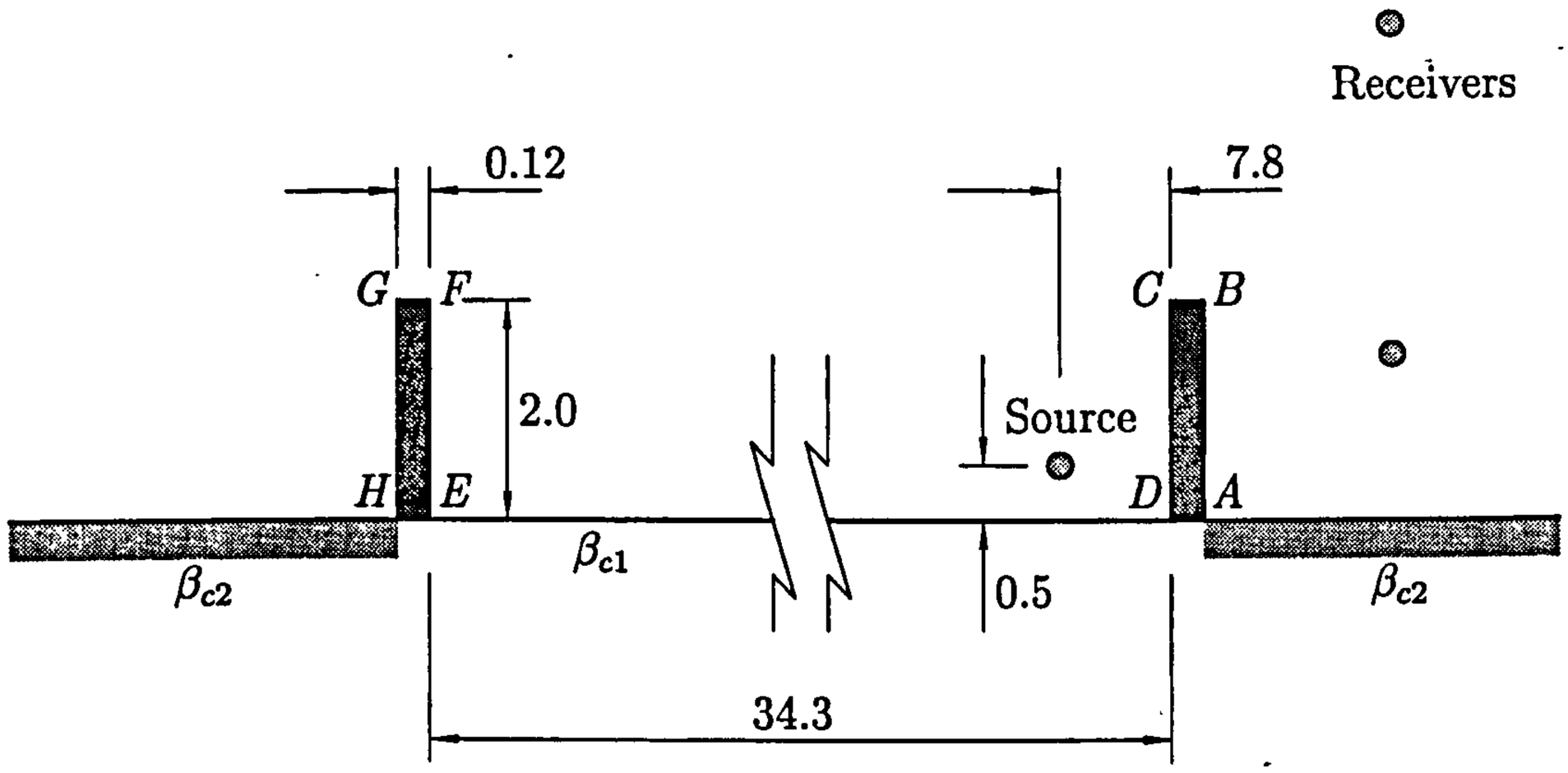

Figure 2.5: Typical parallel barrier arrangement. Dimensions in metres

In this section we describe, implement and test an approximate calculation procedure for such configurations which is much more efficient.

Using the existing method, we would solve the integral equation (2.9) using the Green's function G_{β_c} with $\beta_c = \beta_{c2}$ with the integral extending over $\gamma = \Gamma_1 \cup \Gamma_2$. The new two-stage procedure is based upon the assumption that the pressures on the road surface and the two barriers can be reasonably approximated using the cross-section shown in Figure 2.6, which is identical to that in Figure 2.5 except that to the left of S_2 and to the right of S_1, the original ground surface admittance has been altered to coincide with the surface admittance (β_{c1}) in between the two barriers. The surfaces S_1A and HS_2 (Γ_3) are of the same admittance, β_{c2}, as the ground outside the barriers in the original cross-section (Figure 2.5) and are included to minimise any error in the pressures calculated on surfaces AB and GH.

In the new two-stage procedure (2.9) is first solved for this modified cross-section, with $\beta_c = \beta_{c1}$ and integrating over $\Gamma_2 \cup \Gamma_3$. The same equation is then used to obtain the pressures on the road surface. In the second stage, the original cross-section of Figure 2.5 is used. The pressures at the final receiver positions are now calculated using (2.9) with $\beta_c = \beta_{c2}$ and the integral now extending over $\gamma = \Gamma_1 \cup \Gamma_2$ using the pressures on these surfaces as calculated in Stage 1.

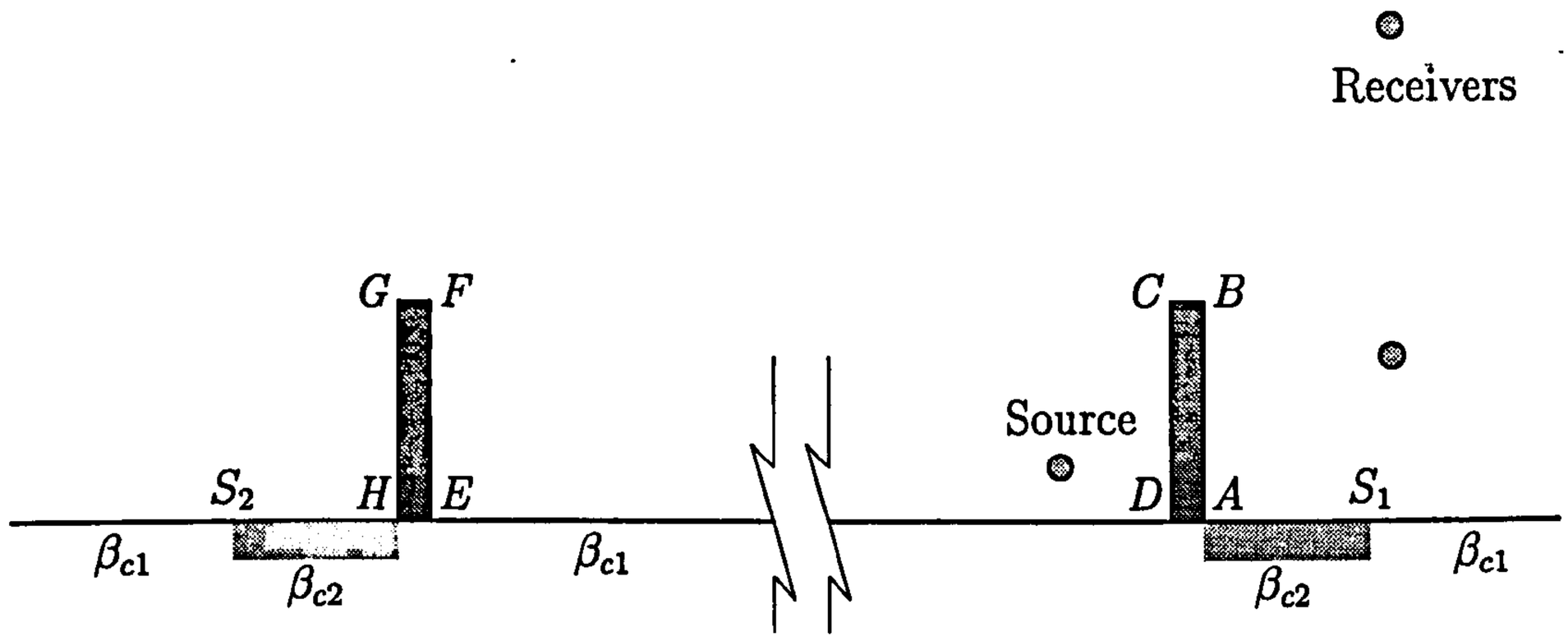

Figure 2.6: Approximated parallel barrier arrangement

We now quantify the reduction in computation time using this two-stage procedure.

As above, let N_1 be the number of elements on the surface of the noise barrier(s), N_2 the number of elements on the road surface, L the number of elements on the grass strips S_1A and HS_2, and c the time taken for a single complex multiplication and addition. Assuming that the number of receiver positions is small compared to N_2 and $N_1 + L$ then the approximate computation time required for the existing BEM can be expressed as

$$\frac{c}{3}(N_1 + N_2)^3 + C_1(N_1 + N_2)^2, \tag{2.31}$$

where C_1 is the time required for a single evaluation of the function $G_{\beta_{c2}}$. Similarly, the time required for the modified solution procedure is

$$\frac{c}{3}(N_1 + L)^3 + C_2(N_1 + L)(N_1 + L + N_2), \tag{2.32}$$

where C_2 is the time required to evaluate $G_{\beta_{c1}}$. Therefore, for typical cases when N_2 is much greater than L, the computing time saved using the modified procedure is considerable. Usually $C_1 \approx C_2$, but if the road surface is rigid so that $\beta_{c1} = 0$ then $C_1 \ll C_2$ so that there are significant additional savings.

2.2.1 Testing of the Modified Solution Procedure

The accuracy and efficiency of the modified solution procedure has been investigated by comparing results with those obtained using the existing BEM on similar cross-sections (i.e. the cross-section tested with the existing method is identical to that used in Stage 2 of the modified procedure). All simulations are based upon the cross-section shown in Figure 2.5 - 2 m high rigid parallel barriers separated by 34.3 m of rigid ground (corresponding to a standard 6 lane motorway with a hard shoulder on each carriageway). Receivers have been positioned at 20, 40 and 80 m from the outer face of one of the barriers and at heights of 1.5 and 4.5 m (as in Section 3.2.1). The source is located between the barriers, 7.8 m from one face and at a height of 0.5 m. The grassland outside of the arrangement is modelled as by the Delany and Bazley formula [31] and is characterised by an effective flow resistivity of $\sigma = 250,000$ Nsm^{-4}, which is within the range proposed in [39]. In the modified solution procedure, the strips S_1A and HS_2 (shown in Figure 2.6) are of adjustable size (the original cross-section is equivalent to defining these strips as being of infinite width). In these tests, the widths of S_1A and HS_2 are both set equal to 0.0, 2.0, 5.0 or 10.0 m.

Predictions of insertion loss from the two methods are presented in Figure 2.7 and 2.8, for frequencies of 500 and 1000 Hz respectively. The following element lengths were used for all simulations and both methods:

500 Hz: 0.09λ on the barriers and strips, 0.12λ on the road,

1000 Hz: 0.12λ on the barriers and strips, 0.17λ on the road.

Results from the modified procedure are shown for $S_1A = HS_2 = 0.0$ and 2.0 m. The results from the two methods differ by at most ± 0.04 dB at both frequencies. No significant difference is observed in the predictions for the different strip widths using the modified procedure. Results obtained using the modified procedure for the cases $S_1A = HS_2 = 5$ and 10 m were similarly observed to agree with those for the 2 m strip.

For the same frequencies, Figures 2.9 and 2.10 plot the modulus of the complex

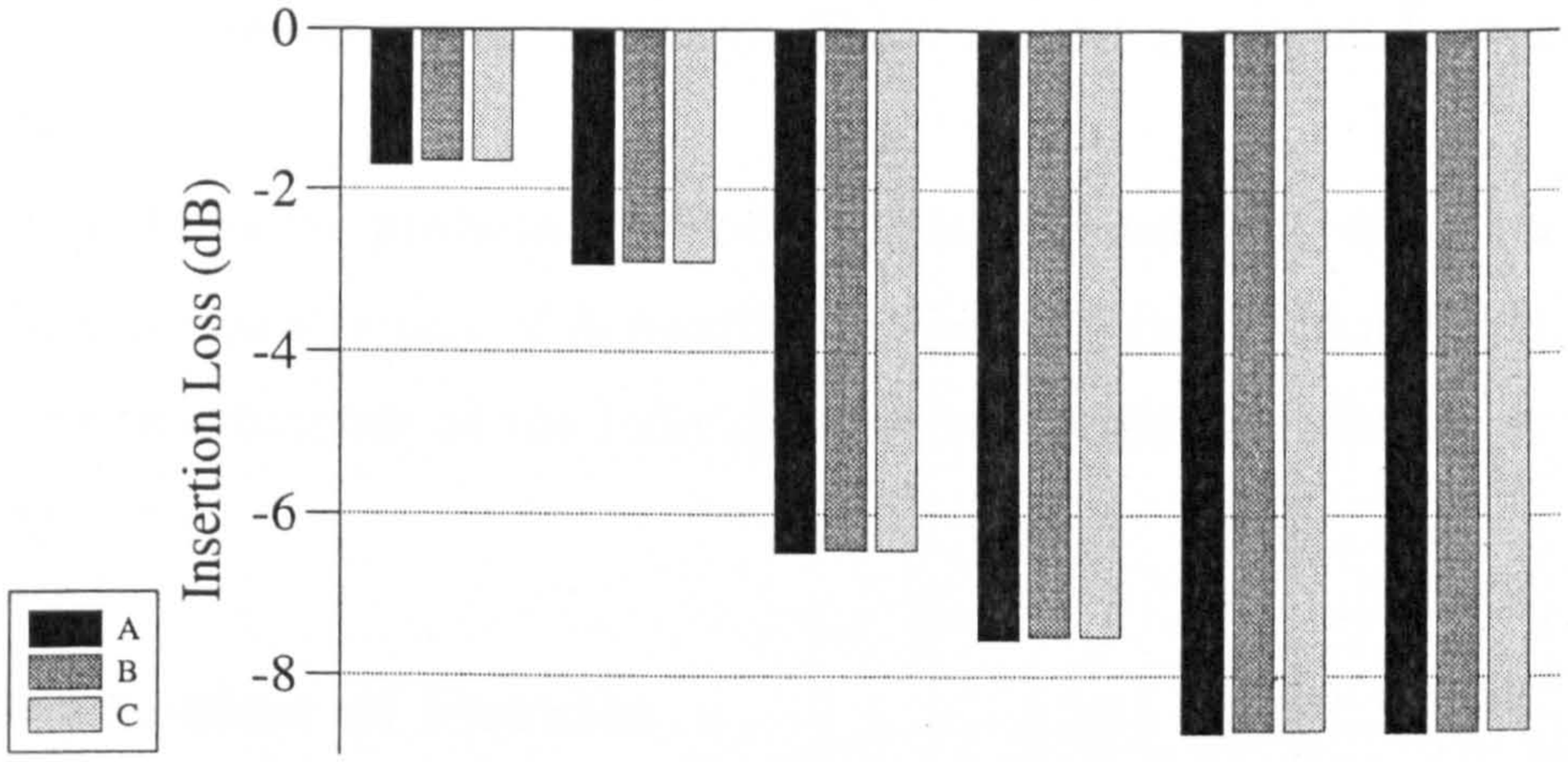

Receiver Position	20, 1.5	40, 1.5	80, 1.5	20, 4.5	40, 4.5	80, 4.5
A: Original method	-1.69	-2.93	-6.47	-7.54	-8.73	-8.72
B: 2m Grass Strip	-1.65	-2.89	-6.43	-7.50	-8.69	-8.69
C: 0m Grass Strip	-1.65	-2.89	-6.43	-7.50	-8.69	-8.68

Figure 2.7: Predicted insertion losses (dB) at 500 Hz (β_{c2} as for grass)

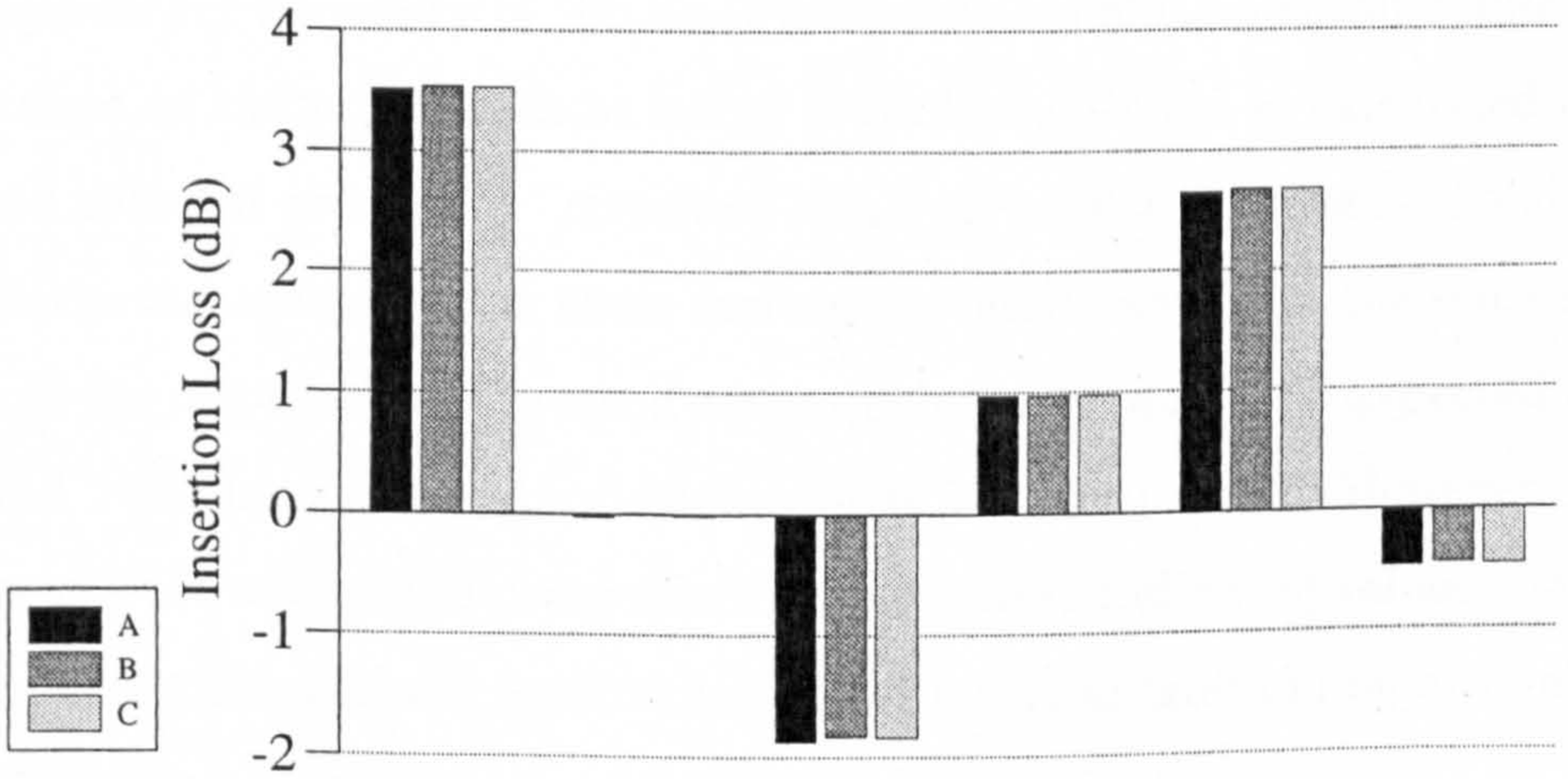

Receiver Position	20, 1.5	40, 1.5	80, 1.5	20, 4.5	40, 4.5	80, 4.5
A: Original method	3.52	-0.02	-1.86	0.94	2.62	-0.49
B: 2m Grass Strip	3.53	0.01	-1.83	0.97	2.67	-0.46
C: 0m Grass Strip	3.52	-0.01	-1.84	0.97	2.67	-0.47

Figure 2.8: Predicted insertion losses (dB) at 1000 Hz (β_{c2} as for grass)

pressure on those boundary elements lying on the barriers, as calculated using both methods; in each case, Figure a) corresponds to the barrier nearest the source position, Figure b) to the barrier farthest away. There is good agreement between the two methods.

Figure 2.11 shows the predicted insertion loss for a broad band spectrum (0.6-3.2 kHz) which is characteristic of A-weighted traffic noise (see Section 3.2.1). The results for the two methods at the individual receiver positions differ by at most ±0.19 dB(A).

2.2.2 Discussion of Results

The insertion losses at the final receiver positions predicted using the modified solution procedure show very good agreement with those from the existing BEM, suggesting that the approximation used is valid. In addition, there is good agreement between the calculated values of $|p|$ on the barrier sides and road surface. The data presented in Figures 2.9 and 2.10 can be considered in terms of specific barrier faces. Using a source frequency of 500 Hz (Figure 2.9), there is no notable difference in the $|p|$ values on those barrier faces facing towards the source as calculated using the modified solution procedure. However, small errors can be observed between results from the two methods. On those surfaces oriented away from the source, the magnitude of the error between method results behaves as would be expected close to the ground, reducing as the strip width increases from zero to 2 m. However on all faces, the errors are minimal in comparison to the corresponding $|p|$ values. Similar variations between the different method results (although greater in magnitude) can be observed for the source frequency of 1000 Hz (Figure 2.10).

Additional testing has also been carried out using ground types other than grassland. Results are presented here for ground having a flow resistivity of $\sigma = 100,000$ Nsm^{-4} (Figure 2.12). The error between the two solution procedures is considerably more significant than for the case of the grassland boundary (Figure 2.11). For the

a) Barrier furthest from source position

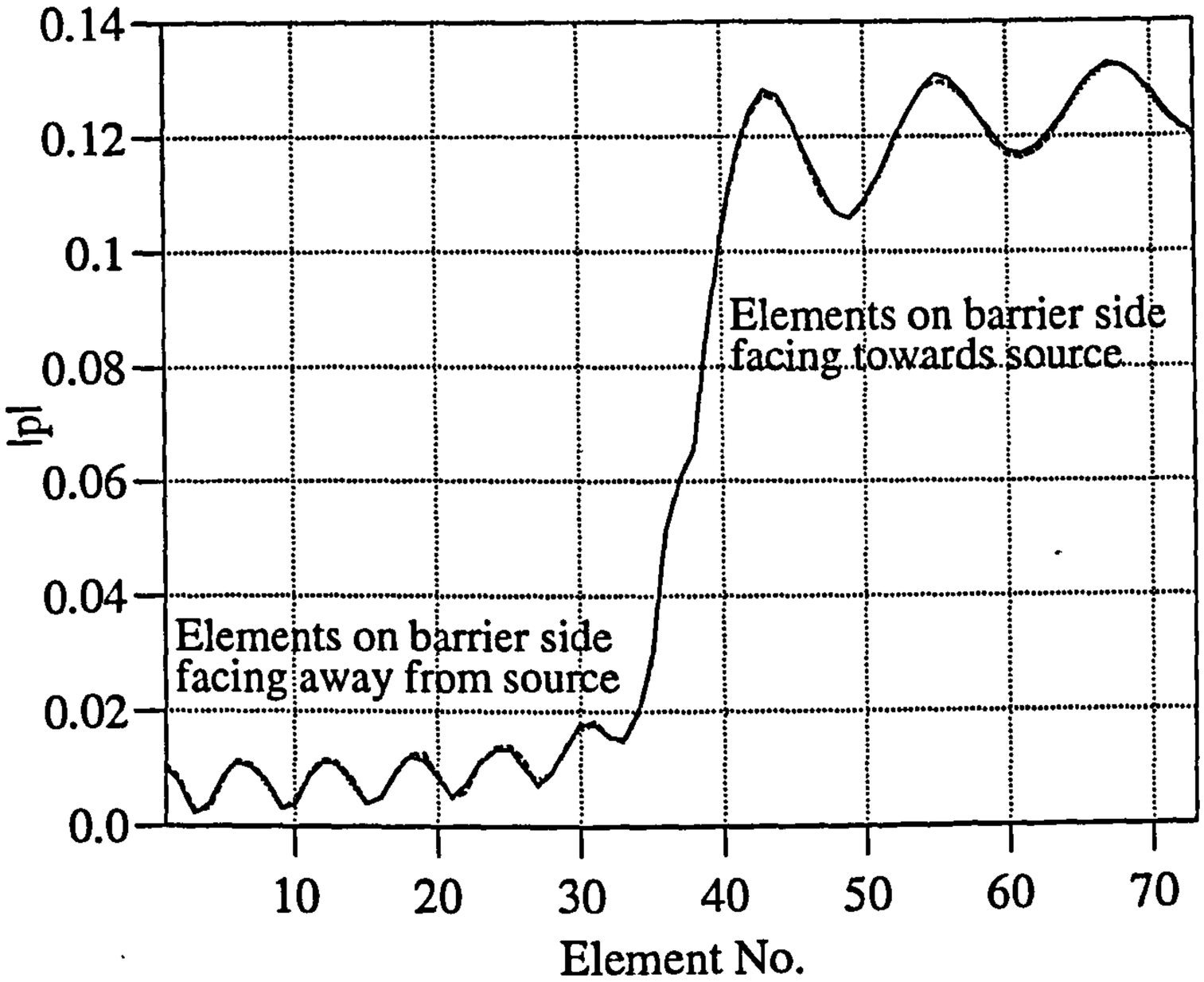

b) Barrier nearest to source position

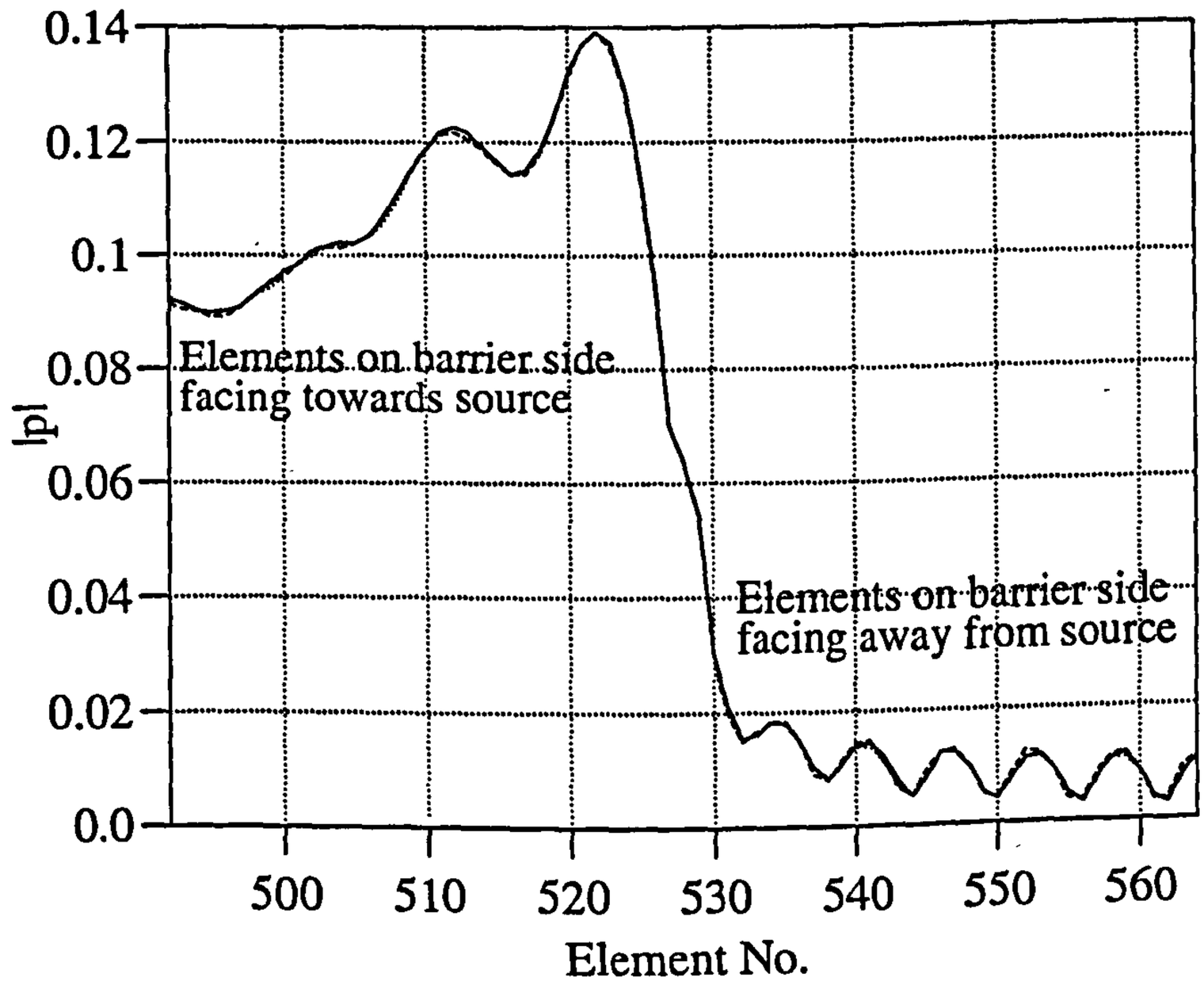

Figure 2.9: Plots of $|p|$ on barrier elements at 500 Hz (β_{c2} as for grass); ——, original program; ·····, 2m width strip; - - - -, 0m width strip.

a) Barrier furthest from source position

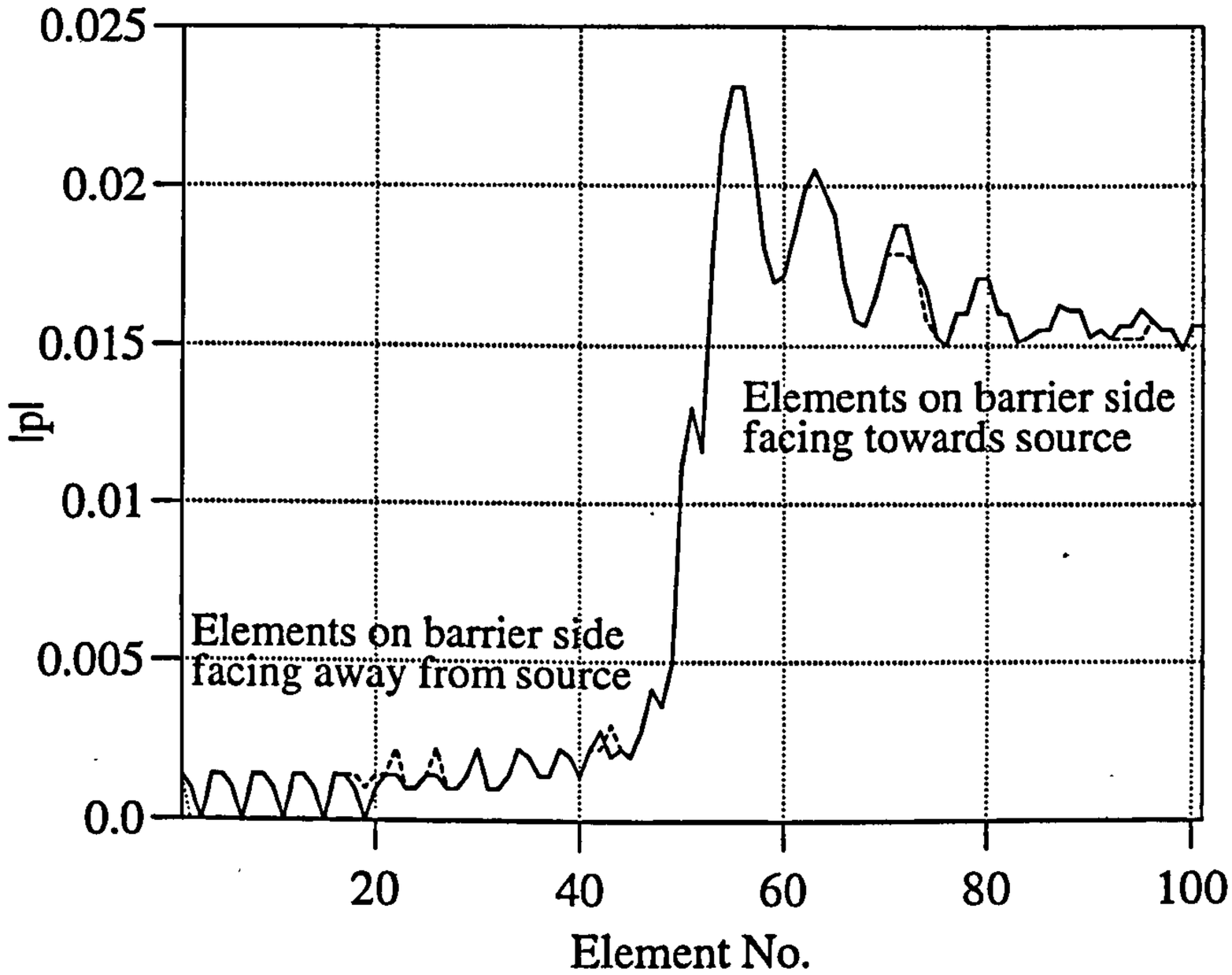

b) Barrier nearest to source position

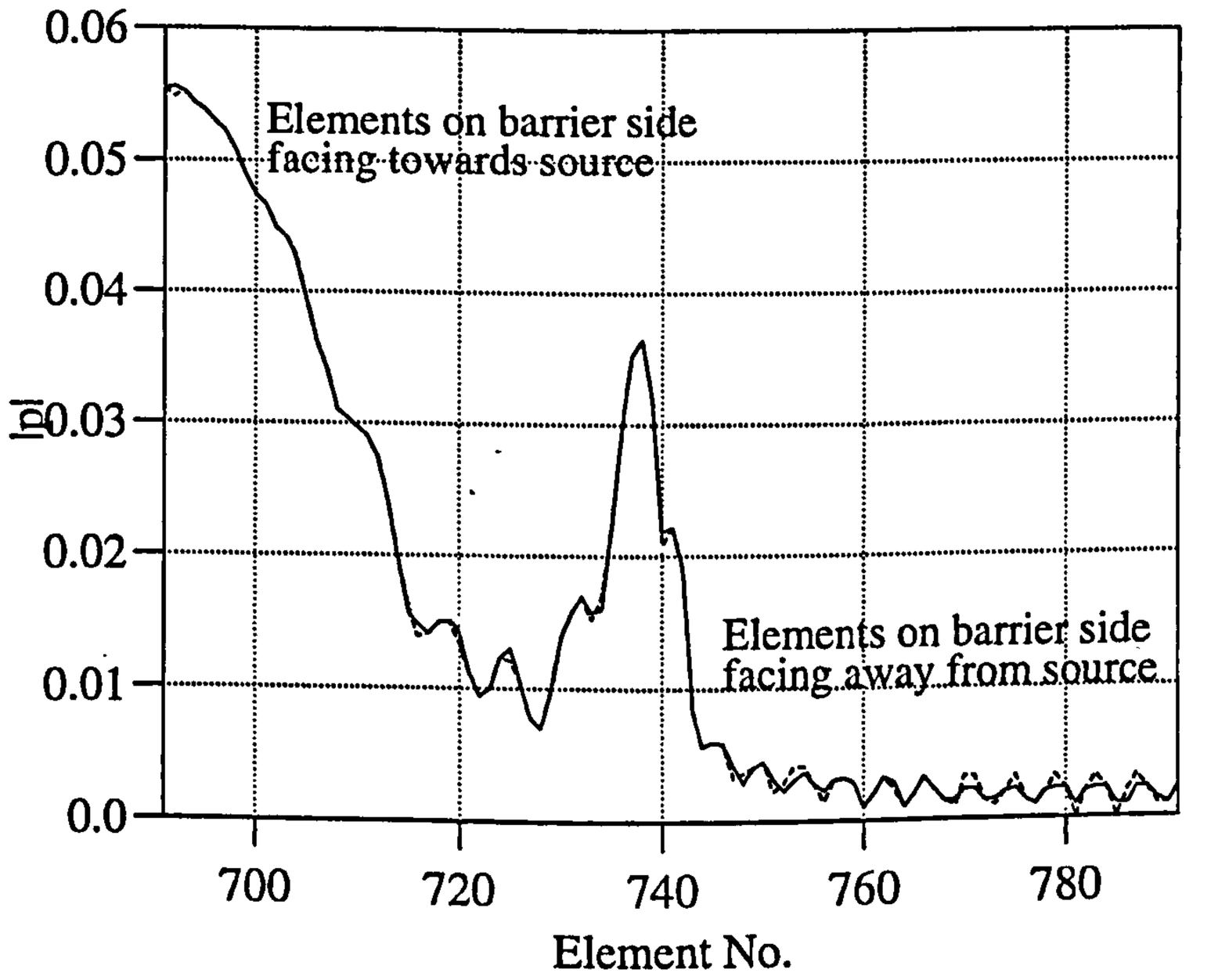

Figure 2.10: Plots of $|p|$ on barrier elements at 1000 Hz (β_{c2} as for grass) ——, original program; ·····, 2m width strip; - - - -, 0m width strip.

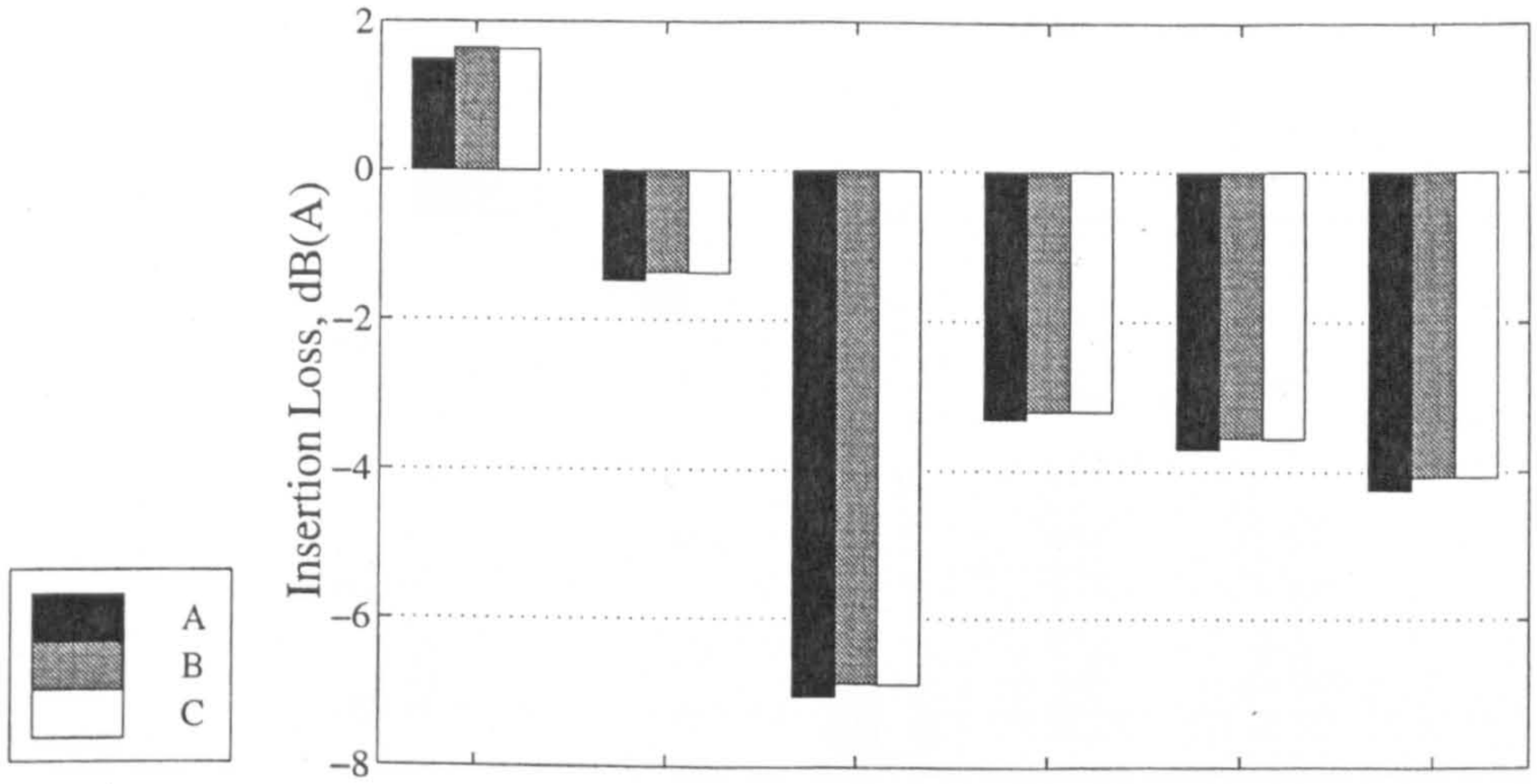

Receiver Position	20, 1.5	40, 1.5	80, 1.5	20, 4.5	40, 4.5	80, 4.5
A: Original method	1.48	-1.47	-7.06	-3.31	-3.70	-4.25
B: 2m Grass Strip	1.64	-1.36	-6.87	-3.20	-3.55	-4.07
C: 0m Grass Strip	1.62	-1.37	-6.88	-3.20	-3.56	-4.07

Figure 2.11: Predicted insertion loss (dB(A)) for an A-weighted traffic noise spectrum (β_{c2} as for grass)

receiver positions considered, the results differ by at most 1.56 dB(A). The magnitude of error between the different strip widths when using the modified solution procedure does not exceed ± 0.02 dB(A). As was observed with the grassland boundary, significantly increasing the width of the strips used outside of the barriers has negligible effect upon the results obtained using the modified procedure.

As (2.31) and (2.32) indicate, the modified solution procedure provides a significant reduction in the computation time. Considering the simulations using β_{c2} appropriate to grass, the computation times for calculating results using a full A-weighted traffic noise spectrum, (together with the reduction achieved by using the modified approach) are summarised in Table 2.1. Similar reductions were achieved for the other ground conditions studied. The modified solution procedure therefore provides similarly or more accurate results to the existing BEM (depending on the

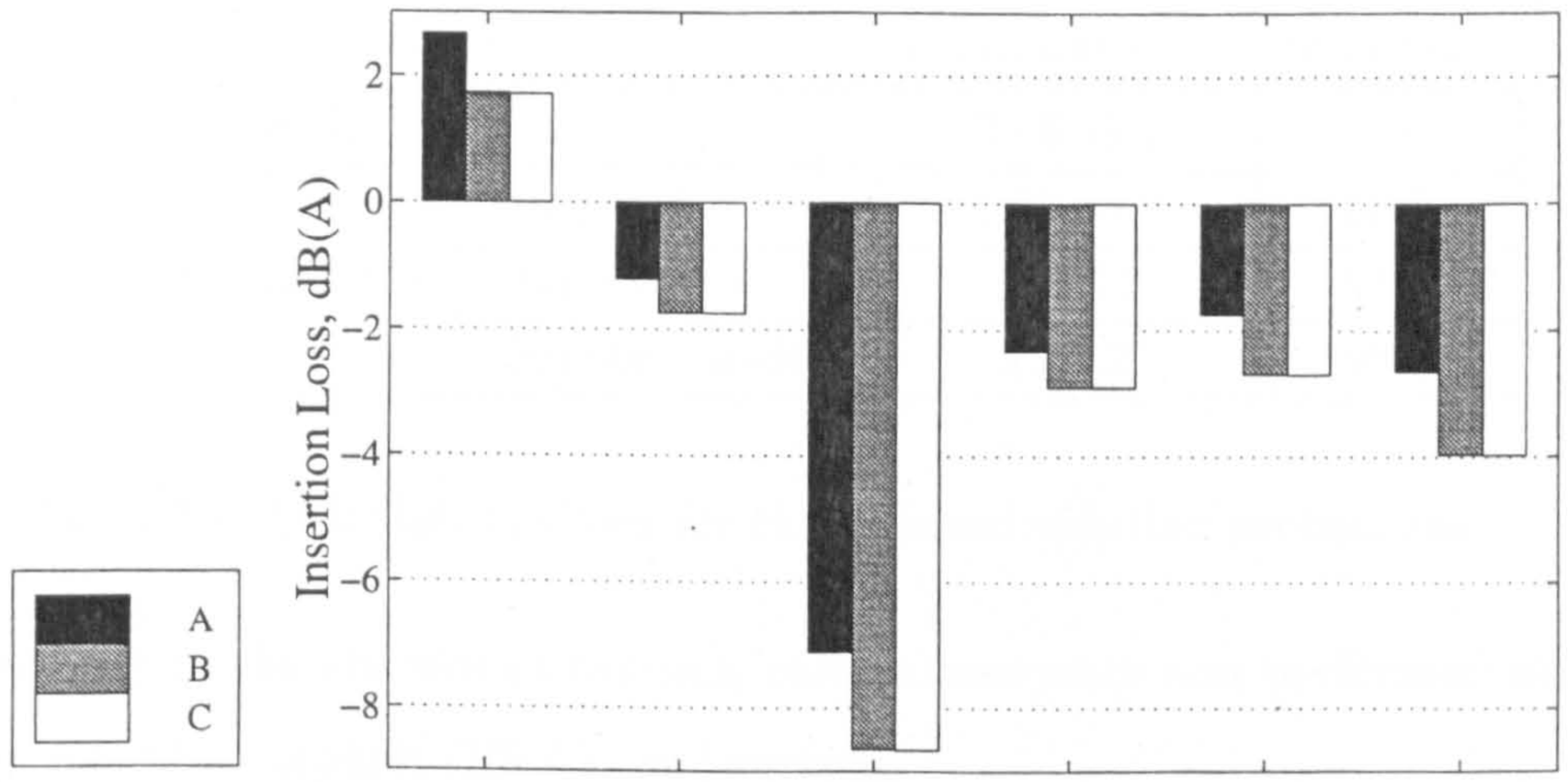

Receiver Position	20, 1.5	40, 1.5	80, 1.5	20, 4.5	40, 4.5	80, 4.5
A: Original method	2.66	-1.20	-7.11	-2.33	-1.74	-2.65
B: 2m Grass Strip	1.73	-1.74	-8.65	-2.91	-2.69	-3.97
C: 0m Grass Strip	1.72	-1.75	-8.67	-2.91	-2.70	-3.98

Figure 2.12: Predicted insertion losses (dB(A)) for an A-weighted traffic noise spectrum (Alternative ground condition)

flow resistivity of the outer ground plane) with a significant reduction in computation time. The contribution of the impedance strips outside of the barriers in the first stage of the new procedure is minimal.

2.2.3 Reported Applications of The Modified Solution Procedure

The successful application of the modified procedure to real problems has been reported by Watts et al [123, 124] in studying the combined effects of noise barriers and porous asphalt (PA) road surfaces, although modified to use the impedance model of Attenborough [10, 11] instead of that and Delany and Bazley [31] (see Section 2.1) as used during the development stages. The work demonstrates the validity of the approach for wider application since calculations were performed for the cases of a single barrier on either side of the carriageway as well as the parallel barrier style arrangement used in the development. To establish the effect of using

method Type		CPU time (hrs:mins:secs)	% time reduction
Standard BEM:		2:46:19.9	—
Modified procedure	(10m strip)	1:11:58.8	56.7
	(2m strip)	13:55.2	91.6
	(0m strip width)	7:49.2	95.4

Table 2.1: Calculation times for the different solution procedures

porous asphalt in the absence of barriers, calculations were also performed using a standard hot-rolled asphalt (HRA) road surface.

The study was based around a typical motorway cross-section (see Section 4.2) with grassland on either side of the carriageway and the effect of both light and heavy vehicles assessed by the incorporation of representative vehicle cross-sections into the model in the nearside lane of each carriageway. The precise selection of the source positions was as in the standard UK road-traffic noise prediction method [32] (see Chapter 4) and the source spectra were calibrated for typical vehicles. Measurements were taken at heights of 1.5 and 4.5 m, at distances of 0, 20 40 and 80 m from the carriageway edge, with the results being presented as an average over all of the positions. The significance of the receiver positions is discussed in Chapters 3 and 4.

In the absence of the barriers, the average predicted advantage of PA over HRA was 8.9 dB(A) and 6.9 dB(A) for the light and heavy vehicles respectively. The greatest advantage at individual receivers was observed when the height of propagation over the PA was small in comparison to that over the grassland. In comparison to unobstructed propagation, the introduction of barriers on the nearside of the road (i.e. the side of the road nearest to the receivers) and tall parallel barriers reduced the benefits of using PA due to the significant reduction in the angle of incidence of reflected waves passing over the nearside barrier and the increased average height of

propagation of the "direct" waves. The benefit was further reduced in the presence of the lorry instead of the car. For barriers on the farside of the road and low parallel barriers, a small improvement was observed when using PA, since the propagation path from the nearside source to the farside barrier is significantly greater than the direct path, allowing the PA to substantially reduce the intensity of the reflected wave. Absorptive materials on the barriers were observed to have minimal effect upon relative improvements of PA over HRA.

2.3 Modifications for the Efficient Analysis of Shallow Cuttings

As observed previously the definition of the Green's function, $G_{\beta_c}(\mathbf{r}, \mathbf{r}_0)$, is such that, when applying the boundary element method of Section 2.1, all surfaces must lie on or above a fixed horizontal datum. Whilst in theory this does not restrict the application of the method, in practice the computational expense of studying cross-sections where γ is large (relative to the wavelength of the source) places some limitations on its use.

In particular this is certainly the case when the cross-section incorporates a cutting and the ground on either side of the cutting is at a higher level. Then the horizontal datum must be taken at or below the bottom of the cutting and the integral over γ in (2.9) must extend over the whole ground surface on at least one side of the cutting out as far as all the receiver positions of interest.

If the source position lies within the cutting then a modified boundary element method can be used, the idea behind which is to use the smallest permissible cross-section at each stage of the calculations. The modifications required, described in this section, are an extension of those developed in Section 2.2 and provide similar gains in computational efficiency.

2.3.1 The Physical Approximation

Consider the simple cross-section $ABCDFGIJKL$ as illustrated in Figure 2.13: a cutting flanked by two embankments. The floor of the cutting is inclined at angle θ to the horizontal and has a normalized surface admittance β_{c1}. The sound source is supposed inside the cutting and the receiver positions of interest lie above the outlying ground, which is assumed to coincide with the x-axis, $y = 0$, and to have admittance β_{c2}. Surfaces AB and KL are also assumed to have admittance β_{c2}. As before, let $G_{\beta_{c2}}(\mathbf{r}, \mathbf{r_0})$ denote the Green's function for the upper half-plane $y \geq 0$ with admittance β_{c2}. Consider also the half-plane lying above the line GF and its extension in both directions and let $\tilde{G}_{\beta_{c1}}(\mathbf{r}, \mathbf{r_0})$ denote the same Green's function but for this half-plane and with admittance β_{c1}.

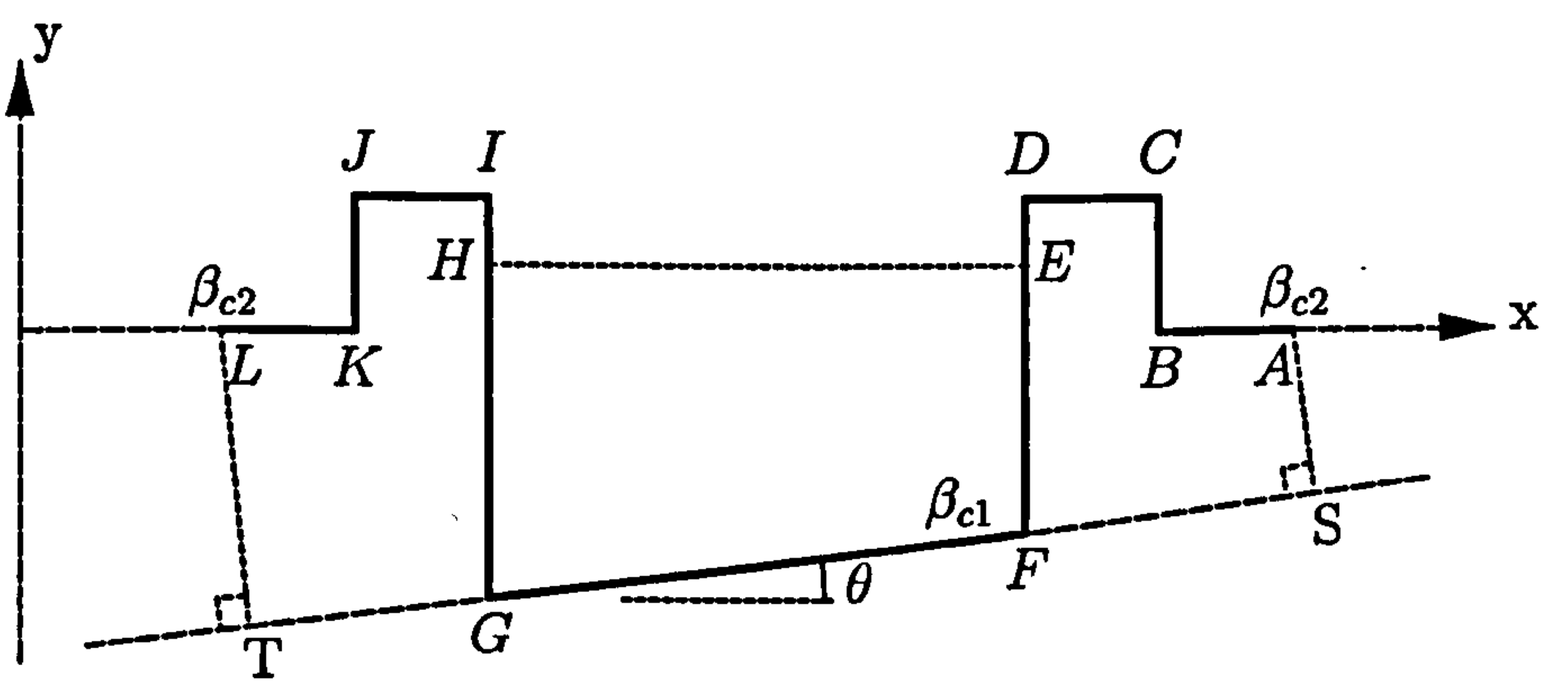

Figure 2.13: Initial cross-section prior to implementation of modified solution procedure. γ_1 is the arc $SABCDF$, γ_2 the arc $GIJKLT$ and $\tilde{\gamma} = \gamma_1 \cup \gamma_2$.

It is reasonable to assume that if the points A and L are sufficiently far from the source, then the geometry beyond these points will have negligible effect upon the sound pressure at some arbitrary point within the cutting. Assume that the angle of incidence θ is small enough so that points A and L lie above the line GF of the cutting floor and let S and T be the orthogonal projections of A and L respectively onto this line.

Let γ_1 denote the polygonal arc $SABCDF$, γ_2 the arc $GIJKLT$ and $\tilde{\gamma} = \gamma_1 \cup \gamma_2$, and let $\widetilde{D}$ denote the upper half-plane above the line GF but excluding those parts of this half-plane lying on or underneath $\tilde{\gamma}$. Let p denote the solution to the original

cutting problem and $\tilde{p}$ denote the approximation to p obtained by replacing the original region of propagation with the region $\widetilde{D}$, where we assume the admittance β to have the same value as in the original problem on $ABCDF$ and $GIJKL$, the value $\beta = \beta_{c1}$ on FG and on its continuation outside $\tilde{\gamma}$, and some arbitrary value, say $\beta = \beta_{c2}$, on LT and AS. Then, at least provided A and L are sufficiently far from the source, we expect $\tilde{p} \approx p$ inside the cutting and on the embankments $GIJK$ and $BCDF$.

The point of this approximation is that $\tilde{p}$ can be computed via the integral equation formulation, (2.9), which holds with p, γ, G_{β_c} and D replaced by $\tilde{p}$, $\tilde{\gamma}$, $\tilde{G}_{\beta_c}$ and $\widetilde{D}$ and with $\beta_c = \beta_{c1}$, i.e.

$$\varepsilon(\mathbf{r})\tilde{p}(\mathbf{r},\mathbf{r}_0) = \tilde{G}_{\beta_{c1}}(\mathbf{r},\mathbf{r}_0) + \int_{\tilde{\gamma}} \left(\frac{\partial \tilde{G}_{\beta_{c1}}(\mathbf{r}_s,\mathbf{r})}{\partial n(\mathbf{r}_s)} - ik\beta(\mathbf{r}_s)\tilde{G}_{\beta_{c1}}(\mathbf{r}_s,\mathbf{r}) \right) \tilde{p}(\mathbf{r}_s,\mathbf{r}_0) ds(\mathbf{r}_s), \tag{2.33}$$

for $\mathbf{r} \in \widetilde{D} \cup \partial\widetilde{D}$.

Stage 1 of the approximate solution procedure is to solve (2.33) to determine $\tilde{p}$ on $\tilde{\gamma}$. Once this is determined we can calculate $\tilde{p}$ elsewhere in $\widetilde{D}$ using (2.33), remembering that $\varepsilon(\mathbf{r}) = 1$ for $\mathbf{r}$ in $\widetilde{D}$. Further, differentiating (2.33) we see that $\nabla\tilde{p}$ can also be computed since

$$\nabla_{\mathbf{r}}\tilde{p}(\mathbf{r},\mathbf{r}_0) = \nabla_{\mathbf{r}}\tilde{G}_{\beta_{c1}}(\mathbf{r},\mathbf{r}_0) + \int_{\tilde{\gamma}} \nabla_{\mathbf{r}} \left(\frac{\partial \tilde{G}_{\beta_{c1}}(\mathbf{r}_s,\mathbf{r})}{\partial n(\mathbf{r}_s)} - ik\beta(\mathbf{r}_s)\tilde{G}_{\beta_{c1}}(\mathbf{r}_s,\mathbf{r}) \right) \tilde{p}(\mathbf{r}_s,\mathbf{r}_0) ds(\mathbf{r}_s). \tag{2.34}$$

Let E and H be points on γ_1 and γ_2 respectively, on the sides of the cutting, such that the line EH lies in the upper half-plane $y \geq 0$. Then the integral formula (2.9) holds if γ is taken to be the polygonal arc $BCDEHIJK$ and $\beta_c = \beta_{c2}$, provided that β on EH is defined as

$$\beta(\mathbf{r}) = \frac{\mathbf{n}(\mathbf{r}) \cdot \nabla_{\mathbf{r}} p(\mathbf{r},\mathbf{r}_0)}{ikp(\mathbf{r},\mathbf{r}_0)} \tag{2.35}$$

where $\mathbf{n}(\mathbf{r})$ denotes the unit normal to EH directed downwards. Thus, for any point $\mathbf{r}$ in the upper half-plane $y \geq 0$ with the exception of points on or below γ,

$$p(\mathbf{r},\mathbf{r}_0) = G_{\beta_{c2}}(\mathbf{r},\mathbf{r}_0) + \int_{\gamma} \left(\frac{\partial G_{\beta_{c2}}(\mathbf{r}_s,\mathbf{r})}{\partial n(\mathbf{r}_s)} - ik\beta(\mathbf{r}_s)G_{\beta_{c2}}(\mathbf{r}_s,\mathbf{r}) \right) p(\mathbf{r}_s,\mathbf{r}_0) ds(\mathbf{r}_s),$$

$$\approx \; G_{\beta_{c2}}(\mathbf{r},\mathbf{r}_0)+\int_\gamma\left(\frac{\partial G_{\beta_{c2}}(\mathbf{r}_s,\mathbf{r})}{\partial n(\mathbf{r}_s)}-ik\beta(\mathbf{r}_s)G_{\beta_{c2}}(\mathbf{r}_s,\mathbf{r})\right)\tilde{p}(\mathbf{r}_s,\mathbf{r}_0)ds(\mathbf{r}_s), \tag{2.36}$$

where we have made the approximations $p\approx\tilde{p}$ on γ and $\nabla p\approx\nabla\tilde{p}$ on EH and we redefine β on EH as

$$\beta(\mathbf{r})=\frac{\mathbf{n}(\mathbf{r})\cdot\nabla_{\mathbf{r}}\tilde{p}(\mathbf{r},\mathbf{r}_0)}{ik\tilde{p}(\mathbf{r},\mathbf{r}_0)} \tag{2.37}$$

Thus the approximation procedure employed has the following stages:

1. Compute $\tilde{p}$ on $\tilde{\gamma}$ by solving the integral equation (2.33) for $\mathbf{r}$ on $\tilde{\gamma}$.

2. Use (2.33) to compute $\tilde{p}$ on EH and (2.34) to compute $\nabla\tilde{p}$ on EH. Hence compute β on EH using (2.37).

3. Use (2.36) to compute p approximately at required receiver points on either side of the cutting geometry.

The above procedure has to be implemented numerically and the issues involved are discussed in the next sub-section. For Stage 1 and to compute $\tilde{p}$ at Stage 2 and p at Stage 3, the approximations discussed in Section 2.1 are used. The next section is concerned therefore primarily with evaluation of expression (2.34) for $\nabla\tilde{p}$.

2.3.2 The Mathematical Formulation

As discussed in Section 2.1, the integral equation, (2.9), can be approximated, for $\mathbf{r}$ in D, by

$$\begin{aligned} p(\mathbf{r},\mathbf{r}_0) \;&\approx\; G_{\beta_c}(\mathbf{r}_0,\mathbf{r})+\sum_{n=1}^{N}\left(B(\mathbf{r},\gamma_n)-ik\beta(\mathbf{r}_n)C(\mathbf{r},\gamma_n)\right)p(\mathbf{r}_n,\mathbf{r}_0)\\ &\approx\; G_{\beta_c}(\mathbf{r}_0,\mathbf{r})+\sum_{n=1}^{N}\left(b(\mathbf{r},\gamma_n)-ik\beta(\mathbf{r}_n)c(\mathbf{r},\gamma_n)\right)p(\mathbf{r}_n,\mathbf{r}_0) \end{aligned} \tag{2.38}$$

where $C(\mathbf{r},\gamma_n)$ and $B(\mathbf{r},\gamma_n)$ denote respectively the single- and double-layer potentials

$$C(\mathbf{r},\gamma_n)=\int_{\gamma_n}G_{\beta_c}(\mathbf{r}_s,\mathbf{r})ds(\mathbf{r}_s) \tag{2.39}$$

$$B(\mathbf{r},\gamma_n)=\int_{\gamma_n}\frac{\partial G_{\beta_c}(\mathbf{r}_s,\mathbf{r})}{\partial n(\mathbf{r}_s)}ds(\mathbf{r}_s) \tag{2.40}$$

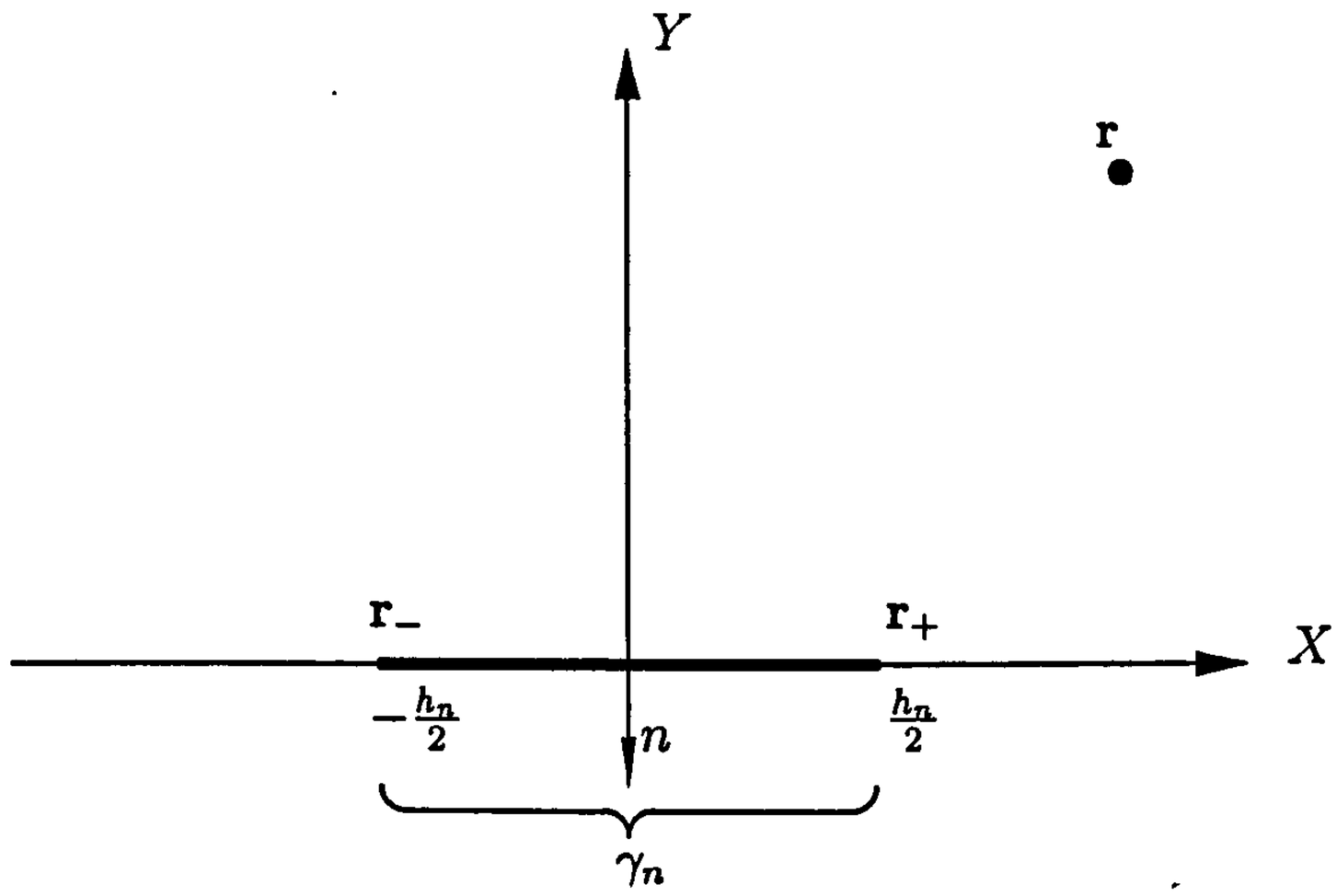

Figure 2.14: The local co-ordinate system for a single barrier element

and $c(\mathbf{r}, \gamma_n)$ and $b(\mathbf{r}, \gamma_n)$ are the approximations to $C(\mathbf{r}, \gamma_n)$ and $B(\mathbf{r}, \gamma_n)$ defined by equations (2.19) and (2.20). From (2.38) the following approximation is deduced:

$$\nabla_{\mathbf{r}} p(\mathbf{r}, \mathbf{r}_0) \approx \nabla_{\mathbf{r}} G_{\beta_c}(\mathbf{r}_0, \mathbf{r}) + \sum_{n=1}^{N} \left(\nabla_{\mathbf{r}} B(\mathbf{r}, \gamma_n) - ik\beta(\mathbf{r}_n) \nabla_{\mathbf{r}} C(\mathbf{r}, \gamma_n)\right) p(\mathbf{r}_n, \mathbf{r}_0). \quad (2.41)$$

The derivation of accurate approximations to $\nabla_{\mathbf{r}} C(\mathbf{r}, \gamma_n)$ and $\nabla_{\mathbf{r}} B(\mathbf{r}, \gamma_n)$, starting from (2.13) and (2.14), is discussed in the remainder of this section in which a local coordinate system, OXY, shall be adopted for each element $\gamma_n, n = 1, 2, \cdots, N$ as shown in Figure 2.14.

The computation of $\nabla_{\mathbf{r}} C(\mathbf{r}, \gamma_n)$ requires, from (2.13), evaluating first of all the partial derivatives of $E(\mathbf{r}, \gamma_n)$, which is given by

$$E(\mathbf{r}, \gamma_n) = \int_{\gamma_n} G_f(\mathbf{r}, \mathbf{r}_s) ds(\mathbf{r}_s). \quad (2.42)$$

Since γ_n is in the horizontal plane of OXY,

$$E(\mathbf{r}, \gamma_n) = \int_{-\frac{h_n}{2}}^{\frac{h_n}{2}} G_f(\mathbf{r}, \mathbf{r}_s) dX_s, \quad (2.43)$$

where $\mathbf{r}_s$ and $\mathbf{r}$ are taken to have coordinates $(X_S, 0)$ and (X, Y) respectively within the local coordinate system, and h_n is the length of γ_n. Partially differentiating (2.43) with respect to X and noting that

$$\frac{\partial G_f(\mathbf{r}, \mathbf{r}_s)}{\partial X} = -\frac{\partial G_f(\mathbf{r}, \mathbf{r}_s)}{\partial X_s}, \quad (2.44)$$

then

$$\frac{\partial E(\mathbf{r},\gamma_n)}{\partial X} = \frac{i}{4}\int_{-\frac{h_n}{2}}^{\frac{h_n}{2}} \frac{\partial H_0^{(1)}(k|\mathbf{r}-\mathbf{r}_s|)}{\partial X_s} dX_s. \tag{2.45}$$

Integrating (2.45) gives

$$\frac{\partial E(\mathbf{r},\gamma_n)}{\partial X} = G_f(\mathbf{r},\mathbf{r}_-) - G_f(\mathbf{r},\mathbf{r}_+). \tag{2.46}$$

Partially differentiating (2.43) with respect to Y,

$$\frac{\partial E(\mathbf{r},\gamma_n)}{\partial Y} = \int_{-\frac{h_n}{2}}^{\frac{h_n}{2}} \frac{\partial G_f(\mathbf{r},\mathbf{r}_s)}{\partial Y} dX_s. \tag{2.47}$$

Now

$$\frac{\partial G_f(\mathbf{r},\mathbf{r}_s)}{\partial Y} = -\frac{\partial G_f(\mathbf{r},\mathbf{r}_s)}{\partial Y_s} \quad \text{and} \quad \frac{\partial G_f(\mathbf{r},\mathbf{r}_s)}{\partial Y_s} = -\frac{\partial G_f(\mathbf{r},\mathbf{r}_s)}{\partial n(\mathbf{r}_s)}. \tag{2.48}$$

Therefore, substituting into (2.47),

$$\begin{aligned}\frac{\partial E(\mathbf{r},\gamma_n)}{\partial Y} &= \int_{-\frac{h_n}{2}}^{\frac{h_n}{2}} \frac{\partial G_f(\mathbf{r},\mathbf{r}_s)}{\partial n(\mathbf{r}_s)} dX_s \\ &= D(\mathbf{r},\gamma_n) \\ &\approx d(\mathbf{r},\gamma_n).\end{aligned} \tag{2.49}$$

From (2.46) and (2.49) it follows that

$$\frac{\partial E(\mathbf{r},\gamma_n)}{\partial x} \approx -n_y(\mathbf{r}_n)\left(G_f(\mathbf{r},\mathbf{r}_-) - G_f(\mathbf{r},\mathbf{r}_+)\right) - n_x(\mathbf{r}_n)d(\mathbf{r},\gamma_n), \tag{2.50}$$

$$\frac{\partial E(\mathbf{r},\gamma_n)}{\partial y} \approx n_x(\mathbf{r}_n)\left(G_f(\mathbf{r},\mathbf{r}_-) - G_f(\mathbf{r},\mathbf{r}_+)\right) - n_y(\mathbf{r}_n)d(\mathbf{r},\gamma_n), \tag{2.51}$$

and

$$\frac{\partial E(\mathbf{r},\gamma_n')}{\partial x} \approx -n_y(\mathbf{r}_n)\left(G_f(\mathbf{r},\mathbf{r}_-') - G_f(\mathbf{r},\mathbf{r}_+')\right) - n_x(\mathbf{r}_n)d(\mathbf{r},\gamma_n'), \tag{2.52}$$

$$\frac{\partial E(\mathbf{r},\gamma_n')}{\partial y} \approx n_x(\mathbf{r}_n)\left(G_f(\mathbf{r},\mathbf{r}_-') - G_f(\mathbf{r},\mathbf{r}_+')\right) - n_y(\mathbf{r}_n)d(\mathbf{r},\gamma_n'). \tag{2.53}$$

Now consider $\nabla_{\mathbf{r}} B(\mathbf{r},\gamma_n)$, with $B(\mathbf{r},\gamma_n)$ given by (2.14), considering first the evaluation of the derivatives of

$$D(\mathbf{r},\gamma_n) = \int_{-\frac{h_n}{2}}^{\frac{h_n}{2}} \frac{\partial G_f(\mathbf{r},\mathbf{r}_s)}{\partial n(\mathbf{r}_s)}. \tag{2.54}$$

From (2.48)

$$D(\mathbf{r},\gamma_n) = -\int_{-\frac{h_n}{2}}^{\frac{h_n}{2}} \frac{\partial G_f(\mathbf{r},\mathbf{r}_s)}{\partial Y_s}\bigg|_{Y_s=0} dX_s. \tag{2.55}$$

Partially differentiating $D(\mathbf{r},\gamma_n)$ with respect to X and noting (2.44) gives

$$\begin{aligned}\frac{\partial D(\mathbf{r},\gamma_n)}{\partial X} &= -\int_{-\frac{h_n}{2}}^{\frac{h_n}{2}} \frac{\partial}{\partial X_s}\frac{\partial G_f(\mathbf{r},(X_s,0))}{\partial Y} dX_S \\ &= \frac{\partial G_f(\mathbf{r},\mathbf{r}_-)}{\partial Y} - \frac{\partial G_f(\mathbf{r},\mathbf{r}_+)}{\partial Y}.\end{aligned} \tag{2.56}$$

Differentiation of (2.5) gives

$$\frac{\partial G_f(\mathbf{r},\mathbf{r}_s)}{\partial Y} = \frac{i}{4}H_1^{(1)}(k|\mathbf{r}-\mathbf{r}_s|)\frac{kY}{|\mathbf{r}-\mathbf{r}_s|}, \tag{2.57}$$

which substituted into (2.56) gives the final solution that

$$\frac{\partial D(\mathbf{r},\gamma_n)}{\partial X} = \frac{ikY}{4}\left\{\frac{H_1^{(1)}(k|\mathbf{r}-\mathbf{r}_-|)}{|\mathbf{r}-\mathbf{r}_-|} - \frac{H_1^{(1)}(k|\mathbf{r}-\mathbf{r}_+|)}{|\mathbf{r}-\mathbf{r}_+|}\right\}. \tag{2.58}$$

Partially differentiating $D(\mathbf{r},\gamma_n)$ with respect to Y and using (2.48) gives

$$\frac{\partial D(\mathbf{r},\gamma_n)}{\partial Y} = \int_{-\frac{h}{2}}^{\frac{h}{2}} \frac{\partial^2 G_f(\mathbf{r},\mathbf{r}_s)}{\partial Y_s^2}\bigg|_{Y_s=0} dX_s. \tag{2.59}$$

Now,

$$\frac{\partial^2 G_f(\mathbf{r},\mathbf{r}_s)}{\partial X_s^2} + \frac{\partial^2 G_f(\mathbf{r},\mathbf{r}_s)}{\partial Y_s^2} + k^2 G_f(\mathbf{r},\mathbf{r}_s) = 0. \tag{2.60}$$

Rearranging and substituting into (2.59) gives

$$\frac{\partial D(\mathbf{r},\gamma_n)}{\partial Y} = -\int_{-\frac{h_n}{2}}^{\frac{h_n}{2}} \frac{\partial^2 G_f(\mathbf{r},\mathbf{r}_s)}{\partial X_s^2}\bigg|_{Y_s=0} dX_s - k^2\int_{-\frac{h_n}{2}}^{\frac{h_n}{2}} G_f(\mathbf{r},\mathbf{r}_s)\bigg|_{Y_s=0} dX_s. \tag{2.61}$$

Evaluating the individual terms on the right hand side of (2.61), from (2.43) we obtain

$$\int_{-\frac{h_n}{2}}^{\frac{h_n}{2}} G_f(\mathbf{r},\mathbf{r}_s)dX_s = E(\mathbf{r},\gamma_n) \tag{2.62}$$

and

$$\begin{aligned}\int_{-\frac{h_n}{2}}^{\frac{h_n}{2}} \frac{\partial^2 G_f(\mathbf{r},\mathbf{r}_s)}{\partial X_s^2} dX_s &= \frac{\partial G_f(\mathbf{r},\mathbf{r}_-)}{\partial X} - \frac{\partial G_f(\mathbf{r},\mathbf{r}_+)}{\partial X} \\ &= \frac{ik}{4}\left\{H_1^{(1)}(k|\mathbf{r}-\mathbf{r}_-|)\frac{(X-X_-)}{|\mathbf{r}-\mathbf{r}_-|}\right. \\ &\qquad \left. -H_1^{(1)}(k|\mathbf{r}-\mathbf{r}_+|)\frac{(X-X_+)}{|\mathbf{r}-\mathbf{r}_+|}\right\}.\end{aligned} \tag{2.63}$$

Substituting for these results in (2.61) gives the final expression

$$\frac{\partial D(\mathbf{r},\gamma_n)}{\partial Y} = \frac{ik}{4}\left\{H_1^{(1)}(k|\mathbf{r}-\mathbf{r}_+|)\frac{(X-X_+)}{|\mathbf{r}-\mathbf{r}_+|} - H_1^{(1)}(k|\mathbf{r}-\mathbf{r}_-|)\frac{(X-X_-)}{|\mathbf{r}-\mathbf{r}_-|}\right\}$$
$$-k^2E(\mathbf{r},\gamma_n)$$
$$\approx \frac{ik}{4}\left\{H_1^{(1)}(k|\mathbf{r}-\mathbf{r}_+|)\frac{(X-X_+)}{|\mathbf{r}-\mathbf{r}_+|} - H_1^{(1)}(k|\mathbf{r}-\mathbf{r}_-|)\frac{(X-X_-)}{|\mathbf{r}-\mathbf{r}_-|}\right\}$$
$$-k^2e(\mathbf{r},\gamma_n). \quad (2.64)$$

From (2.58) and (2.64) it follows that

$$\frac{\partial D(\mathbf{r},\gamma_n)}{\partial x} \approx -\frac{n_y(\mathbf{r}_n)ikY}{4}\left\{\frac{H_1^{(1)}(k|\mathbf{r}-\mathbf{r}_-|)}{|\mathbf{r}-\mathbf{r}_-|} - \frac{H_1^{(1)}(k|\mathbf{r}-\mathbf{r}_+|)}{|\mathbf{r}-\mathbf{r}_+|}\right\}$$
$$-n_x(\mathbf{r}_n)\left\{\frac{ik}{4}\left\{H_1^{(1)}(k|\mathbf{r}-\mathbf{r}_+|)\frac{(X-X_+)}{|\mathbf{r}-\mathbf{r}_+|}\right.\right.$$
$$\left.\left.-H_1^{(1)}(k|\mathbf{r}-\mathbf{r}_-|)\frac{(X-X_-)}{|\mathbf{r}-\mathbf{r}_-|}\right\} - k^2e(\mathbf{r},\gamma_n)\right\}, \quad (2.65)$$

$$\frac{\partial D(\mathbf{r},\gamma_n)}{\partial y} \approx \frac{n_x(\mathbf{r}_n)ikY}{4}\left\{\frac{H_1^{(1)}(k|\mathbf{r}-\mathbf{r}_-|)}{|\mathbf{r}-\mathbf{r}_-|} - \frac{H_1^{(1)}(k|\mathbf{r}-\mathbf{r}_+|)}{|\mathbf{r}-\mathbf{r}_+|}\right\}$$
$$-n_y(\mathbf{r}_n)\left\{\frac{ik}{4}\left\{H_1^{(1)}(k|\mathbf{r}-\mathbf{r}_+|)\frac{(X-X_+)}{|\mathbf{r}-\mathbf{r}_+|}\right.\right.$$
$$\left.\left.-H_1^{(1)}(k|\mathbf{r}-\mathbf{r}_-|)\frac{(X-X_-)}{|\mathbf{r}-\mathbf{r}_-|}\right\} - k^2e(\mathbf{r},\gamma_n)\right\}, \quad (2.66)$$

and

$$\frac{\partial D(\mathbf{r},\gamma'_n)}{\partial x} \approx -\frac{n_y(\mathbf{r}_n)ikY}{4}\left\{\frac{H_1^{(1)}(k|\mathbf{r}-\mathbf{r}'_-|)}{|\mathbf{r}-\mathbf{r}'_-|} - \frac{H_1^{(1)}(k|\mathbf{r}-\mathbf{r}'_+|)}{|\mathbf{r}-\mathbf{r}'_+|}\right\}$$
$$-n_x(\mathbf{r}_n)\left\{\frac{ik}{4}\left\{H_1^{(1)}(k|\mathbf{r}-\mathbf{r}'_+|)\frac{(X-X_+)}{|\mathbf{r}-\mathbf{r}'_+|}\right.\right.$$
$$\left.\left.-H_1^{(1)}(k|\mathbf{r}-\mathbf{r}'_-|)\frac{(X-X_-)}{|\mathbf{r}-\mathbf{r}'_-|}\right\} - k^2e(\mathbf{r},\gamma'_n)\right\}, \quad (2.67)$$

$$\frac{\partial D(\mathbf{r},\gamma'_n)}{\partial y} \approx \frac{n_x(\mathbf{r}_n)ikY}{4}\left\{\frac{H_1^{(1)}(k|\mathbf{r}-\mathbf{r}'_-|)}{|\mathbf{r}-\mathbf{r}'_-|} - \frac{H_1^{(1)}(k|\mathbf{r}-\mathbf{r}'_+|)}{|\mathbf{r}-\mathbf{r}'_+|}\right\}$$
$$-n_y(\mathbf{r}_n)\left\{\frac{ik}{4}\left\{H_1^{(1)}(k|\mathbf{r}-\mathbf{r}'_+|)\frac{(X-X_+)}{|\mathbf{r}-\mathbf{r}'_+|}\right.\right.$$
$$\left.\left.-H_1^{(1)}(k|\mathbf{r}-\mathbf{r}'_-|)\frac{(X-X_-)}{|\mathbf{r}-\mathbf{r}'_-|}\right\} - k^2e(\mathbf{r},\gamma'_n)\right\}. \quad (2.68)$$

The accuracy of the approximations $d(\mathbf{r}, \gamma_n)$ and $e(\mathbf{r}, \gamma_n)$ for $D(\mathbf{r}, \gamma_n)$ and $E(\mathbf{r}, \gamma_n)$ are now examined together with the accuracy of the approximations proposed above for $\nabla D(\mathbf{r}, \gamma_n)$ and $\nabla E(\mathbf{r}, \gamma_n)$. Letting $[\nabla D(\mathbf{r}, \gamma_n)]_{app}$ and $[\nabla E(\mathbf{r}, \gamma_n)]_{app}$ denote the approximations using (2.46), (2.49), (2.58) and (2.64) for $\nabla D(\mathbf{r}, \gamma_n)$ and $\nabla E(\mathbf{r}, \gamma_n)$ respectively, it is seen that

$$|\nabla D(\mathbf{r}, \gamma_n) - [\nabla D(\mathbf{r}, \gamma_n)]_{app}| = |E(\mathbf{r}, \gamma_n) - e(\mathbf{r}, \gamma_n)| \tag{2.69}$$

and

$$|\nabla E(\mathbf{r}, \gamma_n) - [\nabla E(\mathbf{r}, \gamma_n)]_{app}| = |D(\mathbf{r}, \gamma_n) - d(\mathbf{r}, \gamma_n)| \tag{2.70}$$

In Figure 2.15, the errors in $e(\mathbf{r}, \gamma_n)$, $|E(\mathbf{r}, \gamma_n) - e(\mathbf{r}, \gamma_n)|$ and the errors in $d(\mathbf{r}, \gamma_n)$, $|D(\mathbf{r}, \gamma_n) - d(\mathbf{r}, \gamma_n)|$ are plotted against the angle that $\mathbf{r} - \mathbf{r}_n$ makes with the element γ_n, where $E(\mathbf{r}, \gamma_n)$ and $D(\mathbf{r}, \gamma_n)$, given by (2.42) and (2.54) respectively, have been computed accurately using the numerical quadrature functions built into the programming language Matlab. Comparing these plots with Figure 2.15, where $|e(\mathbf{r}, \gamma_n)|$ and $|d(\mathbf{r}, \gamma_n)|$ are similarly plotted, it is observed that errors not exceeding 1% are consistently achieved for an element length of 0.1λ.

To check the FORTRAN code for evaluation of approximations to the $x-$ and $y-$components of $[\nabla D(\mathbf{r}, \gamma_n)]_{app}$ and $[\nabla E(\mathbf{r}, \gamma_n)]_{app}$, also plotted in Figure 2.15 is the modulus of the difference between $[\nabla D(\mathbf{r}, \gamma_n)]_{app}$ and a simple centred finite difference approximation to $\nabla D(\mathbf{r}, \gamma_n)$ implemented in Matlab. Not surprisingly, in view of 2.69, this difference is identical with $|E(\mathbf{r}, \gamma_n) - e(\mathbf{r}, \gamma_n)|$. Similarly compared in Figure 2.15 is $[\nabla E(\mathbf{r}, \gamma_n)]_{app}$ with a finite difference approximation, the difference between the two being identical, as it should be, to $|D(\mathbf{r}, \gamma_n) - d(\mathbf{r}, \gamma_n)|$.

Finally, consider the evaluation of the partial derivatives of the P_{β_c} components (those terms which take account of the contribution resulting from an impedance boundary). Consider first, the partial derivatives of C_p (the single layer potential component), given by

$$C_p(\mathbf{r}, \gamma_n) = \int_{\gamma_n} P_{\beta_c}(\mathbf{r}, \mathbf{r}_s) ds(\mathbf{r}_s). \tag{2.71}$$

a) Near receiver (0.1λ from midpoint of element)

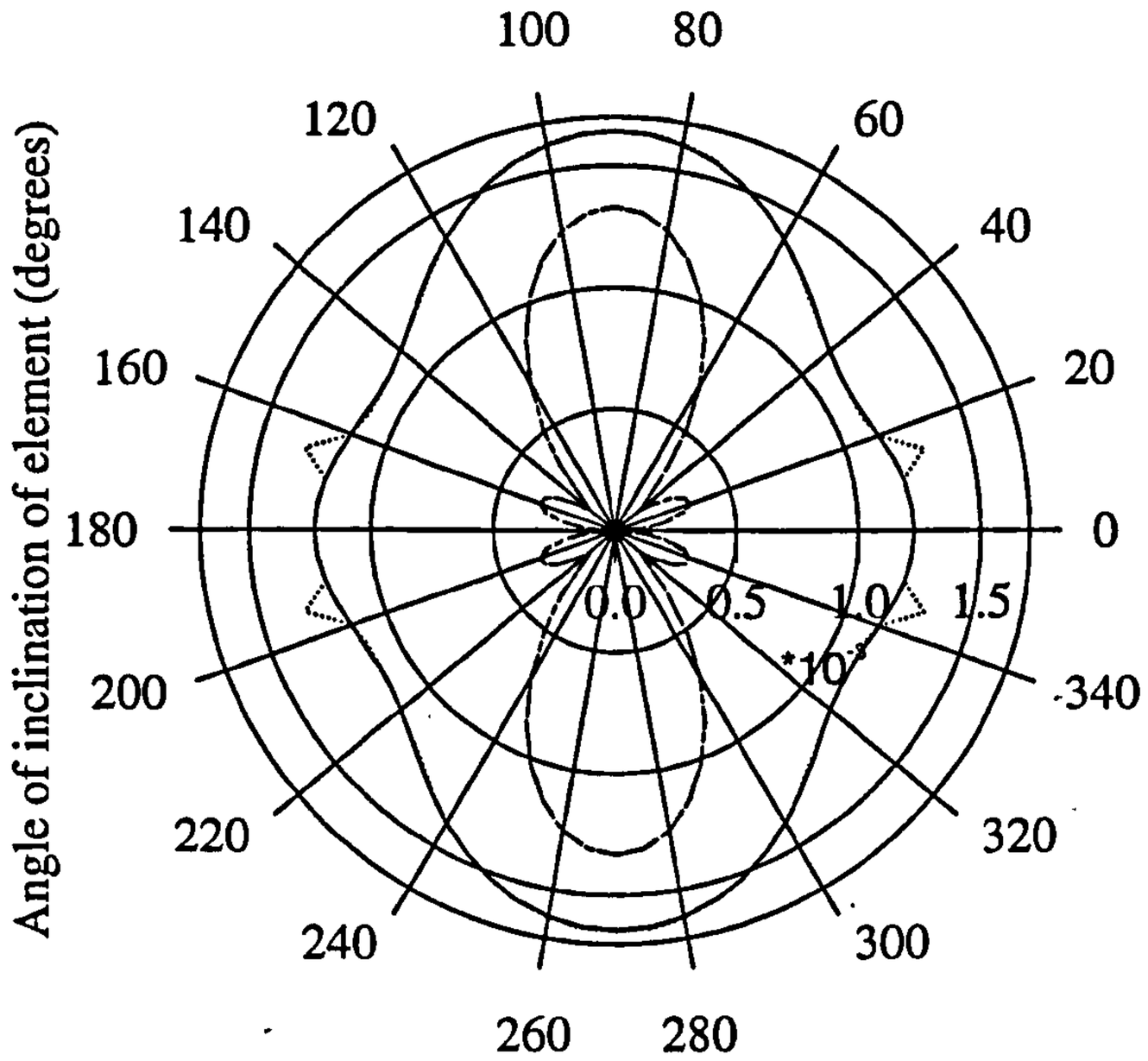

b) Distant receiver (20λ from midpoint of element)

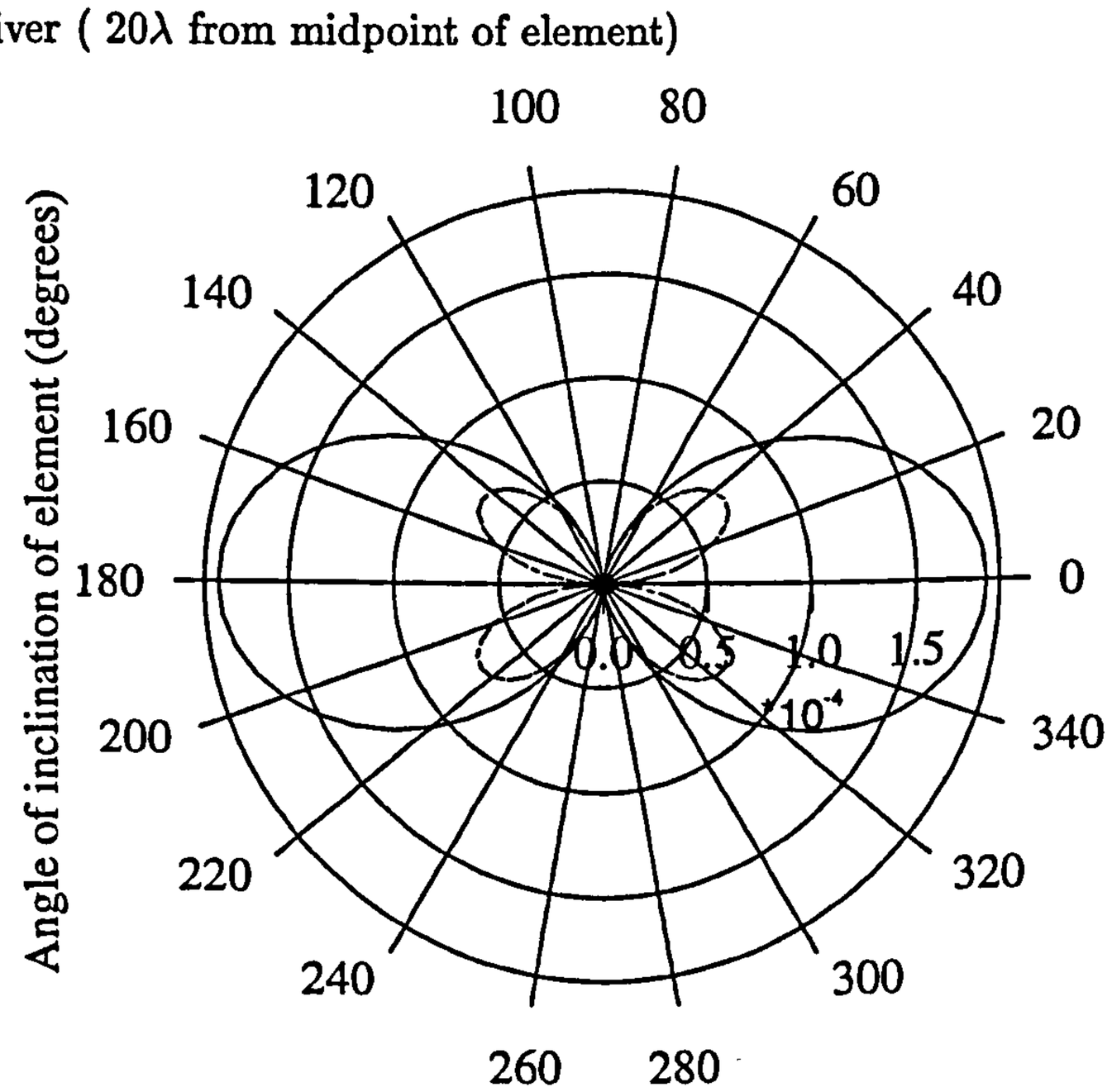

Figure 2.15: Comparison of the errors in $\nabla D(\mathbf{r}, \gamma_n)$ and $\nabla E(\mathbf{r}, \gamma_n)$ with the errors in $E(\mathbf{r}, \gamma_n)$ and $D(\mathbf{r}, \gamma_n)$ respectively ($k = 1.0$, element length $= 0.1\lambda$); ——, |error in $E(\mathbf{r}, \gamma_n)$|; ·····, |error in $\nabla D(\mathbf{r}, \gamma_n)$|; - - - -, |error in $D(\mathbf{r}, \gamma_n)$|; — ·· —, |error in $\nabla E(\mathbf{r}, \gamma_n)$|. The angle of inclination is the angle between the line of the element and that from receiver to element midpoint.

Partially differentiating (2.71) with respect to y gives

$$\frac{\partial C_p(\mathbf{r},\gamma_n)}{\partial y} = \int_{\gamma_n} \frac{\partial P_{\beta_c}(\mathbf{r},\mathbf{r}_s)}{\partial y} ds(\mathbf{r}_s). \tag{2.72}$$

From (2.7) we can express partial derivatives of P_{β_c} in the form

$$\frac{\partial^{a+b+c+d}}{\partial x^a \partial y^b \partial x_s^c \partial y_s^d} P_{\beta_c}(\mathbf{r},\mathbf{r}_s) = k^{a+b+c+d}(-1)^c \frac{\partial^{a+b+c+d}}{\partial \xi^{a+c} \partial \eta^{b+d}} \widehat{P}_{\beta_c}(\xi,\eta) \tag{2.73}$$

where, $\xi = k[x - x_s]$, $\eta = [y + y_s]$. Substituting for (2.73) in (2.72), gives

$$\frac{\partial C_p(\mathbf{r},\gamma_n)}{\partial y} = k \int_{\gamma_n} \frac{\partial \widehat{P}_{\beta_c}(\xi,\eta)}{\partial \eta} ds(\mathbf{r}_s). \tag{2.74}$$

Equation (D23) of Theorem 8 in [17] states that

$$\frac{\partial \widehat{P}_{\beta_c}(\xi,\eta)}{\partial \eta} = -i\beta_c \widehat{P}_{\beta_c}(\xi,\eta) - \frac{1}{2}\beta_c H_0^{(1)}(r), \tag{2.75}$$

where $r = \sqrt{\xi^2 + \eta^2}$. From (2.5), this can be expressed as

$$\frac{\partial P_{\beta_c}(\xi,\eta)}{\partial \eta} = -i\beta_c P_{\beta_c}(\xi,\eta) - 2i\beta_c G_f(\mathbf{r},\mathbf{r'}_s). \tag{2.76}$$

Substituting this into (2.74) gives

$$\begin{aligned} \frac{\partial C_p(\mathbf{r},\gamma_n)}{\partial y} &= -ik\beta_c \left\{ \int_{\gamma_n} P_{\beta_c}(\mathbf{r},\mathbf{r}_s) ds(\mathbf{r}_s) + 2\int_{\gamma_n} G_f(\mathbf{r},\mathbf{r'}_s) ds(\mathbf{r}_s) \right\} \\ &= -ik\beta_c \{C_p(\mathbf{r},\gamma_n) + 2E(\mathbf{r},\gamma'_n)\} \end{aligned} \tag{2.77}$$

Approximations $c_p(\mathbf{r},\gamma_n)$ and $e(\mathbf{r},\gamma_n)$ to the integrals $C_p(\mathbf{r},\gamma_n)$ and $E(\mathbf{r},\gamma'_n)$ in the above equation have been discussed already (see equations (2.19)-(2.21) and neighbouring text). Making these approximations gives the final result that

$$\frac{\partial C_p(\mathbf{r},\gamma_n)}{\partial y} \approx -ik\beta_c h_n P_{\beta_c}(\mathbf{r},\mathbf{r}_n) - 2ik\beta_c e(\mathbf{r},\gamma'_n). \tag{2.78}$$

Partially differentiating (2.71) with respect to x gives

$$\frac{\partial C_p(\mathbf{r},\gamma_n)}{\partial x} = \int_{\gamma_n} \frac{\partial P_{\beta_c}(\mathbf{r},\mathbf{r}_s)}{\partial x} ds(\mathbf{r}_s) \tag{2.79}$$

$$= -\int_{\gamma_n} \frac{\partial P_{\beta_c}(\mathbf{r},\mathbf{r}_s)}{\partial x_s} ds(\mathbf{r}_s). \tag{2.80}$$

Applying the midpoint rule as done in (2.23) to obtain (2.24) we get that

$$\frac{\partial C_p(\mathbf{r},\gamma_n)}{\partial x} \approx -h_n \frac{\partial P_{\beta_c}(\mathbf{r},\mathbf{r}_s)}{\partial x_s}\bigg|_{\mathbf{r}_s=\mathbf{r}_n} = kh_n \frac{\partial \widehat{P}_{\beta_c}(\xi,\eta)}{\partial \xi}\bigg|_{\xi=k[x-x_n]} \tag{2.81}$$

Now consider the partial derivatives of B_p (the double layer potential component), given by

$$B_p(\mathbf{r},\gamma_n) = \int_{\gamma_n} \frac{\partial P_{\beta_c}(\mathbf{r},\mathbf{r}_s)}{\partial n(\mathbf{r}_s)} ds(\mathbf{r}_s) \tag{2.82}$$

which can be written as

$$\begin{aligned} B_p(\mathbf{r},\gamma_n) &= n(\mathbf{r}_s)\cdot \int_{\gamma_n} \nabla_{\mathbf{r}_s} P_{\beta_c}(\mathbf{r},\mathbf{r}_s) ds(\mathbf{r}_s) \\ &= n_x(\mathbf{r}_s)\int_{\gamma_n} \frac{\partial P_{\beta_c}(\mathbf{r},\mathbf{r}_s)}{\partial x_s} ds(\mathbf{r}_s) + n_y(\mathbf{r}_s)\int_{\gamma_n} \frac{\partial P_{\beta_c}(\mathbf{r},\mathbf{r}_s)}{\partial y_s} ds(\mathbf{r}_s). \end{aligned} \tag{2.83}$$

From (2.73)

$$B_p(\mathbf{r},\gamma_n) = -kn_x(\mathbf{r}_s)\int_{\gamma_n} \frac{\partial \widehat{P}_{\beta_c}(\xi,\eta)}{\partial \xi} ds(\mathbf{r}_s) + kn_y(\mathbf{r}_s)\int_{\gamma_n} \frac{\partial \widehat{P}_{\beta_c}(\xi,\eta)}{\partial \eta} ds(\mathbf{r}_s). \tag{2.84}$$

Partially differentiating with respect to x, then

$$\frac{\partial B_p(\mathbf{r},\gamma_n)}{\partial x} = -k^2 n_x(\mathbf{r}_s)\int_{\gamma_n} \frac{\partial^2 \widehat{P}_{\beta_c}(\xi,\eta)}{\partial \xi^2} ds(\mathbf{r}_s) + k^2 n_y(\mathbf{r}_s)\int_{\gamma_n} \frac{\partial^2 \widehat{P}_{\beta_c}(\xi,\eta)}{\partial \xi \partial \eta} ds(\mathbf{r}_s). \tag{2.85}$$

Equations (D26) and (D25) in Theorem 8 of [17] give that

$$\begin{aligned} \frac{\partial^2 \widehat{P}_{\beta_c}(\xi,\eta)}{\partial \xi \partial \eta} &= -i\beta_c \frac{\partial \widehat{P}_{\beta_c}(\xi,\eta)}{\partial \xi} - \frac{1}{2}\beta_c \frac{\partial H_0^{(1)}(r)}{\partial \xi} \\ &= -i\beta_c \frac{\partial \widehat{P}_{\beta_c}(\xi,\eta)}{\partial \xi} - 2i\beta_c \frac{\partial G_f(\mathbf{r},\mathbf{r}'_s)}{\partial \xi} \end{aligned} \tag{2.86}$$

and

$$\begin{aligned} \frac{\partial^2 \widehat{P}_{\beta_c}(\xi,\eta)}{\partial \xi^2} &= (\beta_c^2 - 1)\widehat{P}_{\beta_c}(\xi,\eta) - \frac{1}{2}i\beta_c^2 H_0^{(1)}(r) + \frac{1}{2}\beta_c \frac{\partial H_0^{(1)}(r)}{\partial \eta} \\ &= (\beta_c^2 - 1)\widehat{P}_{\beta_c}(\xi,\eta) + 2\beta_c^2 G_f(\mathbf{r}_s,\mathbf{r}'_s) + 2i\beta_c \frac{\partial G_f(\mathbf{r},\mathbf{r}'_s)}{\partial \eta}. \end{aligned} \tag{2.87}$$

Substitution of these results into (2.85) and using (2.73) gives that

$$\begin{aligned}\frac{\partial B_p(\mathbf{r},\gamma_n)}{\partial x} = \quad & -kn_y(\mathbf{r}_s)i\beta_c\left\{\frac{\partial C_p(\mathbf{r},\gamma_n)}{\partial x}+2\frac{\partial E(\mathbf{r},\gamma_n')}{\partial x}\right\} \\ & -k^2n_x(\mathbf{r}_s)\left\{(\beta_c^2-1)C_p(\mathbf{r},\gamma_n)+2\beta_c^2E(\mathbf{r},\gamma_n')+\frac{2i\beta_c}{k}\frac{\partial E(\mathbf{r},\gamma_n'}{\partial y}\right\}\end{aligned} \tag{2.88}$$

The right hand side of this expression is then approximated using (2.81), (2.52), (2.53) and the approximations $c_p(\mathbf{r},\gamma_n)$ and $e(\mathbf{r},\gamma_n')$ for $C_p(\mathbf{r},\gamma_n)$ and $E(\mathbf{r},\gamma_n')$ defined in (2.21) and the preceeding text.

Partially differentiating (2.84) with respect to y, then

$$\frac{\partial B_p(\mathbf{r},\gamma_n)}{\partial y} = k^2n_y(\mathbf{r}_n)\int_{\gamma_n}\frac{\partial^2\hat{P}_{\beta_c}(\xi,\eta)}{\partial\eta^2}ds(\mathbf{r}_s)-k^2n_x(\mathbf{r}_n)\int_{\gamma_n}\frac{\partial^2\hat{P}_{\beta_c}(\xi,\eta)}{\partial\xi\partial\eta}ds(\mathbf{r}_s). \tag{2.89}$$

Equation (D24) in Theorem 8 of [17] gives that

$$\begin{aligned}\frac{\partial^2\hat{P}_{\beta_c}(\xi,\eta)}{\partial\eta^2} &= -\beta_c^2\hat{P}_{\beta_c}(\xi,\eta)+\frac{1}{2}i\beta_c^2H_0^{(1)}(r)-\frac{1}{2}\beta_c\frac{\partial H_0^{(1)}(r)}{\partial\eta} \\ &= -\beta_c^2\hat{P}_{\beta_c}(\xi,\eta)-2\beta_c^2G_f(\mathbf{r},\mathbf{r}_s')-2i\beta_c\frac{\partial G_f(\mathbf{r},\mathbf{r}_s')}{\partial\eta}\end{aligned} \tag{2.90}$$

Substituting this result and (2.86) into (2.89) gives

$$\begin{aligned}\frac{\partial B_p(\mathbf{r},\gamma_n)}{\partial y} = \quad & -k^2n_y(\mathbf{r}_n)\beta_c^2\left\{C_p(\mathbf{r},\gamma_n)+2E(\mathbf{r},\gamma_n')\frac{2i}{\beta_ck}+\frac{\partial E(\mathbf{r},\gamma_n')}{\partial y}\right\} \\ & +kn_x(\mathbf{r}_n)i\beta_c\left\{\frac{\partial C_p(\mathbf{r},\gamma_n)}{\partial x}+2\frac{\partial E(\mathbf{r},\gamma_n')}{\partial x}\right\}\end{aligned} \tag{2.91}$$

The right hand side of this expression is then approximated using (2.81), (2.52), (2.53) and the approximations $c_p(\mathbf{r},\gamma_n)$ and $e(\mathbf{r},\gamma_n')$ for $C_p(\mathbf{r},\gamma_n)$ and $E(\mathbf{r},\gamma_n')$ respectively.

Within the computer program the approximate partial derivatives of $P_{\beta_c}(\mathbf{r},\gamma_n)$ as given by (2.78), (2.81), (2.88) and (2.91) are not calculated explicitly. However, it is still possible to check the accuracy of the approximations by computing (2.41)

for a specific case in which the exact value of the sum in (2.41) is known. Consider a barrier of arbitrary shape on flat ground of admittance β_c as in Figure 2.1. For an arbitrary source position, $\mathbf{r}_0$, compute (2.41) for the situation when the pressure upon the *nth* element of the barrier is defined as being that in the absence of the barrier, i.e.

$$p(\mathbf{r}_n, \mathbf{r}_0) = G_{\beta_c}(\mathbf{r}_n, \mathbf{r}_0) \tag{2.92}$$

and the admittance of the *nth* element is given, from (2.3), by

$$\beta(\mathbf{r}_n) = \frac{n(\mathbf{r}_n).\nabla G_{\beta_c}(\mathbf{r}_n, \mathbf{r}_0)}{ikG_{\beta_c}(\mathbf{r}_n, \mathbf{r}_0)} \tag{2.93}$$

Under these conditions, the summations in (2.38) and (2.41) should vanish, at least in the limit $h \to 0$. (This is the case since, by Green's theorem applied in the interior of γ in Figure 2.1,

$$\int_\gamma \left(G_{\beta_c}(\mathbf{r}_s, \mathbf{r}_0) \frac{\partial G_{\beta_c}(\mathbf{r}_s, \mathbf{r})}{\partial n(\mathbf{r}_s)} - G_{\beta_c}(\mathbf{r}_s, \mathbf{r}) \frac{\partial G_{\beta_c}(\mathbf{r}_s, \mathbf{r}_0)}{\partial n(\mathbf{r}_s)} \right) ds(\mathbf{r}_s) = 0, \tag{2.94}$$

for $\mathbf{r}, \mathbf{r}_0 \in D$). The value of $\nabla_{\mathbf{r}} p(\mathbf{r}, \mathbf{r}_0)$ as calculated at an arbitrary receiver position, $\mathbf{r}$, should therefore be equal to that calculated at the same coordinates in the absence of the barrier, i.e. it should hold that

$$\nabla_{\mathbf{r}} p(\mathbf{r}, \mathbf{r}_0) = \nabla_{\mathbf{r}} G_{\beta_c}(\mathbf{r}, \mathbf{r}_0) \tag{2.95}$$

The case $\beta_c = 0$ can be considered to provide a further check upon the accuracy of the partial derivatives of $E(\mathbf{r}, \gamma_n)$ and $D(\mathbf{r}, \gamma_n)$.

These comparisons have been carried out by applying the method to the cross-section shown in Figure 2.16, which sits on either a rigid boundary ($\beta_c = 0$) or, in the case of $\beta_c \neq 0$, an impedance boundary having a flow resistivity $\sigma = 20,000 Nsm^{-4}$ and depth $D = \infty$. The coordinates of the source and receiver were (-2.50, 0.50) and (-0.5, 1.0) respectively.

Four frequencies have been considered, namely 250, 500, 1000 and 2000 Hz, using initial element lengths of 0.05λ, 0.08λ, 0.125λ and 0.20λ respectively in the discretization of the obstacle. Three subsequent simulations have been conducted, each time reducing the element length by half. At each frequency, the difference $|\nabla_{\mathbf{r}} G_{\beta_c}(\mathbf{r}, \mathbf{r}_0) - \nabla_{\mathbf{r}} p(\mathbf{r}, \mathbf{r}_0)|$ has been calculated, with $\nabla_{\mathbf{r}} p(\mathbf{r}, \mathbf{r}))$ approximated by the

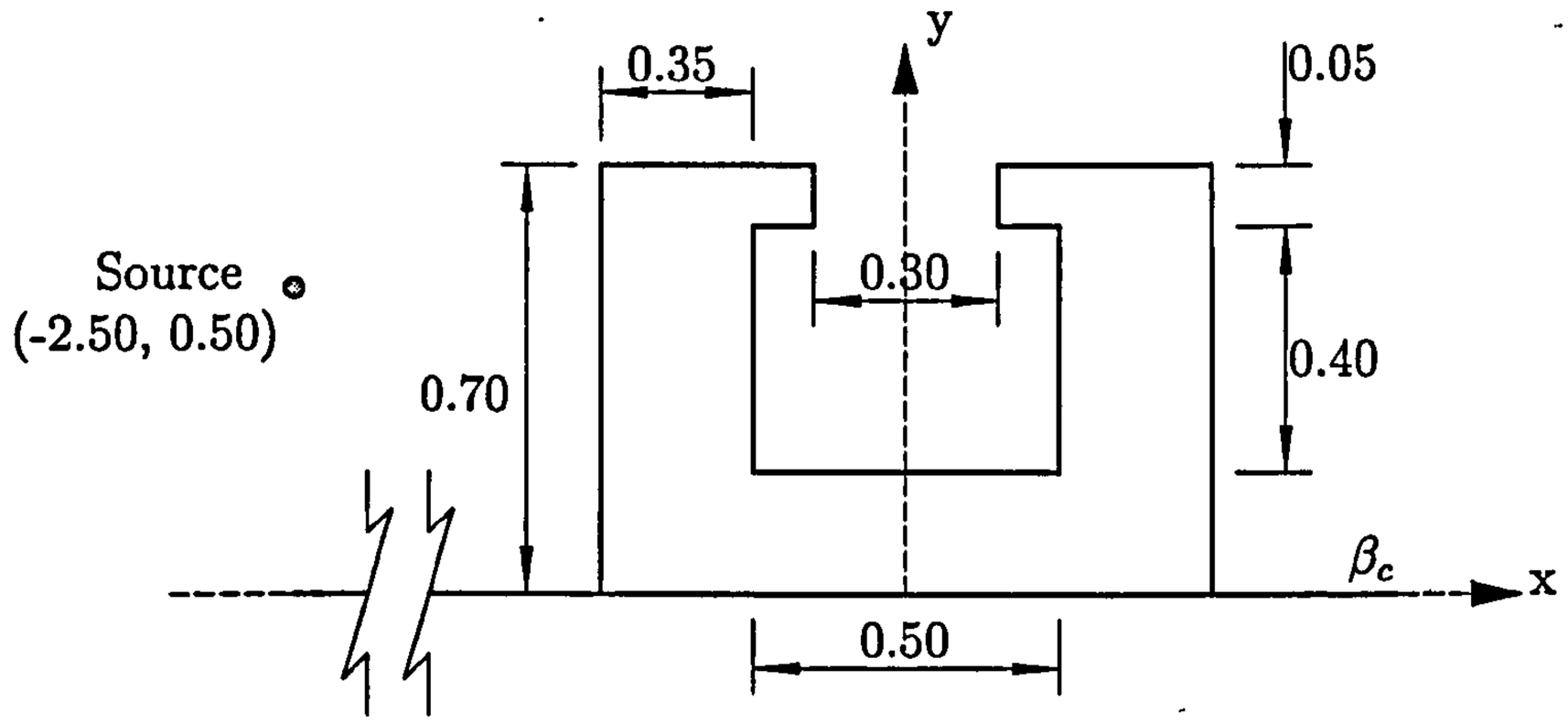

Figure 2.16: Cross-section used to verify the accuracy of the approximations to the partial derivatives of $P_{\beta_c}(\xi, \eta)$. Dimensions in metres.

right-hand side of (2.41) with $\nabla_{\mathbf{r}} B(\mathbf{r}, \gamma_n)$ and $\nabla_{\mathbf{r}} C(\mathbf{r}, \gamma_n)$ approximated as discussed in the above section. Similarly the error $|p(\mathbf{r}, \mathbf{r}_0) - G_{\beta_c}(\mathbf{r}, \mathbf{r}_0)|$, has been calculated with $p(\mathbf{r}, \mathbf{r}_0)$ given by the right-hand side of (2.38). Figure 2.17 plots the modulus of these errors as a function of kh, where k is the wavenumber and h the corresponding element length, for the case $\beta_c \neq 0$.

Considering Figure 2.17a, the modulus of the errors are small compared to the modulus of the corresponding exact solutions, indicating that the formulations are sufficiently accurate. The same observation can be drawn from the results for ∇p (Figure 2.17b). From these results, the estimated order of convergence (EOC) in the error has been calculated and is presented in Table 2.2. Corresponding results for the case $\beta_c = 0$ are shown in Table 2.3. For both cases, the order of convergence is observed to tend towards 1.0, except at the frequency 1000 Hz for the case $\beta_c \neq 0$. The convergence is not as rapid as would normally be expected upon application of the midpoint rule which should give a EOC of 2.0. No clear reason is apparent for this variation. However the accuracy of sound pressure levels predicted using the modified procedure and presented later in this chapter do not appear to be affected when compared with results obtained using other techniques (Section 2.3.3).

a) $|p|$ and corresponding |error|

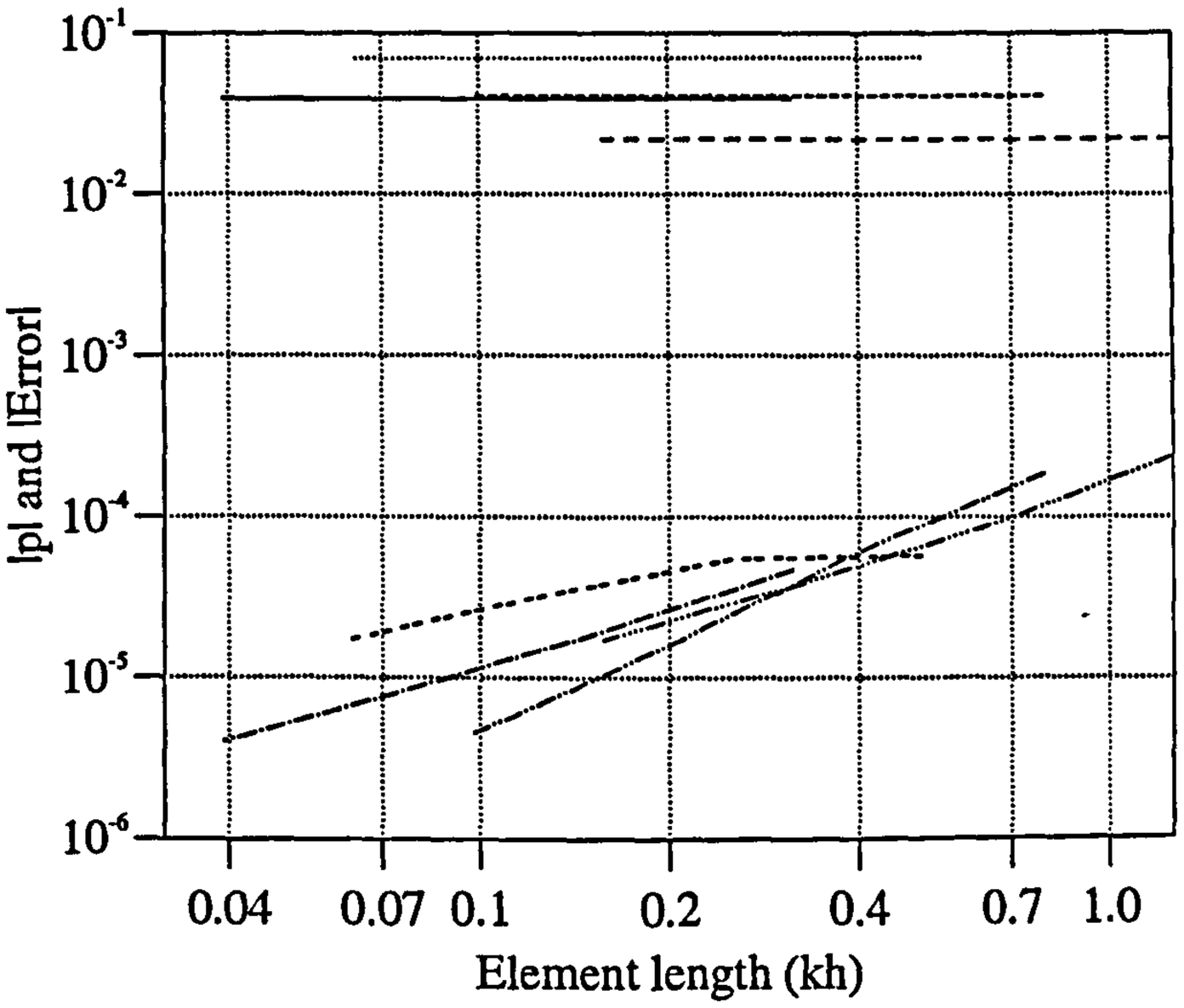

b) $|\nabla p|$ and corresponding |error|

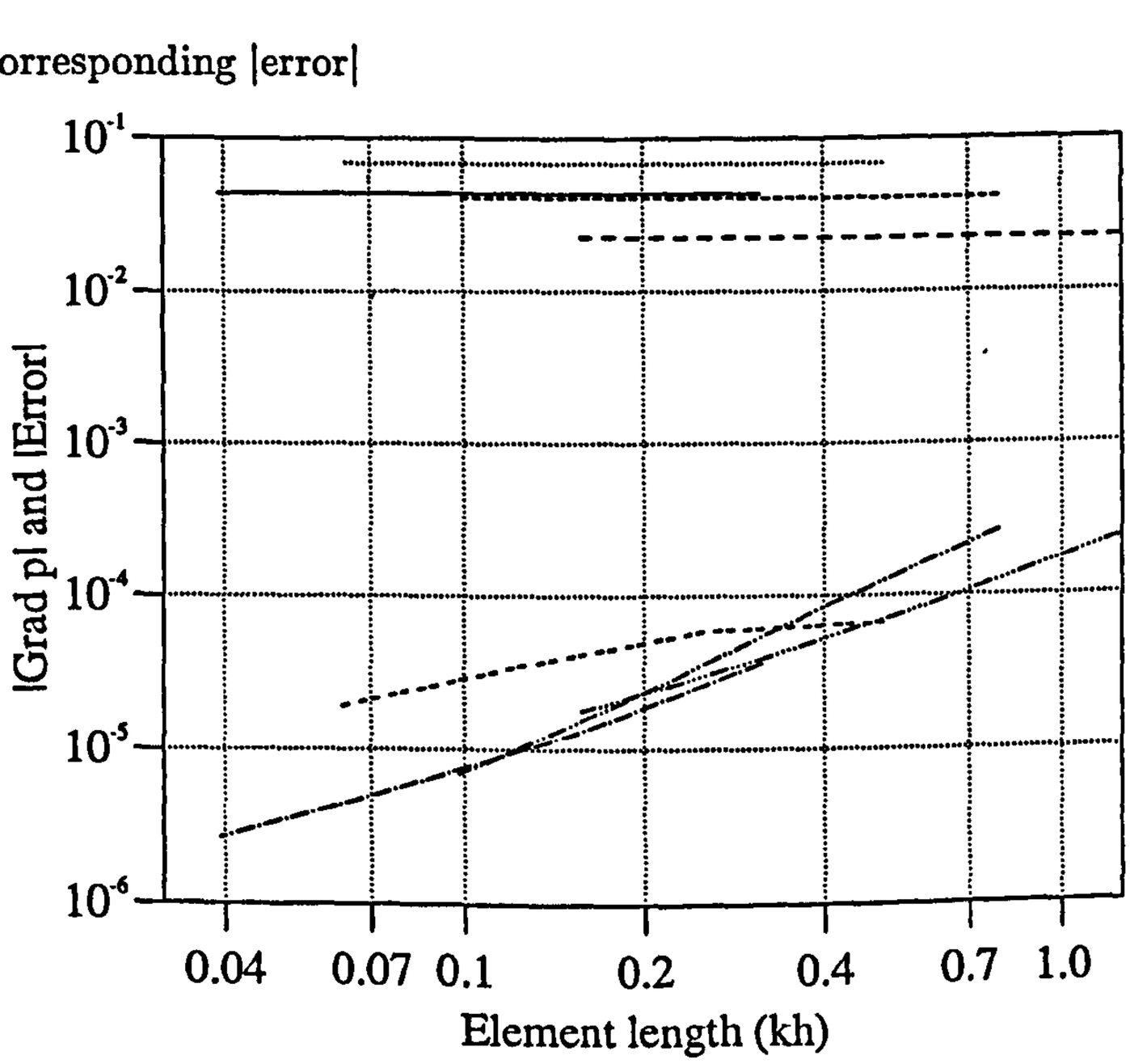

Figure 2.17: $|p|$, $|\nabla p|$ and corresponding |error| for the case $\beta_c \neq 0$; ——, $|p|$ or $|\nabla p|$ (250 Hz); · · · · · ·, $|p|$ or $|\nabla p|$ (500 Hz); - - - -, $|p|$ or $|\nabla p|$ (1 kHz); – – –, $|p|$ or $|\nabla p|$ (2 kHz); – · – ·, |error| (250 Hz); -- -- --, |error| (500 Hz); – ·· – ··, |error| (1 kHz); – · · · – · · ·, |error| (2kHz)

Frequency	kh	|Error in p|	EOC	| Error in ∇p|	EOC
250Hz	0.314	4.64646e-05	1.24727	3.64726e-05	1.46598
	0.157	1.95730e-05	1.17641	1.32027e-05	1.21800
	0.078	8.66011e-06	1.12672	5.67557e-06	1.09078
	0.039	3.96594e-06		2.66471e-06	
500Hz	0.503	5.70063e-05	0.06455	6.62647e-05	0.179762
	0.251	5.45120e-05	0.74807	5.85016e-05	0.72214
	0.126	3.24565e-05	0.89919	3.54636e-05	0.88606
	0.063	1.74027e-05		1.91890e-05	
1000Hz	0.785	1.84283e-04	1.66461	2.60779e-04	1.67191
	0.392	5.81285e-05	1.91656	8.18425e-05	1.83779
	0.196	1.53975e-05	1.75727	2.28955e-05	1.72899
	0.098	4.55469e-06		6.90672e-06	
2000Hz	1.257	2.34960e-04	1.47366	2.36716e-04	1.37683
	0.628	8.46016e-05	1.18335	9.11508e-05	1.22518
	0.314	3.72534e-05	1.10124	3.89892e-05	1.13128
	0.157	1.73640e-05		1.77990e-05	

Table 2.2: Predicted EOC values for the case $\beta_c \neq 0$

Frequency	kh	|Error in p|	EOC	| Error in ∇p|	EOC
250Hz	0.314	2.55696e-04	0.93020	2.90734e-04	1.07722
	0.157	1.34186e-04	1.03825	1.36691e-04	1.09588
	0.079	6.53375e-05	1.03659	6.44656e-05	1.05984
	0.039	3.18506e-05		3.09231e-05	
500Hz	0.502	6.32659e-04	0.99630	7.72375e-04	1.04163
	0.251	3.17140e-04	1.06644	3.51580e-04	1.09840
	0.125	1.51434e-04	1.03899	1.64202e-04	1.05576
	0.063	7.36985e-05		7.89884e-05	
1000Hz	0.785	2.20265e-04	1.37520	3.00240e-04	1.55757
	0.393	8.49119e-05	1.01282	1.01999e-04	1.22304
	0.196	4.20805e-05	0.94493	4.36942e-05	1.00332
	0.098	2.18589e-05		2.17969e-05	
2000Hz	1.257	4.22776e-04	1.73712	4.05940e-04	1.63622
	0.628	1.26820e-04	1.42670	1.30591e-04	1.40855
	0.314	4.71745e-05	1.26974	4.91921e-05	1.26713
	0.157	1.95650e-05		2.04386e-05	

Table 2.3: Predicted EOC values for the case $\beta_c = 0$

2.3.3 Testing of the Modified Solution Procedure

Verification of Accuracy Using an Incident Plane Wave

As a first check of the whole modified solution procedure, a simple case has been considered for which the exact solution can be determined. Consider the cross-section shown in Figure 2.18, of an obstacle composed solely of horizontal and vertical surfaces, and an incident plane wave propagating vertically downwards.

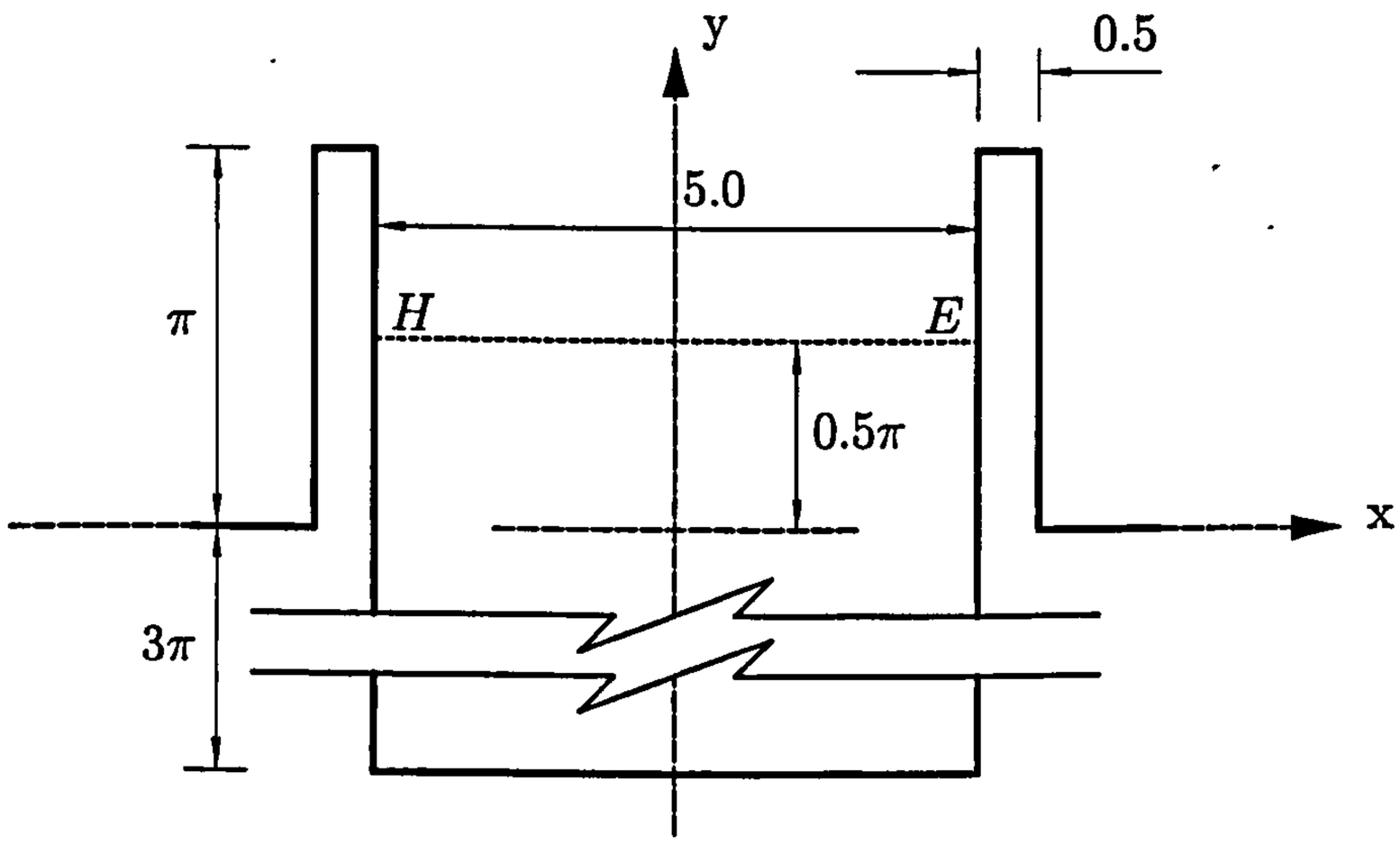

Figure 2.18: Cross-section used for plane wave propagation tests. Dimensions in metres.

Provided that all vertical surfaces are rigid, to ensure that there is no interaction with the incident wave, and that all horizontal surfaces have the same admittance β_c and are of height H such that $H = 0.5n\lambda$, for some integer n, then the exact complex sound pressure at an arbitrary receiver position $\mathbf{r} = (x, y)$ is given by

$$p(\mathbf{r}, \mathbf{r}_0) = e^{-iky} + \frac{1 - \beta_c}{1 + \beta_c} e^{iky}. \tag{2.96}$$

The modified solution procedure of page 34 has been applied using the dimensions given in Figure 2.18, with horizontal surfaces which are either rigid or having an impedance such that $\beta_c = 1$ and appropriate source frequencies ($k = 1.0$ in the rigid and 2.0 in the finite impedance cases respectively). An initial element length of $h = 0.05\lambda$ has been used in the discretization, subsequent simulations using reduced element sizes.

The results are presented in terms of the absolute error in the sound pressure or its partial derivatives, defined as the difference between the exact solution, given by (2.96), and that obtained using the modified solution procedure. Note that $\tilde{p}$, the approximation to p to be computed at Stages 1 and 2, is also given by (2.96) though, of course, the value calculated is not exactly (2.96) as (2.33) is solved numerically.

Figure 2.19 plots the modulus of the error in each of the partial derivatives at receiver positions on the line EH (see Figure 2.18) for the case with rigid horizontal surfaces. The pressures at these receivers are those calculated during Stage 2 of the modified procedure (see 2.3.1). Figure 2.20 plots the equivalent errors for the case having non-rigid horizontal surfaces.

In both figures, it is observed that the modulus of the error is, for the most part, very small in comparison to the modulus of the exact pressure and converging to zero as the element size decreases. The error is greatest upon the element closest to each of the cutting walls (its position relative to local elements being constant, regardless of element size). The magnitude of these errors is attributable to the fact that the point of contact between each wall and the line EH coincides with a node between adjacent elements on the cutting wall. In this instance, the problem lies with Equation (2.41) which predicts that ∇p is infinite at each boundary element node, whereas ∇p is actually continuous up to the boundary except possibly at corner points.

Figure 2.21 plots the modulus of the error in the pressure calculated at receiver positions lying on a horizontal line above the top of the cutting (at a height $y = 2\pi$). These are pressures calculated at the end of the modified solution procedure, i.e. Stage 3 (see Section 2.3.1). In both cases the errors are very small in comparison to the exact solution.

For the fully rigid cross-section (Figure 2.21a), the error recorded above the midpoint of the cutting ($kx = 0$) appears independent of the elements size. Approaching the cutting sides ($kx = 5.0$) there is a sharp increase in error when using larger boundary elements. This trend reduces as the element size is decreased. On

a) Absolute errors in the computation of the x-derivative of the pressure
Exact value of $|\partial\tilde{p}/\partial x| = 0$

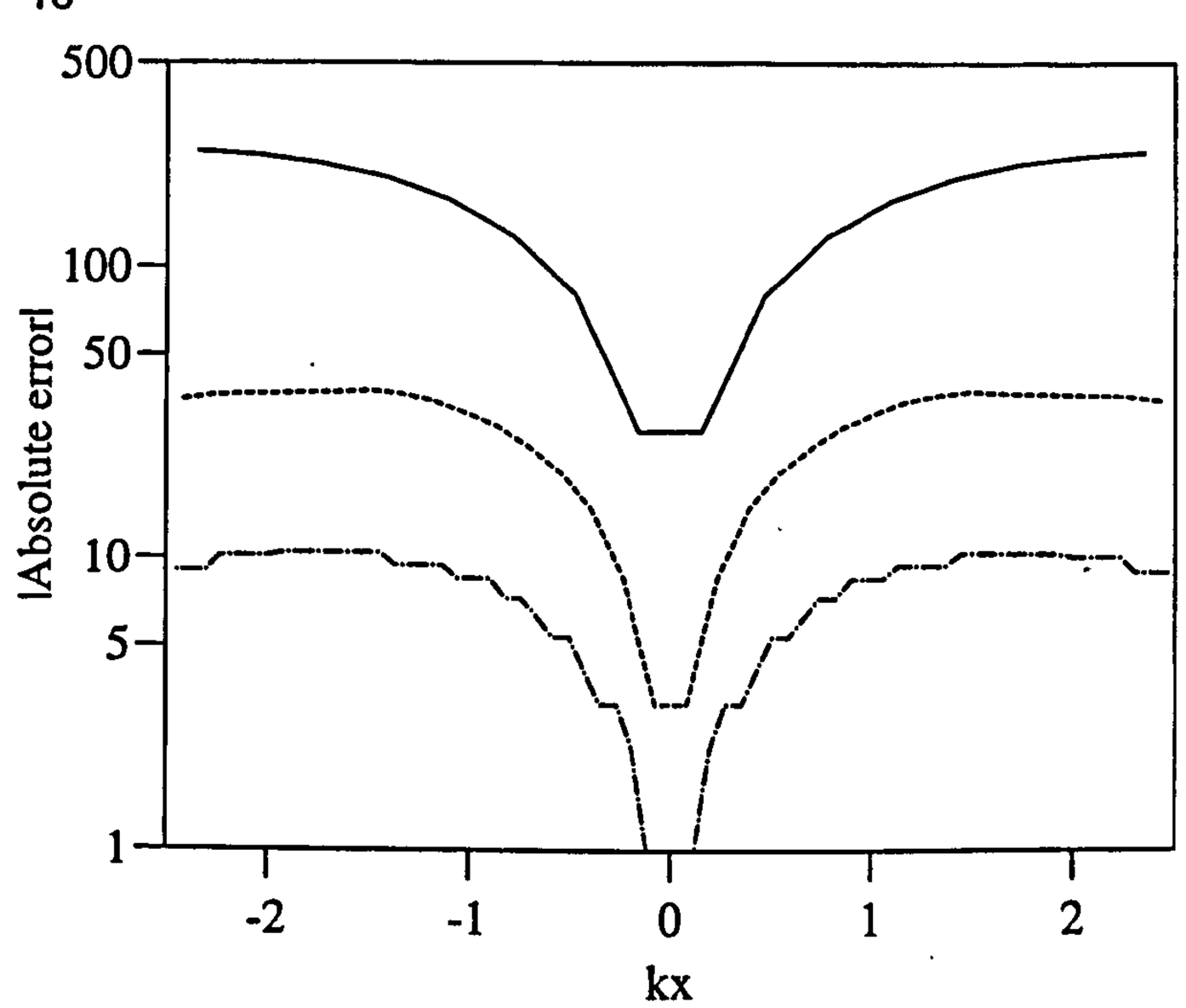

b) Absolute errors in the computation of the y-derivative of the pressure
Exact value of $|\partial\tilde{p}/\partial y| = 2.0$

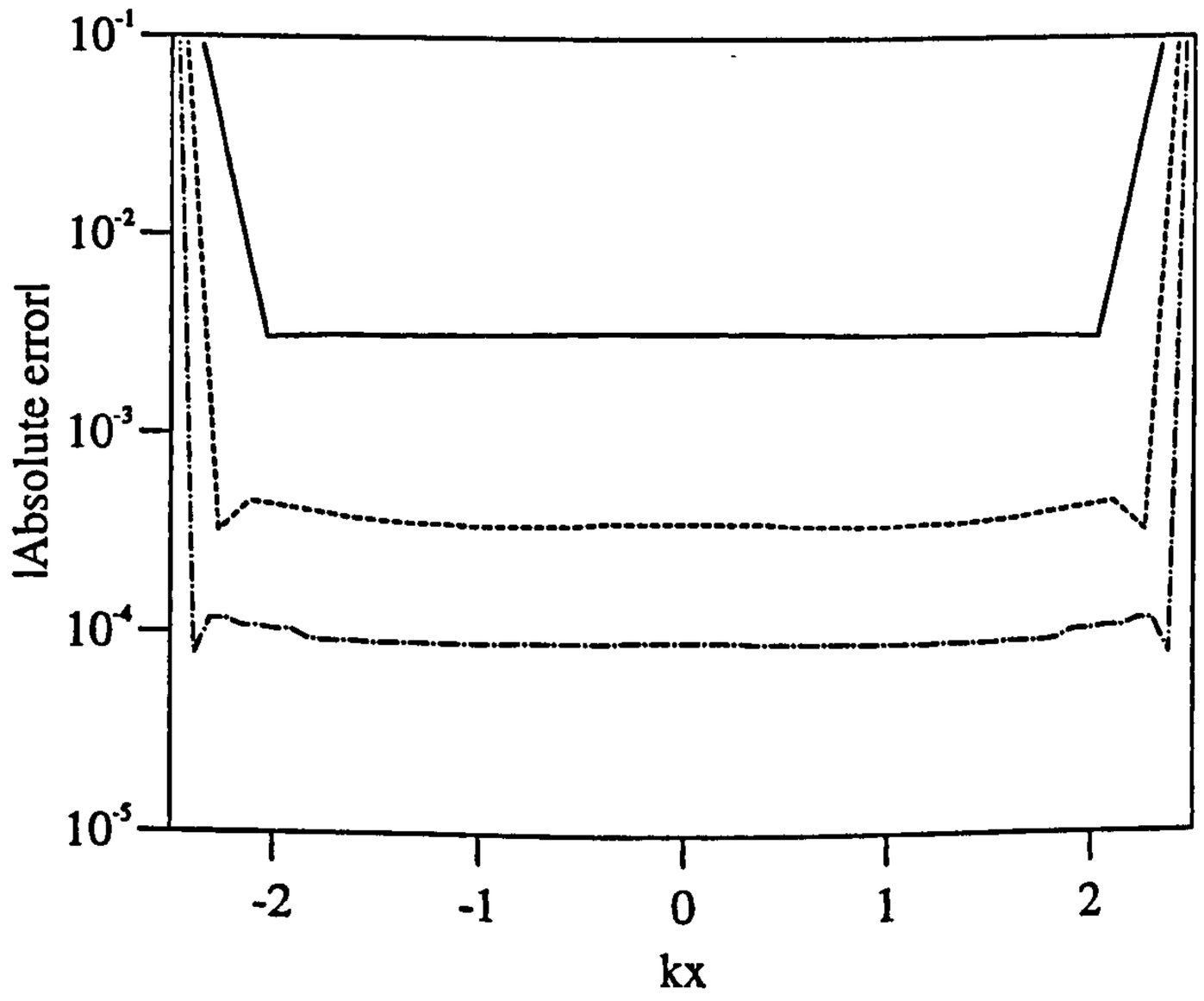

Figure 2.19: The absolute errors in the derivatives of $\tilde{p}$ as calculated along line EH for a fully rigid cross-section, where x is the horizontal distance from the center of the cutting; ——, $h = 0.05\lambda$; - - - -, $h = 0.025\lambda$; –·–·–, $h = 0.0125\lambda$

a) Absolute errors in the computation of the x-derivative of the pressure
Exact value of $|\partial\tilde{p}/\partial x| = 0$

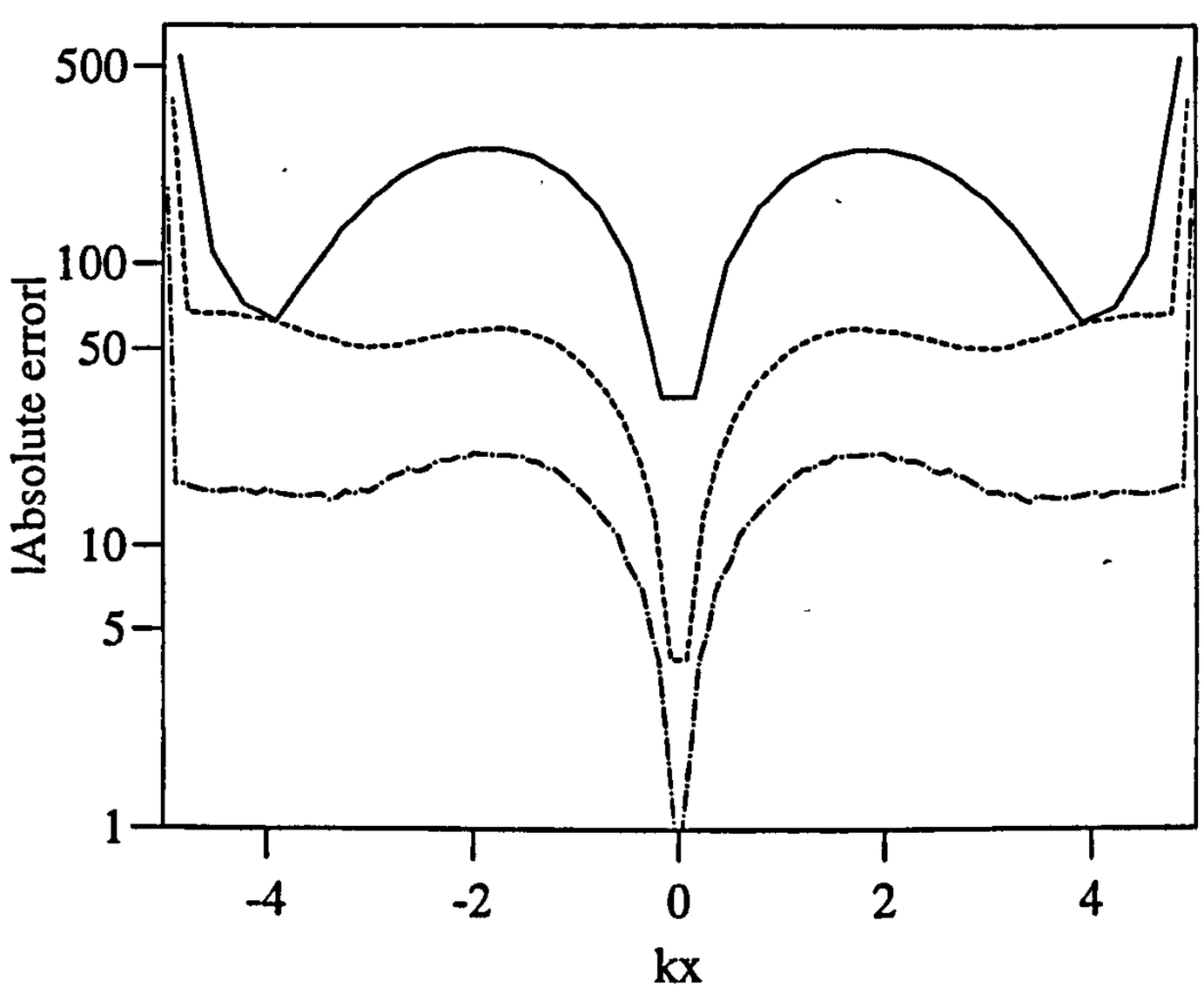

b) Absolute errors in the computation of the y-derivative of the pressure
Exact value of $|\partial\tilde{p}/\partial y| = 1.0$

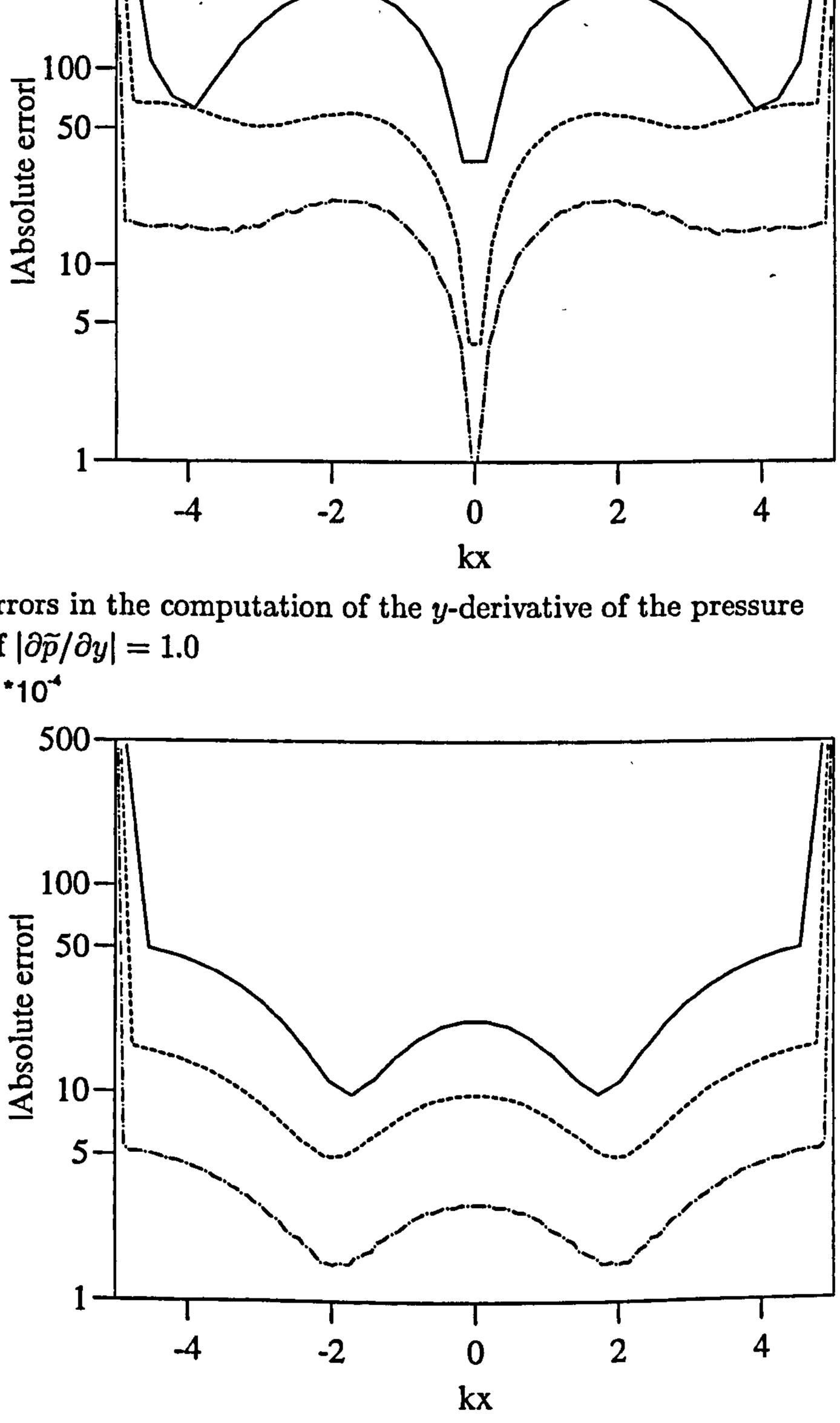

Figure 2.20: The absolute errors in the derivatives of $\tilde{p}$ as calculated along line AB for a cross-section with non-rigid horizontal surfaces, where x is the horizontal distance from the center of the cutting; ——, $h = 0.05\lambda$; - - - -, $h = 0.025\lambda$; —·—·—, $h = 0.0125\lambda$

a) Results for fully rigid cross-section. Exact value of $|p| = 2.0$

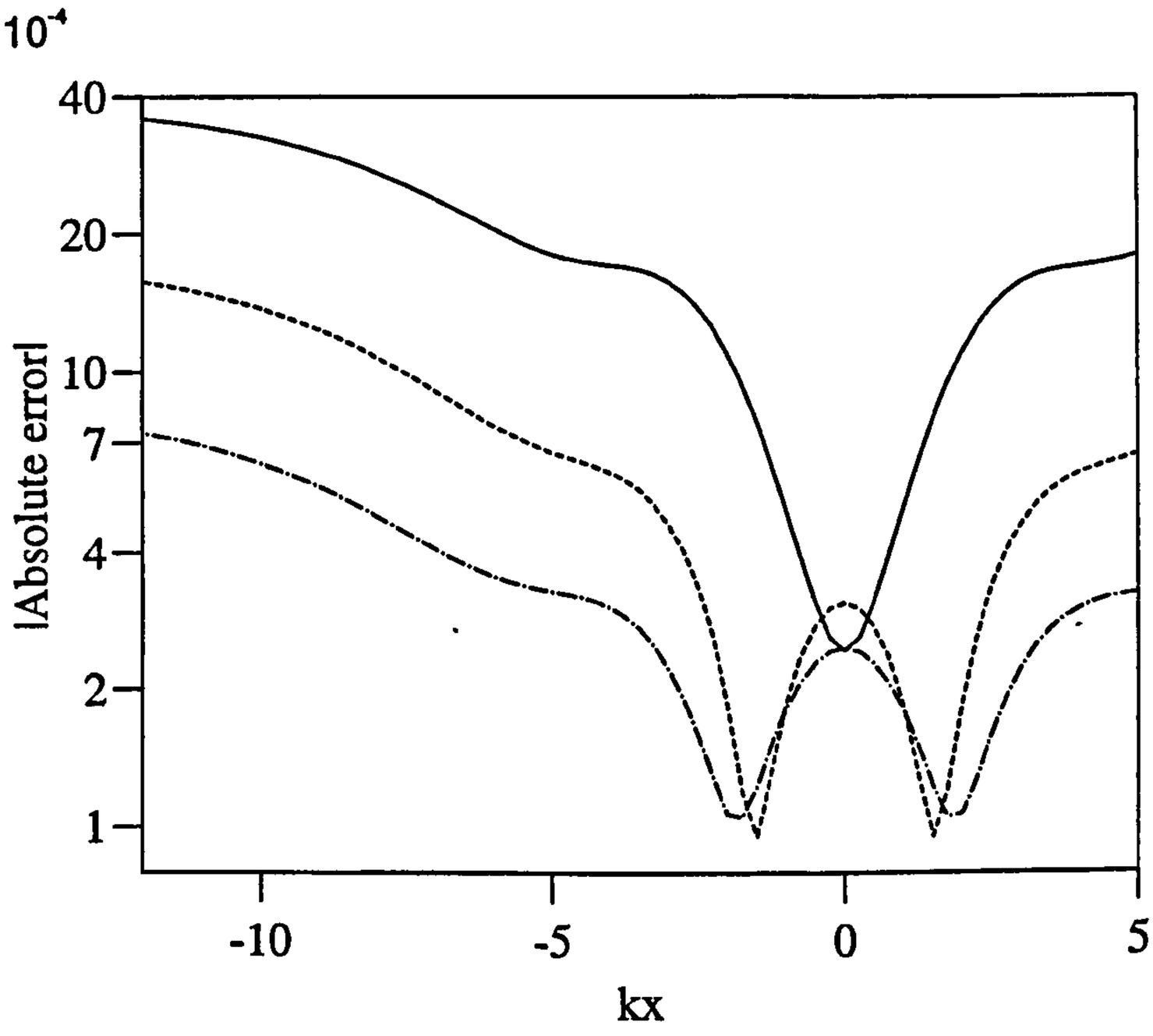

b) Results for cross-section with non-rigid horizontal surfaces. Exact value of $|p| = 1.0$

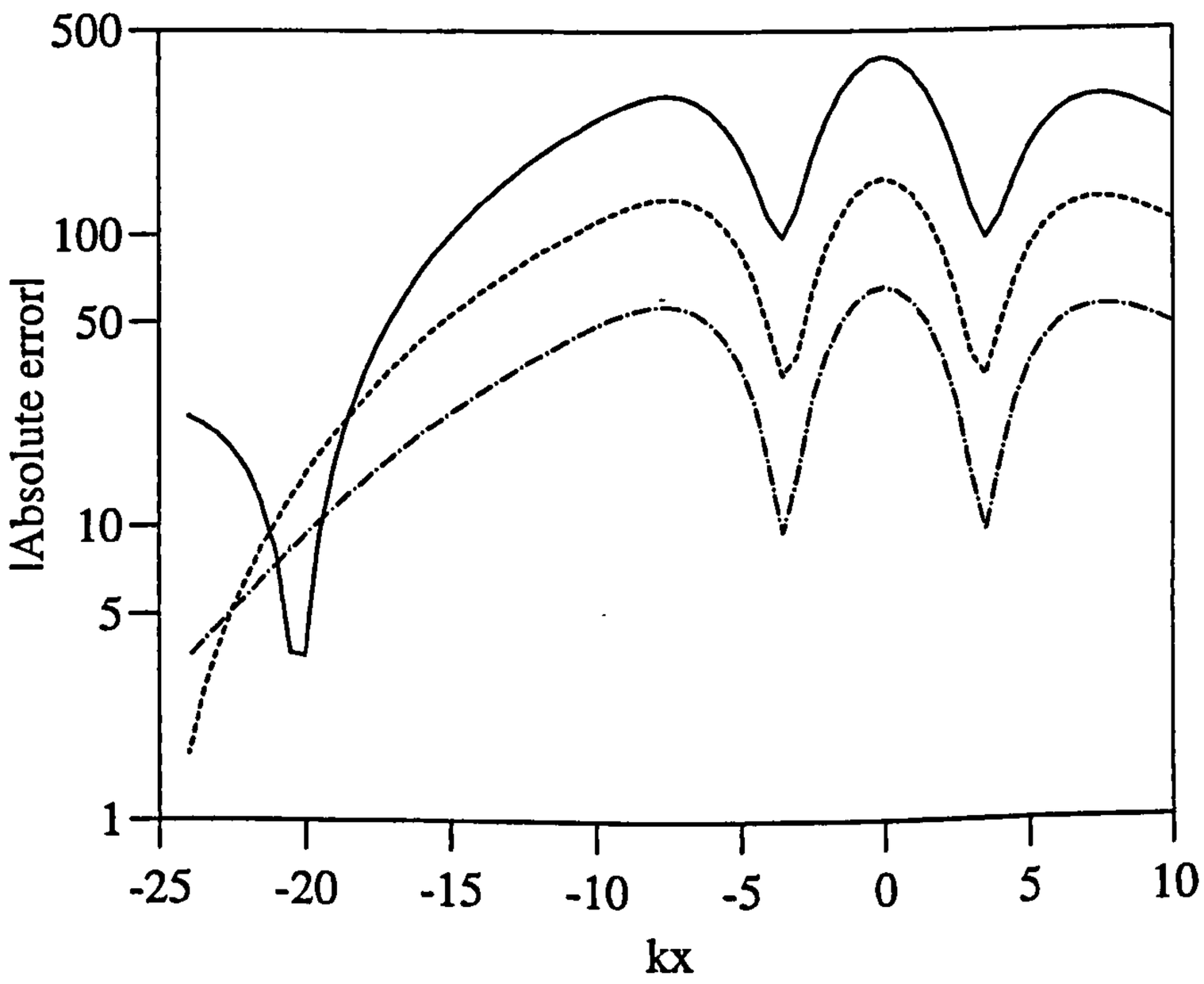

Figure 2.21: The absolute error in p as calculated along a line of receivers lying above the top of the cutting, where x is the horizontal distance from the center of the cutting; ——, 0.05λ; - - - -, 0.025λ; –·–·–, 0.0125λ

either side of the cutting, the magnitude of the error increases steadily as the measurement position moves further away. It is at the furthest receivers where reducing the element size has the greatest effect.

When the horizontal surfaces are non-rigid, the greatest errors occur at the cutting midpoint and approaching the walls ($kx = 10.0$). It is in these areas that the reduction in element size is most significant. On either side of the cutting the error decreases as the receiver moves further away.

Overall, the magnitude of the errors suggests that the problem observed at the elements on line EH closest to the cutting wall has negligible effect upon the final results and that the modified solution procedure is a good approximation to the original boundary element method.

Verification of Accuracy and Efficiency Using The Existing BEM

Simulations have been undertaken using the modified solution procedure and the basic cross-section illustrated in Figure 2.22.

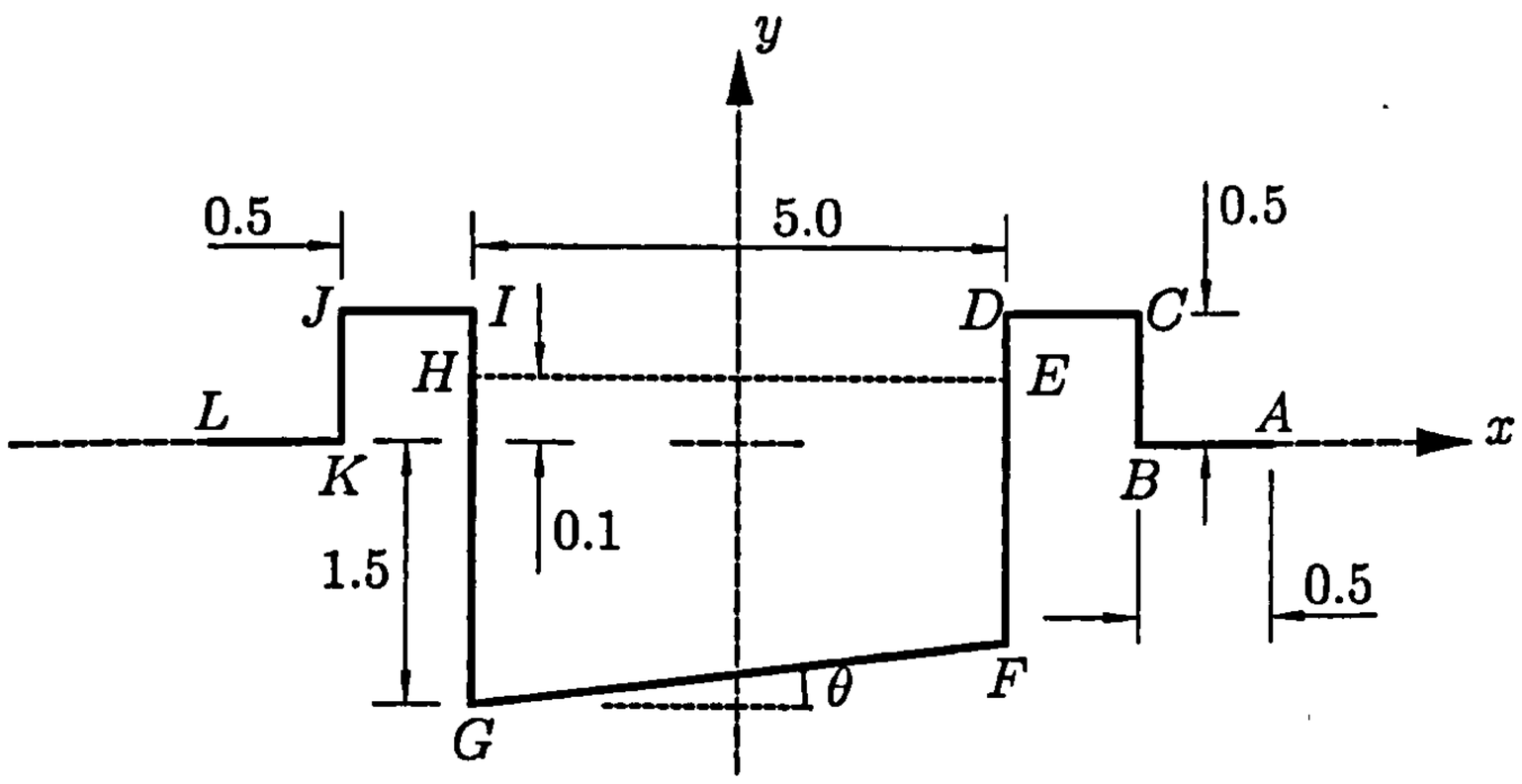

Figure 2.22: Cross-section with cutting used to test the modified solution procedure. Dimensions in metres.

Results have been obtained for both horizontal and inclined cutting floors ($\theta = 0°$ and $3.4°$ respectively). In each case, fully rigid, fully non-rigid and combined rigid/non-rigid cross-sections have been tested. Comparisons have been made with results obtained using the existing BEM and equivalent cross-sections positioned wholly above the line $y = 0$. These are shown in Figures 2.23 and 2.24, representing

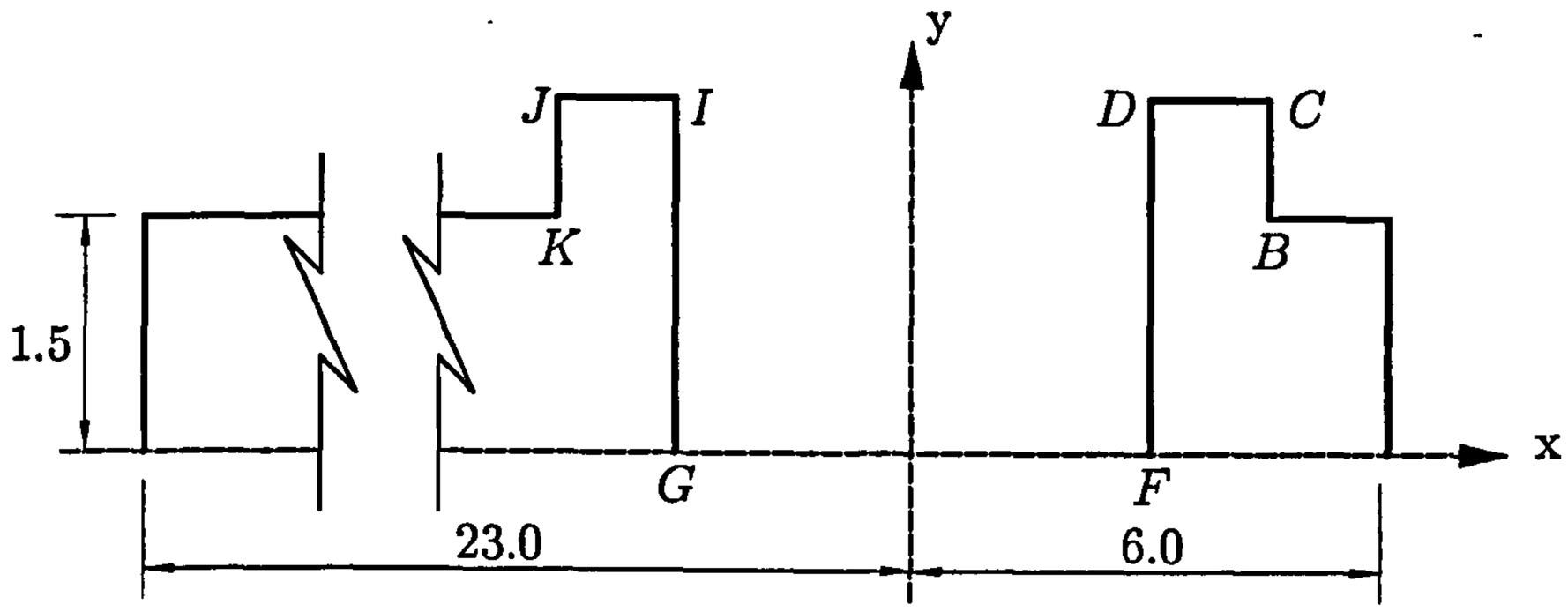

Figure 2.23: Approximation to cross-section and coordinate system used with the existing BEM - Cutting with horizontal floor ($\theta = 0°$). Dimensions in metres.

horizontal and inclined cutting floors respectively. The modified solution procedure assumes during Stage 1 that the ground on either side of $\tilde{\gamma}$ (see Figure 2.13) is of the same admittance, β_{c1}, as the cutting floor. In the calculations with the existing BEM the integral equation solved is (2.9), with $\beta_c = \beta_{c1}$, and γ the part of the boundary defined by the bold line in Figure 2.23 or 2.24.

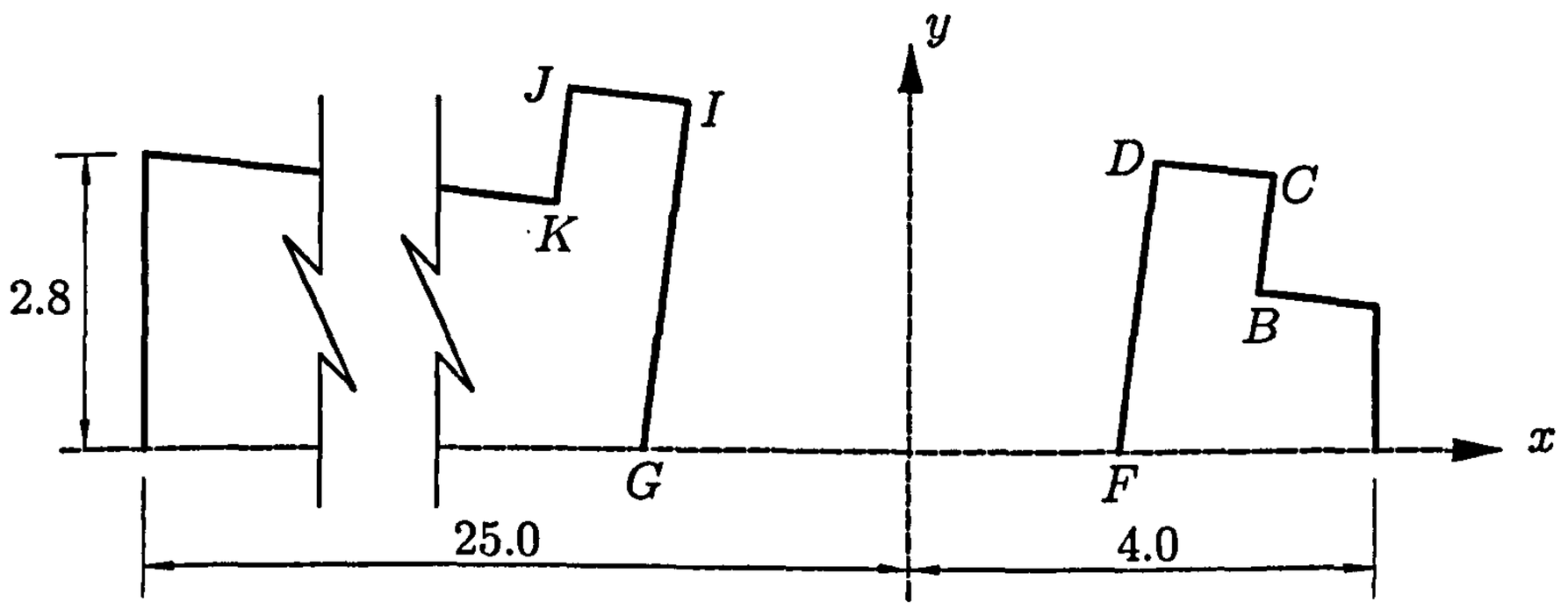

Figure 2.24: Approximation to cross-section and coordinate system used with the existing BEM - Cutting with inclined floor ($\theta = 3.4°$). Dimensions in metres.

For the fully non-rigid tests, the surface impedance characteristics have been defined as follows: The cutting floor has a flow resistivity, $\sigma = 20{,}000$ Nsm^{-4} and effective depth $= \infty$; all other surfaces (including the outlying ground of the *initial* cross-section) have a flow resistivity, $\sigma = 250{,}000$ Nsm^{-4} and effective depth $= \infty$. For the combined test, the cutting floor and outlying ground are assumed rigid, all other surfaces having flow resistivity, $\sigma = 5{,}000$ Nsm^{-4} and effective depth $= \infty$.

Results are presented for an A-weighted third-octave band traffic noise spectrum (0.6 - 3.2 kHz) (see Section 3.2.1) in terms of the error between the existing BEM and the modified procedure i.e. $(SPL_{existing} - SPL_{modified})$ (Each calculation of the SPL for the whole spectrum is a combination of monofrequency sound pressure levels calculated at the 18 third-octave band centre frequencies). The source is located midway between the cutting walls, at a height of 0.25 or 0.2 m above the cutting floor, for $\theta = 0°$ and 3.4° respectively. Receiver positions are located at -5.0, -10.0 and -15.0m from the vertical axis of the cutting and at heights of 1.5 and 4.5m above the outlying ground ($y = 0$ in Figure 2.22). For the existing method, all receiver positions are translated/rotated accordingly.

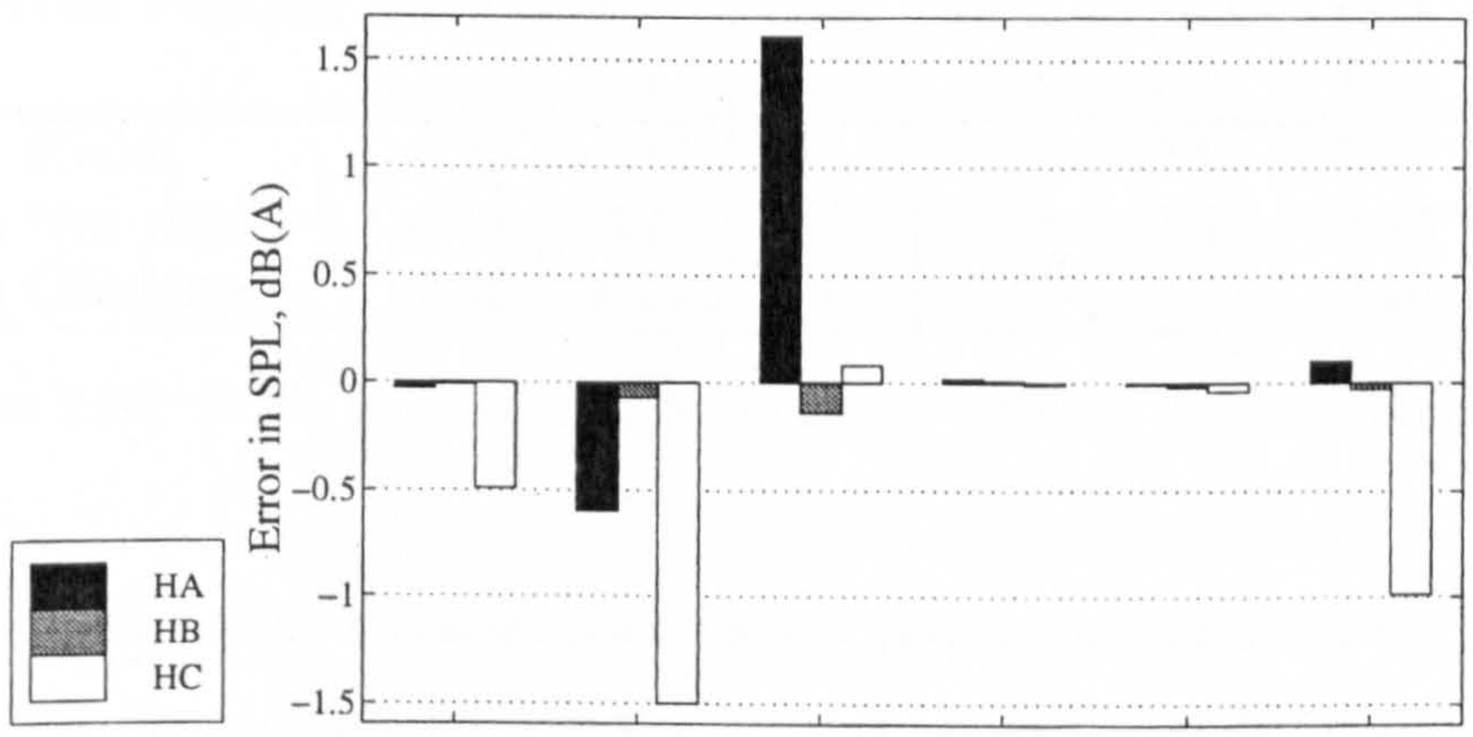

Receiver Position	-5.0, 1.5	-10.0, 1.5	-15.0, 1.5	-5.0, 1.5	-10.0, 4.5	-15.0, 4.5	CPU saving
HA: Rigid	-0.03	-0.60	1.61	0.02	-0.01	0.10	77.2%
HB: Non-rigid	-0.01	-0.07	-0.14	0.01	-0.02	-0.03	66.9%
HC: Combined	-0.49	-1.50	0.08	-0.01	-0.04	-0.99	76.6%

Figure 2.25: Error in SPL, dB(A), for cuttings with a horizontal floor ($\theta = 0°$)

Figure 2.25 shows the error between the results obtained for the cutting with the horizontal floor ($\theta = 0°$ in Figure 2.22). Considering case HB, the fully non-rigid cutting, the agreement between the two methods is very good with the error not exceeding ±0.15 dB(A). For the cross-sections incorporating a rigid cutting floor (HA and HC), greater errors are observed up to ±1.6 dB(A), the poorest agreement being largely in the case where the impedance of the cutting walls is non-zero. The

reduction in CPU time achieved through using the modified procedure is at least 66% of that required by the existing method in all three cases.

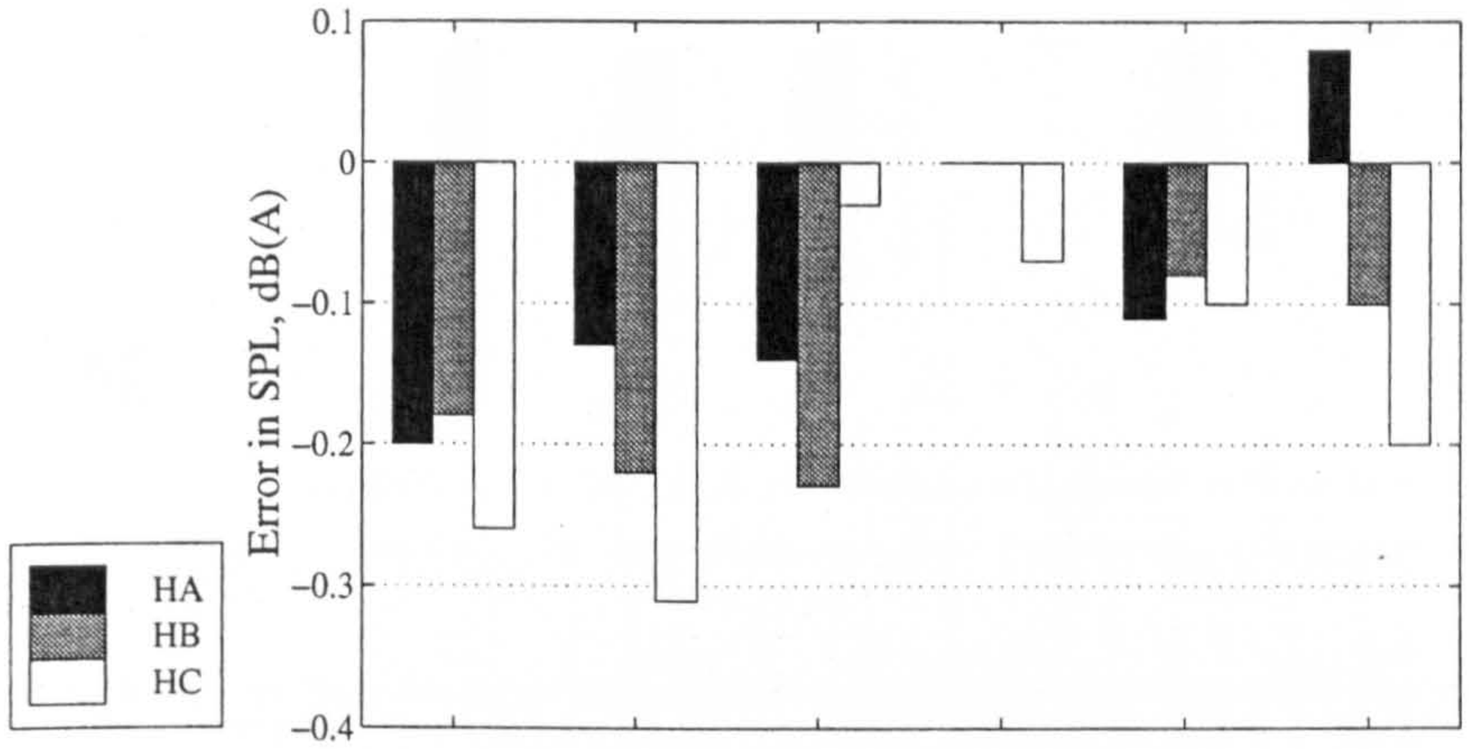

Receiver Position	-5.0, 1.5	-10.0, 1.5	-15.0, 1.5	-5.0, 1.5	-10.0, 4.5	-15.0, 4.5	CPU saving
IA: Rigid	-0.20	-0.13	-0.14	0.00	-0.11	0.08	79.2%
IB: Non-rigid	-0.18	-0.22	-0.23	0.00	-0.08	-0.10	70.7%
IC: Combined	-0.26	-0.31	-0.03	-0.07	-0.10	-0.20	80.0%

Figure 2.26: Error in SPL (dB) for cuttings with an inclined floor ($\theta = 3.4°$)

The errors for the cross-sections incorporating an inclined floor ($\theta = 3.4°$) are presented in Figure 2.26. For the simulations using the modified procedure the line EH is horizontal as in Figure 2.22. In all cases the magnitude of the errors does not exceed ± 0.30 dB(A) and the reduction in CPU time is between 70-80%.

For the cross-section incorporating an inclined floor ($\theta = 3.4°$) and the fully rigid case, (IA), results have also been obtained using the modified procedure with the line EH set parallel to the cutting floor. Figure 2.27 shows that no significant change is evident on changing the inclination of line EH (case ID), in terms of either the magnitude of the error or the reduction in CPU time.

For those cross-sections where the cutting floor is rigid (HA, HC, IA and IC), a plausible explanation for the large magnitude of some of the errors is the coincidence of one or more of the third-octave band centre frequencies with an eigenfrequency of the interior problem of Figure 2.3, leading to non-uniqueness of solution of the

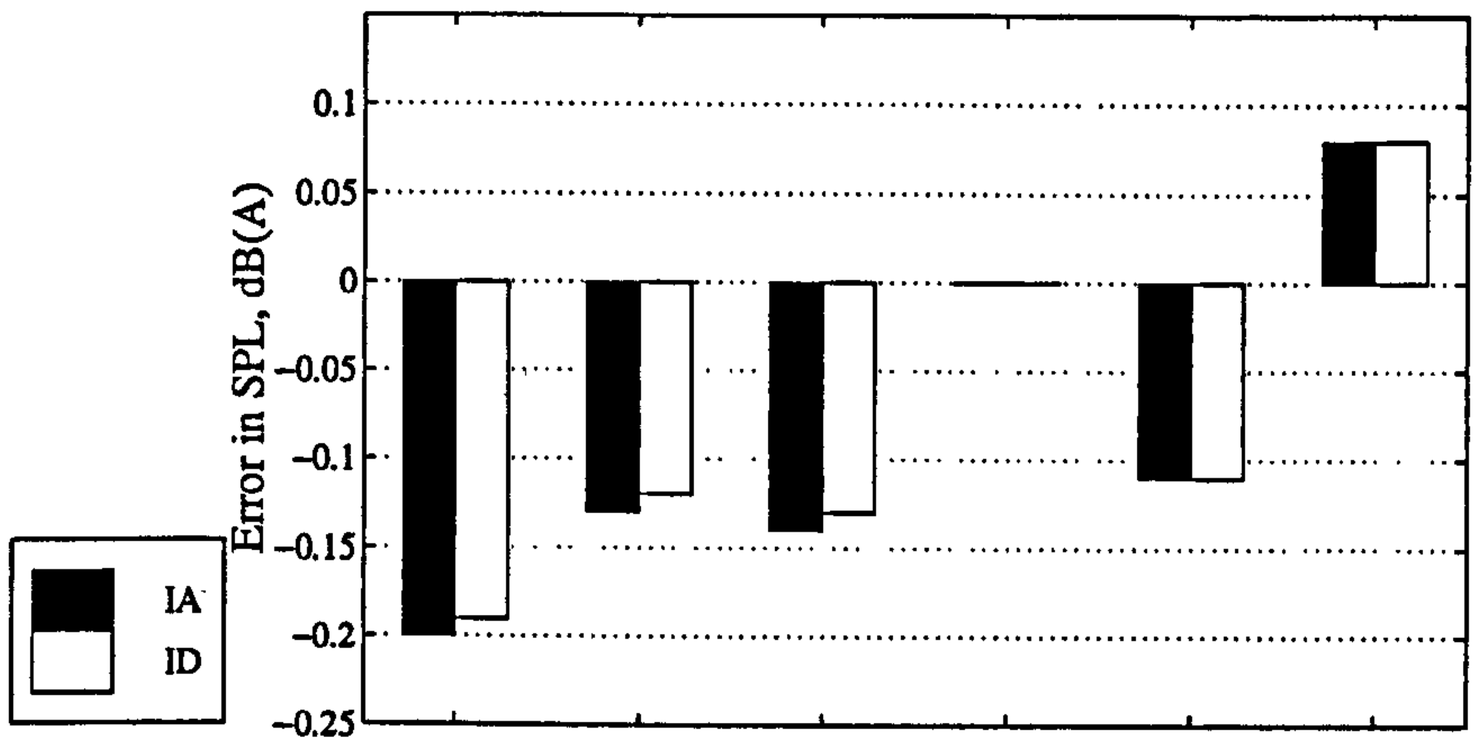

Receiver Position	-5.0, 1.5	-10.0, 1.5	-15.0, 1.5	-5.0, 1.5	-10.0, 4.5	-15.0, 4.5	CPU saving
IA: OldR - NewR	-0.20	-0.13	-0.14	0.00	-0.11	0.08	80.0%
ID: OldR - NewR2	-0.19	-0.12	-0.13	0.00	-0.11	0.08	80.0%

Figure 2.27: Error in SPL, dB(A), for a fully rigid cutting with an inclined floor ($\theta = 3.4°$); OldR: existing BEM; NewR: modified procedure, EH horizontal; NewR2: modified procedure, EH inclined

boundary integral equation (see Note 3 on page 16). Equation (2.30) suggests that this is a greater possibility in the application of the original method rather than the modified procedure, since the area of the interior region underneath γ in the existing method is considerably larger than that underneath $\tilde{\gamma}$.

As a check of this explanation, simulations have been performed for the combined impedance cutting with a rigid horizontal floor (HC) using a non-zero value of β_c (corresponding to a flow resistivity $\sigma = 250{,}000$ Nsm^{-4}) in the existing boundary element method, equation (2.9), and the same non-zero admittance $\beta_c 1$ in equation (2.33) of Stage 1 of the modified solution procedure. Since β_c and β_{c1} no longer coincide with the (zero) admittance of the cutting floor, this involves extra computational cost as the integrals over γ and $\tilde{\gamma}$, in (2.9) and (2.33) respectively, have to be extended to include integration also over the cutting floor FG. Further, the Green's function G_{β_c} in the kernel of the integral equations is much more expensive to compute when $\beta_c \neq 0$. On the other hand, since $\beta_c = \beta_{c1} \neq 0$ (crucially

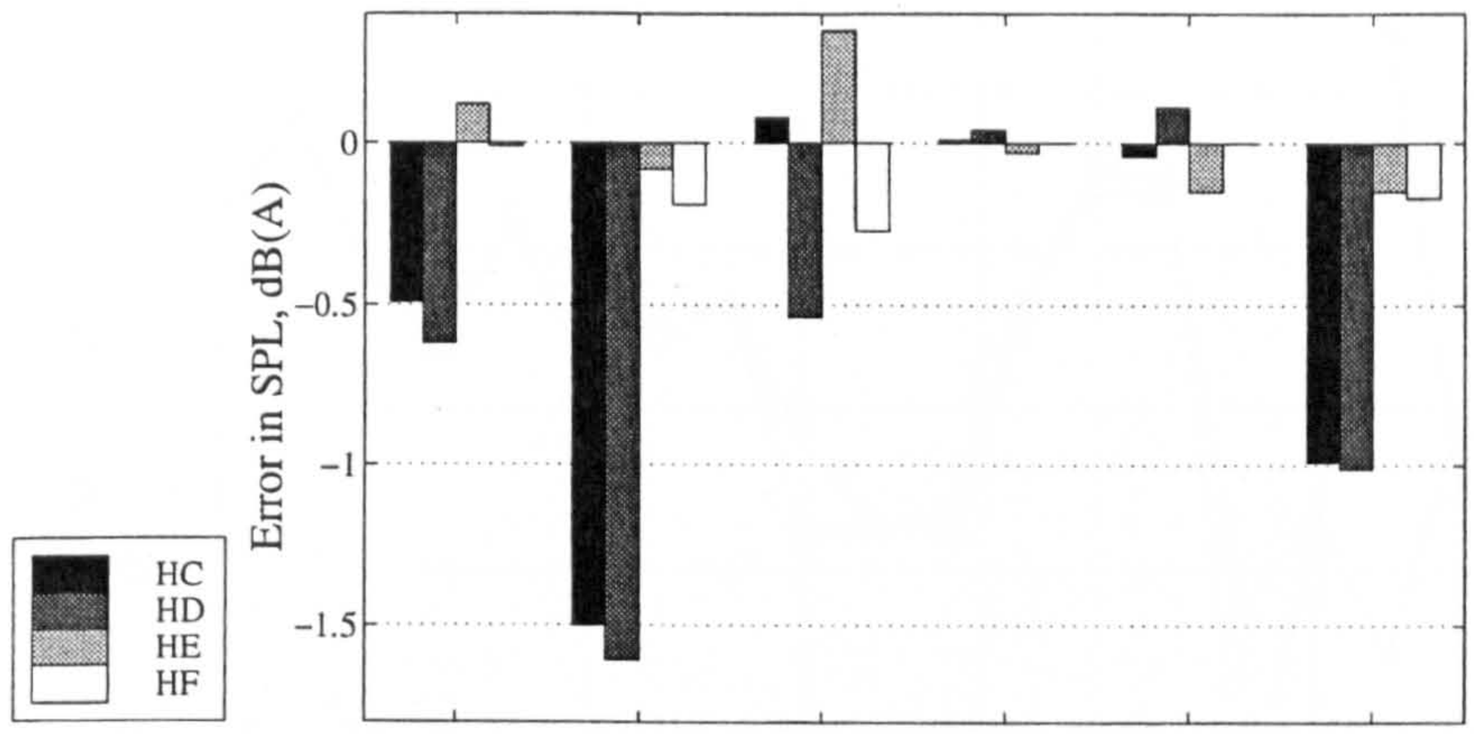

Receiver Position	-5.0, 1.5	-10.0, 1.5	-15.0, 1.5	-5.0, 1.5	-10.0, 4.5	-15.0, 4.5	CPU saving
HC: OldR - NewR	-0.49	-1.50	0.08	0.01	-0.04	-0.99	76.6%
HD: OldA - NewR	-0.62	-1.61	-0.54	0.04	0.11	-1.01	90.5%
HE: OldR - NewA	0.12	-0.08	0.35	-0.03	-0.15	-0.15	-27.1%
HF: OldA - NewA	-0.01	-0.19	-0.27	0.00	0.00	-0.17	48.4%

Figure 2.28: Error in SPL (dB) for the combined impedance cutting with a horizontal floor ($\theta = 0°$); OldR: existing BEM, $\beta_c = 0$; OldA: existing BEM, $\beta_c \neq 0$; NewR: modified procedure, $\beta_{c1} = 0$; NewA: modified procedure, $\beta_{c1} \neq 0$

$\Re\beta_c, \Re\beta_{c1} > 0$) the interior problem of Figure 2.3 no longer has eigenfrequencies.

The differences between the various simulations are presented in Figure 2.28. It is observed that the smallest differences between the modified and existing BEM are achieved for the most part when using non-zero values of β_c or β_{c1} in the respective methods (HF in Figure 2.28). The differences between the existing method, using $\beta_c = 0$, and the modified procedure with $\beta_{c1} \neq 0$ (HE in Figure 2.28) are also a significant improvement on the original comparison with $\beta_c = \beta_{c1} = 0$ (HC in Figure 2.28), although it is observed that the relative efficiency of the modified procedure is seriously affected, the calculations taking over 25% longer than the existing method with $\beta_c = 0$. The indication is that one or more of the third-octave band centre frequencies approximately coincide with an interior eigenfrequency in the modified procedure rather than in the simulation using the cross-section of Figure 2.23, though this could not have been predicted a priori.

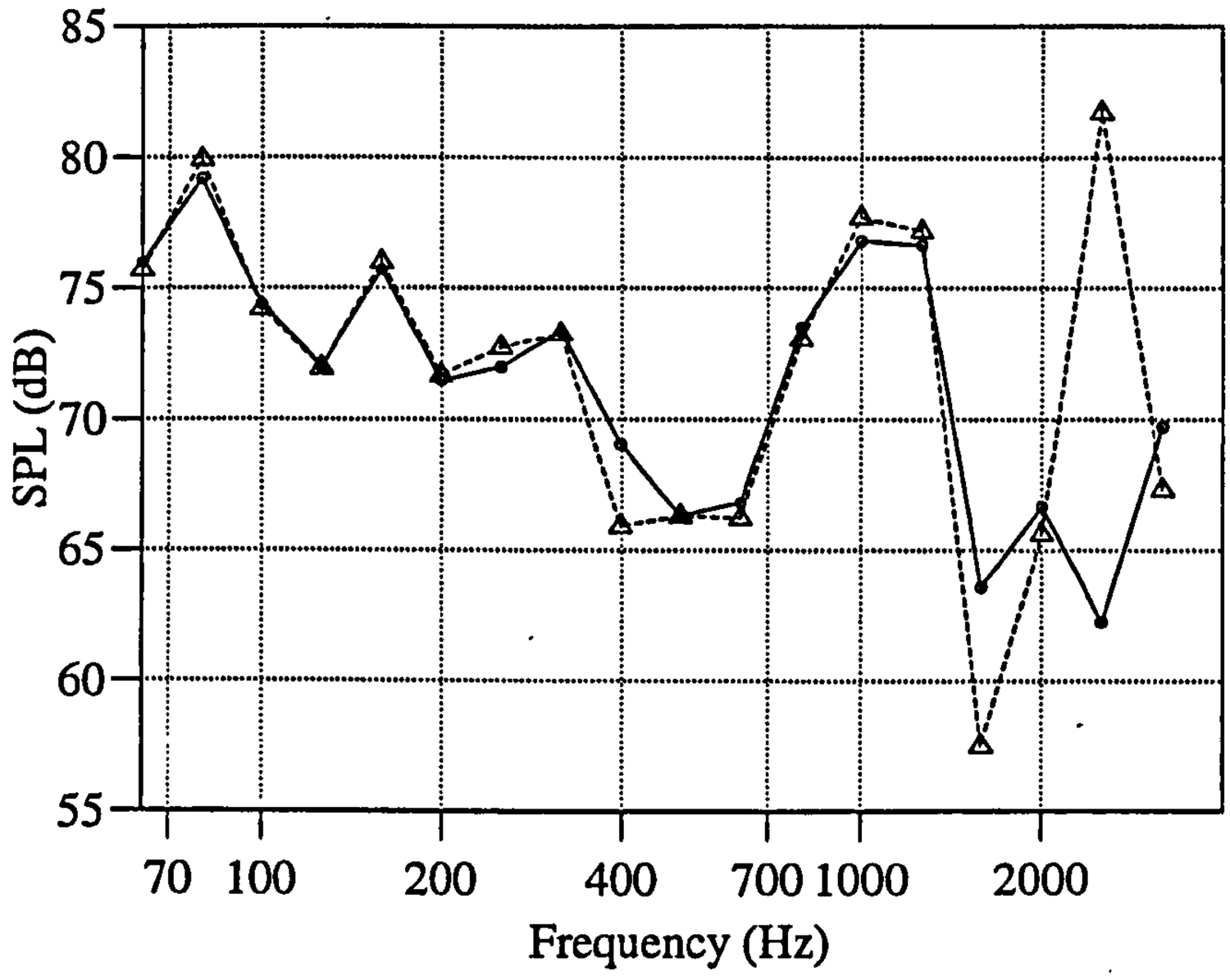

Figure 2.29: Plot of SPL values at receiver coordinates (10.0, 1.5) for the combined impedance cutting with a horizontal floor ($\theta = 0°$); ∘ existing BEM, $\beta_c = 0$; △ modified procedure, $\beta_{c1} = 0$.

When using both $\beta_c = 0$ and $\beta_{c1} = 0$, the broadband error measured at receiver coordinates (10, 1.5) is -1.5 dB(A). Figure 2.29 compares the corresponding SPL spectra. The agreement between the two methods is visibly poor, particularly at 1600 and 2500 Hz.

For the same cross-section, source and receiver positions, Figure 2.30 shows the resultant spectra when using $\beta_c \neq 0$ in the existing method and $\beta_{c1} \neq 0$ in the modified procedure.

Introducing the impedance boundary into the simulation using the existing method affects the SPL predicted at 400 Hz, and 1600 Hz and above, the most notable effect being a reduction of approximately 8 dB at 3150 Hz. Overall this provides better agreement with the original simulation using the modified procedure for frequencies up to 1600 Hz. However, the error at 2500 Hz is not significantly reduced and that at 3150 Hz is increased, leading to the broadband error of -1.61 dB(A) given in Figure 2.28 (HD).

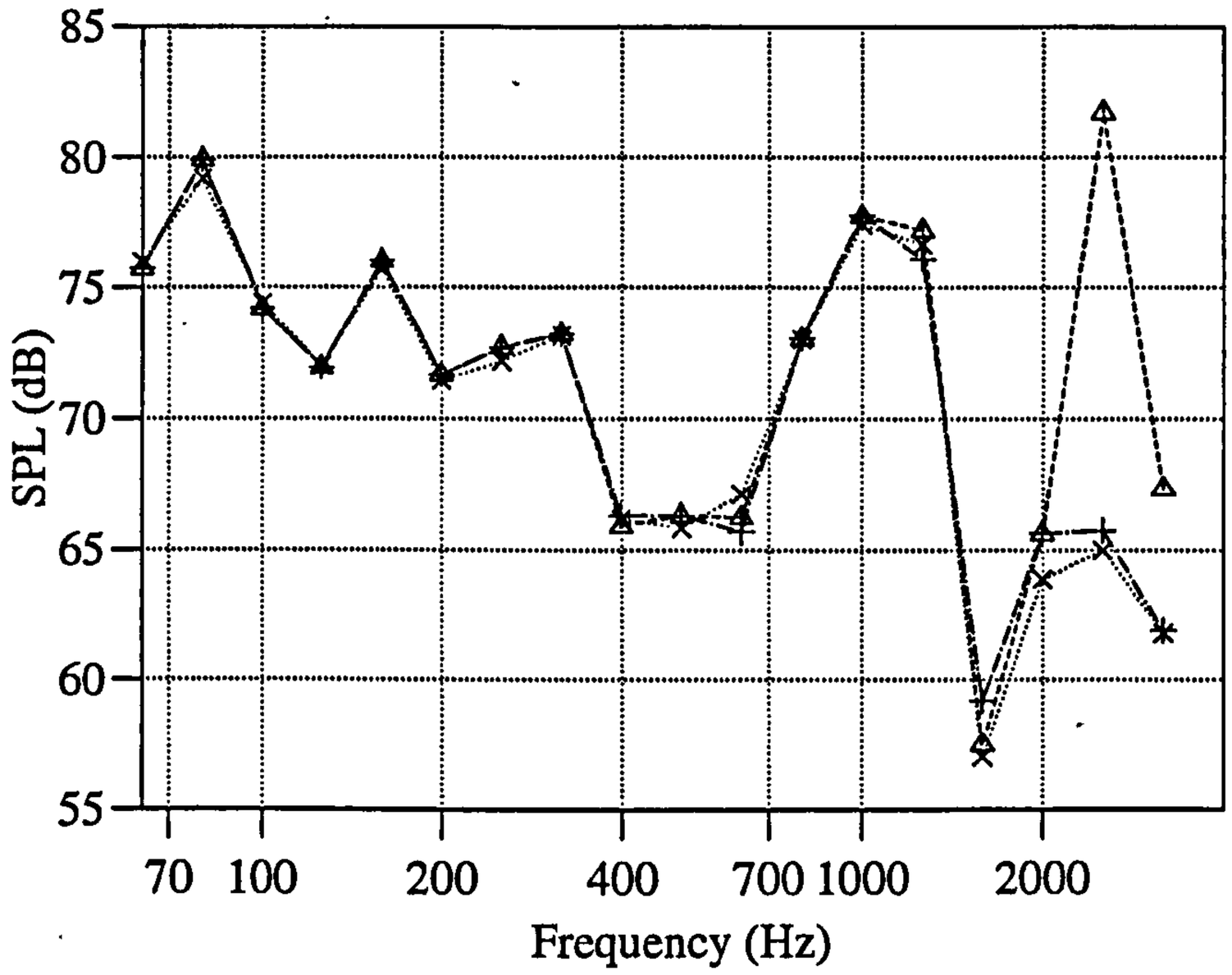

Figure 2.30: Plot of SPL values at receiver coordinates (10.0, 1.5) for the combined impedance cutting with a horizontal floor ($\theta = 0°$); × existing BEM, $\beta_c \neq 0$; △ modified procedure, $\beta_{c1} = 0$; + modified procedure, $\beta_{c3} \neq 0$.

The use of $\beta_{c1} \neq 0$ in the modified procedure provides the greatest evidence that the errors are largely attributable to the occurrence of eigenfrequencies, with a reduction in level of approximately 16 dB at 2500 Hz and 5.5 dB at 3150 Hz. Using the impedance boundary in both methods improves the agreement over most of the frequency range considered, reducing the broadband error to -0.19 dB(A) (HF).

Similarly, Figure 2.31 compares the effect of introducing the impedance boundary for the case of the fully rigid cutting with the inclined floor. The most noticeable improvement is observed at a height of 1.5 m for the receivers at 10 and 15 m from the cutting axis. In this instance the reduction in CPU time is only 5% poorer than that when both β_c and β_{c1} are zero.

It should be noted that the cross-section in Figure 2.22 is small in comparison to actual typical cross-sections and that the receiver positions are in close proximity to the cutting. This is because of the increased computation requirements for modelling

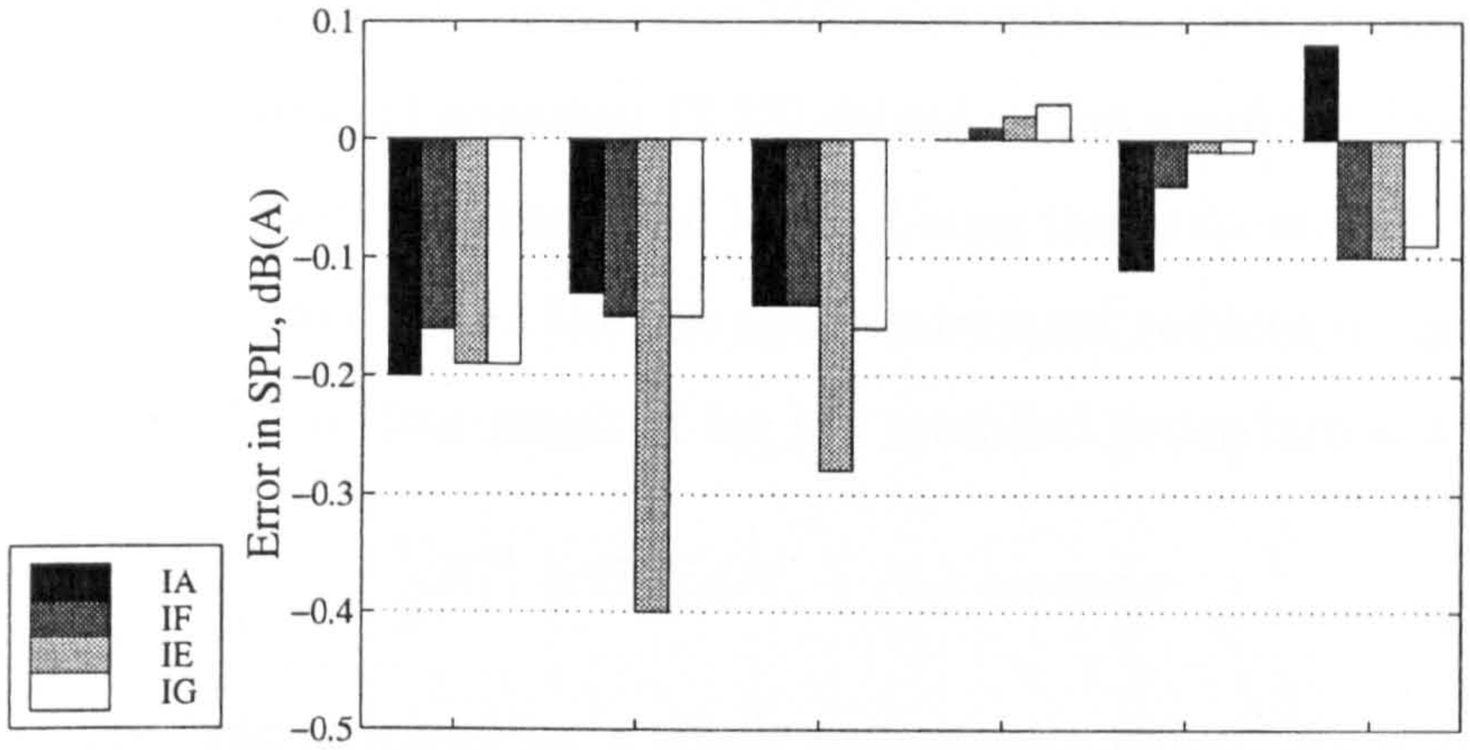

Receiver Position	-5.0, 1.5	-10.0, 1.5	-15.0, 1.5	-5.0, 1.5	-10.0, 4.5	-15.0, 4.5	CPU saving
IA: OldR - NewR	-0.20	-0.13	-0.14	0.00	-0.11	0.08	80%
IF: OldA - NewA	-0.16	-0.15	-0.14	0.01	-0.04	-0.10	71.1%
IE: OldR2 - NewR	-0.19	-0.40	-0.28	0.02	-0.01	-0.10	87.7%
IG: OldA2 - NewA	-0.19	-0.15	-0.16	0.03	-0.01	-0.09	75.4%

Figure 2.31: Error in SPL, dB(A), for a fully rigid cutting with an inclined floor ($\theta = 3.4°$); OldR: existing BEM, horizontal floor, ($\beta_c = 0$); OldR2: existing BEM, inclined floor, $\beta_c = 0$; OldA: existing BEM, horizontal floor, $\beta_c \neq 0$; OldA2: existing BEM, inclined floor, $\beta_c \neq 0$; NewR: modified procedure, EH horizontal, $\beta_c = 0$; NewR2: modified procedure, EH horizontal, $\beta_c \neq 0$.

large cross-sections/distant receivers using the existing BEM (see Section 2.1). For the existing BEM the CPU time required is approximately (c.f. (2.31))

$$\frac{c}{3}{N_f}^3 + C_1{N_f}^2 \text{ seconds} \tag{2.97}$$

where N_f is the number of boundary elements on γ for a given source frequency f, c is the time for a single complex multiplication and addition, and C_1 is the time required for a single evaluation of the function G_{β_c}. The storage requirement when calculating in double precision (8 bytes storage for each real number) is approximately

$$\frac{16{N_f}^2}{1024^2} \text{ MB} \tag{2.98}$$

Consider the cross-section in Figure 2.23. The existing BEM solves the integral equation (2.9) with γ the part of the boundary indicated with a bold line, of total length 32 m. For a source frequency of 3150 Hz and an element size of 0.15λ, then

$N \approx 1960$, requiring approximately 59 MB of RAM. If the furthest receiver were at 40m, then these figures would increase to 3490 elements and 186 MB respectively. By comparison, in the integral equation (2.33) solved in the modified procedure, $\tilde{\gamma}$ (see Figure 2.13) has a maximum length of 11 m. Using the same source frequency and element size, then $N \approx 674$ and the storage requirement reduces to approximately 7 MB of RAM. The CPU time required for the modified procedure is approximately

$$\frac{c}{3}{N_1}^3 + C_2 N_1(N_1 + N_2) \text{ seconds} \tag{2.99}$$

where C_2 is the time required for a single evaluation of $G_{\beta_{c1}}$, N_1 is the number of elements on $\tilde{\gamma}$, and N_2 the number of elements on EH.

To provide a final comparison with the existing BEM, two simulations have been carried out using the cross-sections shown in Figure 2.32. In addition to the increased dimensions, the furthest receiver positions are located a distance of 40 m from the vertical axis. In each case the flow resistivity is set at $\sigma = 7,000$ Nsm^{-4} for the cutting floor and $\sigma = 250,000$ Nsm^{-4} for all other surfaces including the outlying ground. The source position is within the cutting, 2.5 m to the left of the centre line at a height of 0.5 m above the cutting in case a) and 0.26 m in case b). The cross-section used in the original method which is the equivalent of Figure 2.32b has been rotated such that the cutting floor lies on the line $y = 0$. In both of the cross-sections used in the original method the length of γ in equation (2.9) is in excess of 50 m, so as to model propagation out to the furthest receiver positions.

The errors between new and old methods are presented in Figure 2.33. For the most part, the error is less than 0.1 dB in magnitude. The reduction in computation time achieved by implementing the modified solution procedure for these cross-sections is again in the order of 70-80%.

From the results obtained for the different cross-sections, it is evident that the error between the existing method and the modified procedure varies according to the geometry of the cross-section. In cases where the error is particularly poor, evidence has been presented to suggest strongly that this is largely attributable to

a) Cutting with horizontal floor

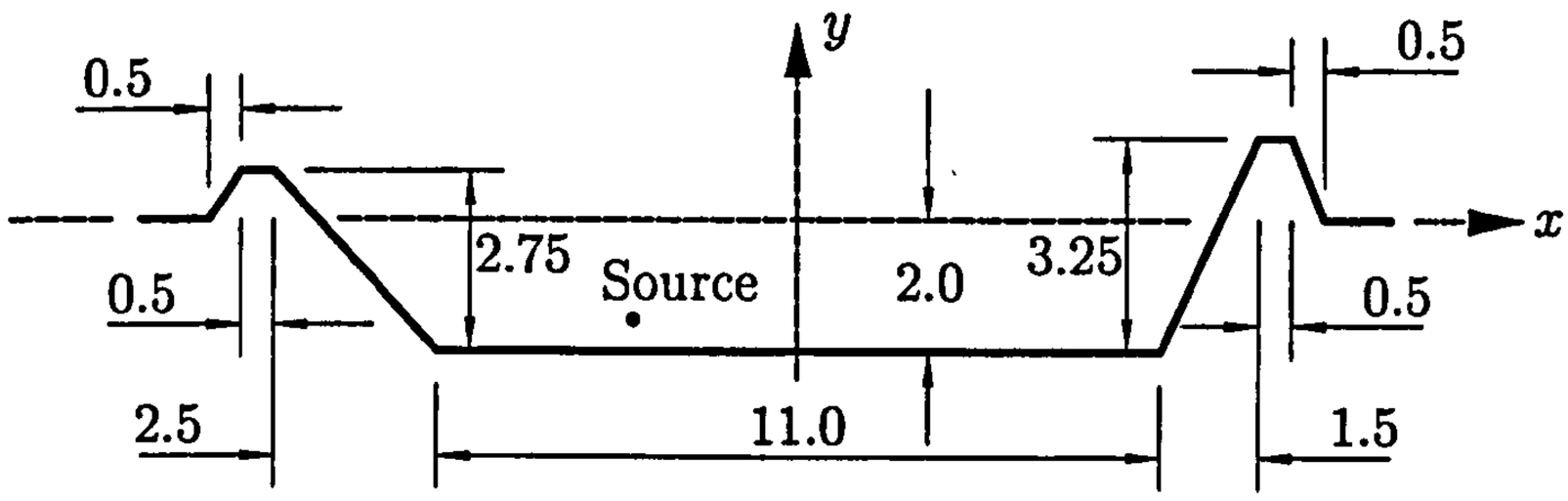

b) Cutting with inclined cutting floor ($\theta = 5.4°$)

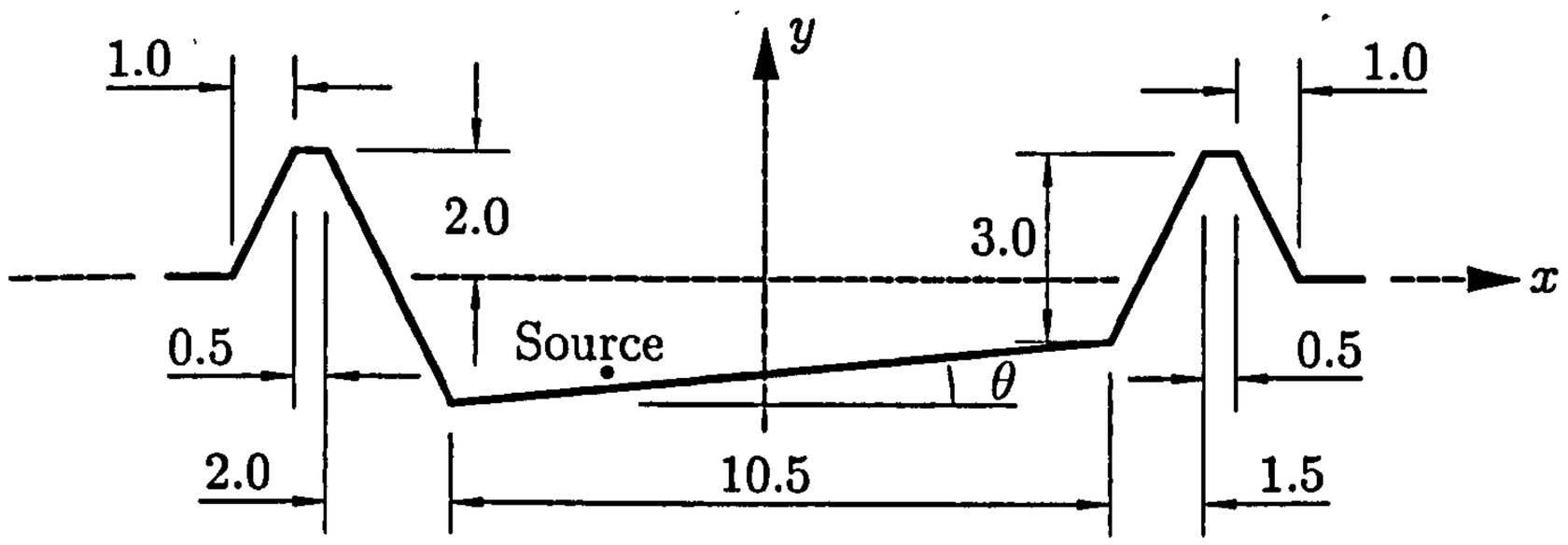

Figure 2.32: Larger cross-sections incorporating cuttings. Dimensions in metres.

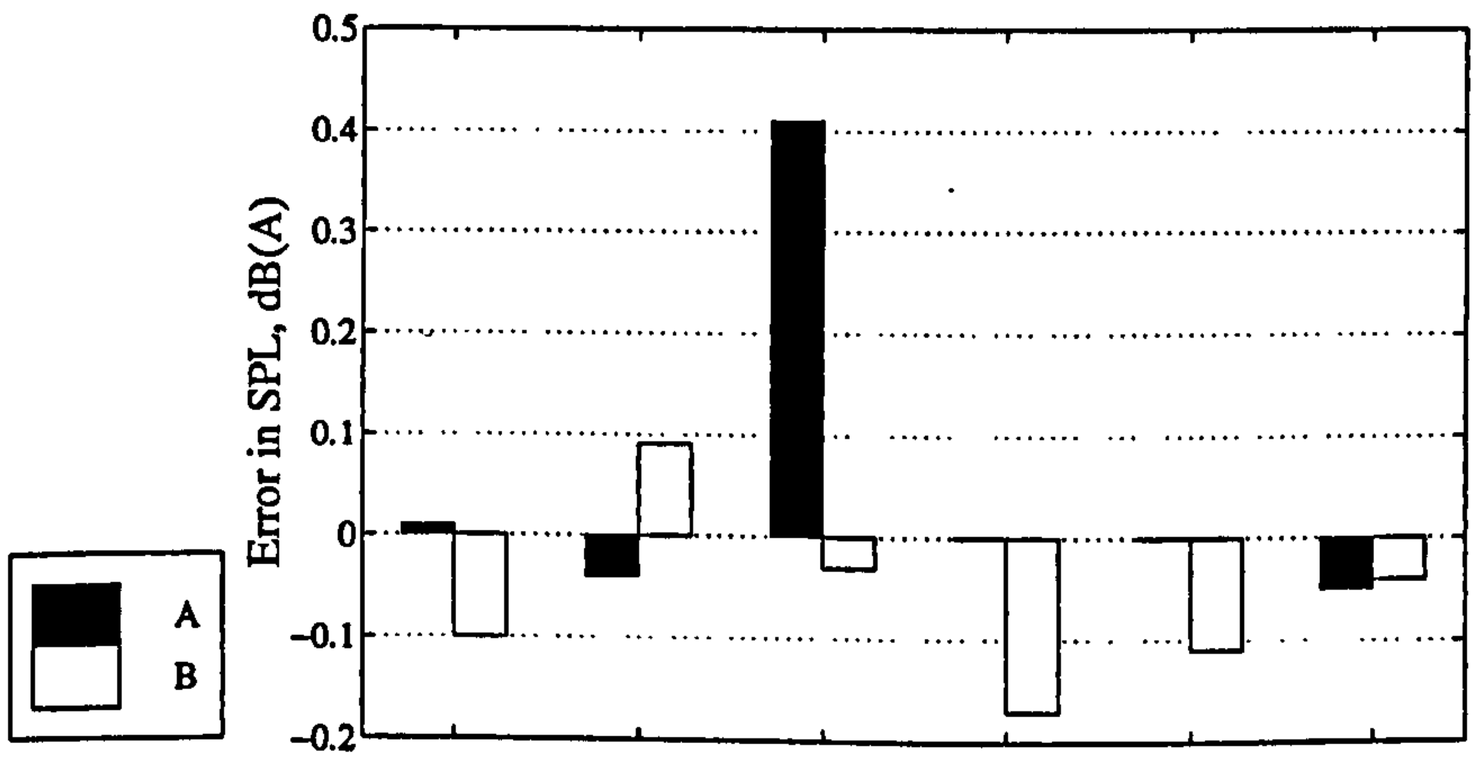

Receiver Position	-20, 1.5	-30, 1.5	-40, 1.5	-20, 1.5	-30, 4.5	-40, 4.5	CPU saving
A: Horizontal floor	0.01	-0.04	0.41	0.00	0.00	-0.05	73.6 %
B: Inclined floor	-0.10	0.09	-0.03	-0.17	-0.11	-0.04	78.9 %

Figure 2.33: Error in SPL (dB(A)) for large cross-sections

the occurrence of eigenfrequencies in either/both methods. This problem can be eliminated through a choice of $\beta_c \neq 0$ in the existing method and during Stage 1 of the modified procedure. Otherwise the agreement between the two methods is generally very good.

Implementation of the modified procedure offers a significant reduction in the computation time required for such cross-sections (generally 75-80% based upon the comparisons presented here). The modified procedure is less computationally efficient when using $\beta_{c1} \neq 0$ during Stage 1, since $\tilde{\gamma}$ then includes the cutting floor. However this offers the most accurate predictions of sound pressure level and, in comparison to using the existing method with $\beta_c \neq 0$, still offers a very useful saving in CPU time.

Comparison with a Coupled Integral Equation Method

An additional check upon the accuracy of the approximate modified solution procedure has been carried out by making comparison with an exact boundary element method which uses a system of coupled integral equations [100, 101]. This independently developed BEM can calculate exactly (if a small enough boundary element size is used) propagation from a cutting lying entirely in the lower half-plane $y \leq 0$ out onto surrounding flat homogeneous impedance ground coincident with the line $y = 0$. The unknowns are the pressure on the sides and bottom of the cutting, and the pressure and its normal derivative at the interface with the upper half plane (the continuation of the flat ground line). Limited results were available from this method, so only a single cross-section has been studied. This is shown in Figure 2.34. The source is 0.5 m above the cutting floor. All non-rigid surfaces have a flow resistivity, $\sigma = 250,000 \text{Nsm}^{-4}$.

The results, in terms of the error in SPL between the methods (coupled integral equation method - modified procedure) are shown in Figure 2.35 (the coordinates of the receiver positions are given relative to point A in Figure 2.34). Three separate calculations using the modified procedure have been made, using different parts of the cross-section to define the cutting floor (the line FG in Figure 2.13); The first calculation uses the grass surface DE as the cutting floor, and $\beta_{c1} \neq 0$ is taken as

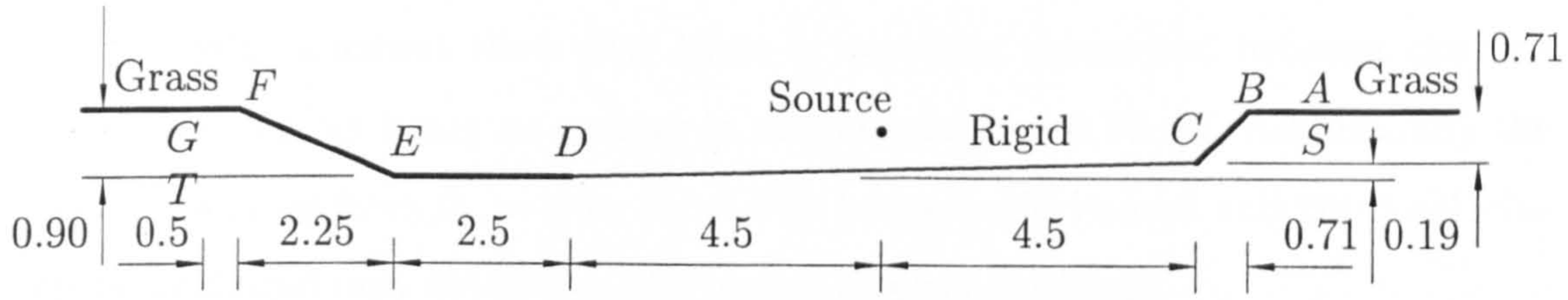

Figure 2.34: Cross-section for verification of method accuracy. Dimensions in metres. In the modified solution procedure $\overline{\gamma}$ is the arc $SABCDEFGT$, where S and T are the projections of A and G, respectively, onto the line of the cutting floor.

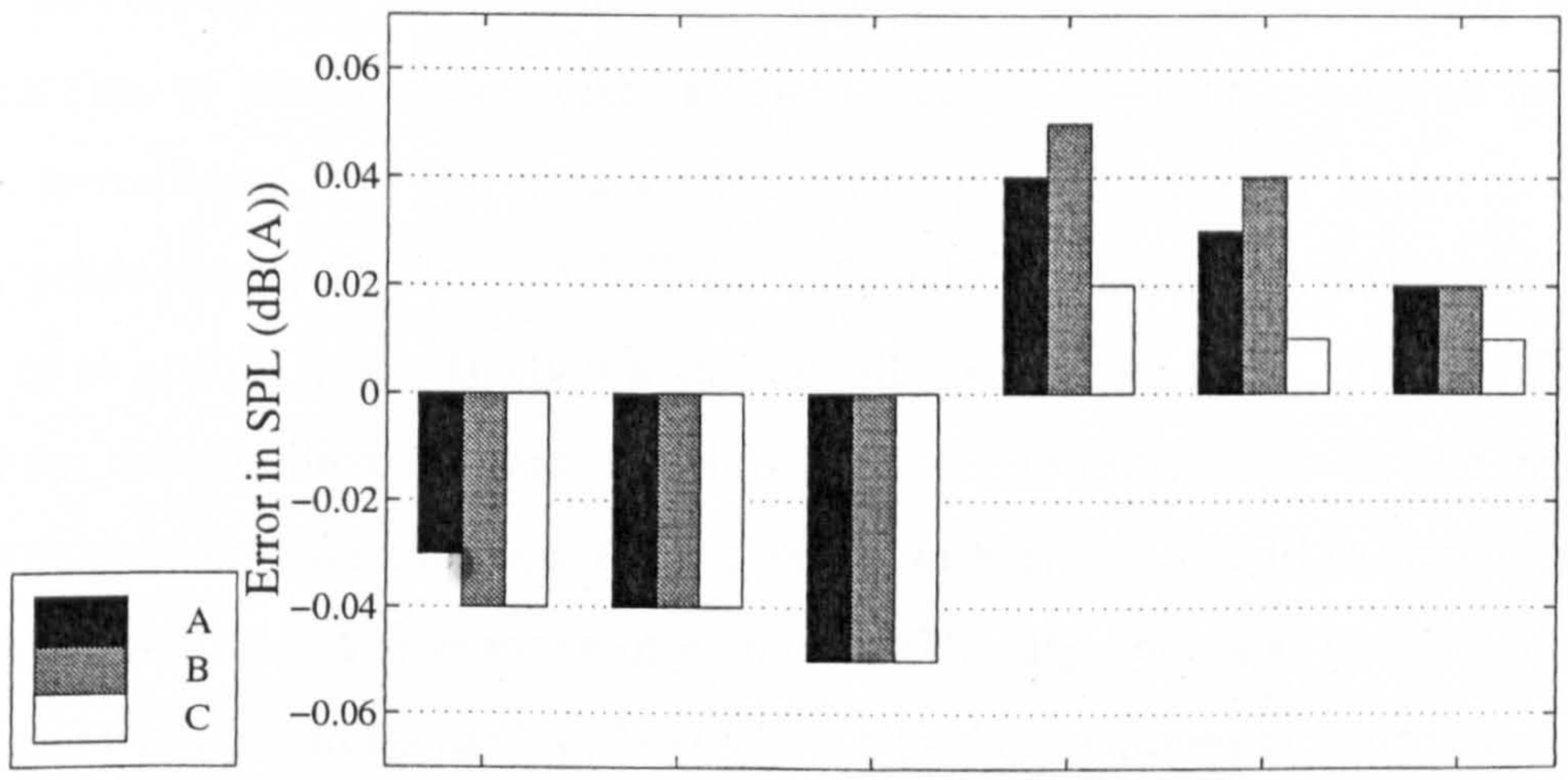

Receiver Position	-40,1.0	-50,1.0	-60,1.0	-40,3.0	-50,3.0	-60,30.
A: 1st calculation	-0.03	-0.04	-0.05	0.04	0.03	0.02
B: 2nd calculation	-0.04	-0.04	-0.05	0.05	0.04	0.02
C: 3rd calculation	-0.04	-0.04	-0.05	0.02	0.01	0.01

Figure 2.35: Error in SPL (dB(A)(A)) between modified solution procedure and coupled integral equation method. 1st calculation: cutting floor defined as AB, $\beta_{c1} \neq 0$; 2nd calculation: cutting floor defined as BC, $\beta_{c1} = 0$; 3rd calculation: cutting floor defined as BC, $\beta_{c1} \neq 0$.

the value for grassland at each frequency. The second and third calculations use the rigid surface CD as the cutting floor with $\beta_{c1} = 0$ in the second calculation, and in the third $\beta_{c1} \neq 0$ takes the same grassland values as in the first calculation.

The results achieved show that there is excellent agreement between the two methods, any errors being no greater in magnitude than 0.06 dB. Additionally the effect of changing from $\beta_{c1} = 0$ to $\beta_{c1} \neq 0$ in between the second and third calculations is small and only evident at the higher receiver positions.

Clearly these results further validate, via a comparison with an independently written and quite different boundary element code, the approximations made in the modified solution procedure.

It is interesting also to compare the efficiency of the modified solution procedure with that of the exact boundary element method based on a coupled integral equation formulation. For the cross-section shown in Figure 2.34, $\tilde{\gamma}$ in the modified solution procedure is the arc $SABCDEFGT$, with S and T the orthogonal projections of A and G, respectively, on the line of the cutting floor. The CPU time required for the modified solution procedure is given by (2.99) with N_1 the number of elements on $\tilde{\gamma}$ and, for the cross-section shown in Figure 2.34 and the calculations reported above, N_2 is the number of elements BF. By contrast, for the coupled integral equation formulation [100, 101], the CPU time required is approximately

$$\frac{c}{3}(N_3 + 2N_2)^2 + C_1 {N_2}^2 \text{ seconds} \tag{2.100}$$

where $N_3 < N_1$ is the number of elements on the sides and bottom of the cutting, $BCDEF$ in Figure 2.34. For large problems, the CPU time consumed is dominated by the first term in (2.99) and (2.100), and this first term is much larger in (2.100) as a set of $N_3 + 2N_2$ simultaneous equations is being solved rather than the N_1 simultaneous equations in the modified solution procedure. As a result, the requirements for storage are similarly in favour of the modified procedure: the modified procedure and coupled integral equation method require respectively

$$\frac{16{N_1}^2}{1024^2} \text{ MB and } \frac{16(N_3 + 2N_2)^2}{1024^2} \text{MB}$$

of RAM.

2.4 Conclusions

The two-dimensional boundary element method is well proven for the study of road traffic noise barriers. However certain characteristics of the method place limitations upon its application. Modifications have been made to the method in order to improve its computational efficiency and to extend the types of cross-section which can be modelled with this method.

The first improvement has been to adapt the method to allow for the efficient simulation of cross-sections in which noise barriers are situated on a ground plane with two distinct impedance values (e.g. a road surface and grassland). The modified two-stage procedure has been applied specifically to model parallel barrier arrangements where the ground between the barriers is of different admittance to that outside. The results obtained give reasonable agreement with those predicted using the existing method and suggest that the inclusion of a small area of ground immediately outside the barrier arrangement during Stage 1 (to model better the outlying ground condition) is unnecessary. Additional simulations with different ground conditions suggest that the accuracy of the modified procedure is reduced when the flow resistivity of the outlying ground is low. For the cases considered, the computational efficiency of the modified procedure (in terms of required CPU time) is better by as much as 90% in comparison to the existing method, making the modified procedure a very useful prediction tool. It is expected that the saving in CPU time will increase with the barrier separation, although not significantly above the figures observed in this study. Successful application of the procedure has been reported for the study of both parallel barrier arrangements and cases of single barriers where different ground types exist on either side of the barrier [124].

The second modification to the method has been made to extend its efficient application to cross-sections where a cutting lies below the level of the main ground plane. The revised method is a three-stage approach. Testing using an incident plane wave and comparison with results predicted using a coupled integral equation method indicate that the modified procedure is accurate in its calculations and

that the approximations used are good. Comparisons with the existing boundary element method are generally very good although the predictions for cross-sections incorporating rigid ground either as the outlying ground plane or the cutting floor show some discrepancy. This has been shown to be largely due to the occurrence of eigenfrequencies in either the existing method or the modified procedure. The reduction in CPU time has been shown from these tests to be commonly of the order of 70-80% and although this figure is reduced when $\beta_c \neq 0$ and $\beta_{c1} \neq 0$, the saving is still significant enough to justify use of the modified procedure. The magnitude of this reduction is more dependant on the proximity of the receiver positions to the cutting rather than the geometry of the cutting itself, the greatest benefit being achieved for very distant receiver positions. Additionally the storage requirements, in terms of RAM, are significantly reduced using the modified procedure.

Chapter 3

Interference-Type Noise Barriers

In this chapter, a study is presented of interference type noise barriers. These are barriers where, in addition to the diffraction over the top edge, sound propagation also occurs along paths directly through the barrier by means of ducts or holes. These additional paths induce a phase change through either the increased pathlength or sound absorption, so that on the far side of the barrier destructive interference occurs between the ducted and diffracted sound paths. A review of previous work is presented in Section 3.1, covering both barriers and individual devices which generate similar effects. A detailed study is then performed upon a device originally reported by Mizuno et al [84, 85]. Section 3.1.4 deals with the origins of the device and subsequent development which has given rise to the profile as presently commercially available. Full scale testing of this configuration has been performed by the author using the Noise Barrier Test Facility at TRL. The layout and procedures followed are described and the results presented in Section 3.2. The acoustic mechanisms of the device are discussed and comparisons made with predictions using the two-dimensional boundary element method described in Chapter 2 on an equivalent cross-section. The efficiency of the device is also compared with a multiple-edge noise barrier profile, which is described in more detail in Chapter 5.

3.1 A Review of Previous Work

Studies have been reported over a number of years which have investigated the performance of a range of different interference-type barrier designs of varying complexity and practicality. The designs broadly fall into 3 categories - barriers with sections of the profile removed or "thnadners", arrays of rigid strips, and waveguide filters - all of which are discussed in the following sections. Some of these designs have been proposed as replacements for standard plane screens, whilst others are intended as an addition to the top of an existing barrier. The final interference device discussed is one which is currently in commercial use.

3.1.1 Thnadner barriers

Studies of the performance of barriers formed from shaped sections or "thnadners", where the profile of the barriers varies along their length, e.g. as shown in Figure 3.1, have been variously reported by several authors. In such instances the degree to which sections of the barrier have been removed is expressed as a percentage of the original area along the length of the barrier. Thus, a 50% open structure (Figure 3.1a) is one which has had 50% of the original area removed. The theory behind such devices is that a deepening of the acoustic shadow can be achieved through interference effects [125]. The set-up and results of the experiments reviewed here are summarised in Table 3.1.

Three different designs of thnadner were tested by Wirt [125] (tests a) in Table 3.1), these being the sawtooth, flat-top and splitter-types as shown in Figures 3.1 and 3.2. The latter type has a profile which varies both parallel and perpendicular to the length of the barrier, the intention being to introduce duct effects as an additional attenuation mechanism. The experiments were performed at 1:16 scale on a surface representative of rigid ground using a broad-band pink noise source (which gives a flat spectrum when plotted in octaves) with a frequency range 75 – 4000 Hz. All three types were treated with sound absorptive felt (having a flow resistivity $\sigma = 60$ cgs rayls and depth as specified in the table), the sawtooth and flat-top designs on the source facing side, and the splitters on both surfaces. The

Test	Device Type (Fig 3.1-3.3)	Device Height (m)	Overall Barrier Height (m)	Reference Barrier (type & height)	Absorptive Treatment on device (depth & σ)	Source			Receiver Positions	ΔIL dB(A)
						Type	Height (m)	Dist.$^{\diamond}$ (m)		
a) [125]	Flat-top, absorptive	2.4	4.8	Reflective 4.8 m	200 mm 60 cgs rayls	BB, P	2.4	19.2	2.1 – 56.1 m at 3 m intervals height = 2.4 m	1 – 4 increasing with distance
	Flat-top, absorptive		6.0*	Absorptive† 6.0 m						1.5 – 4.5
	Saw-tooth, absorptive		6.0*	Absorptive† 6.0 m						-1.5 – 4.0 increasing with distance
	Splitter, absorptive		4.8	Reflective 4.8 m	50 mm 60 cgs rayls					-8.5 – -1.0 increasing with distance
b) [82]	Saw-tooth, reflective	2.4	4.9	Reflective 4.9 m	—	BB, W	1.2	12.2	6.1, 12.2, 24.4, & 36.6 m height = 2.4 m	-3.2 (average)‡
	Saw-tooth, absorptive				200 mm					-2.2 (-1.3)* (average)‡
	Splitter, reflective				—					-6.6 (average)‡
	Splitter, absorptive				200 mm					-2.9 (-2.0)* (average)‡

Source type: BB, broadband source; P, Pink noise spectrum; W, White noise spectrum. ⋆ Barrier height includes 1.2 m height of absorptive section beneath device, ∗ Insertion loss relative to absorptive screen, † Absorptive treatment as for device, ‡ Average level over all receiver positions, ◇ Horizontal distance from face of barrier.

Table 3.1: Thnadner barriers - Summary of experimental arrangements and measured increase in insertion loss, ΔIL, relative to specified reference barriers. Dimensions in metres at full scale.

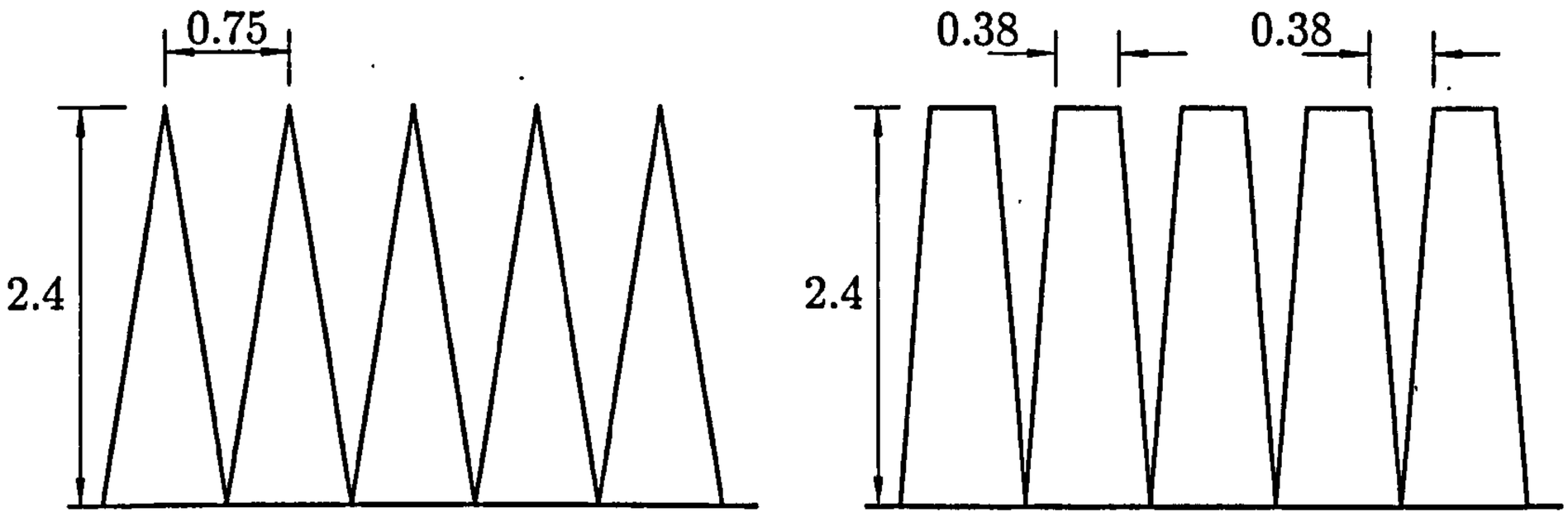

a) saw-tooth thnadners (50 % open) b) flat-top thnadners (25 % open)

Figure 3.1: Thnadner barriers as tested by Wirt [125], viewed perpendicular to the length of the barrier. Dimensions in metres at full scale.

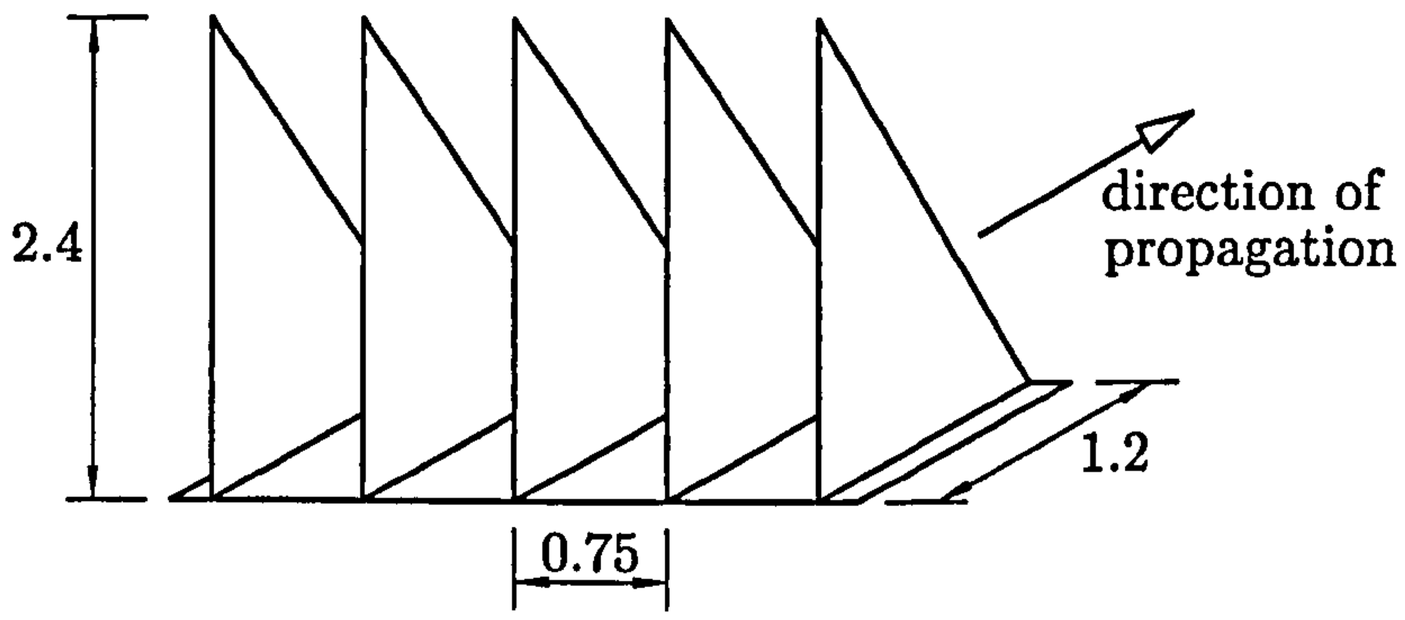

Figure 3.2: Splitter-type thnadner arrangement (84 % open) as tested by Wirt [125]. Dimensions in metres at full scale.

devices shown in Figure 3.1 were mounted on top of a plane reflective screen, and in the case of the splitter-type thnadners (Figure 3.2) on top of a reflective embankment type profile. In the case when the overall barrier height was 6 m rather than 4.8 m, a 1.2 m height plane absorptive screen was inserted between the thnadners and the reflective screen below. However for reasons not explained by Wirt, no increase in source and receiver heights were introduced to allow for the increase in barrier height. The results from these tests are summarised in Table 3.1

The flat-top thnadner was observed to be the most effective design relative to both reflective and absorptive plane screens, providing additional insertion loss of up to 4.5 dB(A) over the distances considered. However comparison between the different designs is hindered by the variation also in barrier and source height. The absorptive splitter panels performed poorly, providing lower screening levels than

the reflective plane screen of the same height, particularly in the region close behind the barrier. Generally the performance of the different devices improved as the receiver moved further from the barrier, and measurements taken at a series of positions parallel to the barrier indicated that the behaviour of the flat-top and saw-tooth profiles was generally uniform. It was proposed [125] that such designs might be advantageous since less material is required than for a plane screen and the attenuation provided is of a similar order. However, no measurements were taken to assess the influence of either the source or receiver height upon the effectiveness of the designs.

May and Osman [82] conducted similar experiments on a surface representative of grassland using both reflective and absorptive sawtooth and splitter-type thnadners mounted atop barriers or walls (tests b), Table 3.1). No precise dimensions are given for the designs, but the overall height was 4.9 m at full scale, compared to an overall height of 4.8 m in the previous study. It is unclear as to the precise characteristics used for the absorptive treatment, although the sound absorption coefficient, α, appears to have been between 0.61 – 0.8. The source position was below the level of the bottom of the thnadners. The results presented in the table are the average levels over the four specified receivers, although two measurements were performed at each receiver; one in which there was a direct line of sight between the source and receiver and one in which the line of sight was interrupted by the array. The results show that all four configurations provided on average 2.2 – 6.6 dB(A) less screening than a simple reflective barrier of the same height. The introduction of absorptive treatment rendered the designs slightly more effective, particularly at the receiver position closest to the barrier. Again, no measurements were performed to investigate the effect of source and receiver height upon the thnadner efficiency.

Hutchins et al [64] conducted a further series of experiments at 1:80 scale on rigid and absorbing ground using the sawtooth and flat-top thnadners tested by Wirt (Figure 3.1) and the test geometry of May and Osman, i.e. a source position 12.2 m behind the barrier at a height of 1.2 m, an overall barrier height of 4.9 m and

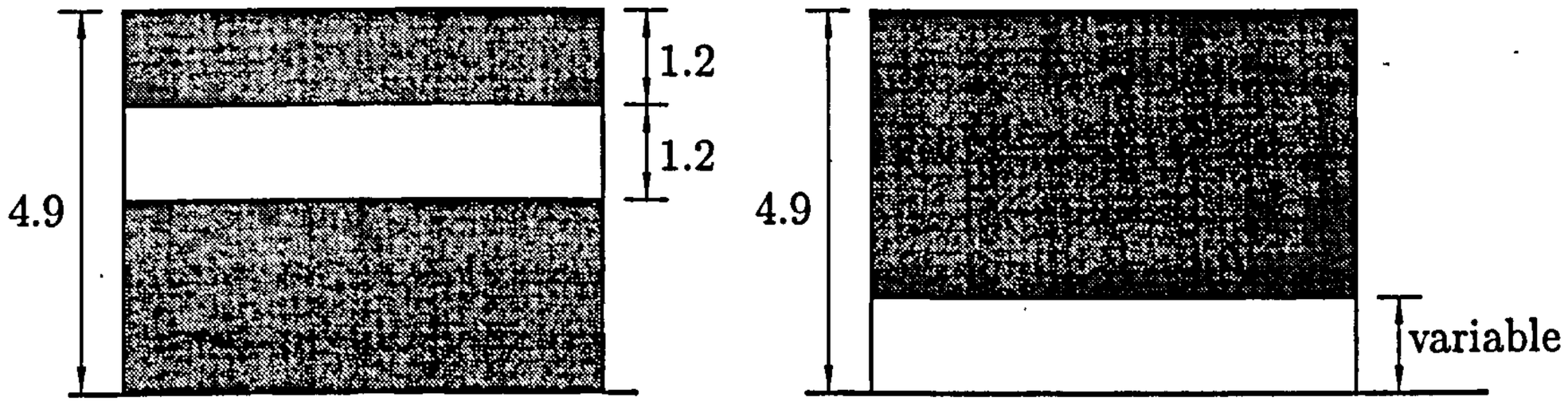

Type (A) Type (B)

Figure 3.3: Barriers as tested by Hutchins et al [64]. Dimensions in metres at full scale.

a single receiver position at 12.2 m from the barrier. For both ground conditions, the thnadner designs were observed to be less efficient than the plane screen of equivalent height. In addition, two designs of reflecting barrier with horizontal sections removed were considered [64] as shown in Figure 3.3. Type A was equivalent to a 50% open thnadner, in terms of the percentage open area in the top 2.4 m, whilst the variable gap in Type B was either 0.5 or 1.0 m. The attenuation provided by these designs was comparable to or worse than that resulting from use of the thnadner devices. In related work, Wassilieff [117] reported on 1:2 and 1:4 scale model experiments using picket barriers. These were similar to the flat-top thnadners of Wirt except that the gaps between adjacent pickets were of uniform width over the height of the barrier.

The reported tests on thnadner designs present a mixed picture, although for the most part it appears that they are less efficient than plane screens of equivalent height even when these are reflective. An accurate assessment is prevented due to the variation in source and barrier height, and the receiver positions chosen in the different studies. Considering the work by Hutchins et al [64] in particular, a single receiver position is insufficient to provide any meaningful insight into the behaviour of the device. For any practical application of such devices to be considered, particularly in the field of road-traffic noise abatement, much more detailed studies would be necessary to establish the effects of source and receiver height upon performance and particularly source positions closer to the barrier. No consideration has been

given as to how these devices would behave if used to provide the full barrier height, i.e. erecting the devices directly onto the ground, and other work, e.g. [121] has shown that significant improvements in screening can be achieved through the use of additional barrier elements without increasing the height of any existing barrier.

3.1.2 Rigid strip networks

Early studies into the acoustic performance of waveguides were carried out by Amram and Stern [3], using arrays of rigid strips arranged in the shape of a prism such that adjacent rows of strips formed slotted ducts (Figure 3.4). At low frequencies where the wavelength of the incident sound is much greater than the width of the strips, the ducts allow the propagation of "slow waves" (i.e. the phase velocity within the waveguide is less than that in free-field). Above the resonant frequency (where the wavelength approaches twice the width of the strips) the prisms were intended to behave as a waveguide filter in that a series of pass-bands and stop-bands occur. In the stop-bands, sound energy is reflected by the prism resulting in backward scattering; less reflection occurs in the pass-bands.

Various shapes of prism were tested at 1:10 scale, the dimensions of which are given at full scale in Figure 3.5. At full scale the test arrangement was as shown in Figure 3.6 [3]: a broadband pink noise source, with frequency range 0.1 - 2 kHz was positioned at 51 m from the centre of the prism under study, the separation being sufficient to approximate incident plane waves. The prism was mounted on a turntable which was rotated in front of the source to allow the effects of different angles of incidence to be measured. The source and receiver microphone were set at the same height. To prevent sound propagation around the sides of the prism, a conical horn was set against one face, with the measurement microphone mounted in the throat of the horn at a distance of 6 m from the prism.

It was observed that the scattering patterns varied depending upon the frequency of the incident noise. The insertion loss resulting from the introduction of the

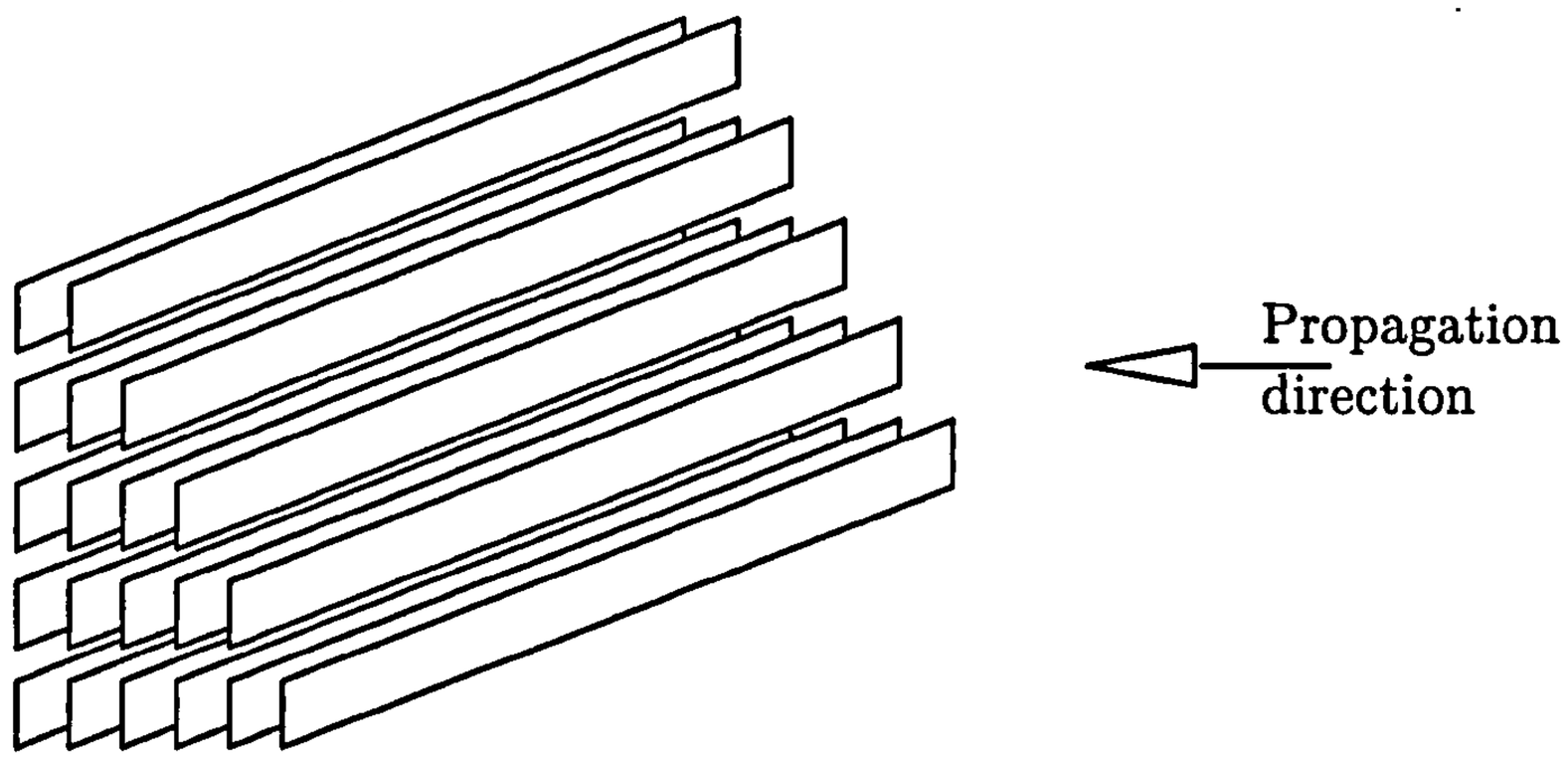

Figure 3.4: Prismatic array of rigid strips as tested by Amram and Stern [3].

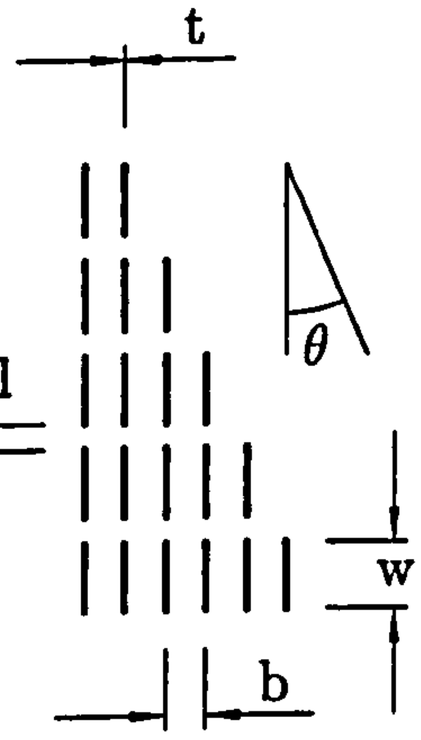

Prism	w	t	l	b	θ (°)	No. of rows	Extra strips /row	Strips in top row
A	0.51	0.03	0.19	0.13	14.0	5	1	2
B †	0.51	0.01	0.19	0.19	15.3	6	2	2
D	0.51	0.01	0.10	0.13	24.0	5	3	3
I	0.19	0.01	0.10	0.13	42.0	10	3	6
H	0.25	0.03	0.25	0.25	56.0	6	3	2

†Prism B is isosceles

Figure 3.5: Different prism arrangements as tested by Amram and Stern [3]. Dimensions in metres at full scale.

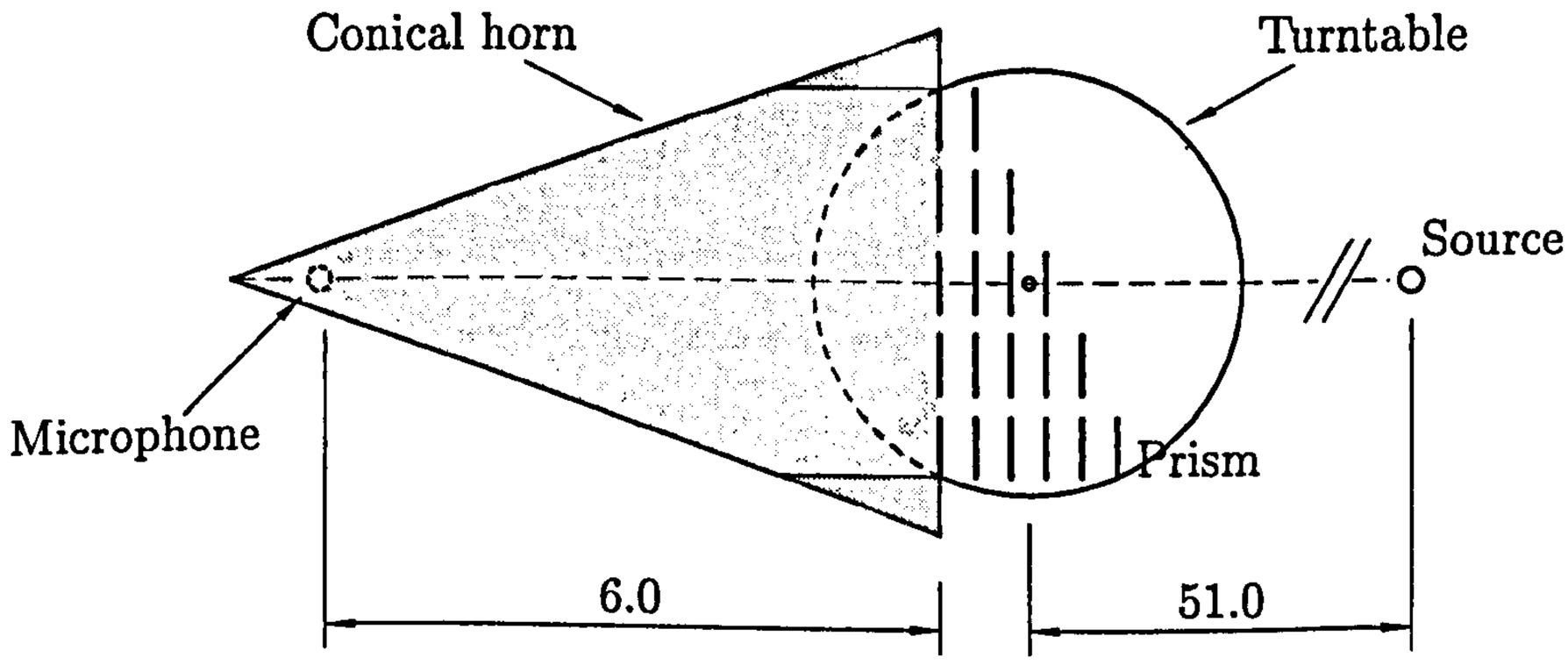

Figure 3.6: Plan view of experimental arrangement used by Amram and Stern [3]

prisms was calculated for each third-octave band of pink noise within the considered frequency range. However this was only for the case of a single receiver position, when the line of sight between source and receiver was perpendicular to the rear face of the prism (Figure 3.6). These results are presented in Figure 3.7

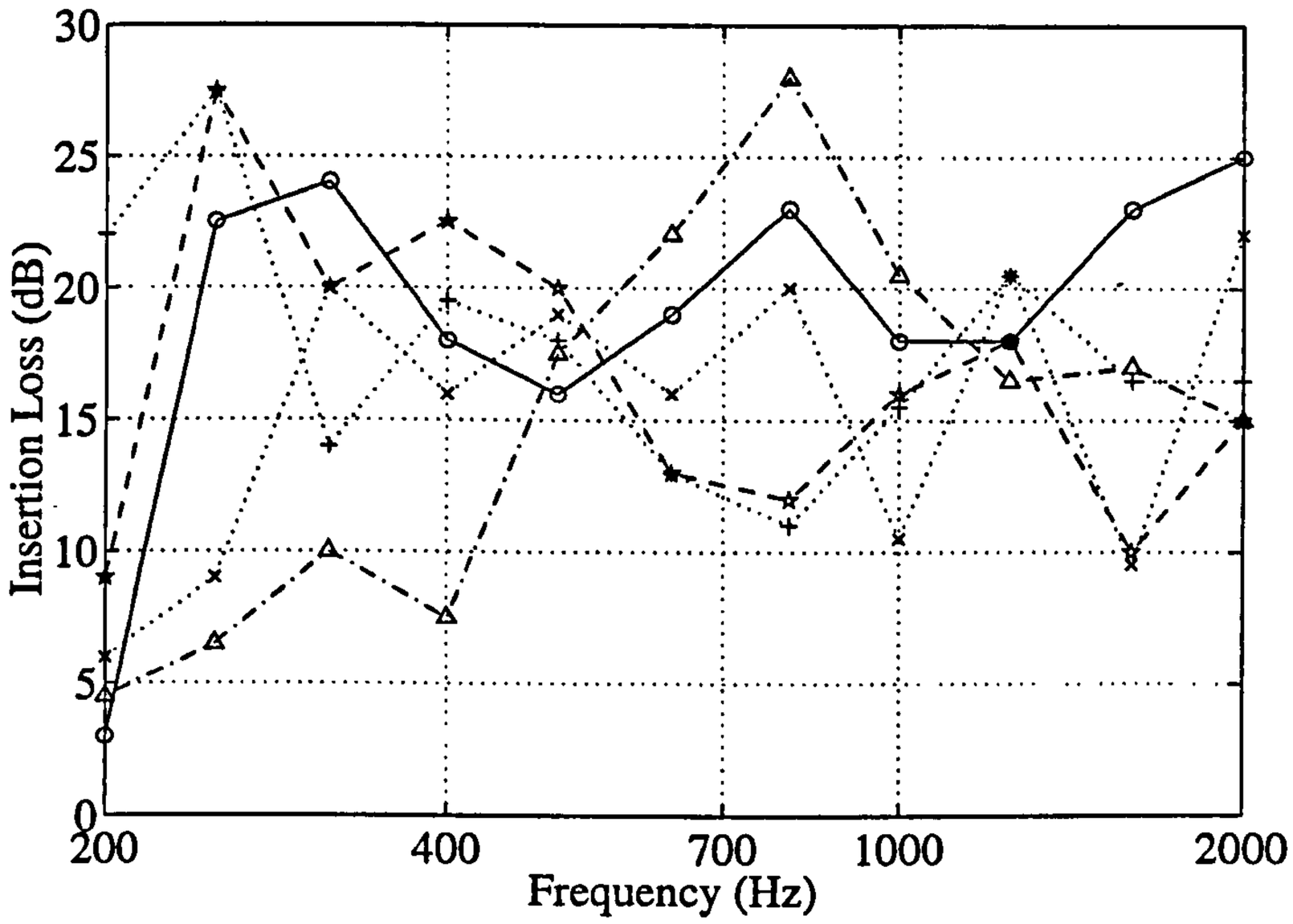

Figure 3.7: Predicted insertion loss spectra for different prism arrangements as tested by Amram and Stern [3]. Prism arrangements as detailed in Figure 3.5: ∘, prism A; ⋆, prism B; +, prism D; △, prism I; ×, prism H.

Although not the most efficient, the isosceles prism with wide horizontal spacing between the strips (prism B in Figure 3.5), equivalent to a 20% open structure (Section 3.1.1) was claimed as providing the behaviour most representative of such an open structure, although the explanation for this choice is unclear. Figure 3.7 shows no single prism to be the most effective over the full frequency range. It was claimed by the authors that comparisons of the prism with a solid barrier showed attenuation levels to be similar, although no details or evidence were presented to substantiate this claim. It was suggested [3] that such a prism may provide a means of enhancing ground effect and that the flexible nature of the structure may provide improved safety conditions if installed as a highway noise barrier. However, the tests reported were conducted in the absence of a ground plane and together with the

limited source and receiver positions considered provide insufficient evidence that such a structure could be effectively used as a purpose-built noise barrier.

In related work, Amram et al [4] extended the study to find an effective theoretical approach to calculate, for a specific prism arrangement, the first stop-band frequency at which 180° phase difference could be achieved relative to propagation in free-field, whilst also optimising the overall effectiveness of the prism through selection of appropriate strip widths and separation.

3.1.3 Waveguide filters

The waveguide filter shown in Figure 3.8 is based upon the rigid strip networks described in [3] and [4], and was tested by Amram and Chvojka [6]. The design is such that at low frequencies, the exit of the waveguide and the rear diffracting edge behave as secondary line sources, the two being coherent over a short bandwidth. When the phase lag between the two paths is 180° and the amplitudes are similar, the effect is to create a vertical dipole line source.

The aim of the tests was to validate a mathematical model for calculating the phase lag and insertion loss between these secondary sources. Experiments were conducted at 1:4 scale under anechoic conditions using the source/receiver geometry of Figure 3.8. The device was at sufficient height above the floor to ignore ground reflections and mounted on a fibreglass block.

The two microphone positions corresponded to the approximate secondary source locations, and the dimensions of the device were chosen to provide optimum attenuation at 500 Hz. The source emitted white noise over the frequency range 200-1000 Hz (at full scale). Good agreement was observed between the measurements and numerical predictions. Total phase reversal between the two paths (through and over the top of the waveguide) was observed to occur around 525 Hz. It was found that the effective frequency range could only be widened by blocking the path from the exit slot to the upper receiver position.

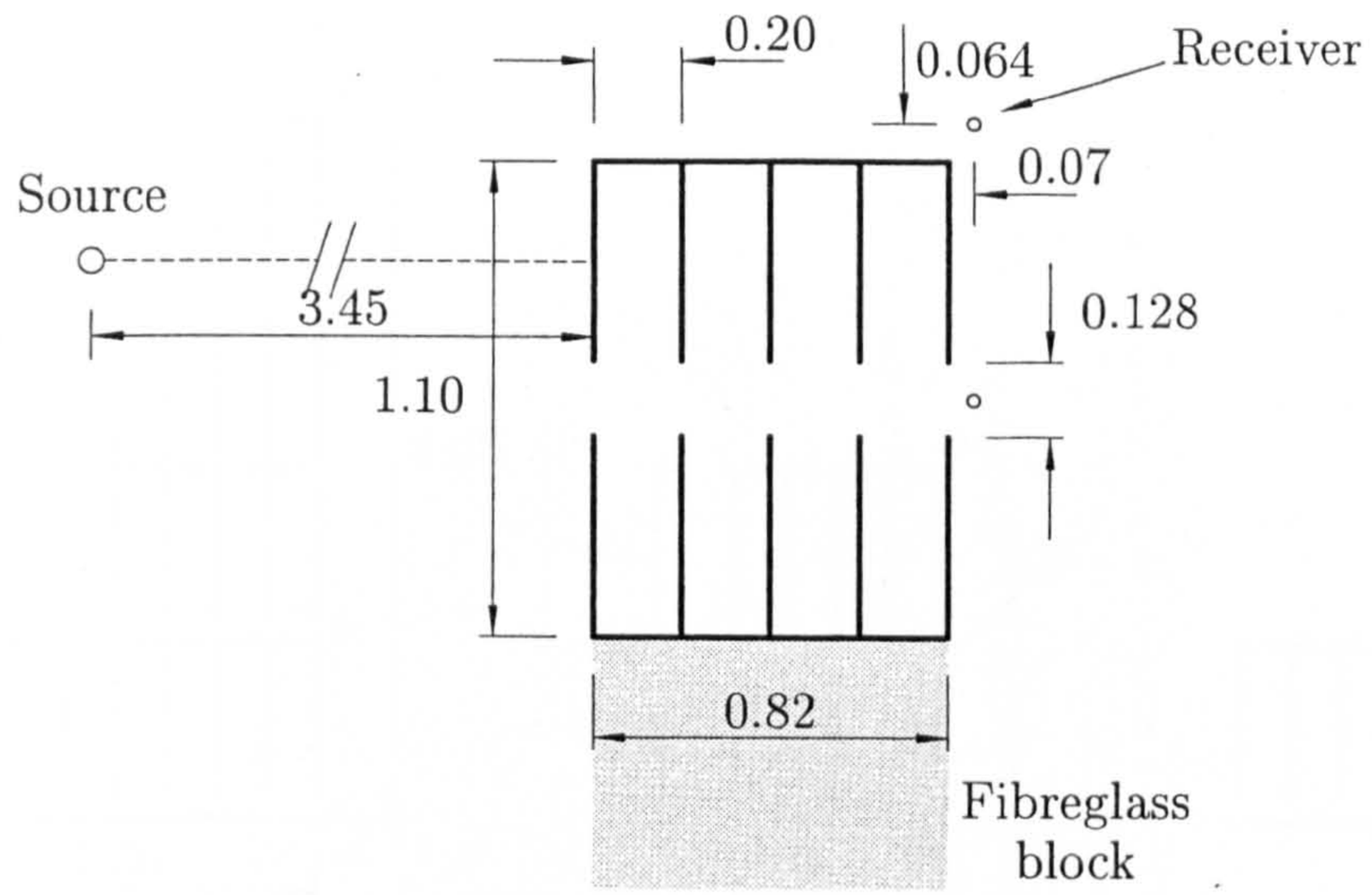

Figure 3.8: Waveguide filter as tested by Amram and Chvojka [6].

The mathematical model was extended by Nicolas and Daigle [96] to allow for reflections in the ground surface. The filter, which was formed from five slots instead of the four tested in the previous study, was inserted into a barrier of the same width such that the barrier extended above and below the filter. The experiments were performed for cases of either rigid or finite impedance ground on the receiver side of the barrier ($\sigma = 30$ cgs rayls in the latter case), but always with rigid ground on the source side. Measurements were taken for various source and receiver heights and separations from the barrier. Good agreement was achieved between the theory and experiments. However comparing the efficiency of the waveguide filter in the presence of the different ground conditions is difficult due to the varying source and receiver positions.

The use of such waveguides and half-waveguides in columns, thereby forming multi-polar barriers as shown in Figure 3.9a has been reported for both scale model and full scale tests [36, 7].

Droin et al [36] performed 1:4 scale model experiments in the absence of the ground for configurations similar to Figure 3.9a, using a source emitting white noise positioned 3 m from the barrier (to approximate incident plane waves). Receiver positions were placed close to the exits of the waveguides and an additional barrier

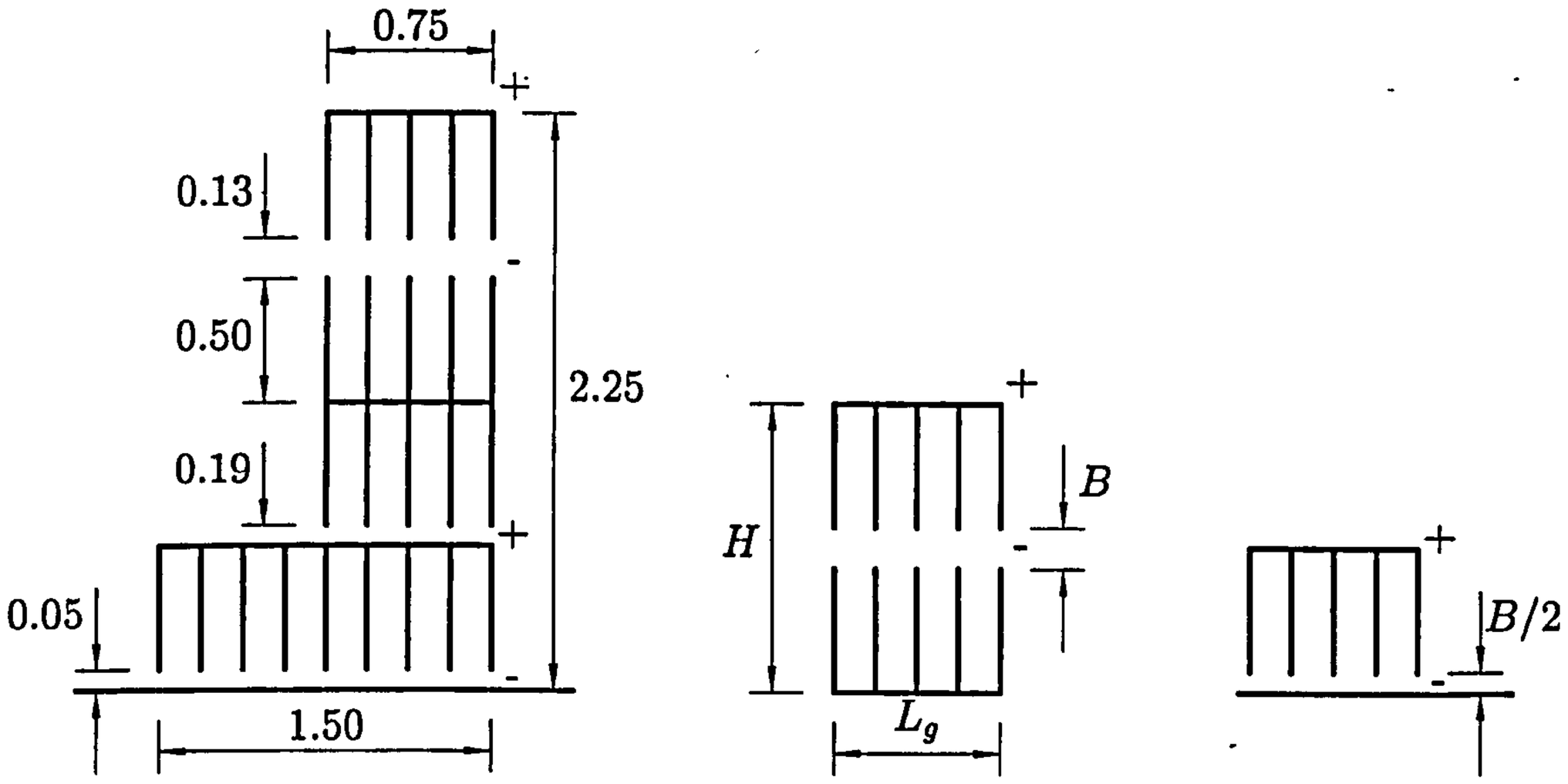

a) Multipolar waveguide

b) Full dipolar waveguide

c) Half waveguide

Figure 3.9: A multi-polar waveguide barrier and its basic components. Dimensions in metres at full scale (from [7]).

mounted on the top of the arrangement to minimise propagation directly over the device. It was established that for a basic waveguide of width L_g comprised of N cavities and with vertical separation B (Figure 3.9b) , the phase lag introduced was similar to that for a half-waveguide at height $B/2$ above a reflective surface. (Figure 3.9c). The experiments also indicated that for a fixed height, H, it is possible to optimise the horizontal dimensions of the waveguide, such that one of width $L_g/2$ provides a similar phase lag to one of width L_g. This was achieved through a reduction in the separation between adjacent strips.

This would suggest that a barrier could be comprised solely of half-waveguides stacked on top of one another, with the possibility of their application as noise barriers improved due to the reduced dimension L_g. However at this stage, no detailed study of the devices had been reported for receivers other than those in very close proximity to the waveguide, particularly with regard to determining the extent of the interference region. Further more, all source positions had been chosen to approximate plane wave incidence, which is not particularly characteristic of road

traffic noise sources and, with the exception of [96], the tests had been conducted in the absence of a ground plane.

These problems were addressed by Amram et al [7, 5], who conducted scale model experiments for both the multipolar device of Figure 3.9 and the same array with only the upper waveguide open (the configuration being similar to mounting the device of Figure 3.9b on a wall). Comparisons were drawn with a solid barrier of the same overall height. The experiments were performed at 1:20 scale. At full scale, the test arrangement was as follows: an array of ultrasonic whistles was placed in the ground, at 41 m from the barrier (on the left hand side in the figure), and an array of 128 receiver microphones sited behind the barrier at distances between 5 and 125.6 m, and heights of 1.2 – 19.2 m above ground. The frequency range of interest (at full scale) was 50 – 1000 Hz.

Relative to the solid barrier, the attenuation provided by the dipolar device varied from ±2dB. However around the tuning frequency of the waveguides, at 100 Hz, the performance of the waveguide improved, with attenuation throughout the shadow zone being consistently better than the solid barrier by as much as 4 dB.

The multipolar waveguide was observed to be more efficient than the dipolar arrangement, providing an additional 1 – 2 dB attenuation relative to the solid barrier at almost all receiver positions. Around the tuning frequency, at 100 – 125 Hz, the additional attenuation was as much as 3 – 5 dB with the performance being maintained even above the shadow zone.

Comparisons between 1:20 scale model and outdoor full scale measurements were made [7, 5] for the same arrangements using a source at 20 m from the barrier in the ground and receivers at 20m from the barrier and heights of 1, 2, 3 and 4 m. In the case of the full scale measurements, an additional source was used at a height of 1.5 m (the two positions being representative of tyre and engine noise sources on a truck). A pink noise spectrum was used. Agreement between the two sets of results was poor, particularly above 400 Hz, with the outdoor measurements giving generally lower relative attenuation levels than the scale model tests. Both

devices proved most effective at the higher receivers although the multipolar device provided generally 2 dB greater relative attenuation than the dipolar waveguide. This is as would be expected since less energy is passing through the barrier. Both devices exhibited enhanced screening around the tuning frequency, at 100 – 125 Hz, where maximum interference effects were expected to occur, the relative insertion losses being of the order 2 – 4 dB. The dipolar waveguide was generally less efficient than the plane screen at all receiver heights in both experiments. The performance of the multipolar waveguide at full scale was more varied; ignoring the enhanced screening around the tuning frequency, relative insertion losses of between -1 – 2 dB (laboratory) and -2 – 3 dB (outdoor, full scale) were measured.

It is observed that there were noticeable differences between the two sets of measuring conditions. In particular, in the outdoor measurements no attempt was made to take account of varying meteorological conditions (see Section 3.2.1), the ground was of different impedance on either side of the barrier and the characteristics of the source was different. To a large degree, this renders comparison between the data sets irrelevant. However the full scale measurements are more representative of conditions which would be encountered if the device were applied as a roadside noise barrier. To verify the potential use as purpose-built noise barriers, further measurements would be required under a balanced set of meteorological conditions.

In associated work, theoretical and experimental studies have been reported which have looked at the effect of the angle of incidence of a source upon such waveguides, using either the standard waveguide of Figure 3.9b, or a column constructed from multiples of the half-waveguide shown in Figure 3.9c. It has been established from these studies that when varying the angle of incidence perpendicular to the entrance slots of the array (i.e in the vertical plane), the performance appears independent of the angle of incidence. However, varying the angle of incidence in the horizontal plane shows the barrier performance to be much more angle dependant. This has implications for the application of such designs as roadside noise barriers. One approach may be to divide the length of the waveguide into

a series of shorter isolated segments through the introduction of vertical splitters (as with the Calmzone interference device in Figure 3.18 of Section 3.1.4), thereby preventing propagation within the waveguide along the length of the barrier.

The most recent developments of these waveguides have been reported by Amram and Masson [9, 79], based on the configurations shown in Figure 3.10, i.e two half-waveguides separated by an expansion chamber. Scale model tests were performed

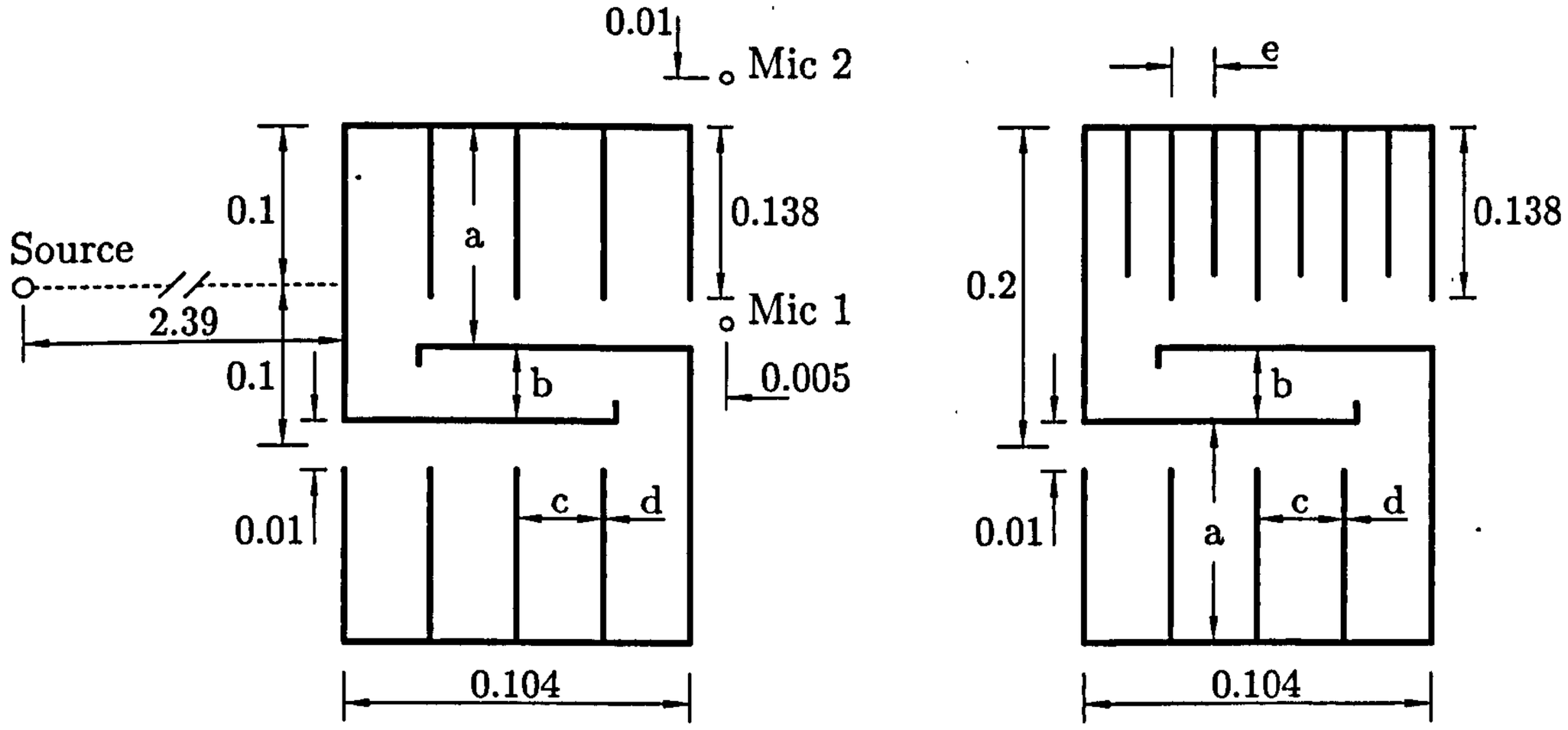

a) Symmetric filter b) Asymmetric filter

Figure 3.10: Waveguide filters as tested by Amram and Masson [9, 79]. Internal dimensions: a = 0.136 m, b = 0.041 m, c = 0.026 m, d = 0.0015 m, e = 0.013 m.

in an anechoic chamber using a 1:3 scale model of a motorway site [9]. Although not specified, the dimensions of the device were chosen to provide optimum attenuation between 500 and 1000 Hz, so as to specifically attenuate HGV noise. The waveguide was mounted onto the top of a barrier (the combined height being 1.1 m) and the whole arrangement positioned on an embankment with flat ground on the receiver side. A cylindrical source was placed at 3.6 m in front of the barrier, an angle of incidence of 30° (with the source below the top of the barrier) being necessary to achieve effective screening over a wide frequency range. Measurements were taken at distances out to 7 m behind the barrier, at angles between −18° and +27° in the vertical plane (0° being directly opposite the exit of the waveguide). It is not clear

as to whether the 3 – 5 dB attenuation achieved with the device, at third octave frequencies in the range 250 – 1250 Hz, was relative to a barrier of the same overall height or simply the additional attenuation provided by the device. Full scale in-situ tests on the same geometry were less successful, although it was found that inclining the waveguide at 15 – −30° improved the performance.

Overall, it appears that the application of such dipolar and multipolar waveguides as noise barriers is restricted, particularly since they are designed to attenuate low frequency noise, e.g. a typical road traffic noise spectrum (Figure 3.24) peaks at 1 – 2 kHz. Although the experiments have validated the predicted phase differences and dipole theory, limited work has been reported on the behaviour of such waveguides over a wider area behind the barrier. More detailed testing is required to establish their true efficiency, and whether the attenuation that they offer can be achieved through the use of simpler and less costly solutions.

3.1.4 The Calmzone Interference Profile

In 1984, Mizuno et al proposed a device for reducing highway noise [84] which was comprised of a series of stacked square ducts, inclined at some angle to the horizontal and reducing in length as the stack height increased, as shown in Figure 3.11a. Such an arrangement is designed to induce a phase lag in sound propagating through the device, thereby generating destructive interference between that and sound propagating directly over the top of the device.

Two devices were tested as part of the study, one with the ducts inclined parallel to the base (Type 2, $\alpha = \beta = 50°$ in Figure 3.11b) and one with the ducts inclined at 30° to the base (Type 2', $\alpha = 80°$, $\beta = 50°$). Otherwise all dimensions were as stated in the figure, with the Type 2 device therefore comprised of a greater number of ducts. It is not specified by the authors whether these experiments were conducted as full-scale or scale model tests. In view of the small duct cross-section and the frequency range of interest (250 Hz - 1.6 kHz), it does not seem unreasonable for the experiments to be 1:4 scale. This is perhaps justified in studies reported later

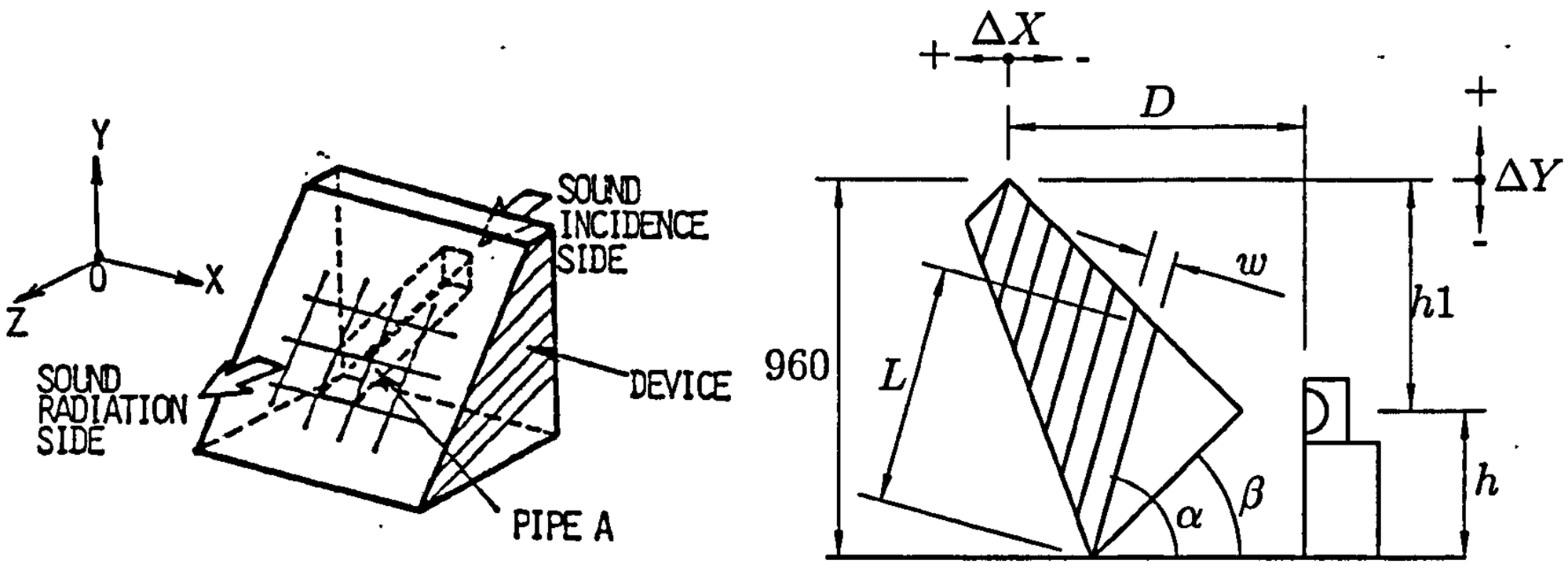

a)The device illustrated in 3D

b) Controlling parameters. $L = 540$ mm, $w = 5$ mm, $\beta = 50°$, h = 540 mm.

Figure 3.11: The interference device proposed by Mizuno et al [84].

in this chapter, where a barrier of the same overall height is introduced behind the device.

The experimental arrangement was as shown in Figure 3.12a with the ground covered by 20 mm of glass wool to minimise any reflection of refracted sound waves. Equipment was developed to allow visualization of the sound field on the radiation side of the device. Figure 3.12b shows the sound field measured behind the Type 2' device for a source emitting white noise over the 1/3 octave band centred on 2 kHz. The white areas denote levels above a reference level of 79 dB, the black areas levels below 79 dB. The interference region generated by the device, denoted C, can clearly be seen. Equations were presented for the theoretical prediction of the sound pressure level within this zone. For a source emitting white noise over the 1/3 octave band centred on 1 kHz, agreement to within 1 dB was achieved between measured and predicted levels at a series of unspecified receivers in the interference zone.

A second experiment was performed using the source/receiver positions of Figure 3.12a and a white noise source. The results are summarised as test a) in Table 3.2. To establish the relative contribution of the interference effects, measurements were also performed with the duct exits sealed. At the lowest receiver position, the measured SPL spectra revealed the device to provide approximately 10 dB insertion loss at

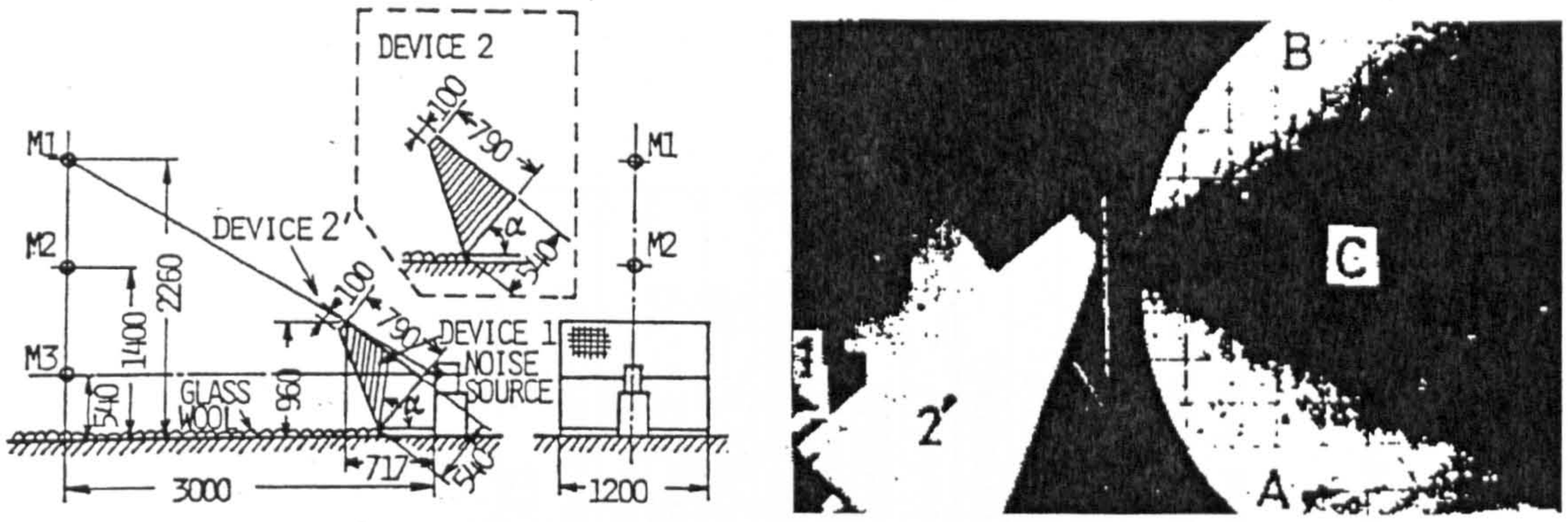

a) Experimental arrangement

b) Sound pressure distribution for interference device

Figure 3.12: The experimental arrangement and preliminary results as from Mizuno et al [84].

each third octave frequency between 250 - 1600 Hz. Sealing the ducts degraded the performance by a uniform 5 dB. At the other receiver positions performance was observed to increase with frequency (Figure 3.13 shows the results at the mid-height receiver position). At these positions, sealing the ducts was observed to decrease the effectiveness of the device by between 6 - 8 dB.

The results indicated that all three receiver positions lay in the interference zone, despite there being a direct line of sight between the source and the highest receiver. The implication of the results is that the interference effect is not restricted to any given third-octave band frequency. No explanation is provided by the authors as to why only the duct exits were sealed when testing the device as a solid barrier.

Further tests were conducted by Mizuno et al [85] to establish a series of design criteria for the device. The effects of varying three different dimensions were studied: duct width, maximum duct length and angle of inclination, denoted by w, L and α respectively in Figure 3.11b. The same experimental setup was used as in the previous tests (Figure 3.12a) with a source emitting white noise over a frequency range 250 Hz – 16 kHz. The type 2' device was used for the investigations into w and α, and the type 2 device for the tests involving changes in L. Unless under

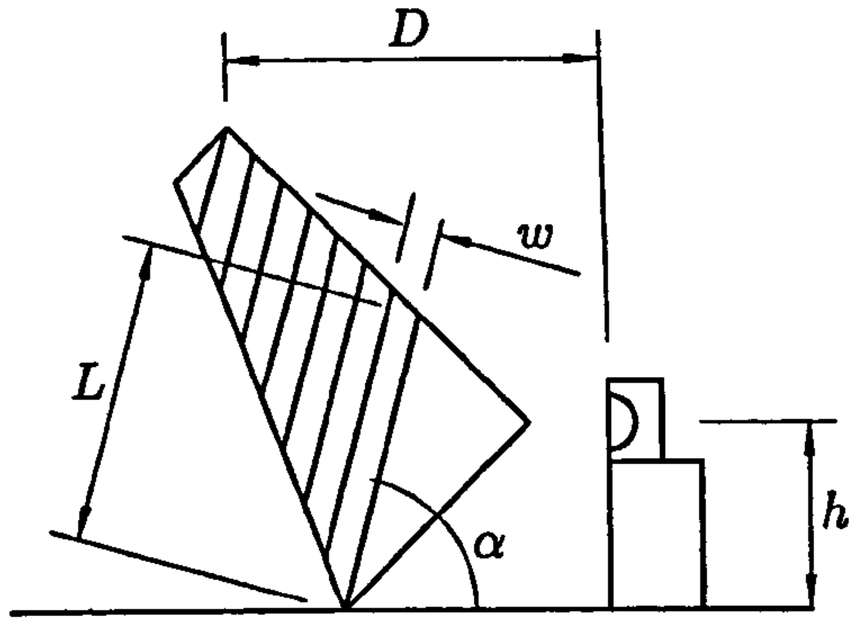

	Type	Device Dimensions			Source Position		Receiver Pos.		*IL* dB over 1/3 octave spectrum*
		L	*w*	*α*	*D*	*h*	Distance‡	Height	
a)	2'	0.54	0.005	80°	0.717	0.54	3.0	0.54	10, uniform (-5)†
								1.40	8 – 27, increasing (-6 – -7)†
								2.26	5 – 32, increasing (-6 – -8)†
b)	2'	0.54	0.005	80°	0.717	0.54	3.0	1.40	8 – 28, generally increasing
			0.020						9 – 23, variable
			0.080						5 – 18, variable
			0.100						5 – 18, variable
c)	2	0.260	0.005	50°	0.717	0.54	3.0	0.54	0 – 23, increasing
		0.325							0 – 24 increasing
		0.540							0 – 24 increasing

* the change in insertion loss with frequency, e.g. 'increasing' denotes the insertion loss increases with frequency. † denotes reduction in device *IL* caused by closing of ducts. ‡ Horizontal distance from source.

Table 3.2: Summary of experimental arrangements and Insertion Losses, *IL*, for interference devices tested by Mizuno et al [84, 85]. Dimensions in metres.

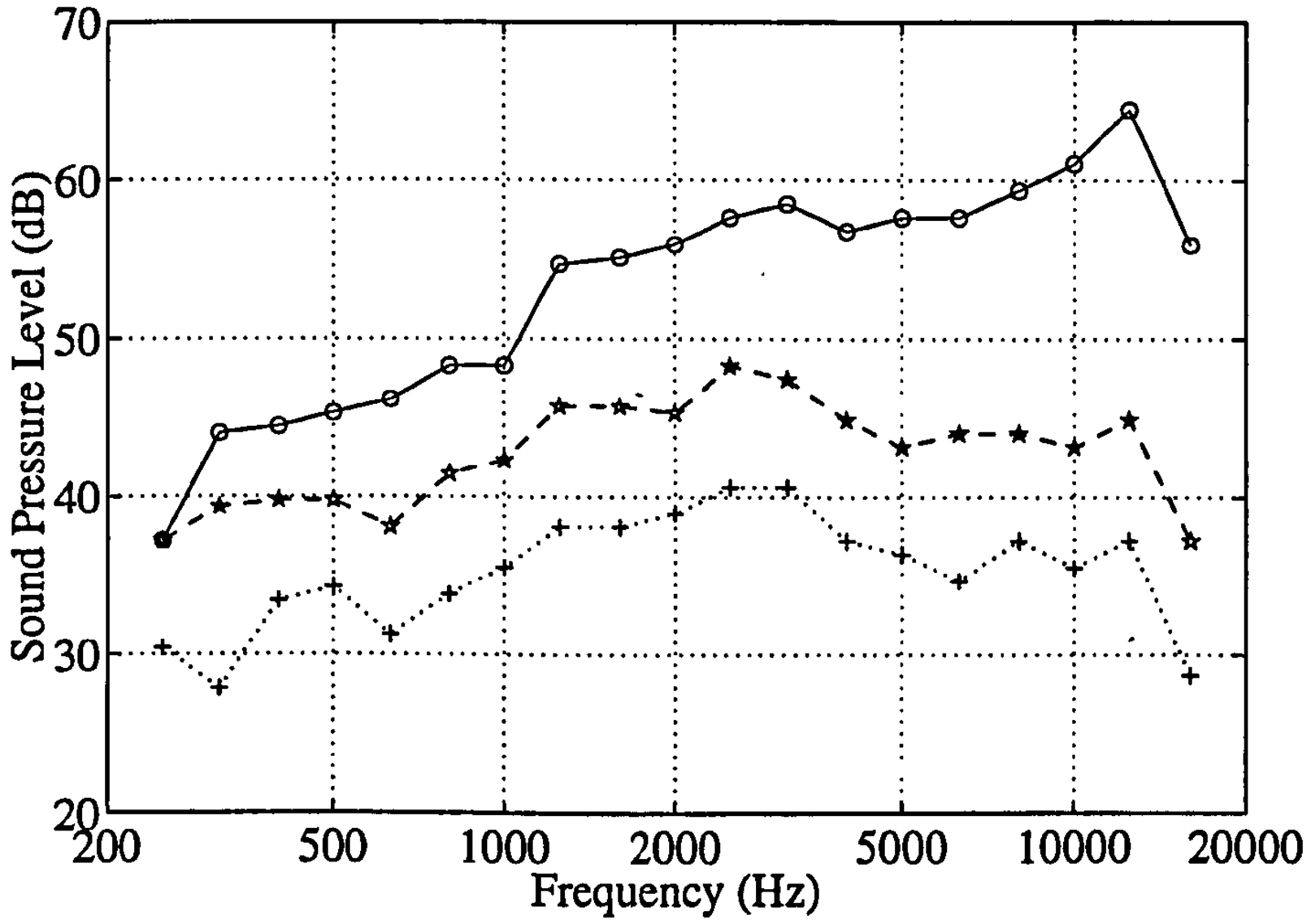

Figure 3.13: Sound pressure level (dB) behind interference device, at receiver coordinates (3.0, 1.40), as measured by Mizuno et al [84]. ∘ no device; ⋆, device; +, device blocked.

study, the following control dimensions were applied: $w = 5$ mm, $L = 540$ mm and $\alpha = 80°$, with $\beta = 50°$ in all cases.

Duct widths of $w = 5$, 20, 50 and 100 mm were studied and all ducts were square in cross-section. The results are summarised as tests b) in Table 3.2 and presented in detail in Figure 3.14. All four cases exhibited similar performances at 1/3 octave frequencies up to 1.6 kHz inclusive. At higher frequencies the insertion loss is observed to decrease with increasing duct width. Overall the most effective configuration was that with the smallest duct width. Figure 3.14 also shows that the frequency at which the insertion loss begins to reduce decreases with increasing duct width. Equations were proposed for determining the highest frequency at which significant attenuation could be maintained. However the theoretical justification for these equations is unclear, since they are based upon a duct which is closed at both ends.

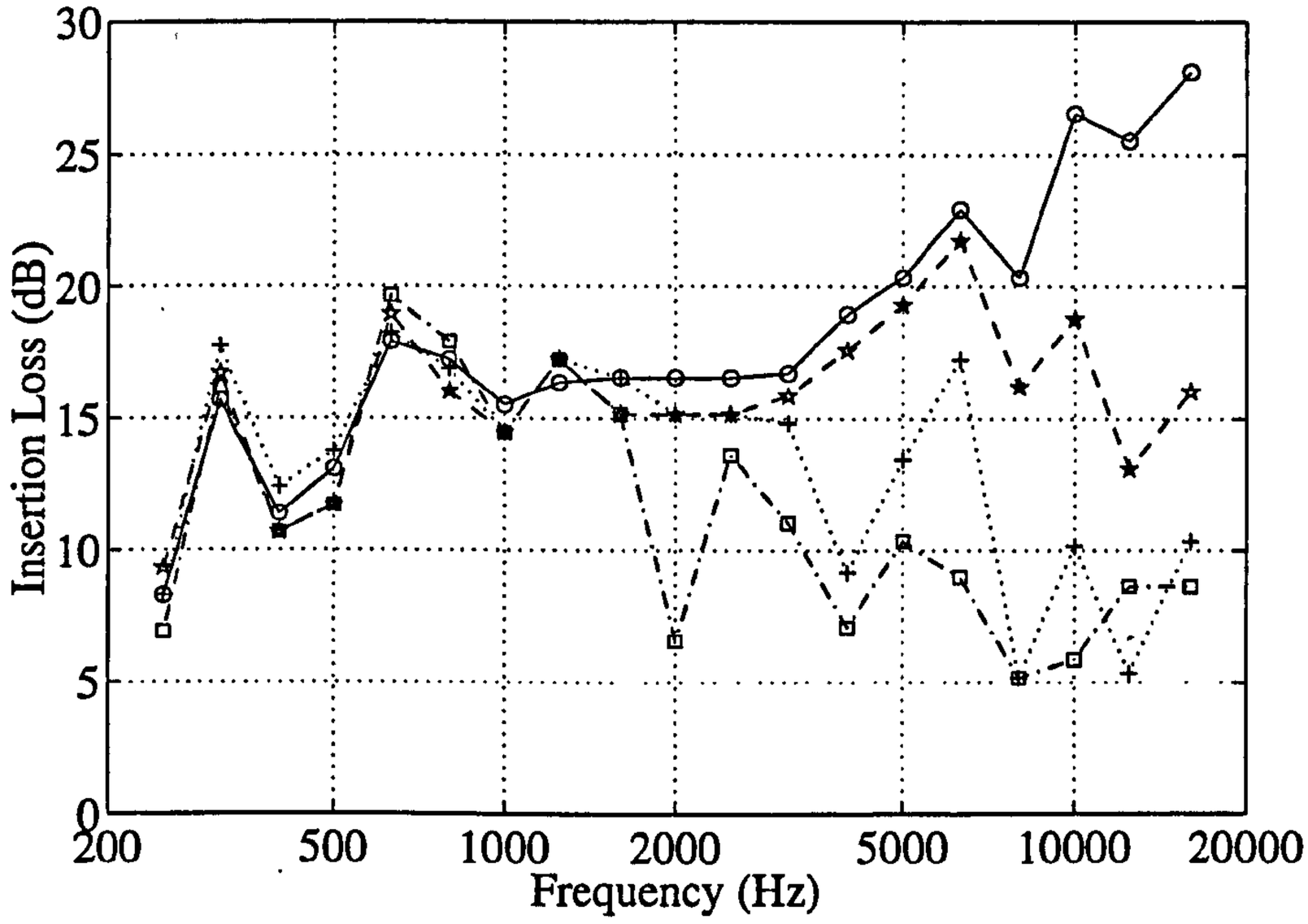

Figure 3.14: Insertion Loss behind interference device at receiver coordinates (3.0, 1.40) as measured by Mizuno et al [85] for varying duct width. ∘, 5 mm; ⋆, 20 mm; +, 50 mm; □, 100 mm.

Using the type 2 device (that with the ducts parallel to the base), three different maximum duct lengths, L, were tested. No justification is given as to how these lengths were selected. The height of the upper-most diffracting edge was maintained throughout at 960 mm (see Figure 3.11b). Consequently for duct lengths less than the control dimension $L = 540$ mm, the device was above ground level. To prevent propagation through this gap, it was filled with a sound absorbent material. The results obtained are summarised as tests c) in Table 3.2. The three configurations exhibited increasing insertion loss with frequency, up to approximately 23 dB, with the performance of the three being similar at the higher frequencies. The longest duct length provided the greatest attenuation throughout the frequency range. The frequency above which significant attenuation could be achieved was observed to decrease with increasing duct length. Standard equations for open-ended pipes were proposed for determining this frequency. It is noted however that the angle of the radiation face appears to have been maintained throughout the three tests. As a result, any decrease in L leads to a reduction in the number of ducts which comprise

the device (since w was also fixed), thereby also reducing the degree to which the device is open (see Section 3.1.1). It does not therefore seem unreasonable that any reduction in screening in these tests is a function of both the length and number of ducts. No allowance for this appears to have been made by the authors.

Since the angle of inclination affects the position of the interference device relative to the source, the size and effectiveness of the interference zone can be expected to vary with α. Duct inclinations of $\alpha = 30°$, $50°$, $60°$, $70°$ and $80°$ were studied again using the type 2' device. The results are summarised as tests a) in Table 3.3 and shown in detail in Figure 3.15. It is seen that the noise reduction generated by the device increases with α, the control dimension of $\alpha = 80°$ providing the greatest attenuation throughout the frequency range. As with the tests investigating variations in L, as the value of α increases, so the number of ducts decreases together with small increases in the corresponding lengths. Consequently, the results presented in Figure 3.15 cannot be attributed solely to variations in α. No comment is made on this by the authors.

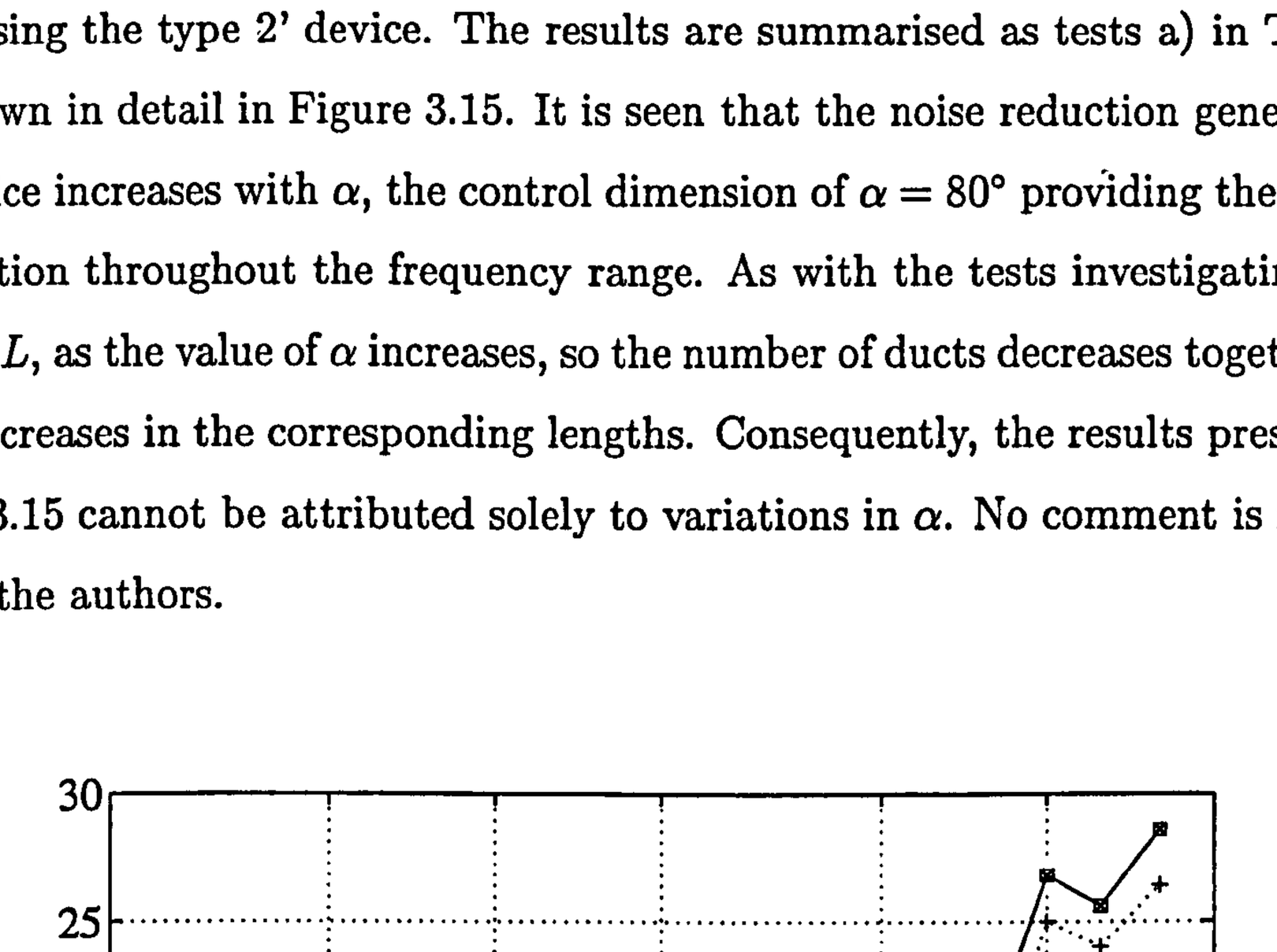

Figure 3.15: Insertion Loss at receiver coordinates (3.0, 1.40) as measured by Mizuno et al [85] for varying duct inclination. ∘, 30°; ⋆, 50°; +, 60°; □, 70°; ×, 80°

Using the equations derived, together with theory from the earlier study, it was

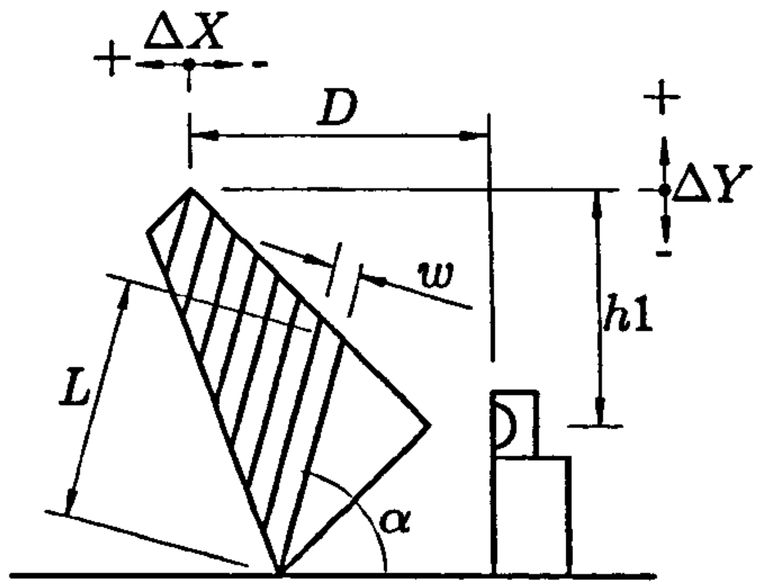

	Type	Device Dimensions			Source Position		Receiver Pos.		IL, dB
		L	W	α	D (ΔX)	$h1$ (ΔY)	Distance‡	Height	over 1/3 octave spectrum*
a)	2'	0.54	0.005	30°	0.717	0.54	3.0	1.40	0 – 17, generally increasing
				50°					2 – 22, generally increasing
				60°					2 – 26, generally increasing
				70°					5 – 28, generally increasing
				80°					8 – 28, generally increasing
b)	2'	0.54	0.005	50°	0.717 (0)	0.54	3.0	1.40	0 – 20, increasing
					0.627 (-0.09)				0 – 20, increasing
					0.807 (0.09)				2 – 17, increasing
					0.897 (0.18)				0 – 15, increasing
					1.077 (0.36)				0 – 12.5, increasing
c)	2'	0.54	0.005	50°	0.717	0.96 (0)	3.0	1.40	0 – 20, increasing
						1.00 (0.4)			0 – 22, generally increasing
						0.75 (-0.21)			0 – 9, decreasing above 1.6 kHz
						0.54 (-0.42)			0 – 3, decreasing above 500 Hz

Table 3.3: Summary of experimental arrangements and Insertion Losses, IL, for interference devices tested by Mizuno et al [85] and Sekiguchi et al [107]. Dimensions in metres. * the change in insertion loss with frequency, e.g. 'increasing' denotes the insertion loss increases with frequency. ‡ Horizontal distance from source.

concluded [85] that design of an optimum device was possible. For this to be feasible, the three parameters w, L and α must be considered simultaneously, since as the above discussion has noted, variations in a single parameter tend to affect the other two. The device based around the control dimensions gave the highest insertion losses in all of the different cases considered. As already observed, the source and receiver positions chosen are unrepresentative of real positions relative to the barrier. A device designed using this approach may not, depending upon individual site and source characteristics, give the same attenuation.

Further research is also reported by Sekiguchi et al [107] in which the effect of the source position upon the behaviour of the device was examined. The experiments were performed using the arrangement illustrated in Figure 3.12a, the type 2 device and a source emitting white noise over a frequency range 0.25 – 4 kHz. It is not specified whether the angle of inclination was the same as in the earlier experiments, i.e. $\beta = 50°$ in Figure 3.11b, although this seems likely. Tests were performed using different separations between the source and interference device, in both the horizontal and vertical planes, denoted as ΔX and ΔY respectively. The reference dimensions ($\Delta X = 0$ mm, $\Delta Y = 0$ mm) are those shown in Figure 3.12, with any changes being relative to these dimensions. With reference to Figure 3.11b, a positive value of ΔX corresponds to an increase in the horizontal separation, whilst a positive ΔY value denotes an increase in the vertical separation between the source and the uppermost edge of the device. Negative ΔY values were achieved by moving the source and receiver positions vertically upwards instead of moving the device. Although measurements were taken at all three receiver positions shown Figure 3.12a, only those for the mid-height position were presented.

ΔX values of -90, 0, +90, +180 and +360 mm were implemented, the results being summarised as tests b) in Table 3.3. It was observed that over almost all of the considered frequency range, the noise reduction resulting from the device decreased with increasing ΔX, and also when the separation reduced from 210 mm ($\Delta X = 0$ mm) to 120 mm ($\Delta X = -90$ mm). The insertion loss for each configuration was

observed to increase with frequency, peaking between 13 – 20 dB at 3.15 kHz. At each frequency below 2.5 kHz, the insertion losses for the five configurations were generally within 5 dB of one another. Considering the limiting cases ($\Delta X = +90$ mm and $\Delta X = -360$ mm), the device performed worse in the latter case below 1 kHz and better at higher frequencies. It is observed that when the position of the device is altered, the relative position of all the receivers also changes. No indication is given as to whether these are full scale measurements, so it is difficult to assess whether an improved approach would have been to maintain the relative positions of the receivers relative to the barrier.

Considering variations in the vertical separation, summarised as tests c) in Table 3.3, then for $\Delta Y = 0$ mm and $\Delta Y = +40$ mm, the insertion loss was observed to generally increase with frequency, peaking at 22 dB for the case $\Delta Y = +40$ mm. For the cases of negative ΔY, the performance relative to $\Delta Y = 0$ was increasingly degraded above 500 Hz, to a maximum of -12.5 dB ($\Delta Y = -210$ mm) and -19 dB ($\Delta Y = -420$ mm). at 4 kHz. It was also observed that as the separation between source and upper edge decreased, so the frequency at which the maximum insertion loss occurred decreased. The performance degradation was most likely due to a change in the position of the interference zone, with the considered receiver position approaching the boundary of the shadow zone. The above argument regarding the receiver positions also holds here. It was concluded that the best screening performance could be achieved by choosing ΔY such that the receiver positions lie close to the middle of the interference zone.

The effects of using the device with a line source instead of a point source were also investigated [107]. The line source was generated using a series of loudspeakers with a separation of 200 mm between adjacent sources. The average attenuation of approximately 16 dB was similar for both the point and line source cases. Although measurements were taken at all three receiver positions, it is unclear as to which receiver these results apply, although it appears to be the receiver at 1.4 m height.

It was proposed that the device could be usefully installed between a source and a plane screen, since the noise level at the top of the screen would be significantly

reduced, thereby further improving noise levels behind the barrier. Tests were carried out using the arrangement shown in Figure 3.16a, consisting of an absorbing barrier behind a type 2 device, with absorbing ground between the two. Although

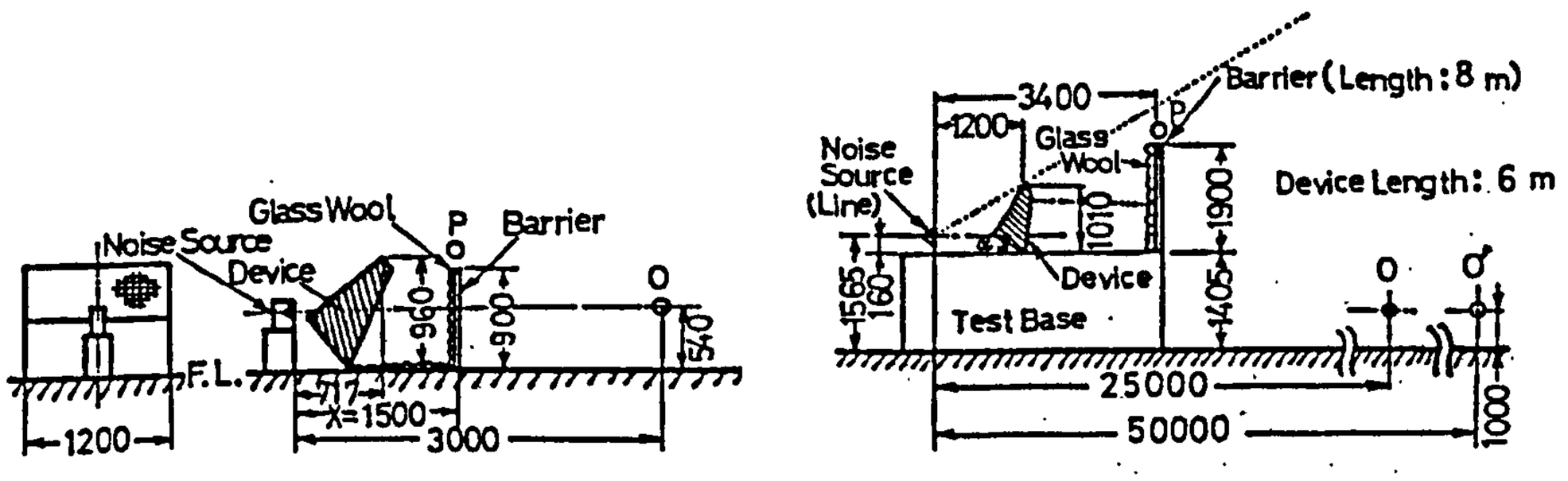

a)Arrangement for anechoic chamber tests b) Arrangement for field tests

Figure 3.16: Experimental arrangements used by Sekiguchi et al [107].

not specified it appears that the source emitted white noise as in the previous tests. Measurements were taken at a single point, 1.5 m behind the position of the absorptive screen. An increase in screening of approximately 8 dB was observed over the full frequency range following introduction of the device between the loudspeaker and barrier. When the ducts were sealed, any interference effects were eliminated, the attenuation being similar to that provided by the absorptive screen in the absence of the device. Measurements taken above the top of the plane screen indicated the interference effect to be approximately 10 dB. A further series of measurements were made reducing the separation between the device and screen. Attenuation at low frequencies was observed to decrease with reducing separation since waves propagated through the device are obstructed by the barrier before they can fully interfere with those diffracted over the top.

Measurements were carried out in the field to establish the performance of the noise control system for very distant receivers. The experimental arrangement is as shown in Figure 3.16b. The geometry of the device was the same as for the previous tests except that the device was a Type 2 model ($\alpha = \beta = 50°$) constructed from

concrete, with the ducts being 50mm in width. The barrier was 1.9m high and constructed from 20mm thick plywood with an absorptive coating on the source side. Measurements were taken with the barrier only, the device and barrier, and the device and barrier with the ducts of the device sealed. An average improvement in insertion loss of approximately 12 dB over the frequency range 0.5 – 4 kHz was observed at receiver O when the device was installed behind the barrier. This reduced to approximately 5 dB when the ducts were sealed and the system behaved as a double barrier. No results were presented for the receiver at 50 m from the source.

Overall the interference device appears to be an effective means of reducing noise, although comparison with the waveguide filters and thnadner designs discussed earlier in the chapter is prevented since it is not specified at what scale the experiments were performed. Field tests have shown that when introduced between a source and an existing screen, significant improvements in screening occur, although this is due to a combination of the interference effects and the presence of two diffracting edges. However, in all of the experiments conducted using this device, measurements have been largely restricted to a single receiver position. Measurements taken at other positions have not been presented, although no explanation has been given for this. Further study is required to perform a full assessment of the capabilities of the device.

Based upon the conclusions drawn from this previous work, Iida et al performed full scale tests [65] using a smaller, simplified version of the device/absorptive barrier combination shown in Figure 3.16. The two components were connected by a rigid horizontal baseplate and the whole arrangement mounted onto a 2 m high reflective barrier as shown in Figure 3.17. A truck travelling at a speed of 100 km/h was used as the noise source, running parallel to the barrier at distances of 3.5 and 7.0 m. Measurements were taken at 5, 10 and 20 m from the barrier, at heights of 1.2 and 3.4 m. The maximum reduction in noise level following introduction of the device was found to be between 5 – 6 dB(A) when the source was 3.5 m from the

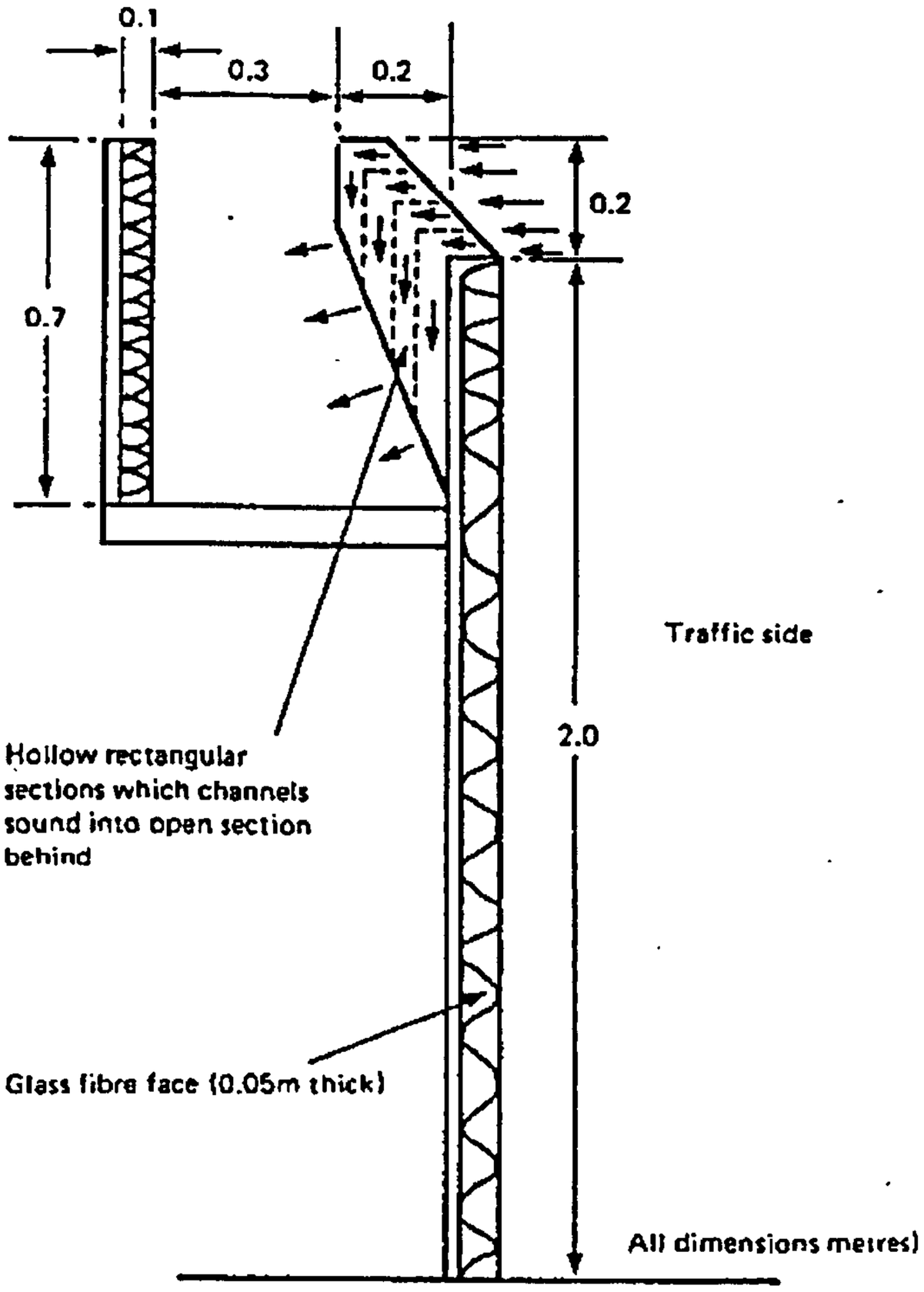

Figure 3.17: Interference device as tested by Iida et al [65].

barrier, although it is unclear whether the measurements made in the absence of the device still featured the absorptive back panel. Similar effects were observed for the alternative source position.

Subsequent development has resulted in the design marketed as Calmzone, shown in Figure 3.18 mounted on top of a barrier. Use of the device on Japanese high speed railways has been reported [35]. Full scale testing of the interference profile on European railways and full-scale laboratory tests have been reported in several studies,

the findings of which, together with the corresponding site layout and source/receiver details, are summarised in Tables 3.4 and 3.5.

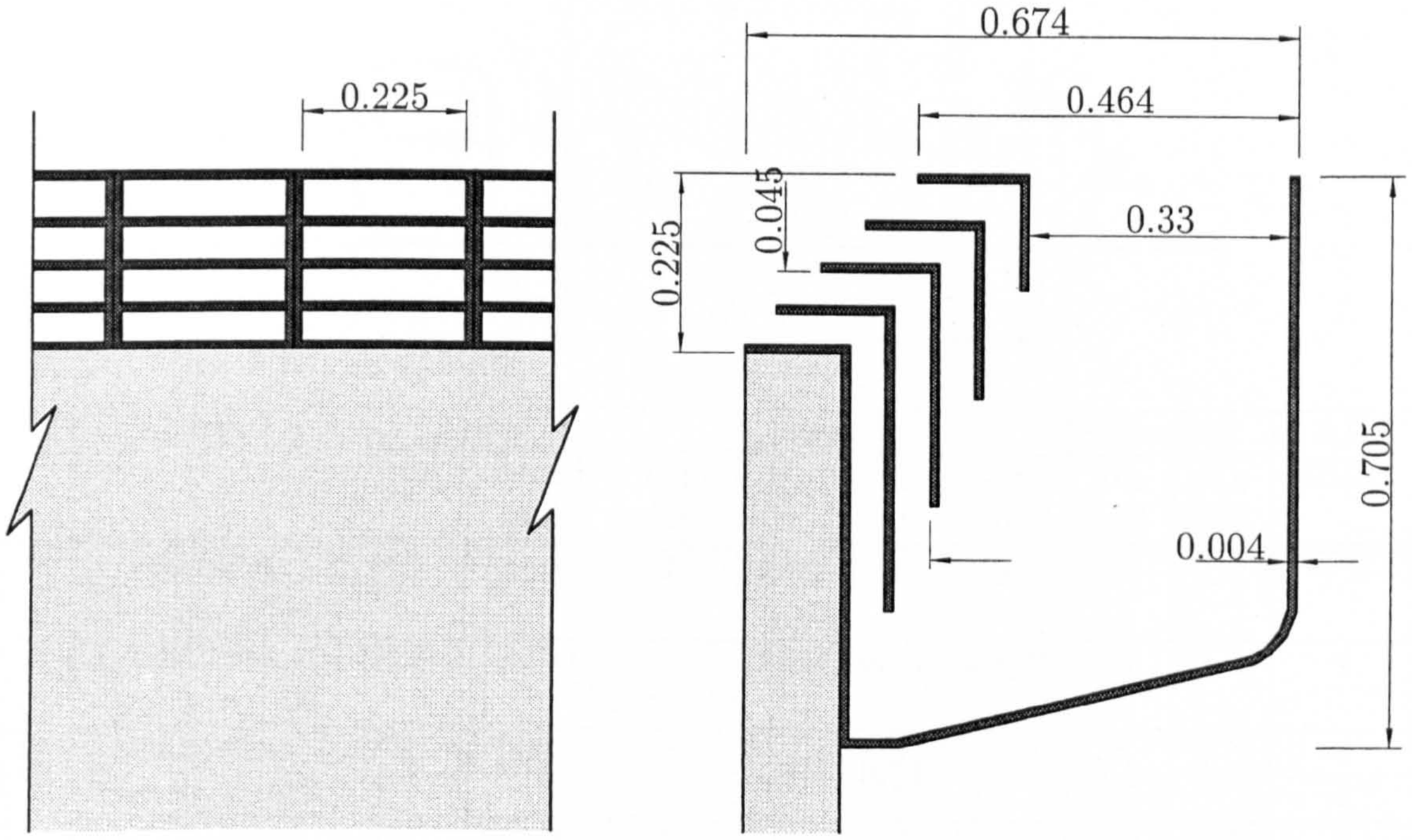

Front elevation (from source side) Side elevation

Figure 3.18: Cross-section of the Calmzone interference device.

Further to the testing of low cantilevered trackside noise barriers [56], both the device of Iida [65] (Figure 3.17) and Calmzone (Figure 3.18) were tested on a high-speed railway at Weilheim, Germany [56], using the layout denoted a) in Table 3.4. Although passenger trains were used to provide the source noise (measurements were taken for the passage of 97 trains), no precise speeds are given, and there is no indication as to whether the results were normalised to a single speed. Mounting the devices on low barriers close to the track suggests that the attenuation "at source" of wheel/rail noise, a dominant component of railway noise (see Chapter 6), was the objective. Both devices performed effectively, reducing the noise level at the single receiver position by an additional 4 – 5 dB(A) relative to the plane screen of the same height.

Additional tests using Calmzone at Weilheim were reported by Hampl et al [48] for similar barriers and identical source/receiver positions (test b) in Table 3.4),

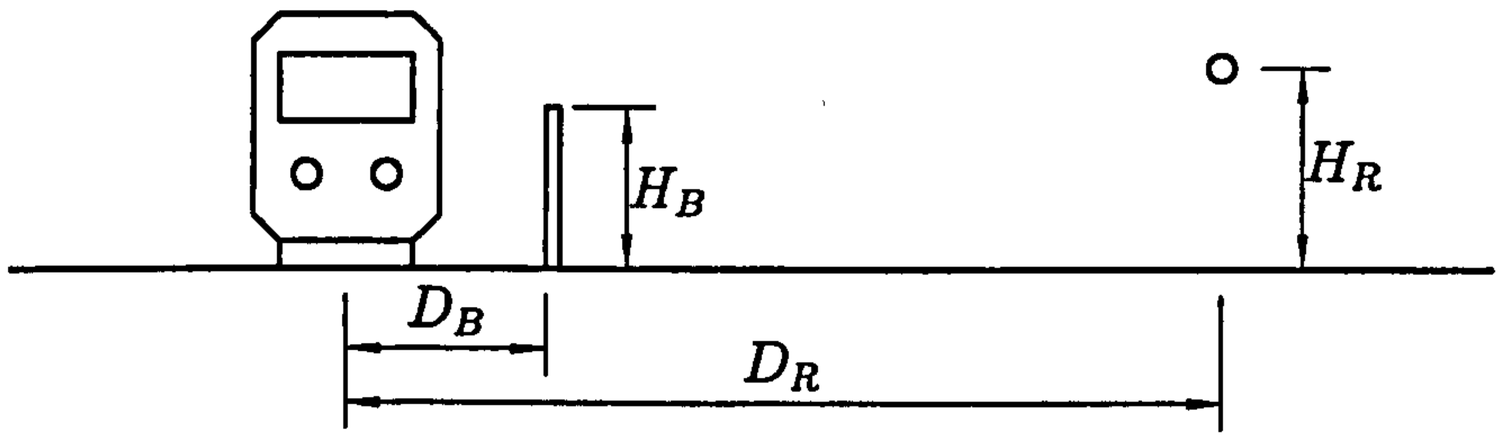

	Location	Source		Barrier				Receiver		ΔIL dB(A)
		Type	Speed (km/h)	Type (m)	D_B (m)	H_B (m)	L_B (m)	D_R (m)	H_R (m)	
a)	Weilheim, Germany [56]	PT	>100	L	1.85	0.74	40.0	7.5	1.2	4-5†
	Weilheim, Germany [56]	PT	>100	L	1.85	0.74	200.0	7.5	1.2	4
b)	Weilheim, Germany [48]	PT	90	L	1.85	0.73	—	7.5	1.2	4
		FT	90							1
c)	Langenlebarn, Austria [48] (Test track)	PT	120	R	4.0	2.0	—	7.5	1.2	6
d)	Kledering, Austria [48] (Goods yard)	FT	50	R	4.0	2.0	—	7.5	1.5	1
e)	Langenlebarn, Austria [71]	FT	—	—	1.5	3.0	185.0	7.5	1.2	3.3
									3.5	3.1
									6.0	-0.6
								25.0	1.2	3.9
									3.5	3.4
									6.0	3.8
f)	Langenlebarn, Austria [71]	PT	—	—	1.5	3.0	185.0	7.5	1.2	6.6
									3.5	2.3
									6.0	0.1
								25.0	3.5	-2.4
									8.0	3.5

Table 3.4: Summary of reported improvements in barrier efficiency, ΔIL, following the introduction of Calmzone (Figure 3.18) to the top of a barrier. I: Measurements using train sources. Train types: PT, passenger train; FT, freight train. Barrier types: L, low; R: reflective. †, measurements performed using device of Iida et al [65] (Figure 3.17). L_B is the length of the barrier.

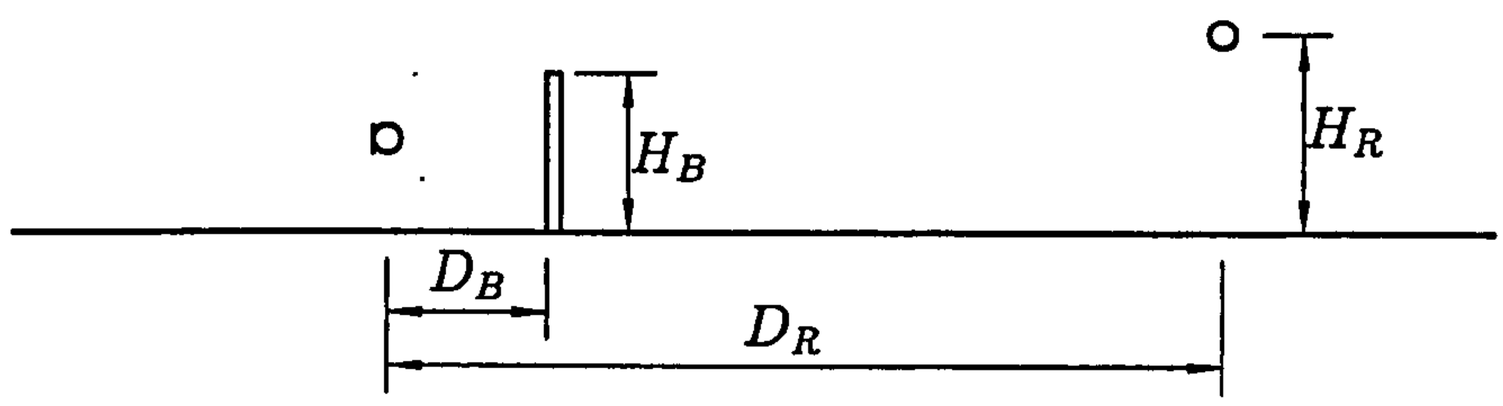

	Location	Source		Barrier				Receiver		ΔIL
		Type	Height (m)	Type	D_B	H_B	L_B	D_R	H_R	dB(A)
(a)	Laboratory	LS	1.6	R	1.0	2.0	—	1.5	1.3	4.0
									1.4	4.7
									1.5	4.7
									1.75	2.7
									2.0	1.1
									2.25	-0.7
								2.0	1.3	4.7
									1.4	5.2
									1.5	3.9
									1.75	2.2
									2.0	0.9
									2.25	-0.3
(b)	Calcinate, Italy, [71]	LS	1.0	A	5.0	3.0	36.0	15.0	1.5	4.7
									2.5	5.0
								20.0	1.5	5.3
									2.5	4.2

Table 3.5: Summary of reported improvements in barrier efficiency, ΔIL, following the introduction of Calmzone to the top of a barrier. II: Measurements using loudspeaker (LS) sources. Barrier types: R: reflective; A: absorbing. L_B is the length of the barrier.

although the speed of the passing trains was reduced. Comparable performance with that of the previous study ($\Delta IL = 4$ dB(A)) was observed for the passenger trains, and distinct interference dips can be observed at 1.6 and 3.15 kHz in the measured SPL spectrum, as shown in Figure 3.19. However for measurements in the presence of freight trains, the improvement in insertion loss following the introduction Calmzone was reduced to 1 dB(A). The difference in levels can be attributed to the change in the dominant source component between the two trains. For freight trains the dominant component is the vibration of the wagon bodies, which is not shielded by such low barriers ($H_B = 0.74$ m).

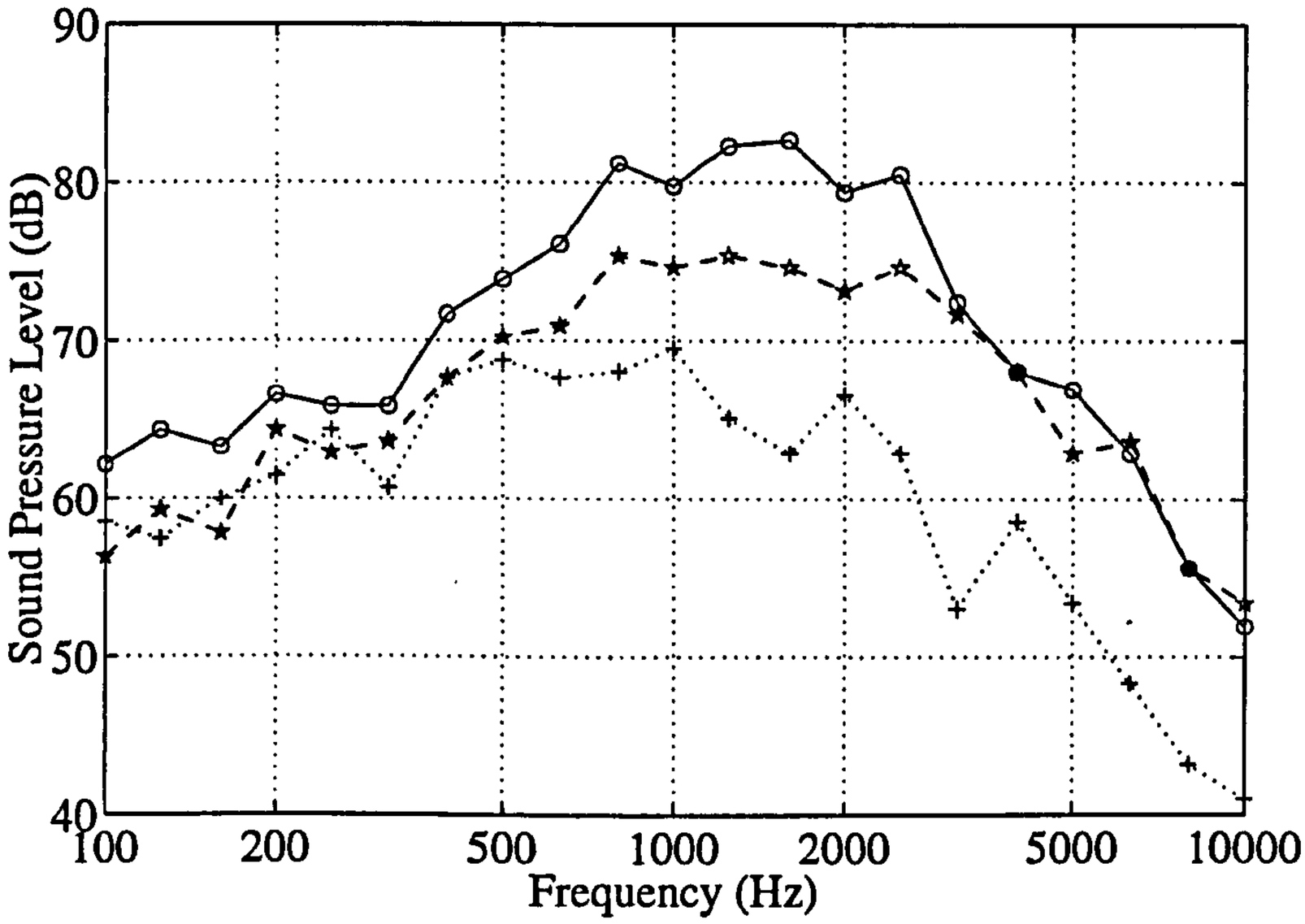

Figure 3.19: SPL for bypass of passenger train (speed = 90 km/h) at Weilheim, Germany [48]. Site geometry given in Table 3.4. ∘, no barrier; ⋆, plane screen; +, plane screen with Calmzone.

A further series of tests at different locations were reported by the same authors, in which the barrier height was increased to 2 m and the distance from the centreline of the track increased to 4 m [48] (tests c) and d) in Table 3.4. However, the same single receiver position was maintained.

The first experiment [48] was performed at Langenlebarn, Austria (test c), Table 3.4). Following the introduction of Calmzone to the top of the barrier, the noise level at the receiver recorded during the bypass of a faster passenger train (speed = 120 km/h) was reduced by 6 dB(A). This indicated that the benefits of Calmzone were maintained even when the device was not in close proximity to the source. However, analysis of the measured third-octave SPL spectrum (Figure 3.20) shows that any interference effects have been largely eliminated. The significant improvement is most likely due to a combination of the small height increase and the presence of the second diffracting edge (see Section 3.2.3 and Chapter 5). Since only a single receiver position has been used, it is not possible to see if this effect is repeated elsewhere at the site. No indication is given as to whether these results are based

upon a single or multiple train bypasses.

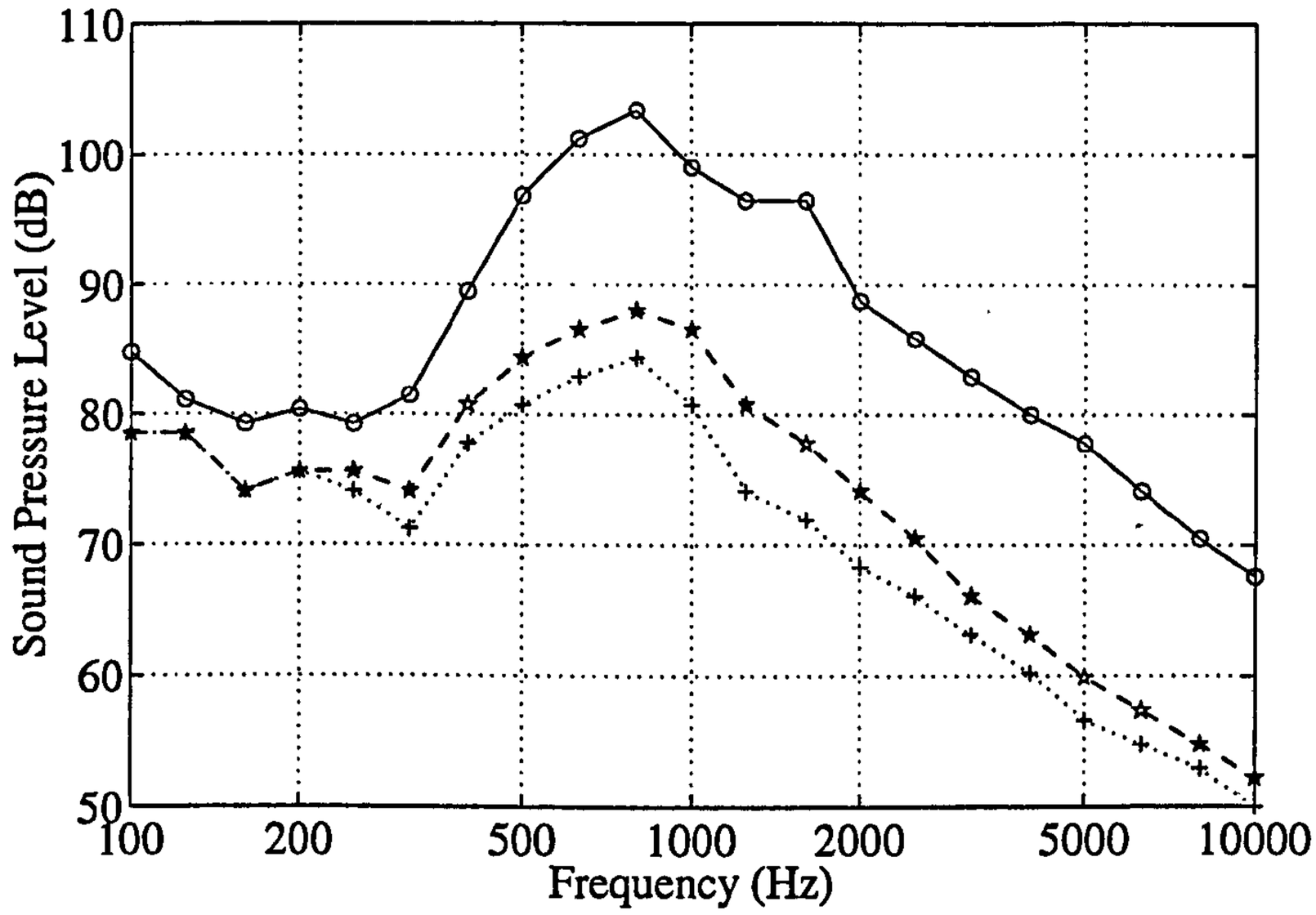

Figure 3.20: SPL for bypass of passenger train (speed = 120 km/h) at Langenlebarn, Austria [48]. Site geometry given in Table 3.4. ∘, no barrier; ⋆, plane screen; +, plane screen with Calmzone.

Tests carried out for the same geometry on the exit loop from a goods yard at Kledering, Austria and performed using the same site geometry [48] indicated less successful performance (test d), Table 3.4). The introduction of Calmzone was observed to provide only an additional 1 dB(A) insertion loss. However, spectral analysis showed low frequency noise to be dominant. Such noise, generated by the locomotive and body rattle/vibration from the goods wagons, is largely outside of the effective range of the interference device.

Experiments were conducted with Calmzone mounted on a 2 m high barrier under laboratory conditions [48], using a loudspeaker in close proximity and a rectangular pulse signal. The results are summarised as test (a) in Table 3.5. The greatest improvements in insertion loss relative to the plane screen, of approximately 4 – 5 dB(A), were recorded at the lower receiver positions. It is noted that the highest

receivers at 2.25 m are in close proximity to the limit of the shadow zone. However at only an additional 0.5 m behind the barrier, the second column of receivers add little insight into the behaviour of the interference device. No explanation is presented by the authors as to why the two groups of receivers were in such close proximity. Similarly, comparison with the full scale tests by the same authors is made difficult, since no variables are held constant between experiments. Despite this, it was concluded that the site geometry strongly influences the performance of the Calmzone device.

Further measurements at Langenlebarn in the presence of both passenger and freight trains have been reported by Kohler et al [71]. The height of the barrier was increased to 3 m, and its proximity to the nearest track reduced to 1.5 m (relative to the centreline). The results are summarised as tests (e) and (f) in Table 3.4. The study was more detailed than that reported in [48] since an additional series of receiver positions were included at 25 m from the track centreline. No details of either the number or speed of the trains have been given. The performance of the Calmzone device is observed to be favourable for both train types (it is suspected that the negative ΔIL value at the (25.0, 3.0) receiver position has been incorrectly stated). Although using different source and receiver positions it is observed that, in contrast to the laboratory experiments (Table 3.5), the performance of the device is maintained at receivers much higher than the top of the barrier.

Tests have also been carried out on a railway line at Calcinate, Italy [71], although using a loudspeaker generating white noise as the source. In this experiment the separation between barrier and source was 5 m, greater than in any of the previously reported studies. Measurements at 10 and 15 m behind the barrier showed the interference device to contribute a significant reduction in noise level of the order of 4 – 5 dB(A). Spectral analysis indicated the device to be effective above 800 Hz. It was observed that the improvement in screening efficiency provided by the Calmzone profile is the result of several superimposed mechanisms, namely the increase in barrier height, the presence of two diffracting edges and interference. However no

investigation into the magnitude of these contributions was reported.

Overall the different studies have proven the Calmzone interference device to be an effective addition to the top of an existing barrier. The use of a rigid back-panel rather than the absorptive one of Iida [65] does not appear to have had any detrimental effect upon the performance. The effect of varying the position of the device relative to the source or receivers is difficult to assess based on these reported experiments since no three of the four relevant parameters (D_B, H_B, D_R and H_R from Tables 3.4 and 3.5) were consistent between the different studies. With the exception of [56], no information has been given as to how many train bypasses have been used to derive the different results, or whether variations in speed or atmospheric conditions have been taken into account. Only in the experiments of [71] were sufficient receiver positions considered to allow an improved measure of the wider performance of the device to be determined. Generally though, it would seem that the device is effective over a reasonable area behind the barrier, although the degree of screening appears dependant upon the type of source used, or more specifically the spectral content.

The experimental and theoretical work reported in the remainder of this chapter has been carried out to assess the performance of the Calmzone device over a wider area, and to attempt to quantify the contributions from the different mechanisms described above.

3.2 Full scale and computational studies of Calmzone

3.2.1 Full-scale Measurement and Analysis Procedures

Full scale testing of the Calmzone device has been carried out by the author using the Noise Barrier Test Facility at the Transport Research Laboratory, Crowthorne, Berkshire, UK. The facility is situated on a flat grassland site, free of any reflecting

surfaces which may affect recorded noise levels. At one end of the site a level section of asphalt, approximately 40 m in length and 35 m at the widest point, has been laid to represent a typical road surface (Figure 3.21).

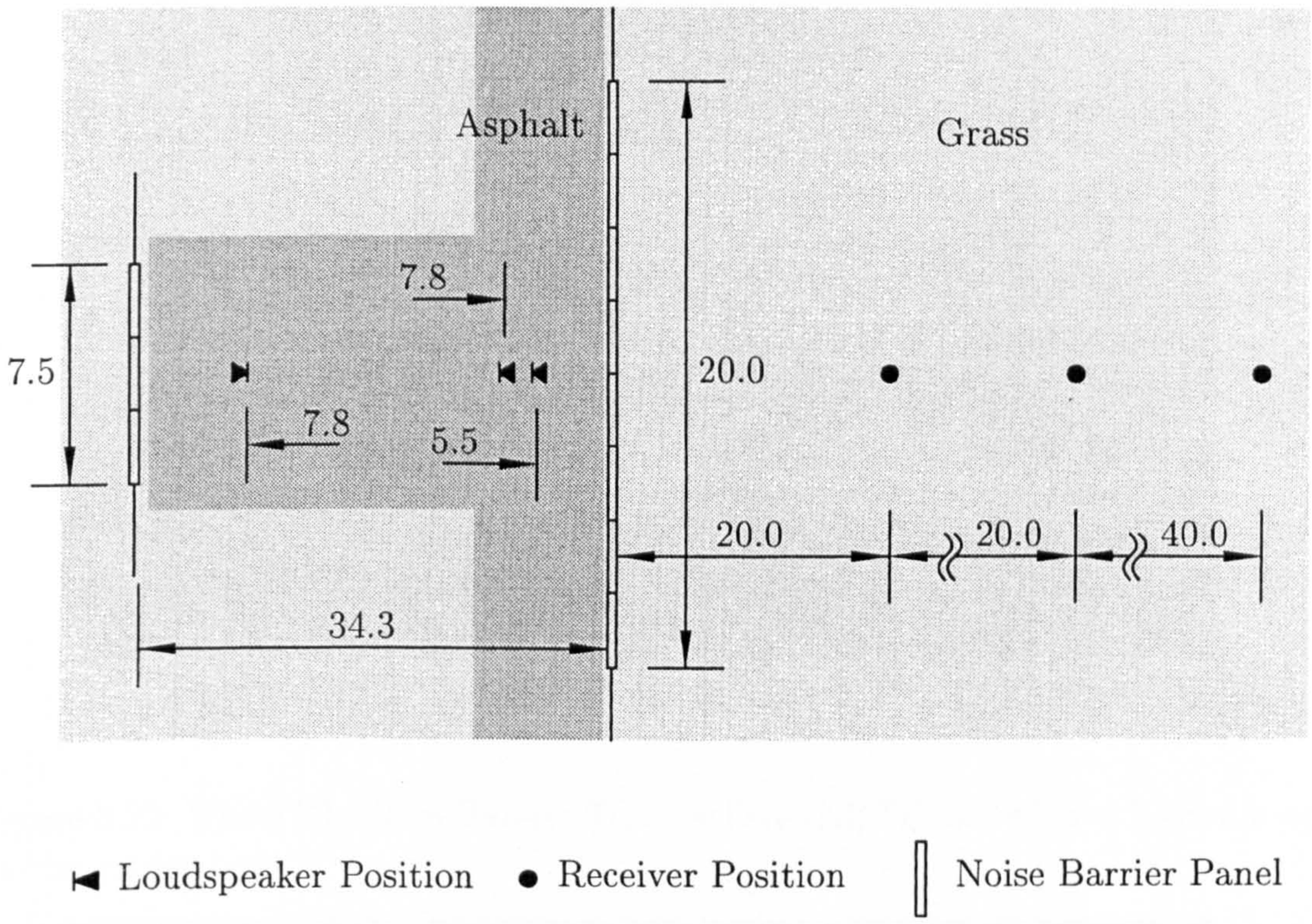

Figure 3.21: Plan of the TRL Noise Barrier Test Facility (NBTF). Dimensions in metres.

A 20m long noise barrier has been constructed adjacent to one edge of the asphalt. This consists of nine 2 m high I-section posts, into which can be slotted a variety of 0.5 m deep panels. The bottom half-metre of the barrier is formed by a permanent concrete panel with plane reflecting surfaces. If required, the posts can be extended to allow a total barrier height of 3 m. Figure 3.22 shows the test facility with a 2.0 m high T-profile noise barrier erected. At the opposite end of the asphalt, similar I-section posts are positioned to allow for the erection of a 7.5 m long noise barrier. This is only used during studies of parallel barrier configurations (tests upon these configurations are detailed in Chapter 4). The separation between the barriers is 34.3 m, characteristic of a standard motorway having three lanes and a hard shoulder on each carriageway.

A static dual-cone loudspeaker, rated at 800 W, is used as the noise source

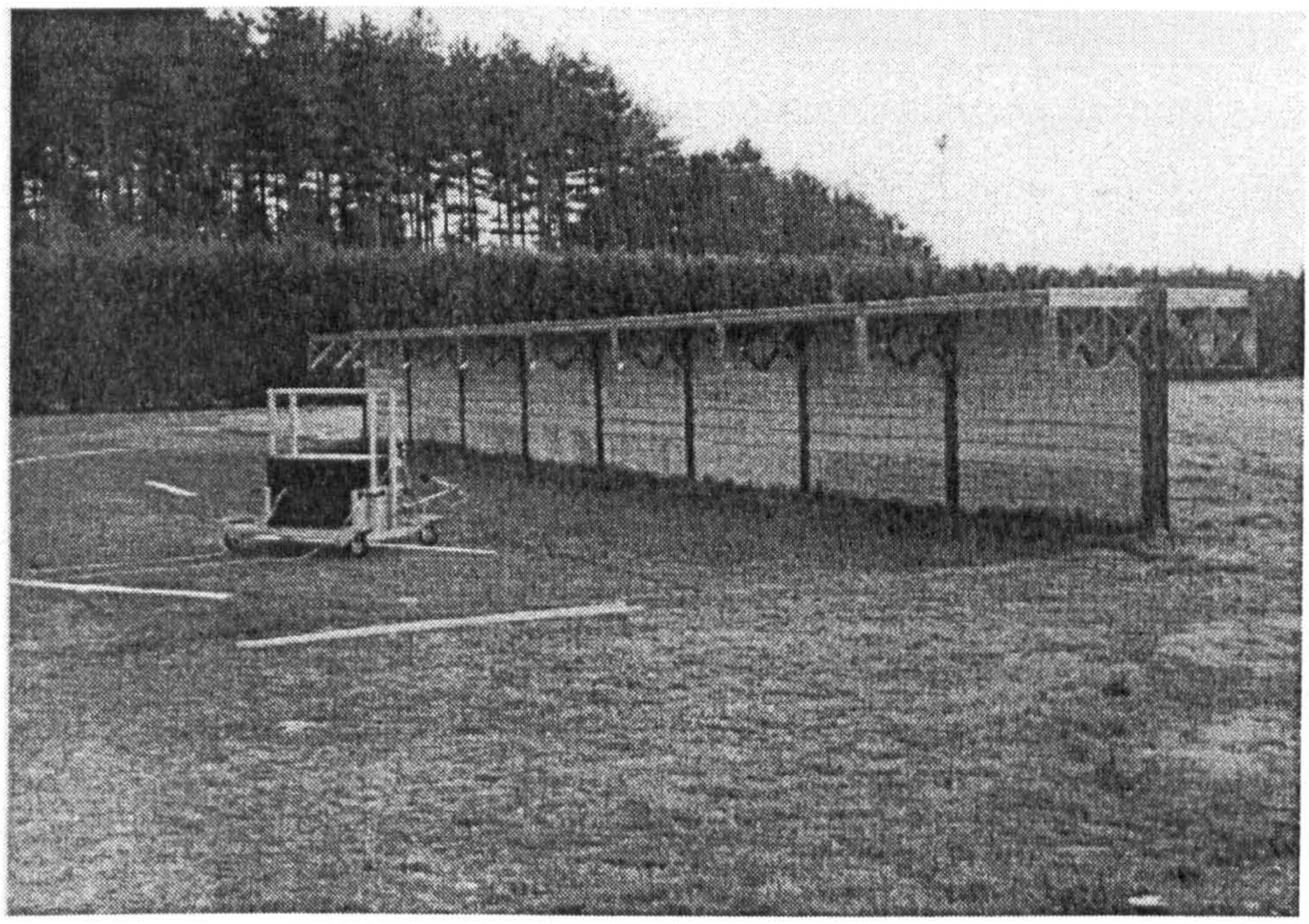

Figure 3.22: The TRL Noise Barrier Test Facility (NBTF) showing a T-profile noise barrier under test.

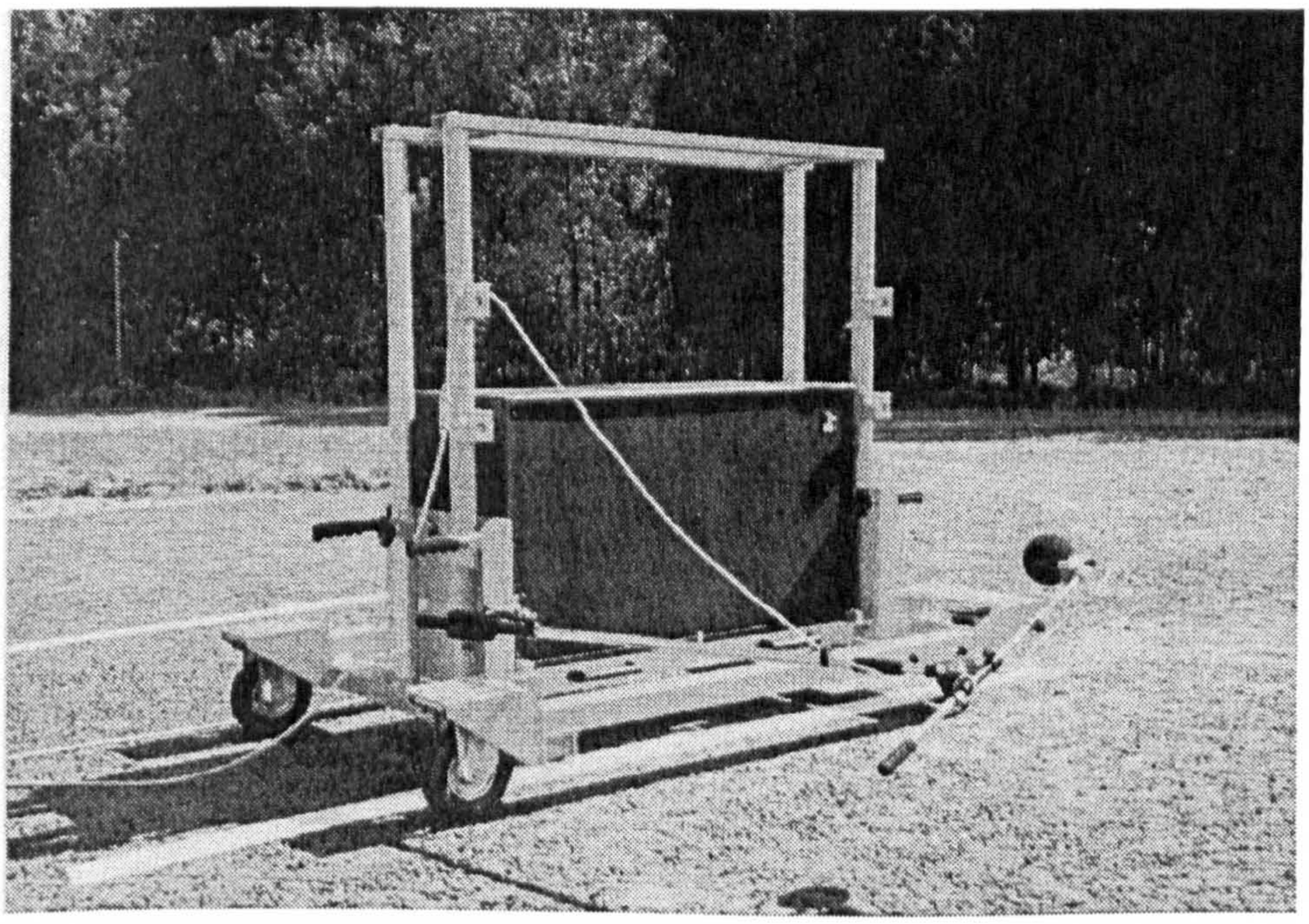

Figure 3.23: Loudspeaker noise source as used on the TRL barrier facility.

(Figure 3.23). This is capable of delivering noise levels above 110 dB at 1 m from the speaker, for a frequency range 0.1-3.2 kHz. Such high levels ensure that any contribution from background noise is insignificant compared to that emitted by the loudspeaker, even at the furthest receiver positions. Generating random noise at approximately 110 dB in each third-octave band at 1 m from the speaker produces levels approximately 15 dB above the background level. This cannot be performed simultaneously for all octave bands, so the sound is broadcast separately in four frequency bands: 0.1-0.2 kHz, 0.25-0.5 kHz, 0.63-1.25 kHz and 1.6-3.2 kHz. A reference microphone is positioned at 1 m from the speaker face to allow output levels to be monitored and adjusted if necessary. Random noise in each of the four frequency bands is played through the loudspeaker over 20 second periods. The speaker is mounted on a portable trolley to allow its position relative to either barrier to be varied.

The noise broadcast via the loudspeaker is sampled over a 16 second period simultaneously at three microphone positions, 20, 40 and 80 m behind the main barrier. Measurements are taken at these positions for two microphone heights, 1.5 and 4.5 m, each height requiring a separate run. For single barrier tests, the loudspeaker is positioned at distances of 5.5 and 7.8 m from the barrier (for single barrier tests), its axis being 0.5 m above the asphalt. Consequently, the combination of source and receiver positions results in twelve different measured levels. The chosen distances correspond to the effective positions of the traffic source, with respect to noise barriers sited at the carriageway edge, on dual carriageway roads and motorways respectively and are as assumed within the standard traffic noise prediction method used in the UK [32]. The axis of the speaker is set as horizontal and aligned with the three microphone positions.

In situations involving real traffic streams, the noise at an arbitrary receiver position behind a barrier is a result of the contribution of many sources moving along a road. As such the traffic stream can be regarded as an incoherent line source. In general, insertion loss values for an incoherent line source are lower than those for a point source at normal incidence, as observed in Chapter 2 (see also, for example, calculations in [66, 37]). Consequently insertion losses for an incoherent

line source cannot be used directly. However, scale model tests [72] indicate that the relative screening performances of different barrier configurations are similar for the cases of an incoherent line source and a point source at normal incidence.

A computer based sound level meter allows measurements to be made simultaneously at all four microphone positions. The levels measured in each one-third octave band are then stored for further analysis. During the measurement periods the wind speed and direction are recorded at 1 second intervals close to the middle of the test site. Temperature, relative humidity and barometric pressure levels are also recorded. For each individual barrier option studied the procedure is for measurements to be taken under a range of wind conditions, thereby allowing sufficient data to be recorded to predict a reasonably accurate estimate of the sound pressure levels corresponding to zero wind speed. Control measurements taken in the absence of the barrier allow the screening performance of the barrier (insertion loss) to be calculated.

The analysis procedure is as follows: The recorded sound pressure levels in each octave band are normalised for a source level of 110 dB at the reference microphone and then weighted using the normalised, A-weighted road traffic noise spectrum based upon measurements taken in various European countries and reviewed within the noise barrier standards committee CEN TC 22/WG6/TG1. This spectrum is presented in Figure 3.24. The one-third octave band levels are then combined to produce an overall SPL.

For each of the overall adjusted levels, the average wind speed component normal to the barrier, from source to receiver, is calculated using the recorded wind data. Since measurements were performed under different conditions, the levels can be regressed against the wind speed component to obtain the levels for zero wind speed, as shown in Figure 3.25. To avoid excessive wind noise affecting levels behind the barrier, measurements were only taken for wind speeds of less than 4 m/s.

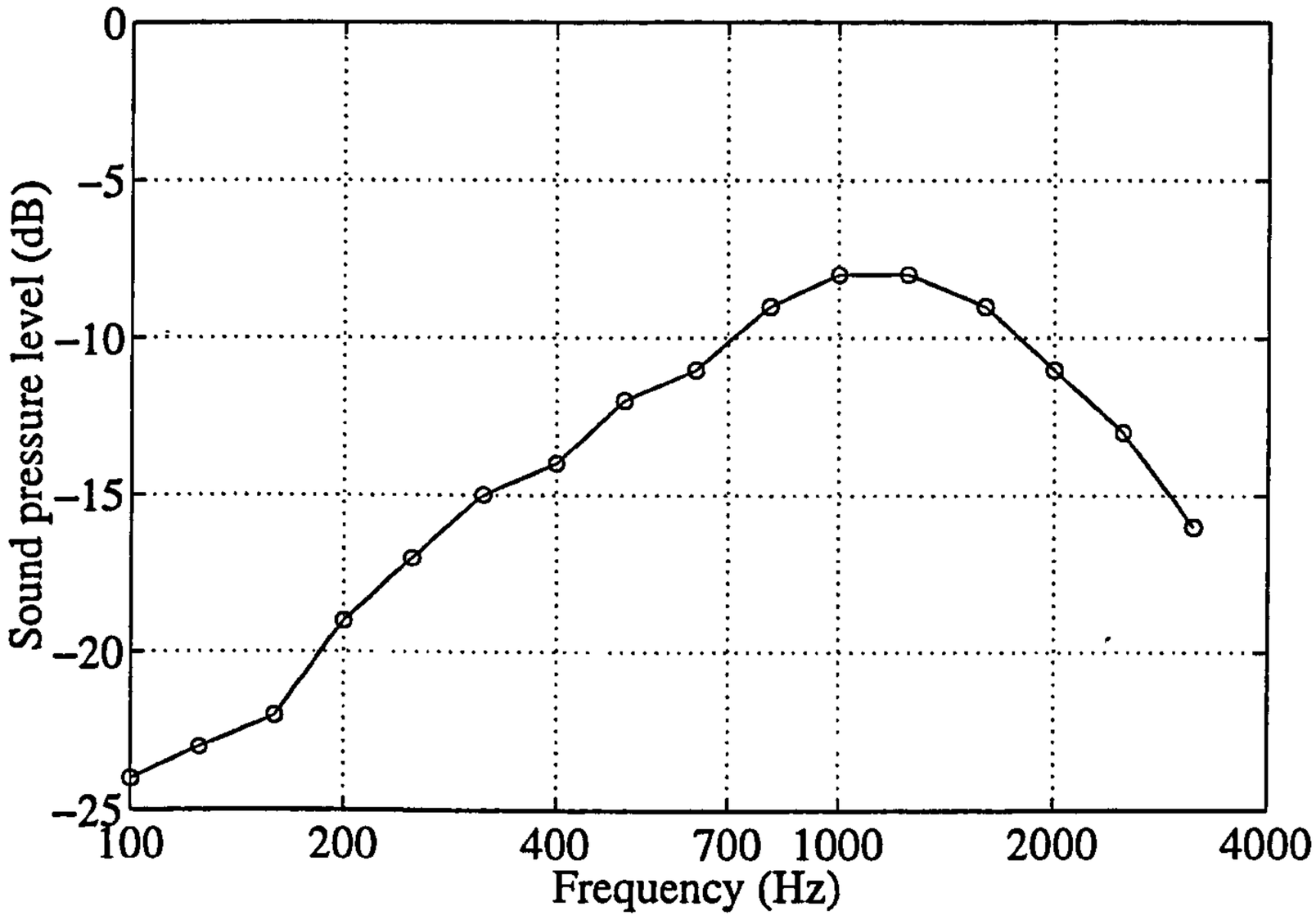

Figure 3.24: Normalised A-weighted one-third octave band spectrum used as the traffic noise source (normalised to zero dB).

3.2.2 Configuration of The Interference Device

The Calmzone interference device, as illustrated in Figure 3.18 was mounted upon a reflective barrier 2 m high and 20 m in length. Figure 3.26a) shows the device when viewed from the source side of the barrier, with the duct entrances clearly visible. Figure 3.26b) shows the view from the receiver side of the barrier. An additional series of tests were carried out whereby the entrances to the ducts of the device were sealed off using 12 mm plywood panels. The resultant measured levels could then be compared with those for the basic device to establish the degree of screening resulting from destructive interference. To obtain the insertion loss contribution of the basic device, insertion losses obtained from previous tests on reflective screens of 2.0 and 2.5 m in height have been interpolated by linear interpolation to obtain an estimate for a barrier having the same overall height (2.225 m).

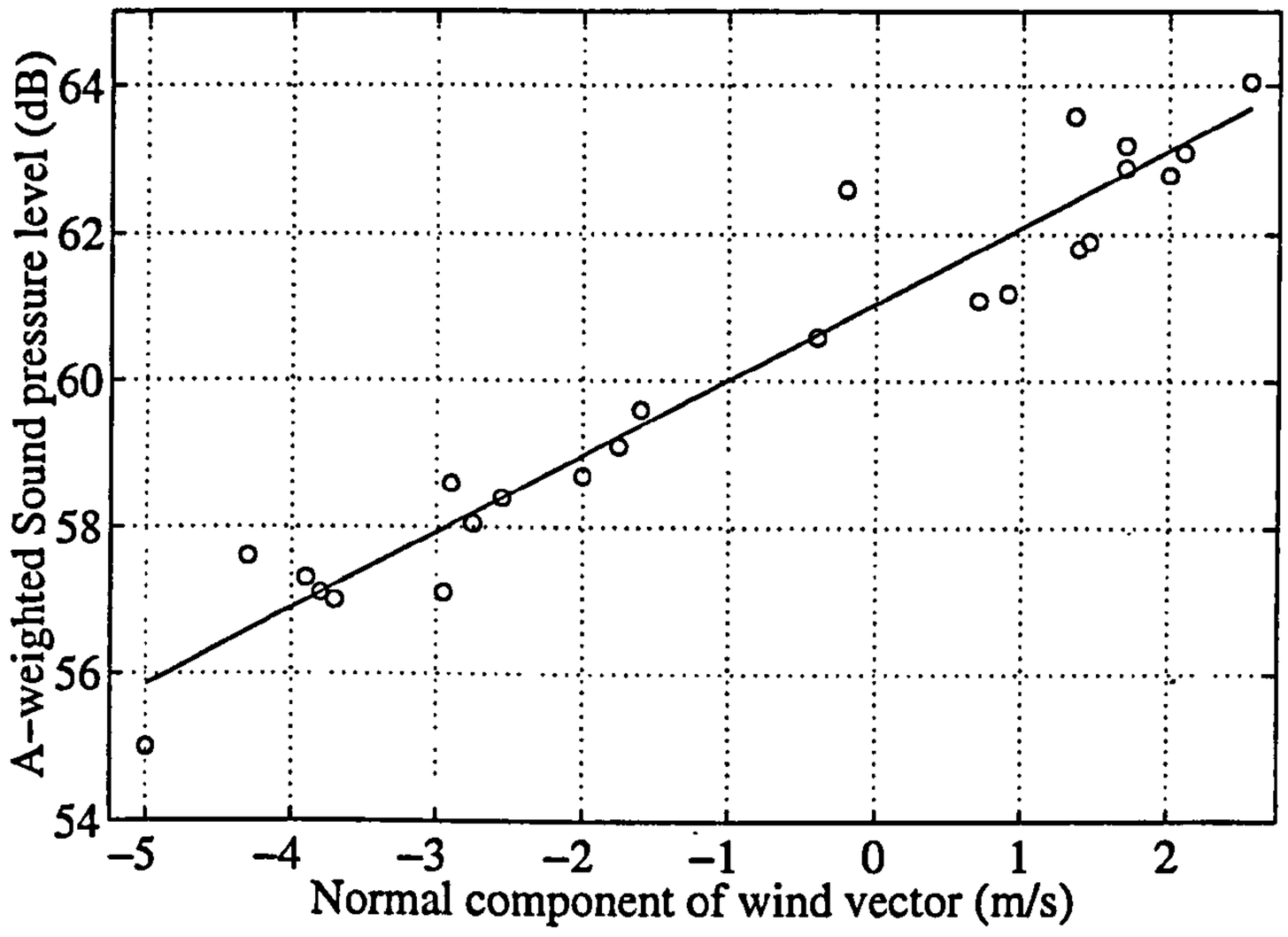

Figure 3.25: A-weighted SPL plotted against average normal component of wind vector. Source position at 5.5 m in front of the barrier, microphone at 40 m behind the barrier at a height of 1.5 m.

3.2.3 Theoretical predictions

Theoretical simulations have also been carried out using the boundary element method described in Chapter 2, Section 2.1, for the same source, receiver and barrier configurations as in the full scale experiments. Although the practical results have been obtained for a point source, the boundary element predictions are for a coherent line source. As discussed in Chapter 2, scale model experiments [72, 57] have shown that excess attenuation and insertion loss predictions for a single barrier and a coherent line source agree well with those for a barrier and point source at normal incidence. However, variations in the predicted SPL values will occur as the measurement position moves away from the barrier.

Using the Delany and Bazley model [31] to describe the various surface impedances, the following values of flow resistivity have been assigned within the model; $1E20$ Nsm^{-4} for the barrier and asphalt surfaces, thereby defining a highly reflective surface, and 250,000 Nsm^{-4} for the grassland on the far-side of the barrier, which is within the range proposed in [39].

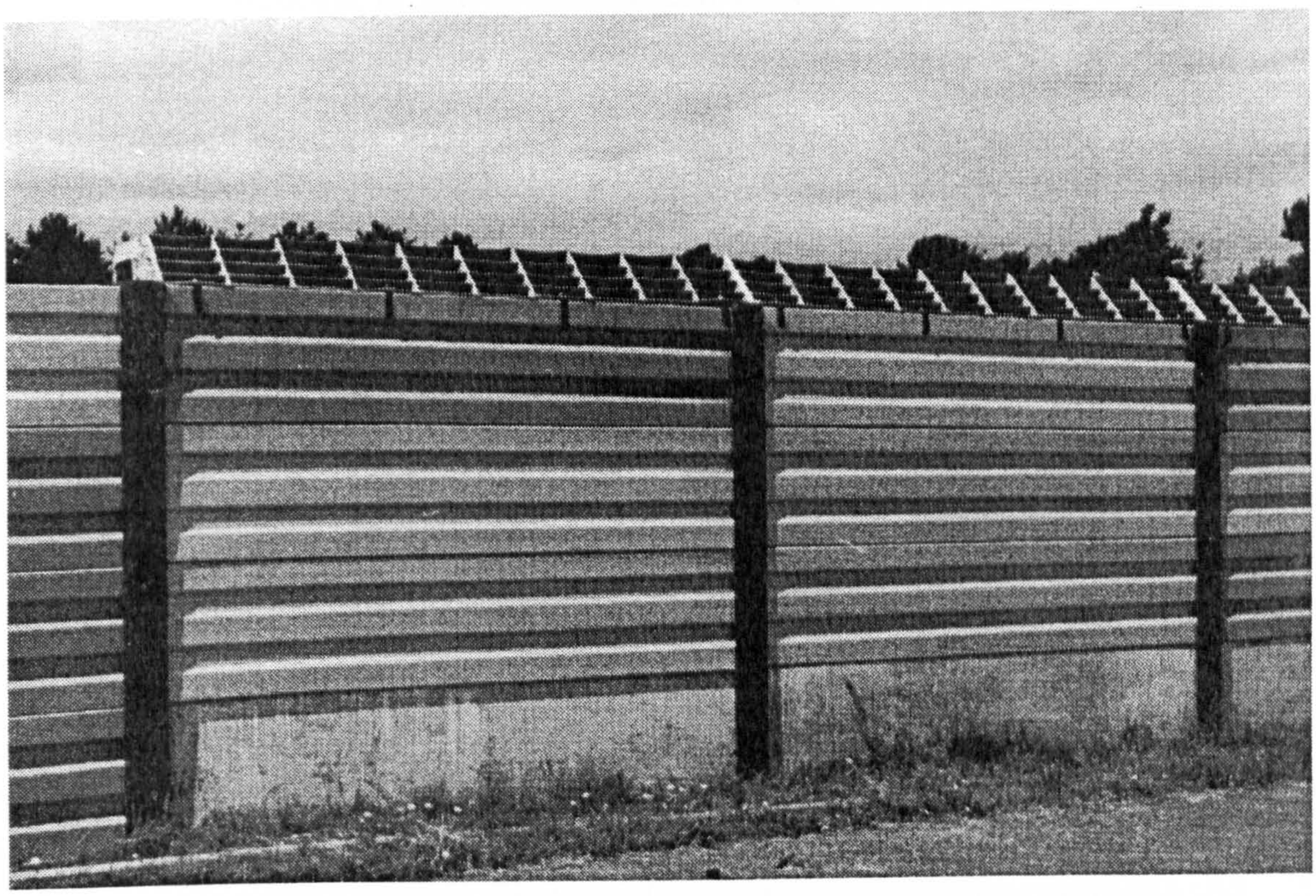

a) View from the source side of the barrier

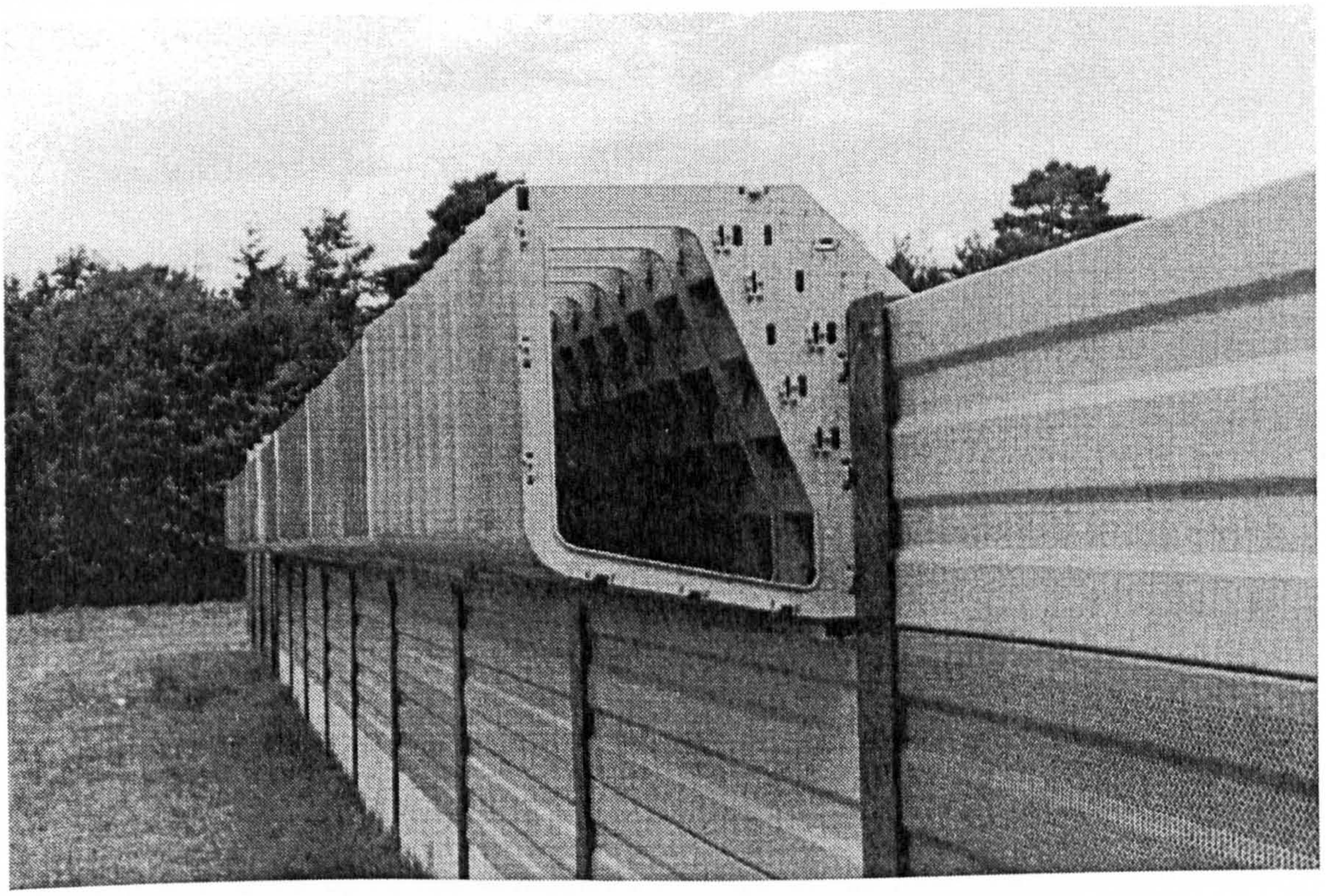

b) View from the receiver side of the barrier

Figure 3.26: The Calmzone Device mounted on a 2 m high reflective barrier at the TRL barrier facility.

The two-dimensional nature of the method means that the ducts of the interference profile could not actually be modelled along the length of the barrier. The actual device consists of a series of stacked ducts 225 mm wide (Figure 3.18), whilst in the model the equivalent three-dimensional device has ducts of infinite width. However because of the small wall thickness (4 mm), it is not considered that this would be a source of significant discrepancy between the theoretical predictions and the measurements.

Barrier Option	Average wind-normalised A-weighted SPL (number of repeat measurements	Reduction in average noise level compared with 2m*/ 2.225m high, barrier dB(A)	Boundary element method (BEM) predictions of average reduction, dB(A)
Simple reflective			
a) 2m high (reference)	64.8 ± 0.1†	—	—
b) 2.5m high	63.1 ± 0.1	1.7	1.9
Multiple Edge			
c) 1m wide‡ reflective (0.5 m deep panels)	62.4 ± 0.1	2.4	1.4
d) 1m wide‡ absorptive (0.5 m deep panels)	62.3 ± 0.1	2.5	2.1
e) 1m wide‡ absorptive (1 m deep panels)	62.1 ± 0.1	2.6	2.6
Interference Device			
f) Original Condition	62.1 ± 0.1	1.9	1.5
g) With ducts blocked	62.8 ± 0.1	1.2	1.0

* For the interference device comparisons were made with a simple barrier of identical height (2.225m)
†Standard error of mean of measurements
‡ Symmetrically arranged panels, one on either side of the barrier, separation between each panel and the barrier being 0.5m

Table 3.6: Average noise levels behind barriers and reductions in average noise levels behind the barrier.

The performance of the different barrier configurations and devices tested are presented in Table 3.6. The A-weighted sound pressure levels equate to zero wind speed and are based upon the arithmetic average of the levels at the six measurement positions for both source positions (i.e. the average of twelve values). The

corresponding relative insertion losses are presented for each arrangement; these being the differences between the average sound pressure level and that for the simple reflective barrier of identical height. In the case of the interference devices, the reference height is taken as 2.25 m, which is the overall height of a 2 m barrier fitted with the device. Previous tests carried out on the test facility in the absence of any barriers have shown that the average insertion loss over the six considered receiver positions for the 2 m high simple reflective barrier is 10.3 dB(A). The measurements show that the introduction of the interference device improves average screening by 1.9 dB(A). When the ducts of the device are blocked, this is reduced to 1.2 dB(A). The relative insertion losses obtained using the boundary element method are also included in the table and show less predicted improvement using the device, although the relative effect of blocking the ducts is similar.

Results are also included for three different multiple-edge configurations mounted on a 2 m high barrier as studied in a previous series of experiments [118]. In these cases, two additional panels either 0.5 m or 1.0 m deep are arranged parallel to the main barrier such that there is no increase in height, as illustrated in Figure 3.27. The panels are arranged symmetrically on either side of the barrier, the separation between the barrier and panel being 0.5m. This type of barrier is discussed in more detail in Chapter 5. Since there is no increase in height, the results for these barriers in the table are presented relative to a 2 m high plane barrier. These results show a larger improvement in average relative insertion loss than is observed for the interference device.

Figure 3.28 compares the SPL's measured in the presence of the device at the individual receivers, both with and without the ducts blocked, with the corresponding levels for the plane screen of equivalent height. For both source positions, the levels recorded at the 4.5 m receivers are higher than those at the corresponding 1.5 m height receivers. In addition, the decay rates for the high receivers are approximately 6 dB/doubling of distance with the changes in path difference between the direct and diffracted wave being relatively small. Considering the lowest receivers,

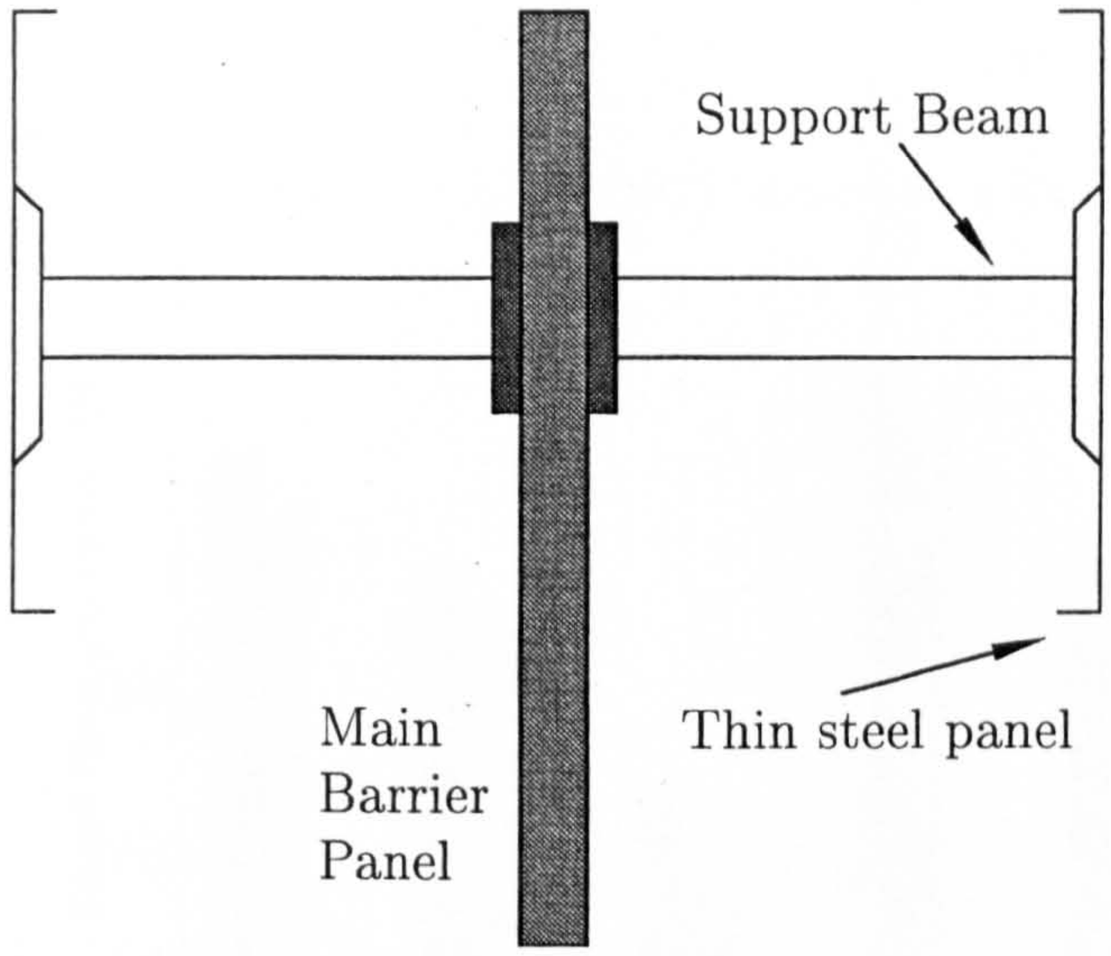

Figure 3.27: Cross-Section through symmetrical multiple edge profile, including intermediate support beam

although the decay rate between the 40 and 80 m receivers is similar to that for the high positions, the rate from 20 – 40 m is noticeably less, particularly for the more distant source. In this instance, the change in path length is more pronounced, but the decay rate due to geometrical spreading is offset by the 40 m receiver being less deeply in the shadow zone.

At all positions, the introduction of the interference device is observed to reduce the average noise levels behind the barrier. For the near source position the improvement is generally constant, except for deep in the shadow zone, being between 2.1 – 2.8 dB(A). However the levels are less stable for the more distant source. With the ducts blocked there was generally a small increase in the noise level, although the resultant levels were still lower than the corresponding levels measured behind the simple barrier of equivalent height.

Figure 3.29 plots the insertion loss spectra obtained from the boundary element predictions for the device, both with and without the ducts blocked, and the equivalent height plane screen for the source position at 5.5 m and the receiver position at 40 m behind the barrier, height 1.5 m. The device appears effective at frequencies of 500 Hz and above although, with the exception of 1 kHz, the results are relatively small up to 1.6 kHz. Blocking the ducts reduces the efficiency of the device above

a) Source position: 5.5m

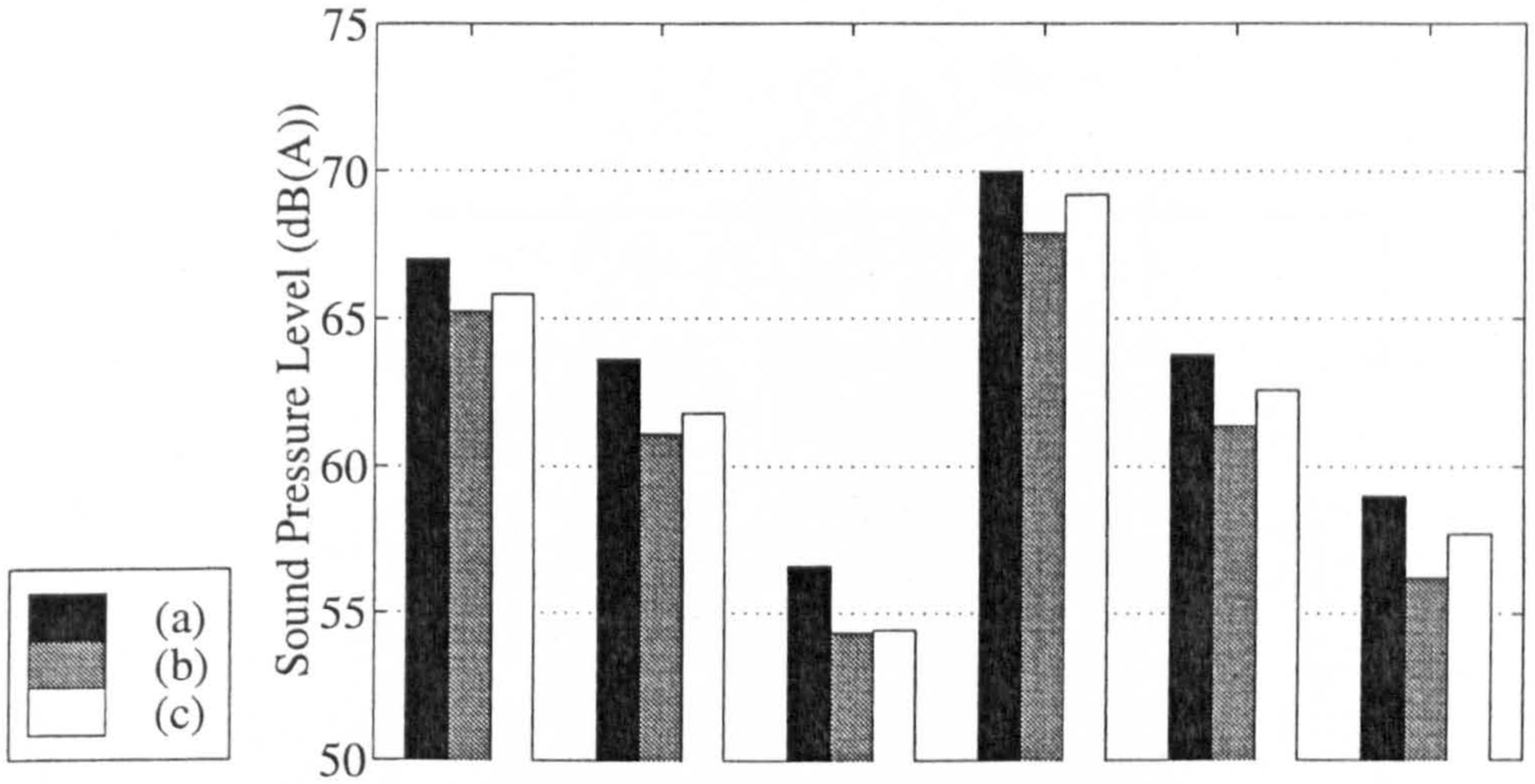

Receiver Position	20, 1.5	40, 1.5	80, 1.5	20, 4.5	40, 4.5	80, 4.5
A: 2.225m barrier	67.02	63.66	56.61	70.00	63.80	59.02
B: Device	65.25	61.08	54.32	67.92	61.37	56.22
C: Device (blocked)	65.82	61.82	54.41	69.20	62.60	57.73

b) Source position: 7.8m

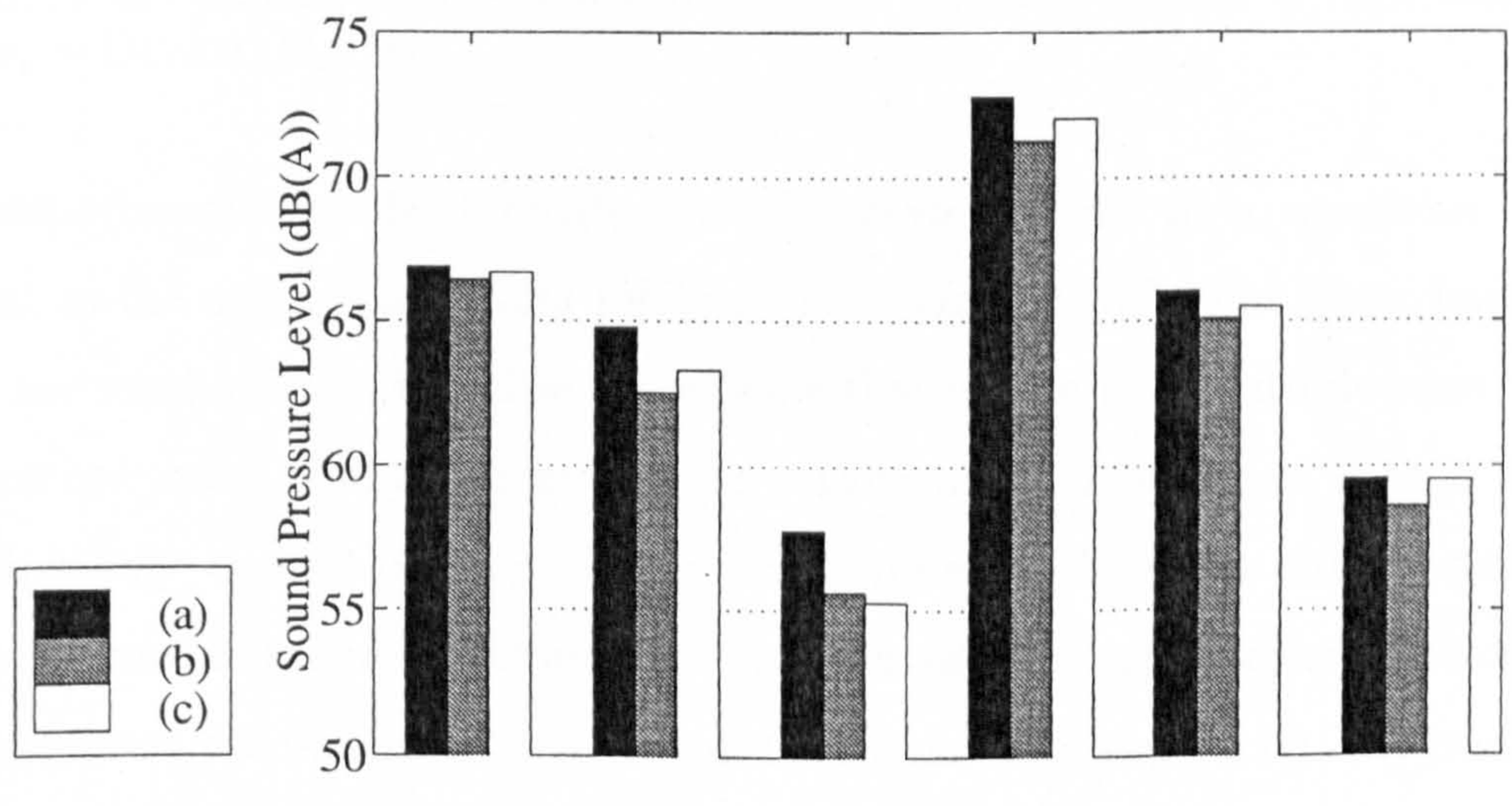

Receiver Position	20, 1.5	40, 1.5	80, 1.5	20, 4.5	40, 4.5	80, 4.5
A: 2.225m barrier	66.88	64.78	57.77	72.74	65.98	59.55
B: Device	66.43	62.53	55.61	71.22	65.07	58.61
C: Device (blocked)	66.67	63.29	55.26	71.96	65.47	59.52

Figure 3.28: Sound Pressure Levels, dB(A), obtained from full-scale measurements using the Calmzone device.

800 Hz.

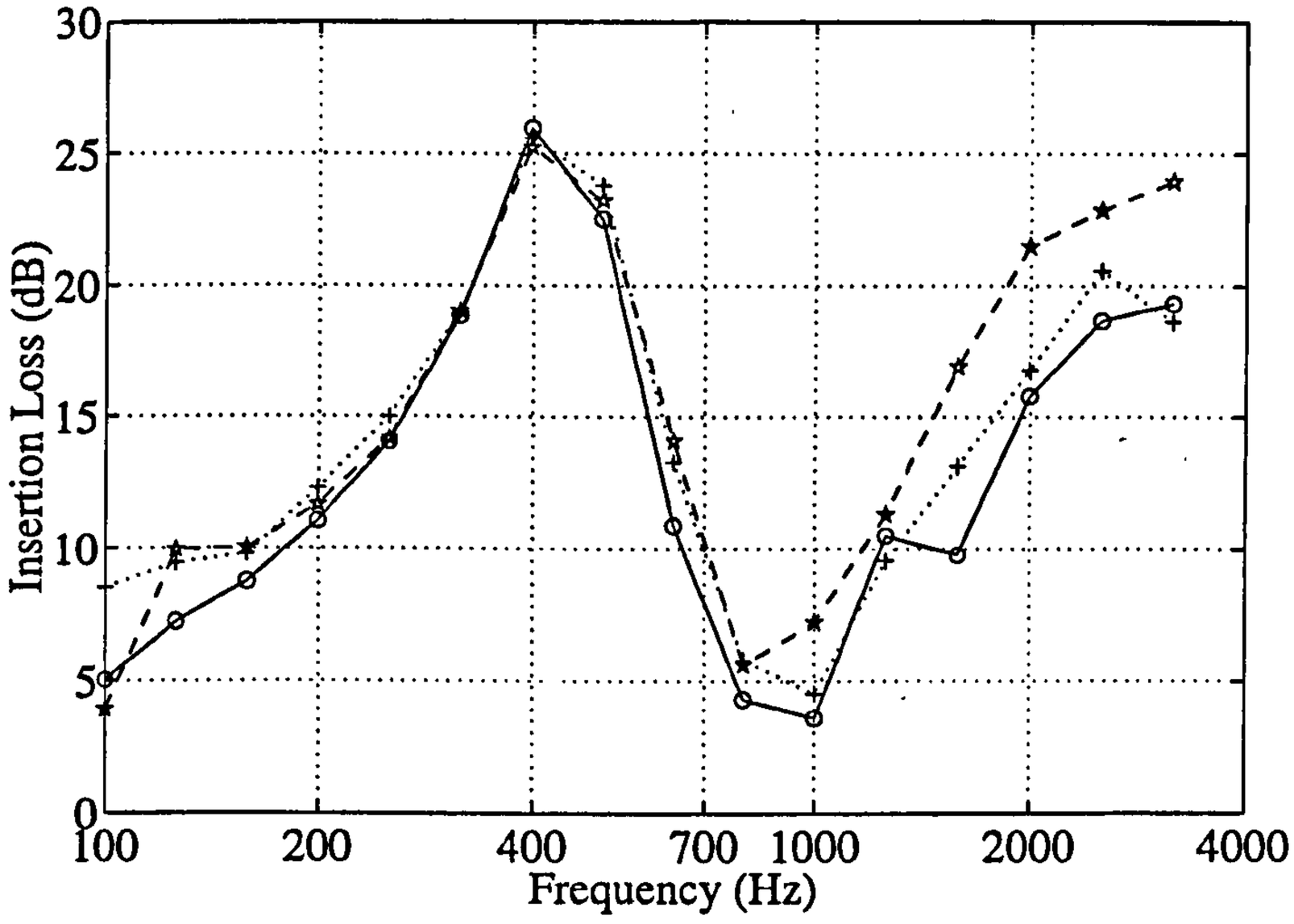

Figure 3.29: Predicted insertion loss spectra at a height of 1.5 m and a distance of 40 m behind the barrier, source at 5.5 m from the barrier; o, 2.225 m high barrier; *, Device, + Device (blocked).

The experimental results indicate that the device produced a significant improvement in the average screening relative to the equivalent height plane barrier. However the results shown in Table 3.6 indicate that on average, multiple-edge configurations are more effective at improving performance. It is noted though that the multiple-edge designs considered here are symmetric. In many site conditions where the barrier is in close proximity to the carriageway, safety reasons prohibit the introduction of outstanding elements on the source side (e.g. [121]). Theoretical predictions by Crombie et al [26] have indicated that the benefits of multiple-edge designs are reduced when the additional diffracting edges are mounted asymmetrically on the far side of the barrier. In such cases the interference device would provide a more comparable level of screening.

Following the blocking of the ducts, the device still offers significant reduction in

noise levels behind the barrier. It can be see from the results that the ducts provide approximately one third of the total reduction in noise level. The boundary element results show a similar effect, although the reduction is proportionately smaller. Since any interference effects will have been prevented, the remaining attenuation can be attributed to the presence of two diffracting edges. The efficiency of the device does not appear to be dependant on the position of the receiver, although the relatively small change in source position does appear to deteriorate performance by a varying degree.

Study of the results in terms of frequency indicate that the greatest improvements occur at frequencies above 500 Hz. Gains at the higher frequencies can be attributed in part to the effects of the twin diffracting edges formed by the stacked ducts and the back panel of the device. Previous results from similar full scale tests on different multiple-edge profiles [118] indicate that these effects do not occur below 400 Hz.

Blocking the ducts decreases the performance of the device at frequencies above 800 Hz. Earlier tests [84, 85, 107] suggest that this is due to the elimination of interference effects generated as a result of phase lags induced upon sound propagating through the ducts. The results in Figure 3.29 suggest that the most significant interference effects occur around 1 kHz and 3.15 kHz. The ducts behave as band-pass filters allowing sound of certain frequencies to pass through, in addition to inducing the phase changes as a result of the difference in path length between the ducted sound and that propagated directly over the top of the device. These effects are controlled by the dimensions of the ducts. On the interference profile tested, the ducts are believed to be tuned to specific frequencies, although precisely how these frequencies are determined is unknown, particularly in view of the shape of the ducts. Approximate path differences, δ can be calculated which suggest that for the longest duct a phase difference of π radians can be achieved at frequencies of 200, 600 and 1000 Hz where $\delta \approx \lambda/2$, $3\lambda/2$ and $5\lambda/2$ respectively (λ being the wavelength). In Figure 3.29, a noticeable difference is observed at 1 kHz, although not at the lower frequencies. The boundary element method could be easily applied

to model variations in duct geometry and overall duct dimensions with the aim of further enhancing performance. However since a suitable relationship is not available for relating interference dips to specific duct lengths, such modifications could not be efficiently determined.

The results of tests using the prototype device with a moving truck as the source [65] and tests using the production variant with a railway train source [48], all with a 2 m high barrier, have indicated maximum improvements in screening of 6 dB.This is significantly higher than observed at any individual receiver position in the current tests. Although here the comparisons have been made with a barrier of equivalent height, the additional 225 mm is unlikely to account for more than 1 dB of the screening reduction. The presence of absorptive treatment on the back panel in [65] will also only have limited effect (absorptive material placed on or near a diffracting edge has been found to provide only a small improvement in screening [118]). The most likely possibility is due to the variation in the source and receiver positions. Indeed, the variation between results for the 5.5 and 7.8 m source positions measured by the author provides some evidence of this. It is possible that the zone of significant interference is limited in extent and critically dependant on the position of the source. This would agree with observations made during the development of the device [107]. A further consideration is variations in the source spectra between road and rail traffic, at factor whose importance is dependant as to which frequencies individual ducts of the Calmzone profile are tuned to. Figure 3.24 shows a typical A-weighted road traffic noise spectrum to peak at approximately 1 kHz. Figure 6.1 in Chapter 6 compares several different railway noise spectra, which can be seen to peak at frequencies between 800 – 2500 Hz.

The modest performance over a wide area exhibited in the present tests is due principally to the presence of the twin diffracting edges rather than to interference effects. Further work would be required to establish the extent of the area over which the production device is most effective.

3.3 Conclusions

The full scale measurements have shown that the Calmzone sound interference device increases the average screening performance by 1.9 dB when compared with a simple barrier of identical height. However, the improvement was not as great as that observed following the introduction of multiple-edged barrier profiles; previous work at TRL has shown such profiles improve the average screening by 2.5 dB under similar test conditions. The device produced consistent improvement in screening over a wide area, although some variation was observed depending upon the source position.

It is considered that the primary reason for the noise reduction is the presence of the back panel which behaves as a second diffracting edge. The results obtained here suggest that approximately one third of the reduction produced is attributable to the interference effect produced by the phase delay introduced by the stacked vent system.

Earlier tests upon both the prototype and production device indicated greater improvements in screening than observed here. It is thought that this is due to the more limited range of receiver positions and the smaller source/barrier separation used in those tests, and the relationship between the tuning frequencies of the device and the spectrum of the source. The experiments carried out by Iida et al [65] suggest that the position and range of the interference zone is strongly affected by the position of the source relative to the device. Further testing would be required to define the range of geometries which would lead to optimum performance.

The experimental results indicate that the boundary element method is useful for the study of complex barrier geometries. It is considered that the method could be used to further develop the device by optimizing dimensions to promote a greater degree of interference between sound paths.

Chapter 4

Parallel Barrier Arrangements

It is not uncommon under appropriate circumstances that, as part of a traffic-noise abatement scheme, vertical barriers are installed on both sides of a carriageway. Since sound is reflected between the two barriers, the resultant insertion loss is less than that which would be achieved through the construction of a single plane screen. In principal there are two main propagation paths - that passing directly from the source to be diffracted over the front barrier and that reflected in the rear barrier prior to diffraction over the front. It is a reduction in this reflected contribution which is necessary to improve screening performance. This can be achieved by incorporating absorbent treatment onto the traffic-facing sides of the barrier or by sloping these surfaces by a small angle. Both methods appear efficient in simple numerical and experimental model investigations [111, 109, 83], although in practice the former is preferable since the latter involves only a redirection of sound energy and unexpected effects are possible under actual site and atmospheric conditions.

It is desirable to be able to predict these effects. A review of previous work is presented. The remainder of this chapter is concerned with the application of the 2-D boundary element method, as presented in Chapter 2, to such problems. A modified procedure is presented to improve the accuracy of the numerical predictions. A method for converting the model results to their point source equivalents is described and comparisons made with full-scale measurements performed using a

variety of barrier configurations on the TRL Noise Barrier Test Facility (as described in Chapter 3). The use of multiple barriers on one side of the carriageway is not considered in this study.

4.1 A Review of Previous Work

The effects of noise reflected between parallel barrier arrangements on opposite sides of the carriageway have been previously reported in a number of studies. Tobutt and Nelson [111] used a computer model, validated against experimental data, to perform simulations of parallel barriers with and without absorptive treatment. The barriers were 3 m high and 45 m apart. It was observed that the introduction of absorptive treatment improved the screening efficiency by 1.5 - 3 dB(A) at distances between 20 and 70 m behind the barriers and up to a height of 4.5 m above ground.

Results obtained by Slutsky and Bertoni [109], using a model designed to predict the effects of absorptive treatment and tilted surfaces upon parallel barrier arrangements, also demonstrated the benefits of such enhancements. For the case of 4.5 m high barriers with a separation of 45 m, the introduction of absorptive material reduced the predicted noise at a receiver 45 m behind the barrier by as much as 4 dB depending on the height of the source (however, the height of this receiver position was not specified). This compares favourably with the results of Tobutt and Nelson for a similar geometry. When the width of the roadway and corresponding barrier separation was reduced to 18 m [109], the average noise reduction at the same receiver position resulting from using absorptive material increased to a maximum of approximately 6 dB. The same study found that applying an outward tilt to the barriers, i.e. inclining them away from the source, can be beneficial. For barriers with a separation of 45 m, an outward tilt of 5° was sufficient to restore the screening performance to that of a single barrier for source heights up to 2.5 m. For a reduced separation of 18 m, the required angle of tilt increased to 20°. However, it is unclear whether the outward tilt was applied to both or a single barrier. Hothersall and Crombie [59] conducted boundary element simulations of outwards-inclined parallel barriers. Their results provided further evidence that as the angle of tilt is

increased, so the degradation in insertion loss over that of a single vertical screen is reduced. It was also observed that dividing the sloping surface into a series of vertically stacked sloping sections reduced screening efficiency.

Field trials on 3 m high parallel barriers with a separation of 74 m [46] showed no significant reduction in performance as a result of the farside barrier. This was partly explained by the large separation, which does not seem unreasonable considering the reduction in performance between absorptive and reflective barriers noted by Slutsky and Bertoni as the separation is increased. However, a study on the M6 motorway in the UK by Nelson et al [93] also failed to show a degradation in performance following the introduction of 3 m high reflective barriers on the farside of the carriageway, the separation between the two barriers being approximately 33 m. Possible contributors to the contrary results include meteorological effects and the scattering of reflected noise from vehicle bodies, although the latter is only likely to occur in the presence of high traffic volumes. Watts [119, 120] reported results of an in-depth full-scale study of parallel barrier arrangements, based upon configurations suggested to be effective by previously reported work. These results are presented in more detail in Section 4.3.

4.2 Theoretical Study of Parallel Barrier Behaviour Using The Boundary Element method

4.2.1 Results Using Line Sources

The simulations detailed in this section have been performed using the unmodified boundary element method of Section 2.1 and the basic geometry illustrated in Figure 4.1: two barriers, both of height 2 m are separated by 34.3 m, this distance being equivalent to the width of a six-lane motorway with a hard shoulder on each carriageway. Receiver positions have been set at 20, 40 and 80 m from the outside face of one of the barriers and at heights of 1.5 and 4.5 m. These positions correspond with those used in full scale tests on the Noise Barrier Test Facility at TRL (see Section 3.2).

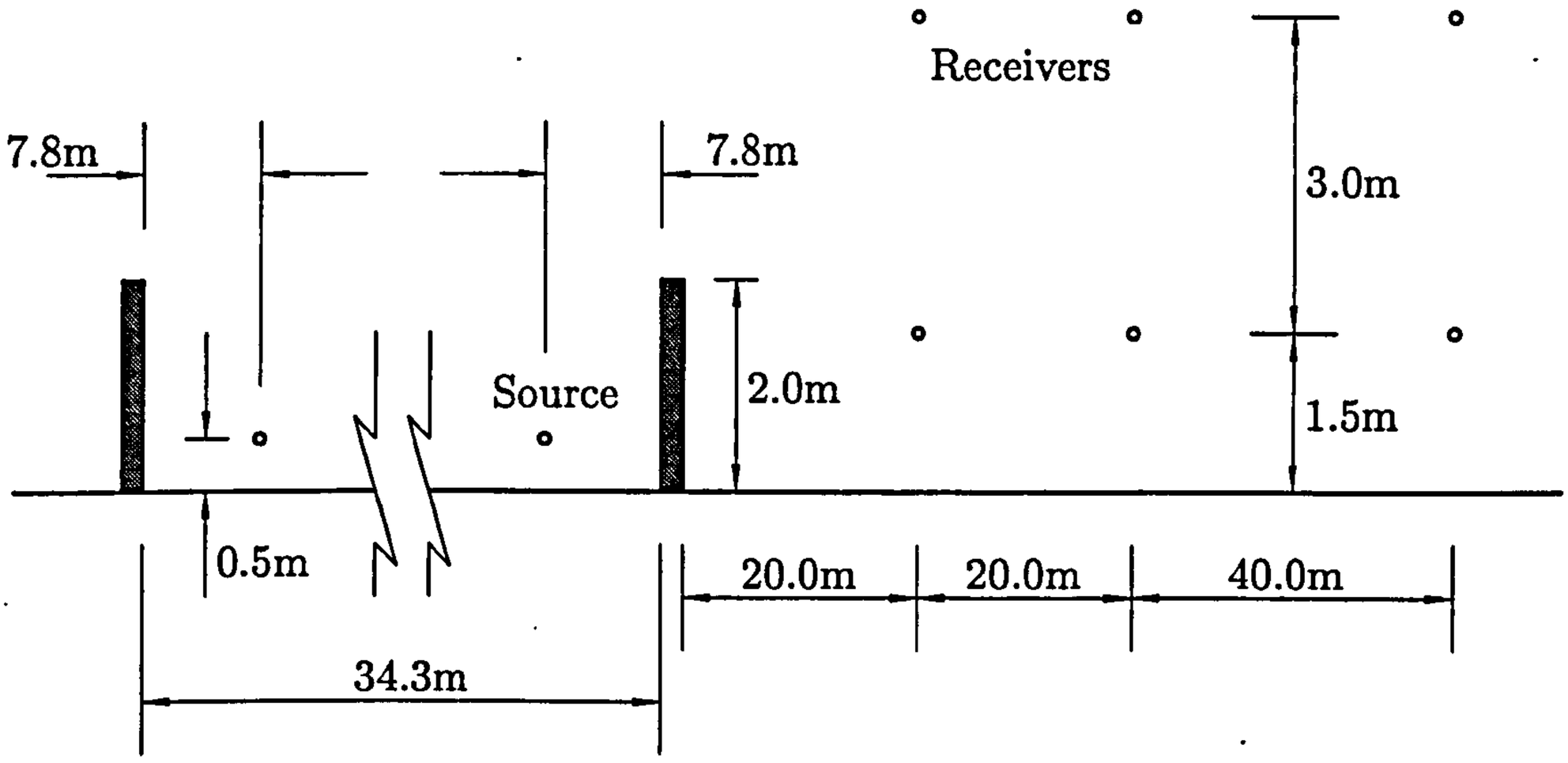

Figure 4.1: Layout of typical parallel barrier arrangement.

The situation being modelled (for all barrier arrangements considered in this section) is the simplest case - 2 source positions (each considered in a separate simulation), each at a height of 0.5 m above the carriageway and at a distance of 7.8 m from the inside face of one of the barriers (again corresponding to the NBTF full-scale tests). Obviously, the accuracy of the results in relation to practical road conditions varies greatly depending on the number and placement of sources. A minimum of two source positions are usually necessary for modelling almost any road (although this is not applicable in the standard UK prediction method, Calculation of Road Traffic Noise (CRTN), [32] where all sources are condensed into a single traffic stream). This number will also increase if it is desired to model different types of traffic, since the height of the source above ground level will vary depending on the vehicle being modelled. The sound pressure levels for each receiver position are then logarithmically combined in the standard way to produce a single SPL value at each receiver showing the effect of both sources simultaneously.

The predicted degradation in insertion loss due to the addition of the second barrier at the considered receiver positions using the boundary element method is shown in Table 4.1.

These can be compared with results obtained from the CROSECT method [111] and those using the standard UK traffic noise prediction method, CRTN [32]. The

Receiver Positions		Insertion Loss Degradation (dB(A))			
Distance (m)	Height (m)	Boundary Element Method	CROSECT Model	CRTN Method	Boundary Element Method using shield
20.0	1.5	6.72	3.93	1.72	3.61
40.0	1.5	6.68	5.02	1.81	3.70
80.0	1.5	5.77	5.95	1.95	4.07
20.0	4.5	7.22	3.69	2.32	5.26
40.0	4.5	9.33	6.48	2.49	6.02
80.0	4.5	8.23	7.03	2.77	5.56

Table 4.1: Comparison of insertion loss degradation (dB(A)) obtained using different methods of calculation.

CRTN method has been developed from measured data and its predicted insertion loss degradation values are significantly different to those of the boundary element method. In both the CRTN and CROSECT predictions, all traffic streams are condensed to a single line source. As a result, for the geometry considered in these simulations all receivers lie within the shadow zone. However, in the case of the boundary element method where 2 source positions are used, the highest receivers at 20 and 40 m from the barrier lie within the illuminated zone generated by the source furthest away. The results from the CROSECT model are systematically and significantly greater than those obtained using the CRTN method and the results from the boundary element method greater than those from CROSECT for the most part. The CRTN results lie within a range of approximately 1 dB(A), whilst the results from the other models are within a range of between 3 – 3.5 dB(A).

4.2.2 A Modified Procedure For Simulating Parallel Barrier Arrangements

The boundary element method provides an accurate determination of the wave field for the particular problem posed. However, there are three significant differences between this and the practical situation:-

i. the method assumes that the ground is perfectly flat and that the barriers are

exactly vertical. This latter assumption can lead to an over-estimation of the number of multiple reflections between rigid barriers,

ii. the method assumes that all propagation in the region between the barriers is unimpeded. In a roadway situation, this is clearly not true, since propagation will be impeded by the sides of vehicles.The effects of reflections between barriers and vehicles, particularly high-sided vehicles, has been discussed elsewhere, e.g. [27, 60, 61]

iii. the method is two-dimensional so that the three-dimensional situation which is modelled is of a coherent line source in an infinite roadway of constant cross-section. In practice, vehicles approximate to point sources so that rays suffering multiple reflections from the barriers attenuate at a rate of 6 dB/doubling of distance, whereas in the model, the attenuation rate is 3 dB/doubling of distance.

Various options are available to overcome these differences (see Section 4.1) although some are more effective than others. In the case of i), a small change in the vertical angle of the barriers (Table 4.2) or a more accurate reproduction of their profile will have some effect, as will changing the profile of the ground surface. However, the latter is less preferable due to a considerable increase in the computational expense of the solution (see Section 2.1).

To simulate propagation impeded by the sides of vehicles, it is necessary to include an appropriately shaped cross-section of the vehicle into the boundary element geometry. However, maintaining the (7.8, 0.5) source position used within CRTN and on the TRL barrier facility renders accurate placement of the "vehicle body" difficult. If the source is placed too close this can result in an over-prediction of the sound pressure on boundary elements in the immediate vicinity. Consequently a "box-shield", as illustrated in Figure 4.2 has been incorporated into the input data as an alternative.

Being two-dimensional, the shield is formed from three faces, each having an absorbent lining. The horizontal faces have the same treatment (a statistical absorption coefficient, α, of 0.4) and the face at the rear of the shield an α value of

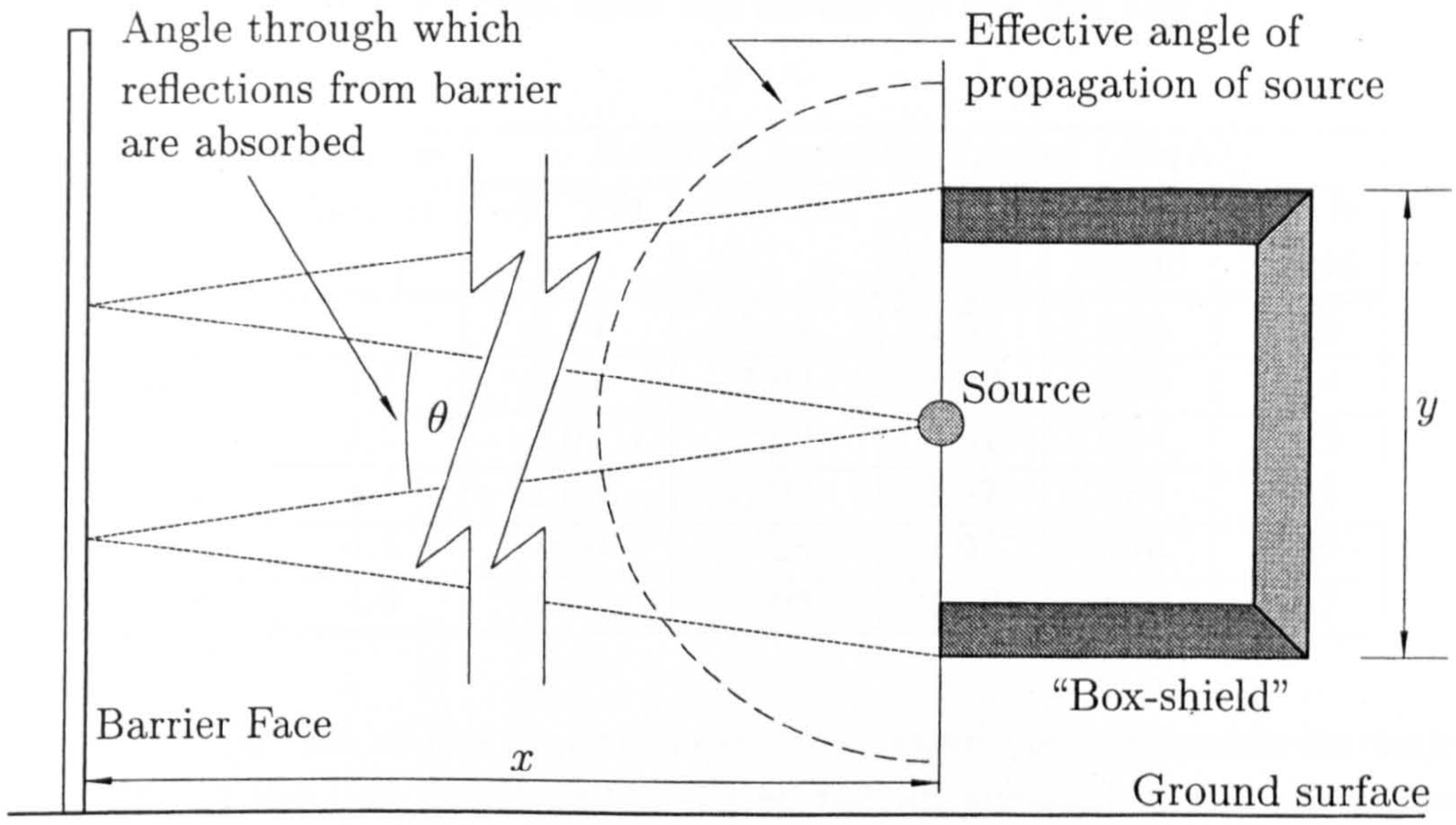

Figure 4.2: Cross-section detailing "box-shield".

0.9. The source is positioned midway between the horizontal faces and vertically aligned with the front of the shield. The placement of the source at this position is important and results in two effects - the first is to "halve" the angle of propagation, i.e. waves from the source radiating into the shield are effectively cut out (Figure 4.2). To simulate sound propagation from the other side of the vehicle, it is necessary to undertake an additional simulation with the shield rotated through 180°. The second effect is to absorb reflections from the barrier with a low angle of incidence. The angle θ through which these reflections are affected will depend on the separation, y, of the horizontal faces of the shield and the distance, x, between the shield and the barrier (Figure 4.2). The dimensions chosen for the shield correspond to those of the loudspeaker cabinet used on the NBTF (Figure 3.23), i.e. height $y = 0.57$ m, depth $= 0.445$ m. The height of the shield above ground (0.215 m) also matches the experimental conditions. Results generated using this approach together with the basic geometry of Figure 4.1 are included in Table 4.1. Using the two source positions involved the addition of results from four separate simulations. A reduction of the order of 3 dB(A) in the insertion loss degradation in comparison with the basic boundary element method results is observed. In both cases, the source strength is identical. The changes in results are attributable to the

absorption of the sound reflected from the barrier by the box shield.

Receiver Positions		Relative Insertion Losses (dB(A))				
Distance (m)	Height (m)	−2° Tilt	+2° Tilt	0° & Shield	−2° & Shield	+2° & Shield
20.0	1.5	4.14	3.14	2.37	3.75	3.70
40.0	1.5	3.42	3.62	1.90	2.38	2.94
80.0	1.5	2.07	2.09	0.91	1.54	1.95
20.0	4.5	1.88	0.98	1.57	2.64	2.11
40.0	4.5	4.26	3.25	2.97	4.76	4.46
80.0	4.5	4.34	3.03	1.89	4.12	3.67

Table 4.2: Comparison of the improvement in insertion loss achievable through the incorporation of the box shield and/or tilted barrier surfaces in the basic parallel barrier geometry of Figure 4.1

Table 4.2 compares the improvements in calculated insertion losses (from the boundary element method) which can be achieved through the incorporation of the shield and/or barrier tilting in the basic geometry of Figure 4.1. It is possible to relate the data in Table 4.2 to the boundary element results using the shield in Table 4.1. Incorporating both the tilting of the barriers and the box shield within the boundary element method will decrease the insertion loss degradation to bring the predicted values closer to those obtained using the CRTN method. It is expected that the CRTN results would give a better indication of the practical situation since the method is derived from site measurements.

To investigate the third difference, it is interesting to modify the results produced by the method such that they are equivalent to those for a point source. In undertaking this conversion, it is necessary to make a series of assumptions:-

i. that the line from the point source to the receiver is perpendicular to the barriers,

ii. that each barrier has a definable highest point which is visible from the source position. The highest point of the front barrier should be visible from the receiver position and that of the rear barrier should be visible from the top of the front barrier,

iii. that the barriers are infinitely long,

iv. the pressure component at a particular receiver for a specific ray path (in the line source case) is multiplied by the inverse of $\sqrt{R}$ to convert to a point source, where R is the length of that ray path from source to receiver,

v. that there are only two significant contributory ray paths

R_1 - the diffracted path from the source to the top of the front barrier to the receiver,

R_2 - the diffracted path from the source to the rear barrier to the top of the front barrier to the receiver

as shown in Figures 4.3 and 4.4, and that these ray paths are assumed to be incoherent due to the large path difference and large frequency bandwidth.

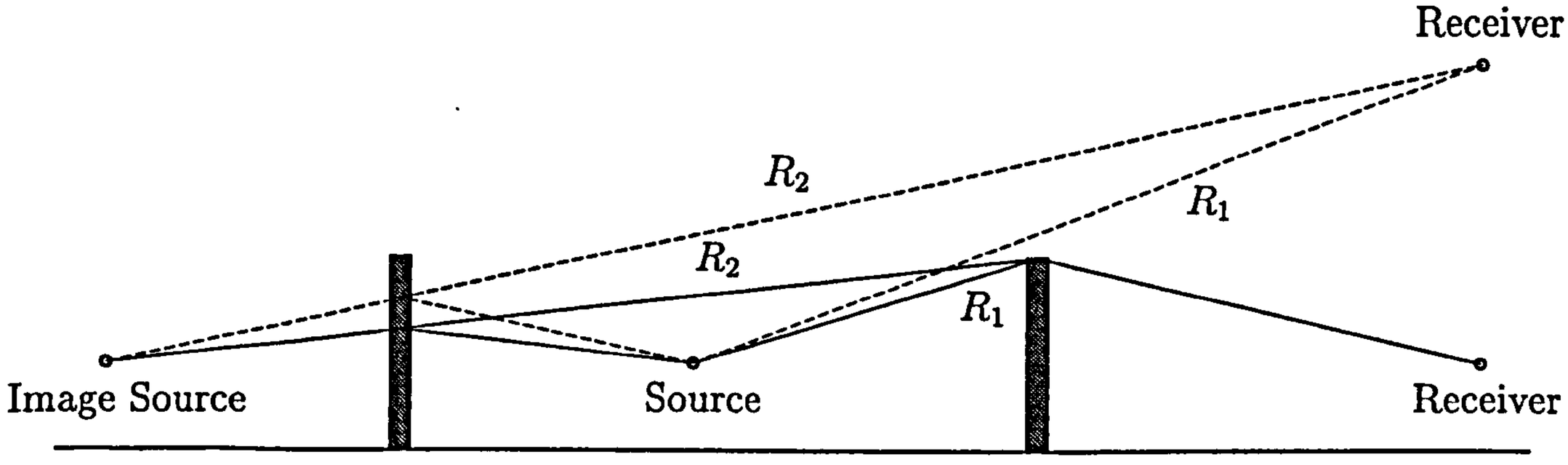

Figure 4.3: Possible raypaths, including those where front barrier is not visible from image source

The conversion is applied to the final A-weighted results, the method being as follows:

The total sound pressure level at the receiver due to both paths in the line source case is

$$SPL = 10\log\left(10^{(SPL_1/10)} + 10^{(SPL_2/10)}\right), \tag{4.1}$$

where SPL_1 is the pressure due to R_1 and SPL_2 is the pressure due to R_2. Rearranging and inverting gives

$$SPL_2 - SPL_1 = 10\log\left(10^{(SPL-SPL_1)/10} - 1\right). \tag{4.2}$$

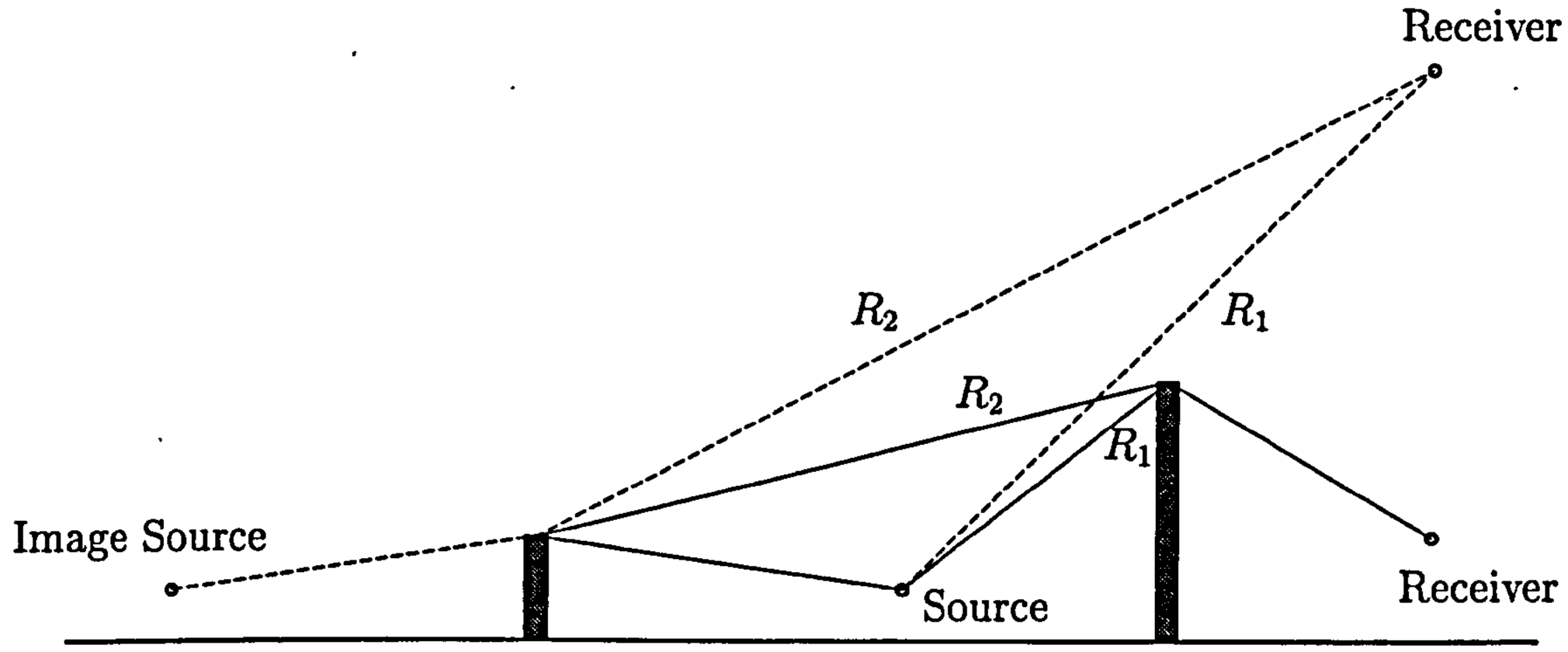

Figure 4.4: Possible ray paths, including those where front barrier is visible from image source

Define the insertion loss degradation in the line source case, $DEGL$, as the difference between the insertion loss for the front barrier ($SPL_D - SPL_1$) and the insertion loss for both barriers ($SPL_D - SPL$);

$$\begin{aligned} DEGL &= SPL_D - SPL_1 - (SPL_D - SPL) \\ &= SPL - SPL_1, \end{aligned} \tag{4.3}$$

where SPL_D is the direct sound pressure level.

Then the difference between the SPL's of the two ray path contributions (for the line source case), $DSPLL$, is (from (4.2) and (4.3))

$$\begin{aligned} DSPLL &= SPL_2 - SPL_1 \\ &= 10\log\left(10^{DEGL/10} - 1\right) \end{aligned} \tag{4.4}$$

Now calculate the path lengths for the two ray paths, R_1 and R_2, as illustrated in Figures 4.3 and 4.4 and specified as follows:

R_1 - either the direct path from source to receiver (if the latter is visible from the source) or the path via the top of the front barrier

R_2 - If the top of the front barrier is not visible from the image then either the path

i. from the image of the source in the rear barrier direct to the receiver, if the image is visible, or

ii. from the image of the source to the top of the front barrier to the receiver.

Otherwise either the path

iii. from the image of the source to the top of the rear barrier to the receiver,

or

iv. from the image of the source to the receiver with diffraction at the top of each barrier

Now for a line source,

$$\text{Intensity} \propto \frac{1}{R} \text{ and pressure} \propto \frac{1}{\sqrt{R}}$$

whilst for a point source,

$$\text{Intensity} \propto \frac{1}{R^2} \text{ and pressure} \propto \frac{1}{R}.$$

Therefore, to convert a SPL from a line source to the point source equivalent, the following formula should be used:

$$SPL_{point} = SPL_{line} + 10\log\left(\frac{R_{ref}}{R}\right) + C, \tag{4.5}$$

where R denotes either R_1 or R_2, R_{ref} is a reference distance of 1.0 m, and C is a constant depending only on the strengths of the point and line sources. So to convert $DSPLL$ to its point source equivalent, $DSPLP$, we use the formula

$$\begin{aligned} DSPLP &= SPL_2 + 10\log\left(\frac{R_{ref}}{R_2}\right) - SPL_1 - 10\log\left(\frac{R_{ref}}{R_1}\right) \\ &= SPL_2 - SPL_1 - 10\log\left(\frac{R_2}{R_1}\right) \\ &= 10\log\left[\frac{R_1}{R_2}\left(10^{(SPL-SPL_1)/10} - 1\right)\right], \end{aligned} \tag{4.6}$$

the last line obtained using (4.2). But also, similarly to (4.4)

$$DSPLP = 10\log\left(10^{DEGP/10} - 1\right),$$

where $DEGP$ is the insertion loss degradation for the point source case. Rearranging this equation gives

$$DEGP = 10\log\left(1 + 10^{DSPLP/10}\right) \tag{4.7}$$

This formula together with (4.6) gives a method of calculating the degradation loss for each receiver position in turn from the computed sound pressure levels in the line source case with and without the second barrier (SPL_1 and SPL). Although these results are of use individually, they can be combined to produce a single value for the insertion loss degradation due to multiple point sources, the procedure for which is as follows.

Let $SPLL_j, j = 1, 2, ...$ denote the sound pressure level calculated by the standard two-dimensional boundary element method and $SPLP_j, j = 1, 2, ...$ the point source equivalent, when the source is at position j and only the front barrier is present. Assuming that the main ray path is R_1 (as defined previously), then from (4.5),

$$SPLP_j = SPLL_j - 10\log\left(\frac{R_1}{R_{ref}}\right) + C. \tag{4.8}$$

The sound pressure level at the receiver point with both the front and rear barriers present is

$$SPLP'_j = SPLP_j + DEGP_j. \tag{4.9}$$

The insertion loss degradation with all point sources present, $ILDP$ is given by

$$ILDP = SPLP' - SPLP, \tag{4.10}$$

where $SPLP$ is the logarithmic sum of $SPLP_1$, $SPLP_2$,... and $SPLP'$ that of $SPLP'_1$, $SPLP'_2$,...

4.2.3 Comparison of Theoretical Results For Line Sources and Equivalent Point Sources

Table 4.3 compares predictions of insertion loss degradation using the standard boundary element method with identical results adjusted by the above procedure to their point source equivalents for two different parallel barrier arrangements (in both cases, neither tilting surfaces nor shield have been incorporated). The geometry used is that of the barrier arrangement in Figure 4.1, i.e 2 m high barriers with a separation of 34.3 m, and two sources, each at a height of 0.5 m above the carriageway

and at a distance of 7.8 m from one of the barriers. In the second case, the barrier furthest from the receiver positions has been made absorptive (the inner face of the barrier having an α value of 0.7) - this will have the effect of bringing the performance of the arrangement closer to that of a single barrier.

Receiver Positions		Insertion Loss Degradation, dB(A)			
		Reflective Barriers		Far Barrier Absorptive	
Distance (m)	Height (m)	Line Source	Point Source	Line Source	Point Source
20.0	1.5	6.72	4.57	1.42	0.80
40.0	1.5	6.68	5.26	1.15	0.79
80.0	1.5	5.77	4.96	1.41	1.12
20.0	4.5	7.22	5.37	1.52	0.96
40.0	4.5	9.33	7.82	1.94	1.43
80.0	4.5	8.23	7.18	1.83	1.46

Table 4.3: Comparison of degradations in Insertion Loss, dB(A), obtained from the Boundary Element Method, with those adjusted to a point source scenario.

The attenuation rates for a point and line source are 6 and 3 dB/doubling of distance respectively. For a single barrier the insertion loss is very similar for the point and line source cases, since the path lengths of the direct ray and the ray over the top of the barrier are approximately equal. However, for the parallel barrier condition, the ray reflected from the opposite barrier is much greater in length than the ray over the near barrier and this difference causes the appreciable change between the line and point source results in Table 4.3. When the far barrier is absorbent, the effect of the ray reflected from this surface is reduced and this effect is illustrated in Table 4.3.

4.3 Comparison Between Theoretical and Full Scale Experimental Results

As already observed, it is the reflected contribution from the barrier furthest from the receiver position which degrades the screening efficiency of parallel barriers. In this section we describe the results of full scale outdoor tests, in which the author

participated as part of the PhD programme, and which have been reported by Watts [120], to assess the effectiveness of physical changes to the barrier geometry. The configurations tested have been suggested (Section 4.1) to give improved screening over the basic arrangement of two plane, vertical, rigid screens, and included the introduction of absorptive or tilted surfaces, additional diffracting edges and median barriers (i.e. positioned at the centre of the roadway). The tests were conducted using the experimental facilities and procedure described in Section 3.2, with the layout as used in the boundary element simulations earlier in this chapter, i.e. two barriers separated by a 34 m strip of asphalt, with a loudspeaker placed at 7.8 m from and facing either barrier (i.e. 4 separate tests were required for each barrier configuration, the results being logarithmically combined to give an overall SPL value) with the axis of the speaker 0.5 m above the asphalt surface. As with the previously discussed full scale measurements, the receivers were positioned at 20, 40 and 80 m from one of the barriers and at heights of 1.5 and 4.5 m. With the exception of the tests using parallel reflective vertical screens, the properties and the geometry of the front barrier were maintained throughout.

The different configurations are illustrated in Figure 4.5, together with the manner in which the principle propagation path and the first reflected path from a source between the barriers are diffracted, reflected or absorbed by each barrier arrangement. In the case of the median barriers, a source position on both sides is shown. In detail, the designs are as follows:

a) Single reflective nearside barrier, height = 2.0 or 3.0 m.

b) Parallel reflective barriers, height = 2.0, 2.5 or 3.0 m. Increasing the height of the barriers produces additional screening of both the direct and reflected noise.

c) Parallel barriers with the near barrier (that nearest the receivers) reflective and the far barrier absorptive, height = 2.0 m. The introduction of absorptive treatment helps reduce reflection effects, so that the arrangement behaves more like a single rigid barrier (case a)). The figure shows the effect of a perfectly

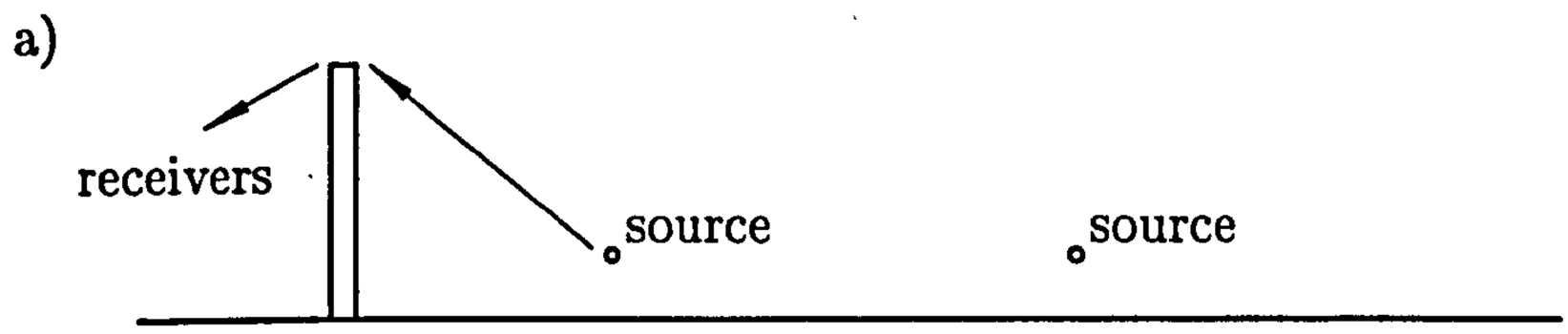

Figure 4.5: Parallel barrier arrangements as tested on the Noise Barrier Test Facility; a) reference barrier arrangement, no farside barrier; b) reflective farside barrier; c) absorptive farside barrier; d) tilted farside barrier; e) farside barrier with tilted mid-section; f) absorptive median barrier with rigid farside barrier.

absorptive barrier. The absorption coefficient for the absorptive panels, α is approximately 0.8.

d) Parallel screens with the far screen inclined at at either 5, 10 or 15° away from the road, height = 2.0 m. Inclining the far screen helps redirect any reflected sound such that if the angle is sufficient, it will not be diffracted by the nearside barrier.

e) Parallel barriers with the mid 1.0 m of the far barrier inclined at 10° away from the road, height = 2.0 m. This performs in a similar manner to case d)

f) Parallel reflective barriers with either a 1.125 or 1.25 m high absorptive median barrier, height of main barriers = 2.0 m. The introduction of the median barrier provides an additional diffracting edge for both the direct and reflected sound. Making the barrier absorbent helps reduce reflected sound from the nearside barrier at low angles of incidence and additionally absorbs sound which would be reflected from the farside barrier. Clearly such a barrier could only be implemented on a dual carriageway.

Theoretical predictions of these parallel barrier arrangements, for the same barrier, source and receiver geometry as the full-scale experiments, have been performed using the boundary element method and the "box-shield" modification proposed in Section 4.2.2. However, it should be noted that these calculations were performed before the development of the two-impedance ground modification presented in Section 2.2. Consequently to reduce the computation time, since 4 simulations were required for each barrier arrangement, the calculations were performed using rigid ground rather than grassland outside the two barriers in the area of the receivers.

The results presented in Section 4.2.3 illustrate how, for parallel barriers, relative insertion losses are affected by the use of a line or point source. For increased accuracy of comparison it is therefore necessary to adjust the results to a consistent source type. The boundary element method results can be adjusted to their point source equivalents using the approximate method of Section 4.2.2. Alternatively, the

experimental point source results can be adjusted to line source equivalents using the approximate method of Watts [120], described in the following paragraph.

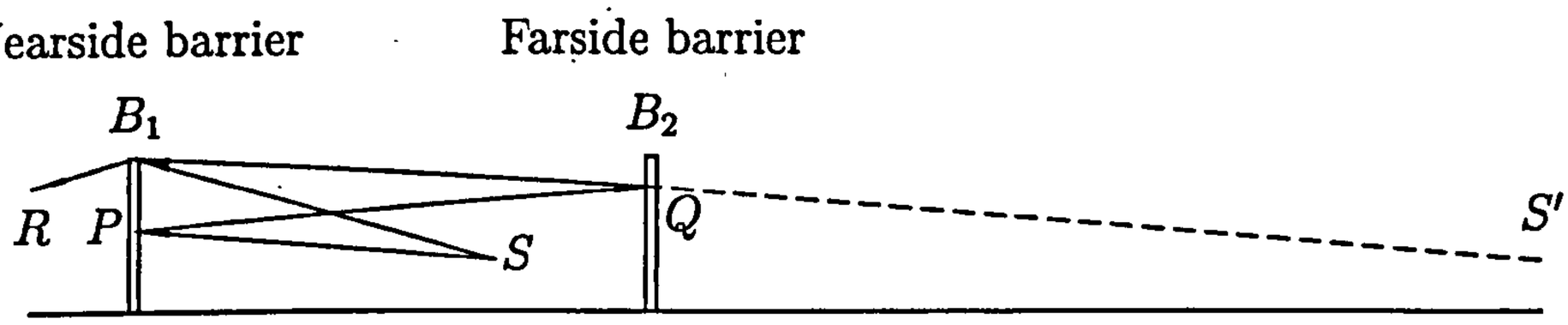

Figure 4.6: Cross-section of a typical parallel barrier arrangement showing significant direct and reflected sound rays from a directional loudspeaker source, S, facing the receiver position, R.

Consider the simplified barrier arrangement of Figure 4.6. The loudspeaker is assumed pointing towards the nearside barrier and receiver position, R. Since this source is directional, no consideration is given to sound rays emitted by the source towards the farside barrier. The following correction must therefore be applied for all 4 source positions/orientations. Let the direct path from source to receiver over the nearside barrier (SB_1R) be distance d. The first reflected pathlength ($SPQB_1R$) is then of length $d+2w$ (to a good approximation) where w is the separation of the two barriers. Define the barrier correction (that proportion of the energy removed by the barrier) at receiver R resulting from barrier B_1 in front of the source S as A_0 and the correction for barrier B_2 in front of the image source S' as A_1. If I_0 is the intensity of the source S at 1 m, then the intensity at R, I_s for a point source (spherical spreading) is given by

$$I_s = A_0 I_0 d^{-2} + A_1 I_0 (d+2w)^{-2}. \tag{4.11}$$

The intensity at receiver R, I_c, which corresponds to cylindrical spreading, i.e. a line source at S instead of a point source, can be approximated by

$$I_c = f(A_0 I_0 d^{-1} + A_1 I_0 (d+2w)^{-1}), \tag{4.12}$$

where f is a constant which arises from the difference in screening of a line and point source. Eliminating I_0 then

$$I_c = f I_s \frac{A_0 d^{-1} + A_1 (d+2w)^{-1}}{A_0 d^{-2} + A_1 (d+2w)^{-2}}. \tag{4.13}$$

A_0 and A_1 can be obtained using the calculation method given in CRTN [32]. From the subsequent calculated value of I_c, the sound pressure level at R can be calculated from $R = 10 \log I_c$. If the contribution from the first reflected path is insignificant, then the following equation is used:

$$I_c = f I_s d \tag{4.14}$$

This equation can thus be used for options other than those where the two barriers are both vertical. When calculating relative sound pressure levels, the constant f is eliminated. These equations are applicable to all source positions although in cases on the test facility where the loudspeaker is oriented towards the far barrier, the most direct path will include one reflection. These equations are based upon two contributions: the direct path and the first reflected path. The method can be further expanded to account for further reflections between the barriers (see Appendix 2, [120]).

The average sound pressure levels over the 6 receiver positions obtained from the full-scale measurements are presented in Table 4.4 for the different configurations in Figure 4.5. It is noted that the overall level at each receiver is the logarithmic combination of the levels for the 4 different speaker orientations. Also presented are the corresponding average insertion losses relative to a single 2 m high reflective barrier at the nearside position, where a positive relative insertion loss means a reduction in the screening performance. Using the method of Watts [120] described above the individual SPL results have been converted to their line source equivalents and the appropriate average insertion loss degradations calculated. These, together with the degradations predicted using the boundary element method, i.e. for a coherent line source, are also included in the table.

Considering the individual barrier performances in terms of the experimental point source results, it is observed that increasing the height of the single barrier by 1 m improves the screening performance by approximately 3.5 dB(A) (tests (i) and (ii) in the table). The introduction of a 2 m high reflective screen on the far

Barrier option	Average SPL dB(A)	Relative Insertion loss dB(A)		
		Point Source	Line Source	BEM Result
a) Single barrier				
i) 2 m reflective	70.8	0.0	0.0	0.0
ii) 3 m reflective	67.2	-3.5	-3.4	-3.5
b) Parallel barriers with far barrier reflective				
iii) 2 m high	73.8	3.1	4.4	4.7
iv) 3 m high	71.1	0.4 (3.9)†	2.0 (5.4)	2.2 (5.7)
c) Parallel barriers with far barrier absorptive				
v) 2 m high	71.1	0.3	0.5	1.2
d) & e) Parallel barriers with far barrier tilted				
vi) 0°	73.3	2.5	3.9	4.7
vii) 5°	72.2	1.5	1.8	1.8
viii) 10°	71.0	0.2	0.3	0.6
ix) 10° (centre 1 m only)	71.3	0.5	0.7	2.1
x) 15°	70.7	-0.4	-0.1	0.3
f) Parallel barriers with absorptive median barrier				
xi) 1.12 m high	70.5	-0.2	0.2	0.4
xii) 1.25 m high	69.7	-1.0	-0.8	0.1

Table 4.4: Average noise levels and relative insertion losses behind different parallel barrier options (from [120]). † bracketed values denote insertion loss relative to the 3 m single barrier.

side of the carriageway, (iii), degrades the screening performance by approximately 3 dB(A). Increasing the height of both barriers to 3 m, (iv), compensates considerably, although the average insertion loss is still slightly less than that of the 2 m single screen. However a considerable degradation in performance is observed in comparison to the 3 m single barrier. The introduction of an absorptive screen should (Section 4.2.3), depending on the absorption coefficient, α, of the absorber, minimise degradation effects. This is observed in the experimental averages, the degradation loss being approximately the same as observed when increasing the height of the two rigid screens. Tilting the inner face of the far barrier reduced the

insertion loss degradation, the most effective performance being observed for the 15° tilt, test (x). It is noted that the result for the 0° tilt case is different to that for the plane reflective parallel arrangement, even though the two cases are equivalent. This is attributed to differences in the surface type on the far barrier, being plywood panelling in the former case and aluminium in the latter. Tilting only the middle 1 m of the screen, (ix), has less effect than when the whole screen is inclined. The introduction of the absorptive median barrier effectively eliminates any degradation resulting from the introduction of the farside screen.

When the experimental results are adjusted to their line source equivalents (Table 4.4), high increases in the average relative insertion loss (i.e degradations in screening performance) of between 1.3 – 1.6 dB(A) are observed when a vertical rigid barrier is present on the far side. This is a result of the significant contribution of the reflected component. When the far barrier is inclined, the difference is less pronounced. The boundary element predictions using the standard coherent line source are observed to generally overestimate the degradation compared to the adjusted measurements, although being generally within 1 dB(A). The rank order of the different configurations based on the boundary element predictions is similar to that for the experimental results. The most significant difference in the line source results is for the case when the central 1 m of the far barrier is inclined at 10°, although the reason for this is unclear. The errors between the BEM results and the adjusted measurements may be attributable largely to the difference in the outlying ground conditions noted previously. Other contributory factors are the perfect geometry and reflective surfaces in the model, although the incorporation of the box-shield goes some way to reducing these effects. Such conditions cannot be realistically met in most site conditions. The best agreement between the methods occurs when the faces of opposing barriers are not vertical.

The performances of some of the different parallel barrier arrangements at the different receiver positions, as modelled using the boundary element approach, are compared in Figures 4.7 and 4.8. The results for the plane reflective 2 m high screen in the nearside position are also included. The figures indicate that noise levels

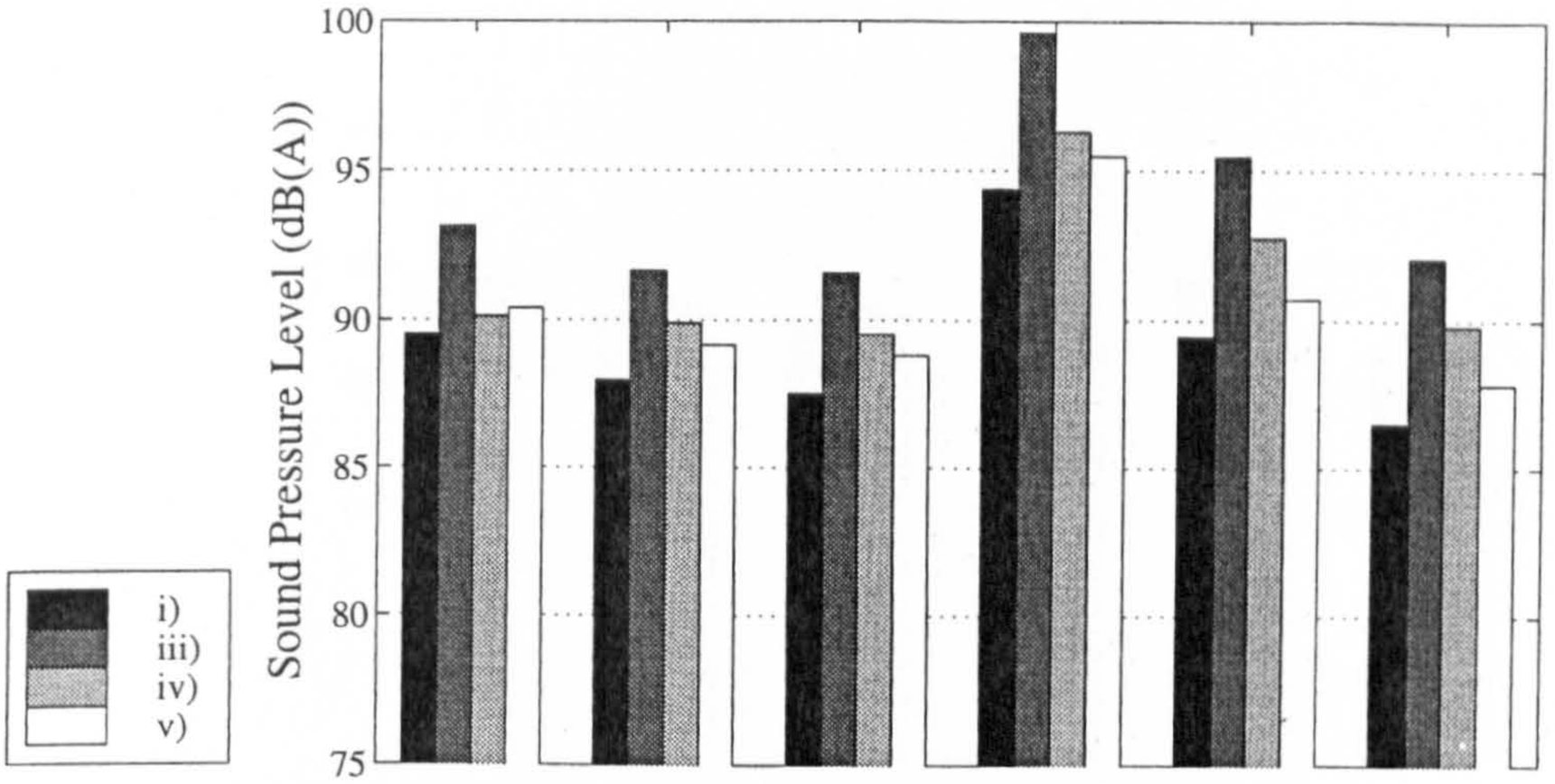

Receiver Position	20, 1.5	40, 1.5	80, 1.5	20, 4.5	40, 4.5	80, 4.5
Option i)	89.50	87.96	87.52	94.37	89.47	86.52
Option iii)	93.11	91.66	91.59	99.63	95.49	92.08
Option iv)	90.12	89.91	89.53	96.31	92.77	89.84
Option v)	90.39	89.14	88.79	95.50	90.71	87.85

Figure 4.7: Predicted sound pressure levels, dB(A), using the BEM for different parallel barrier arrangements; i) Single 2 m barrier; iii) 2 m reflective parallel barriers; iv) 3 m reflective parallel barriers; v) 2 m parallel barriers, far barrier absorptive.

were generally higher at the 4.5 m receiver position than those at 1.5 m, the rate of attenuation being at least 3 dB/doubling of distance, the rate corresponding to cylindrical spreading. It is observed that the high receivers at 20 and 40 m lie in the illuminated zone for the far source position when the barriers are 2 m high. The decay rates at the lower receivers are considerably less. Reduced differences between the 20 and 40 m position occur since any reduction through geometrical spreading will be offset by the receiver at 20 m being much deeper in the shadow zone. Effects at more distant receiver positions can be considered in terms of the different source components used in these tests. When the source is in the far side position or in the nearside position and oriented towards the far barrier position, the change in path length from one receiver to the next is relatively small because of the width of the road. Although the direct path from the nearside source over the top of the near barrier is the dominant component, in the absence of ground absorption, the

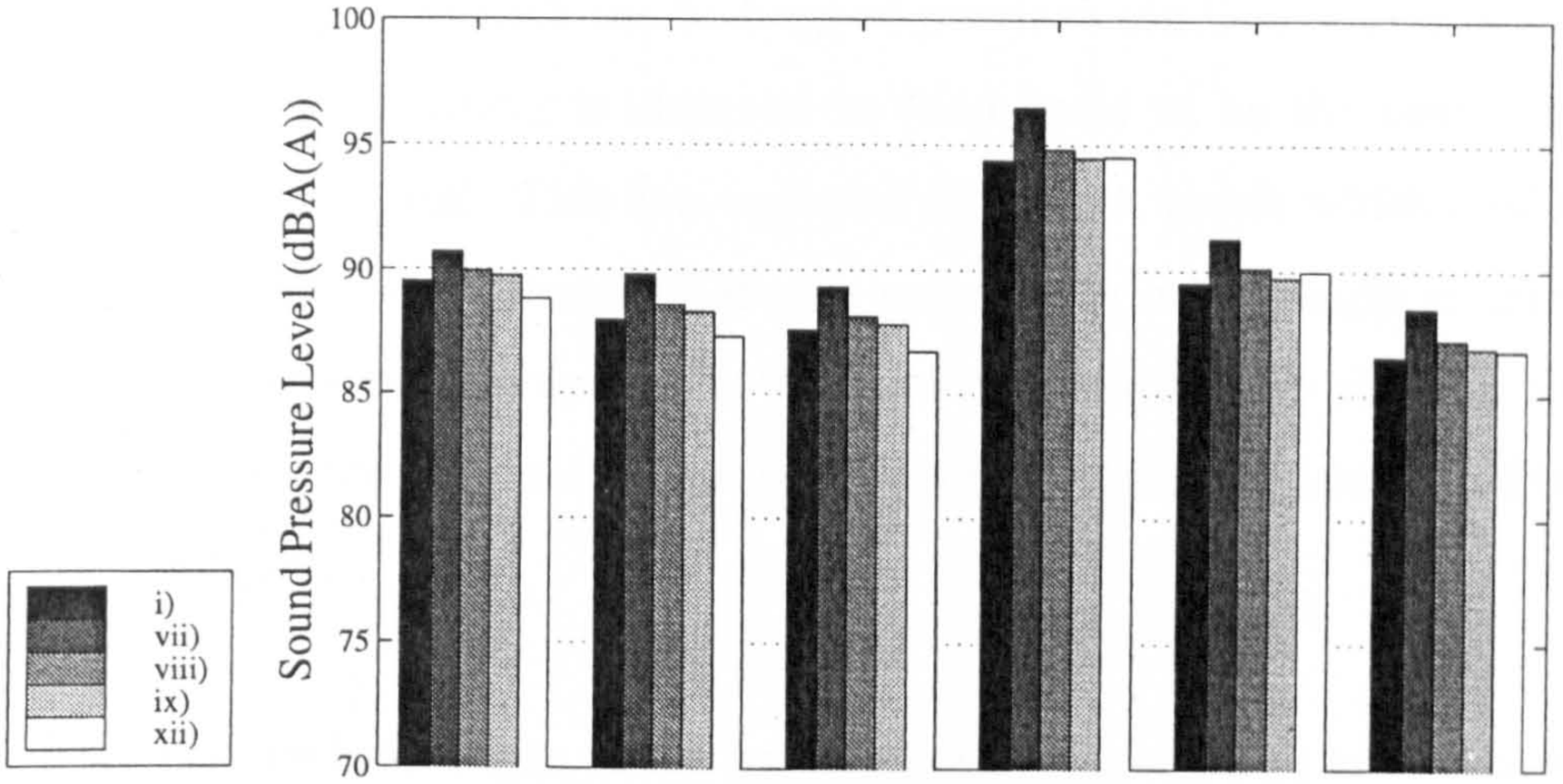

Receiver Position	20, 1.5	40, 1.5	80, 1.5	20, 4.5	40, 4.5	80, 4.5
Option i)	89.50	87.96	87.52	94.37	89.47	86.52
Option vii)	90.69	89.79	89.27	96.49	91.28	88.49
Option viii)	89.94	88.56	88.10	94.81	90.14	87.19
Option ix)	89.72	88.29	87.77	94.48	89.69	86.88
Option xii)	88.79	87.25	86.68	94.51	89.96	86.76

Figure 4.8: Predicted sound pressure levels, dB(A), using the BEM for different parallel barrier arrangements; i) Single 2 m barrier; vii) 2 m parallel barriers, far barrier tilted at 5°; viii) 2 m parallel barriers, far barrier tilted at 10°; ix) 2 m parallel barriers, far barrier tilted at 15°; xii) 2m parallel barriers, 1.25 m absorptive median barrier.

contributions from the other source positions/orientations are relatively constant, thereby reducing the decay of the combined level.

4.4 Conclusions

The introduction of a reflective screen on the farside of the carriageway degrades the performance of a plane rigid screen by approximately 3 dB(A) (4 dB(A) for a line source) depending on the composition of the reflective surface of the far screen. The introduction of absorptive treatment reduces the degradation loss by minimising reflections in the far barrier. For the current tests, the reduction is approximately 3.5 dB(A) for the line source case. The results indicate that inclination of the barrier

at angles of $\geq 10°$ are sufficient to minimise diffraction of reflected sound over the front barrier. This is in line with the findings of previous studies. The introduction of an absorptive median barrier is observed in these tests to be the best means of restoring screening potential. This is a new and significant result which could have potential applications. These barriers absorb waves with a low angle of incidence which would otherwise be reflected in the far barrier, in addition to absorbing direct and reflected waves from the far side source. The effect of the additional diffracting edge is also beneficial.

Provided that the limitations of the boundary element method are realised, additional features can, if required, be introduced to account for the presence/effect of vehicle bodies (e.g. see [123, 121]) and geometrical imperfections in the barriers and ground surface. In such a manner, the boundary element method is an effective tool for modelling parallel barriers, particularly if the modified procedure of Section 2.2 is used. However, full scale testing is crucial to confirm the theoretical predictions.

The development of a straightforward approximation has allowed the transformation of line source results to those of a point source. Whilst this adjustment procedure does not provide results detailing the absolute performance of the barrier, combining data from stages of this adjustment with data from the original boundary element method allows the insertion loss of such an arrangement using multiple point sources to be calculated.

Whilst not necessarily producing exact results, the method can be used as a basis for generating predictions as to the relative performance of parallel barrier arrangements in both point and line source cases.

Chapter 5

Multiple-edge Noise Barrier Profiles

Previous work has reported the benefits of including additional diffracting edges to enhance the screening potential provided by a single plane barrier. One such design in particular, developed by Crombie, Watts et al [23, 25, 26, 118, 121], is based around multiple edges on a single foundation, the form of the device when viewed along the axis of the barrier being that of a trident although the panels are unconnected (see Figures 5.1 and 5.2). Full scale tests of this design on a major UK motorway have been carried out [121] in which the panels were mounted asymmetrically on the side of the barrier facing away from the traffic. The results obtained suggested that the performance of the configuration is strongly influenced by the geometry of the installation site.

In this chapter a study is presented, using the boundary element method of Chapter 2, whereby the arrangement of the panels has been varied through the inclusion of closing panels and absorptive treatment to establish an optimum geometry, the performance of which can be expected, for reasons to be explained, to be less dependant on site conditions. An important consideration was that the design should be practical with minimal manufacturing complications.

5.1 A Review of Previous Work

Studies of multiple barrier arrangements have shown that the use of double barriers, i.e. two barriers between the source and receiver, offers increased screening performance over a single plane screen. It appears that the insertion loss decreases with reducing barrier separation. This seems reasonable since the additional insertion loss due to the second screen should reduce approximately to zero with zero separation.

Hayek [49, 50] performed a mathematical analysis and 1:5 scale model experiments of such arrangements. At full scale, the height of the two barriers was 4.5 m and separations of 0.15, 0.30 and 0.60 m were tested. A line source, formed by a series of moving loudspeakers, was positioned at 18.0 m from one of the barriers and at a height of either 0.5 or 2.4 m above a rigid ground surface (to represent a car and truck noise source respectively). Receiver positions were selected behind the second barrier at distances of 18.0, 36.0, 72.0 and 102.0 m, and heights of 0.376, 1.5, 3.0 and 6.0 m. In some of the tests, either one or both of the barrier faces oriented towards the source were covered with sound absorptive material. Measured and calculated insertion losses showed an improvement of 7 – 9 dB(A) over a single barrier of the same height.

Crombie et al [27] performed boundary element simulations of double barrier arrangements. The basic cross-section involved a 3 m high barrier 15 m away from a source in rigid ground. Further barriers were then positioned in between such that the line of sight between the source and the rear barrier grazed their upper edge(s). The closest barrier was at 3 m. Receiver positions were at 20, 50 and 80 m behind the far barrier. An increase of approximately 2 dB(A) in the average insertion loss was observed for different double barrier separations in comparison to a single 3 m barrier at the same position as the front barrier. Compared to a 3 m single barrier at 15 m, the most effective double barrier arrangement was with the front barrier 3 m from the source, the insertion losses being 14.4 and 19.2 dB(A) respectively.

Comparisons were also made between double barriers of the same height and variable separation, and single barriers of varying height. The effect of varying source height was also studied, although the barrier heights were determined assuming that the source was still in the ground. The results obtained indicated that for positive source heights, the additional barrier had little effect until its height was sufficient to graze the line of sight between the source and rear barrier. Scale model experiments on arrangements from [27] were conducted by Crombie and Hothersall [24]. Good agreement was observed between boundary element predictions and experimental results.

Full scale measurements of double barrier arrangements have been reported [23, 118] which were conducted using the experimental test facility, procedure, and source and receiver positions described in Section 3.2.1. Three configurations were tested and compared to a plane 2 m screen, namely 2 m high barriers with a separation of either 4 or 8 m, and a mixed height combination with 8 m separation. In the latter case the front barrier (that nearest the source) was 1.25 m high, the rear barrier 2.0 m. On average over the 6 receivers, the mixed height combination provided marginally lower insertion losses than the plane screen. The other arrangements provided on average at least 3 dB(A) additional insertion loss, although the improvement generated through increasing the separation was only of the order of 0.5 dB(A).

A comprehensive study was undertaken by Crombie [23] (also reported in [25, 26]) in which the double barrier principle was extended to multiple diffracting edges upon a single foundation. Such a device was proposed as being a means of improving the performance of a plane screen with no increase in the overall height and without the ground requirements of double barriers. The tests were performed using the standard 2-D boundary element method (Section 2.1) and were based around a 3 m vertical rigid screen on rigid ground. The source position was 15 m from the barrier and in the ground. Receivers were located at 20, 50 and 100 m behind the barrier, at heights of 0, 1.5 and 3.0 m. In the majority of cases the top edge of the additional

panel was at the same height as the top of the main barrier. For this geometry, the addition of a 1 m panel 0.5 m from the source side of the barrier improved the average insertion loss by 1.9 dB(A). This was equivalent to the introduction of a second 3 m high barrier at a distance of 0.5 m from the basic plane screen on the other side of the screen to the source. The insertion loss was degraded when the panel was mounted on the receiver side of the barrier, since sound diffracted between the panel and upright was directed towards the receivers rather than the source. It was observed from the results that the panels should be of sufficient depth to prevent significant diffraction around the lower edges. However, with the panel mounted on the source side at a separation of 0.5 m, increasing the depth from 1.0 to 1.5 m caused a reduction in insertion loss, suggesting that destructive interference effects between rays passing over the top of the device and rays diffracting around the bottom edges of the panels contribute to the effectiveness of the design.

The introduction of additional edges further improved the predicted average insertion losses, although with diminishing returns. The introduction of absorptive treatment was observed to have little effect. Connecting the panels to the upright with a horizontal plate, thereby preventing propagation through the bottom of the gaps between the surfaces reduced the performance. This can be attributed to the reduction in diffraction effects already discussed and the possibility of increased levels at the top of the barrier due to reflection of the diffracted waves in the bottom panel. Lining the inner surfaces with absorbing treatment helped to offset these increased levels.

1:20 scale model experiments on a barrier with twin diffracting edges reported in the same work [23] gave very good agreement with boundary element predictions.

Also reported in [23, 118] are full scale simulations of 4 symmetrical multiple-edge profiles, using the test facility, procedure, and source and receiver positions described in Section 3.2.1. The barriers were 2 m high with either 0.5 or 1.0 m deep panels and separations of 0.5 m (and also 1.0 m for the 0.5 m panel arrangement). Three of the configurations used a main upright where the top 0.5 m was absorptive. Similar average insertion losses were obtained for all configurations, between 2.4 and

2.7 dB(A). The most effective design was the part absorptive upright with 0.5 m panels and 1.0 m separation. However, the performance was not as good as that of the 2 m high double barrier configurations. The insertion losses determined from the full scale experiments were in good agreement with the BEM predictions for the receivers at (40, 1.5), (80, 1.5) and (80, 4.5). Otherwise the theoretical simulations underestimated the performance of the multiple edge designs. It was suggested that some of the error may have been a result of inaccurate representation of the grassland on the far side of the barrier in the boundary element method.

The original concept of the design, i.e. multiple diffracting edges on a single foundation has been jointly patented by the University of Bradford and the Transport Research Laboratory. Following the full-scale trials of the multiple-edge configuration, Watts [121] reported upon full-scale in-situ tests of the design alongside the M25 motorway in the UK. An engineered prototype was used, known as the RTB profile (see Figures 5.1 and 5.2) developed with the assistance of Radian Engineering. The trials were conducted at three different sites chosen to represent a range of different conditions.

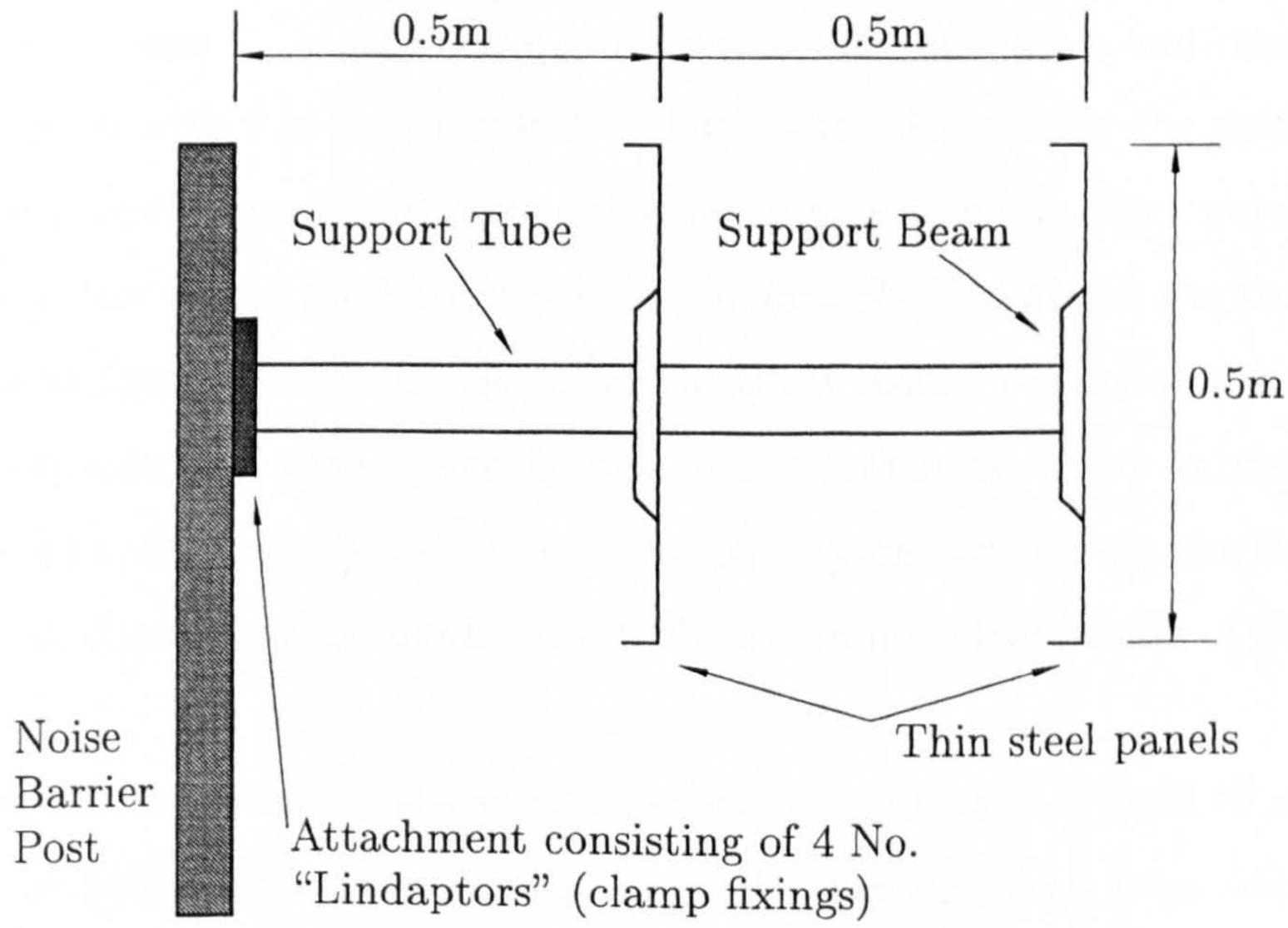

Figure 5.1: Cross-section through asymmetrical RTB profile.

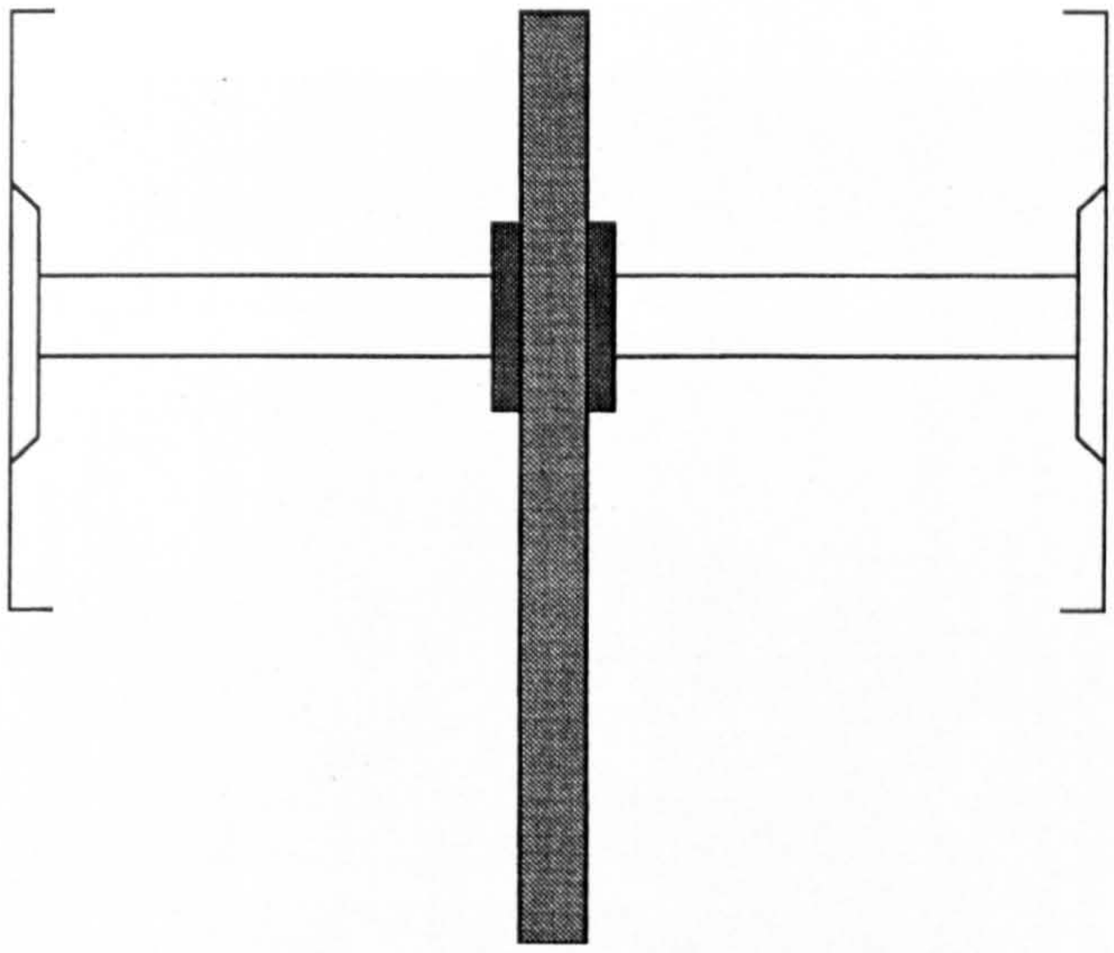

Figure 5.2: Cross-Section through symmetrical RTB profile.

Site A was chosen as representative of an essentially flat site, with the 8 lane motorway on a slight embankment approximately 1.7 m above the surrounding ground. Barriers of height 2 m were installed on both sides of the carriageway at the edge of the hard shoulder. At site B, the motorway was also 8 lanes wide and constructed on a 5 m high embankment. The 3 m high barriers were erected on both sides of the carriageway adjacent to the hard shoulder. Figure 5.3 shows the asymmetric profile erected at site B. At site C the motorway was 6 lanes wide and running in a 4 m deep cutting with 2 m high barriers on both sides. Separating the cutting from the outlying ground were 2.5 m embankments on which the barriers were erected. Consequently, the top of the barrier was approximately 7 m above the road and 4 m above the outlying ground. In each case, the RTB profile was installed over a 100 m length of barrier. At sites A and B, due to the proximity of the barriers to the carriageway, the additional panels were mounted asymmetrically on the far side of the barrier, as shown in Figure 5.1. At site C the symmetrical profile of Figure 5.2 was used.

Measurements were taken at a series of receiver positions at 15 and 25 m behind the barrier, at heights of 1.5 and 4.0 m. At site B, measurements were additionally taken at the most distant receiver at a height of 6 m. Measurements at site C were restricted to a single receiver position 18 m behind the barrier at a height of 4 m.

Figure 5.3: Asymmetric multiple-edge profile as erected at site B on the M25 motorway

Levels were recorded over 10 minutes intervals both before and after the installation of the profile and normalized for zero wind speed (using the procedure described in Section 3.2.1). Results were presented in terms of L_{Aeq} and L_{10}, i.e. the average A-weighted level over each 10 minute period and the level exceeded for 10% of the time over the measurement period.

The best improvement in screening performance over the existing barriers was observed at site A, being 1.5 – 3.8 dB(A) in terms of L_{10}. At site B, a maximum reduction of 1.9 dB(A) was observed at the highest, most distant receiver, and a small increase in level was observed at the 1.5 m height receiver at 15 m. At site C, the improvement in L_{10} at the single receiver position was 1.4 dB(A).

The results indicated that the performance of the RTB profile is influenced by site conditions. It was observed that the improvement in screening decreased as the efficiency of the existing barrier increased. For the plane screen, the greatest

screening occurred when the source and receiver were well below the top of the barrier. It was considered that in such cases the introduction of the profile may result in diffracted sound reaching the receiver which would otherwise not do so, as a result of sound leakage between the panels. It was suggested that a means of reducing this might be either to close the bottom of the device or treat the panels with sound absorbent material.

5.2 Optimisation of an asymmetric multiple-edge profile

Further to the conclusions of Watts [121], an attempt has been made to identify an optimum design for the asymmetric RTB profile. This has been done using the 2-D boundary element method outlined in Chapter 2. However, due to circumstances reported in Section 2.1, the simulations have been restricted to modelling barriers on flat level ground rather than on the top of an embankment.

For conformity, the tests have been conducted using the site geometry reported for previous theoretical and experimental tests (Chapters 3 and 4), namely receiver positions at 20, 40 and 80 m behind the barrier and at heights of 1.5 and 4.5 m, with a 10 m wide road surface, and grassland beyond the barrier. However, only a single source position has been used - that at 7.5 m from the barrier, at a height of 0.5 m. Cross-sections with a barrier on both sides of the carriageway have not been considered. In all of the cases, the additional panels have been mounted asymmetrically onto a plane screen, on the opposite side of the barrier to the source as at sites A and B in [121]. The Delany and Bazley model [31] has been used to describe the impedance of the various barrier and ground surfaces, with the following values assigned: 1E20 Nsm^{-4} for the reflective barrier surfaces and the asphalt road surface, and 250,000 Nsm^{-4} for the grassland on the receiver side which is within the range proposed in [39].

The following options have been considered and are illustrated in their simplest

form in Figure 5.4; (i) the standard multiple-edge design as proposed by Crombie et al [23, 25, 26], using two additional panels; (ii) tilting the diffracting edges or introducing distortions into the panels; introducing a horizontal or inclined baseplate to form (iii) a fully closed or (iv) partially open profile.

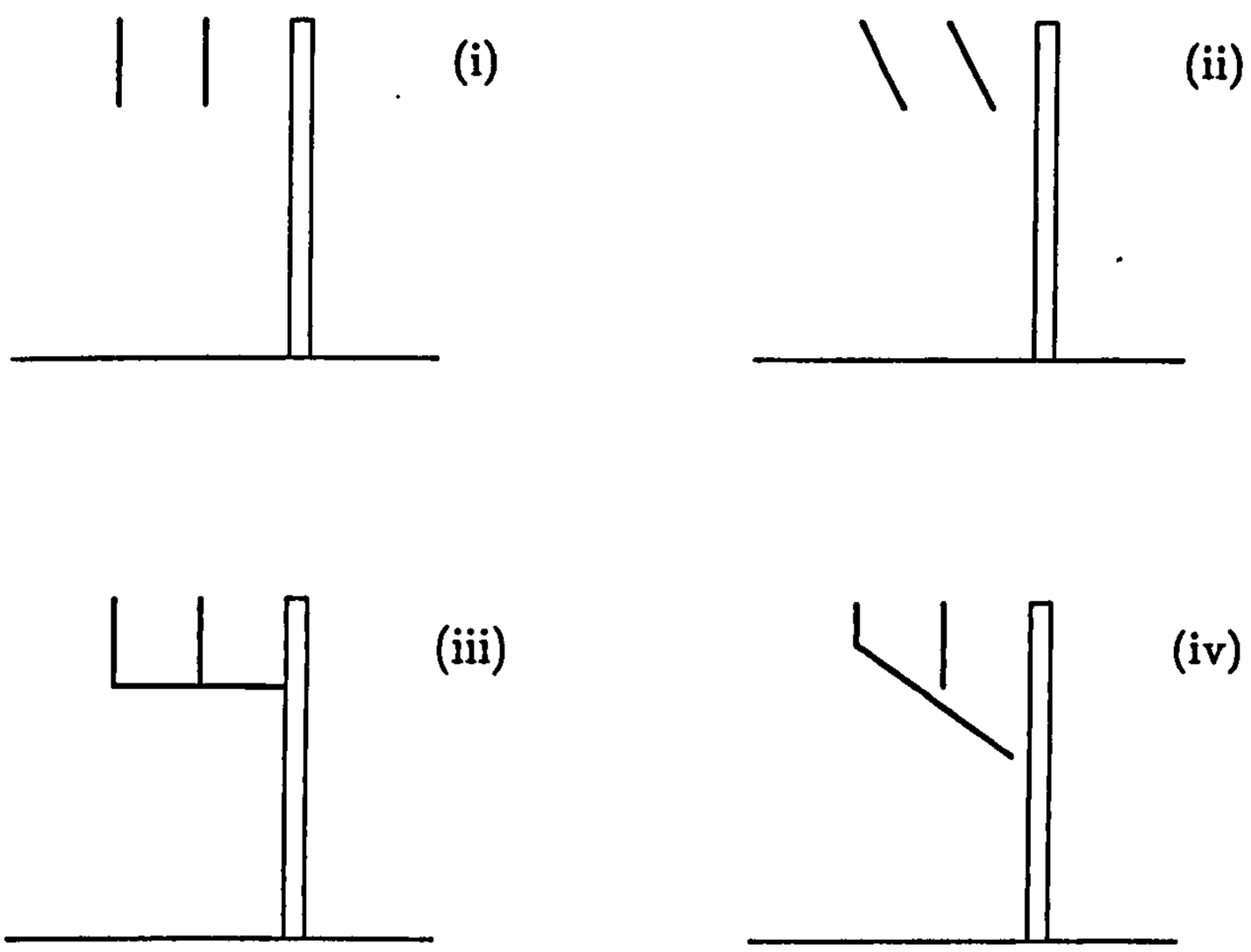

Figure 5.4: Examples of the different types of cross-section tested as part of the optimisation

In some of the tests, absorptive treatment has been applied to the additional panels and the upper sections of the main barrier. In the case of the full-scale, physical barrier arrangements, it was envisaged that this treatment would be applied in the form of a spray-on sound absorptive material. This has been modelled in the BEM simulations, using the Delany and Bazley equations, by a rigid backed porous layer having a flow resistivity of $\sigma = 160,000$ Nsm^{-4} and depth, $d = 0.018$ m, resulting in an absorption coefficient of $\alpha = 0.5$. These values of σ and d were selected as giving the best approximation to the octave band absorption coefficients of one such commercially available material.

All of the different designs have been based around a 2 m high reflective barrier

(in keeping with the full scale tests of [118] and the in-situ tests [121] at sites A and C) and two additional diffracting edges. The dimensions of the basic profile are presented in Figure 5.5a. The additional panels are 0.5 m deep and 0.012 m thick (from [118]), with the separation between adjacent diffracting edges being 0.5 m. Unless specified otherwise, this separation has been maintained for the different configurations.

The results will be presented in terms of the improvement in insertion loss relative to the 2 m high rigid plane screen, averaged over the six receiver positions. Due to computational restrictions, calculations have been restricted to third-octave band centre frequencies between 63 Hz and 3.15 kHz, using the A-weighted traffic noise spectrum presented in Figure 3.22 of Chapter 3.

5.2.1 The effect of simple variations on the basic profile

For the basic asymmetric profile, (a) in Figure 5.5, an average improvement in insertion loss of 0.97 dB(A) has been observed relative to the rigid plane screen. This is slightly less than predicted by Watts et al [118] where the improvement was 1.4 dB(A), although this was for the case of a symmetrical multiple-edge configuration. It is also noted that this earlier result is an average of predictions made for two source positions (5.5 and 7.8 m), and there is a slight change in the definition of the grassland on the receiver side of the barrier (depth, $d = \infty$ here, $d = 0.1$ m in [118], $\sigma = 250,000 \text{Nsm}^{-4}$ in both studies).

The first tests involved simple changes to the basic profile. These were the introduction of absorptive treatment onto the panel faces (and also the upper 0.5 m of the main barrier), and closing the gaps at the bottom of the panels with a rigid horizontal baseplate, as shown by designs (b) and (c) respectively in Figure 5.5. Arrangement (d) is a combination of these two modifications, with absorptive treatment also applied to the baseplate. The insertion losses at the individual receiver positions are summarised in Figure 5.6.

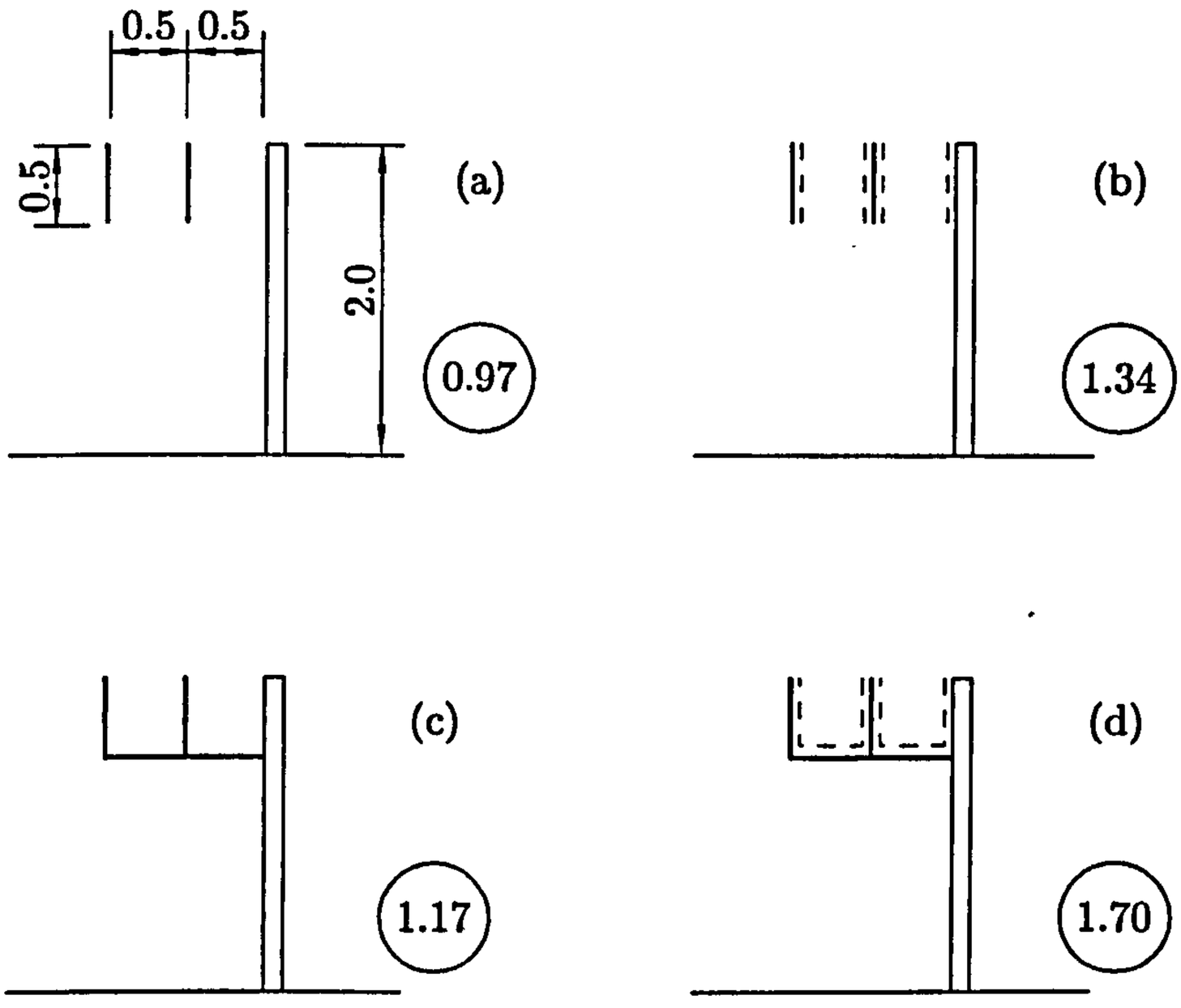

Figure 5.5: Relative mean insertion losses, dB(A), for simple open and closed asymmetric multiple-edge barrier configurations. Dashed lines denote absorptive surfaces.

As might be expected, all three designs (b) – (d) perform more effectively on average than the basic multiple-edge profile. The introduction of absorptive treatment immediately increases the average screening by approximately 0.4 dB(A), with the effect being most significant at the 1.5 m height receivers. This would suggest a reduction in sound leakage between the panels, although a significant degree of diffraction is maintained at the bottom edges. It is observed, comparing arrangements (b) and (c), that treating the profile with sound absorptive material is marginally more beneficial on average than adding the rigid baseplate. Study of the improvements at the individual receivers for these configurations (Figure 5.6) reveals the closed device, (c), to be more effective at the closest low receiver, but less effective elsewhere. The largest differences are observed at the 4.5 m receivers. This would suggest leakage to be problematic at low heights relatively close to the barrier, whilst diffraction from the bottom edges of the panels contributes to improving insertion losses at

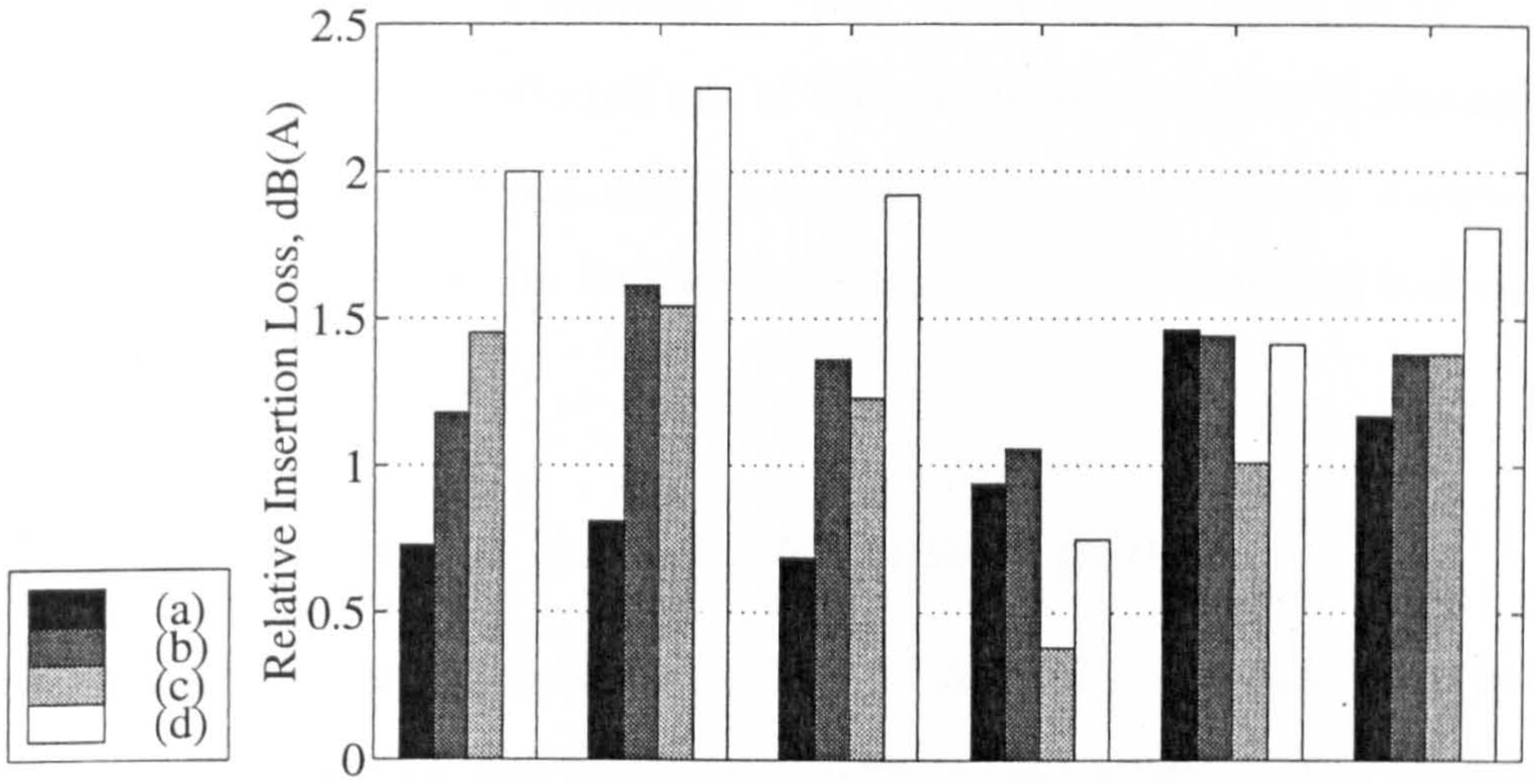

Receiver Position	-20.0, 1.5	-40.0, 1.5	-80.0, 1.5	-20.0, 4.5	-40.0, 4.5	-80.0, 4.5	Mean
Profile type (a)	0.73	0.81	0.69	0.94	1.46	1.17	0.97
Profile type (b)	1.18	1.61	1.36	1.06	1.44	1.38	1.34
Profile type (c)	1.45	1.54	1.23	0.38	1.01	1.38	1.17
Profile type (d)	2.00	2.28	1.92	0.75	1.41	1.81	1.70

Figure 5.6: Relative insertion losses, dB(A), for simple open and closed asymmetric multiple-edge barrier configurations.

greater distances. Additionally, sound diffracted between the panels is being reflected out of the closed device. Incorporating both the horizontal baseplate and absorbent treatment onto all internal surfaces results in the most effective design, providing on average an additional 0.7 dB(A) insertion loss relative to the reference configuration. The insertion loss predicted at the lowest receiver positions is generally increased by at least 0.5 dB(A), although the levels at the high 20 and 40m receivers are still higher than for the basic profile, (a).

However design (d) is, as it stands, an impractical solution, since the 'channels' formed by the additional panels/base would accumulate debris, whilst the sealed base prevents drainage. This is turn might lead in time to a reduction in the screening performance of the multiple-edge profile. The former problem might be treated, without damaging acoustic performance, by the use of a mesh cover over the top of the barrier. Were the base to be both inclined and open at some point (as for

example with the Calmzone device (Chapter 3) which includes drainage holes), the drainage problem would be overcome. This latter modification might reduce the likelihood of sound being reflected out of the profile, particularly if absorptive treatment is applied to the internal surfaces of the device. The tests on designs (b) – (d) suggest that performance can be significantly affected by reducing leakage between the panels.

5.2.2 The effect of inclined/cranked panels

Closing the multiple-edge profile at the base of the additional panels has been shown to be effective providing absorptive treatment is also applied. It is considered that an alternative means of reducing sound leakage, whilst maintaining diffraction at the bottom edges of the panels, would be to tilt the panels such that the positions of the upper diffracting edges remain unchanged, but the separation of the bottom edges is reduced. The designs tested are shown in Figure 5.7: namely (e), both panels tilted at 26.5°; (f) the same design with absorptive treatment on both panels; (g) the first panel (that nearest the barrier) tilted at 26.5°, the second at 45°, with absorptive treatment on the receiver-facing surfaces; (h), the first panel tilted at 45°, the second at 56° with absorptive treatment on the receiver-facing surfaces; (i), the first panel tilted at 45°, the second at 56°, with absorptive treatment on the source-facing surfaces;

Two variations on the tilted panels have also been considered and are shown as designs (j) and (k) in Figure 5.7. These both use cranked panels, the upper section being inclined at 26°, the lower at 64°. The lower sections are of sufficient length to reduce the separations at the bottom edges of the panels to 0.125 m as shown in the figure. Type (j) has absorptive treatment applied to the top 0.5 m of the main barrier and those surfaces tilted at 26°, whilst design (k) includes treatment on all of the tilted surfaces. The results of all the tests are summarised in Figure 5.8.

All of the designs provide some improvement over the basic type (a) profile, on average between 0.3 – 0.7 dB(A). Inclining both panels at 26° provides approximately 0.5 dB(A) improvement, with the most significant change being observed at the low

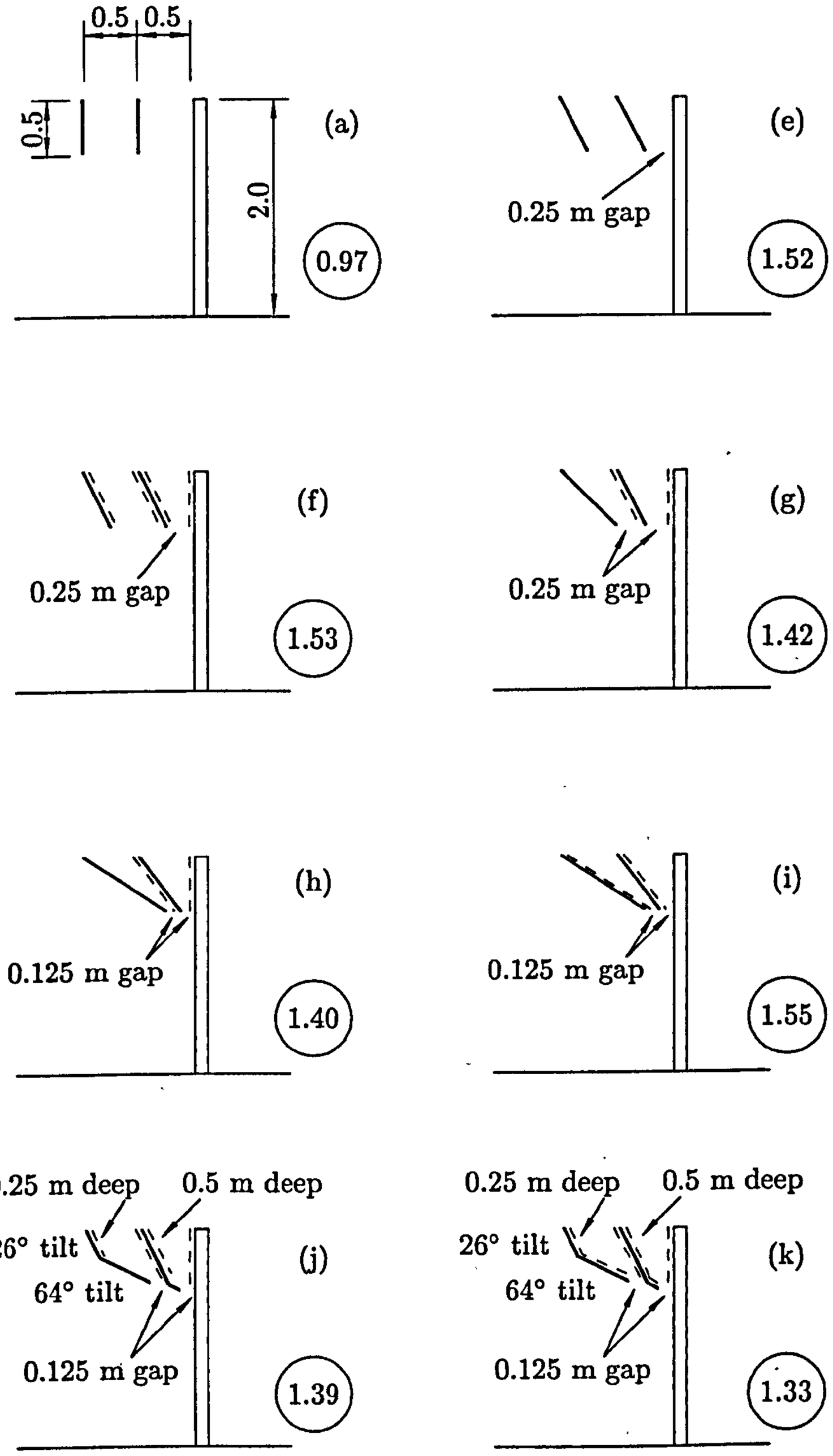

Figure 5.7: Relative mean insertion losses, dB(A), for asymmetric multiple-edge barrier configurations - inclined panels. Dashed lines denote absorptive surfaces.

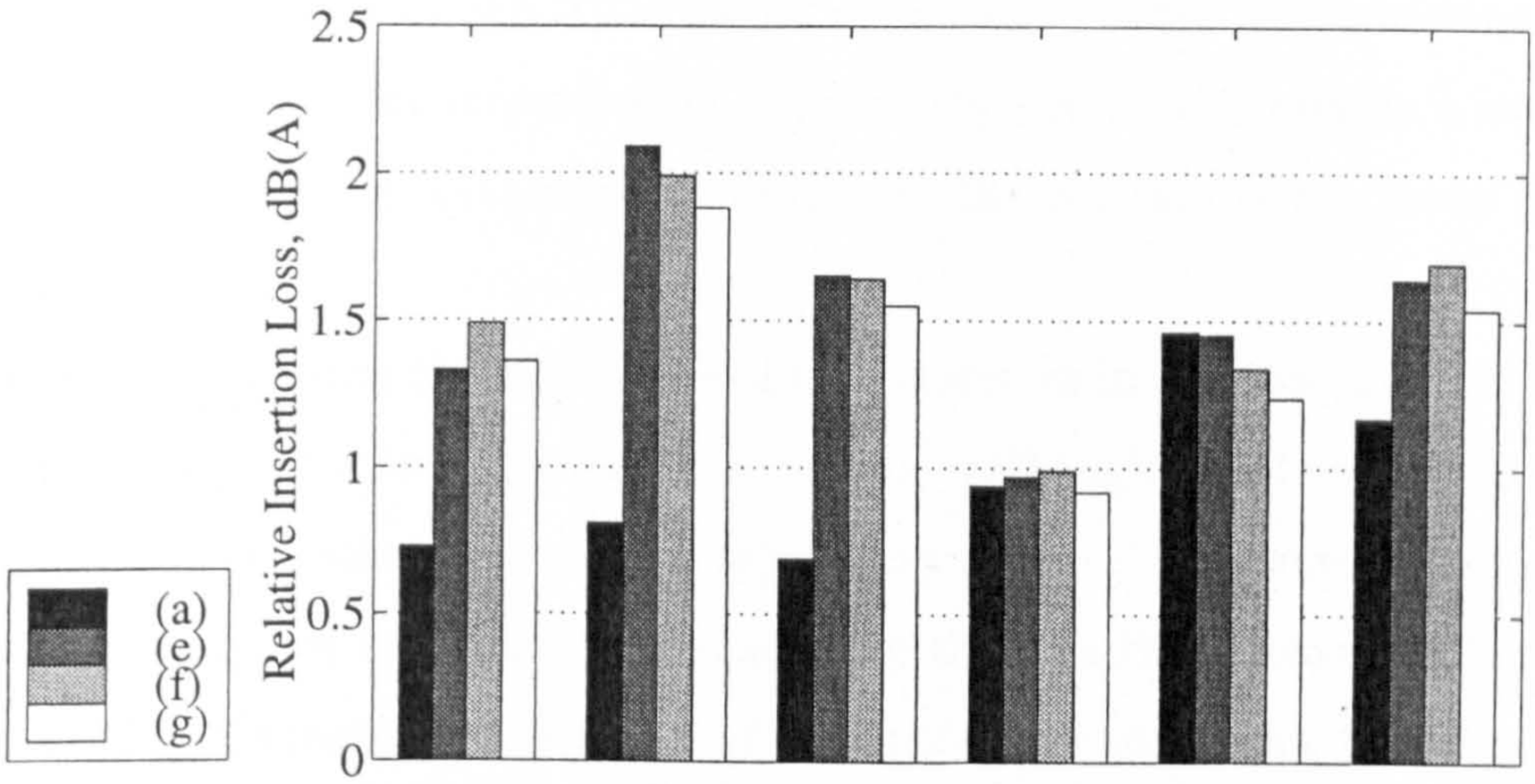

Receiver Position	-20.0, 1.5	-40.0, 1.5	-80.0, 1.5	-20.0, 4.5	-40.0, 4.5	-80.0, 4.5	Mean
Profile type (a)	0.73	0.81	0.69	0.94	1.46	1.17	0.97
Profile type (e)	1.33	2.09	1.65	0.97	1.45	1.64	1.52
Profile type (f)	1.49	1.99	1.64	0.99	1.34	1.70	1.53
Profile type (g)	1.36	1.88	1.55	0.92	1.24	1.54	1.42

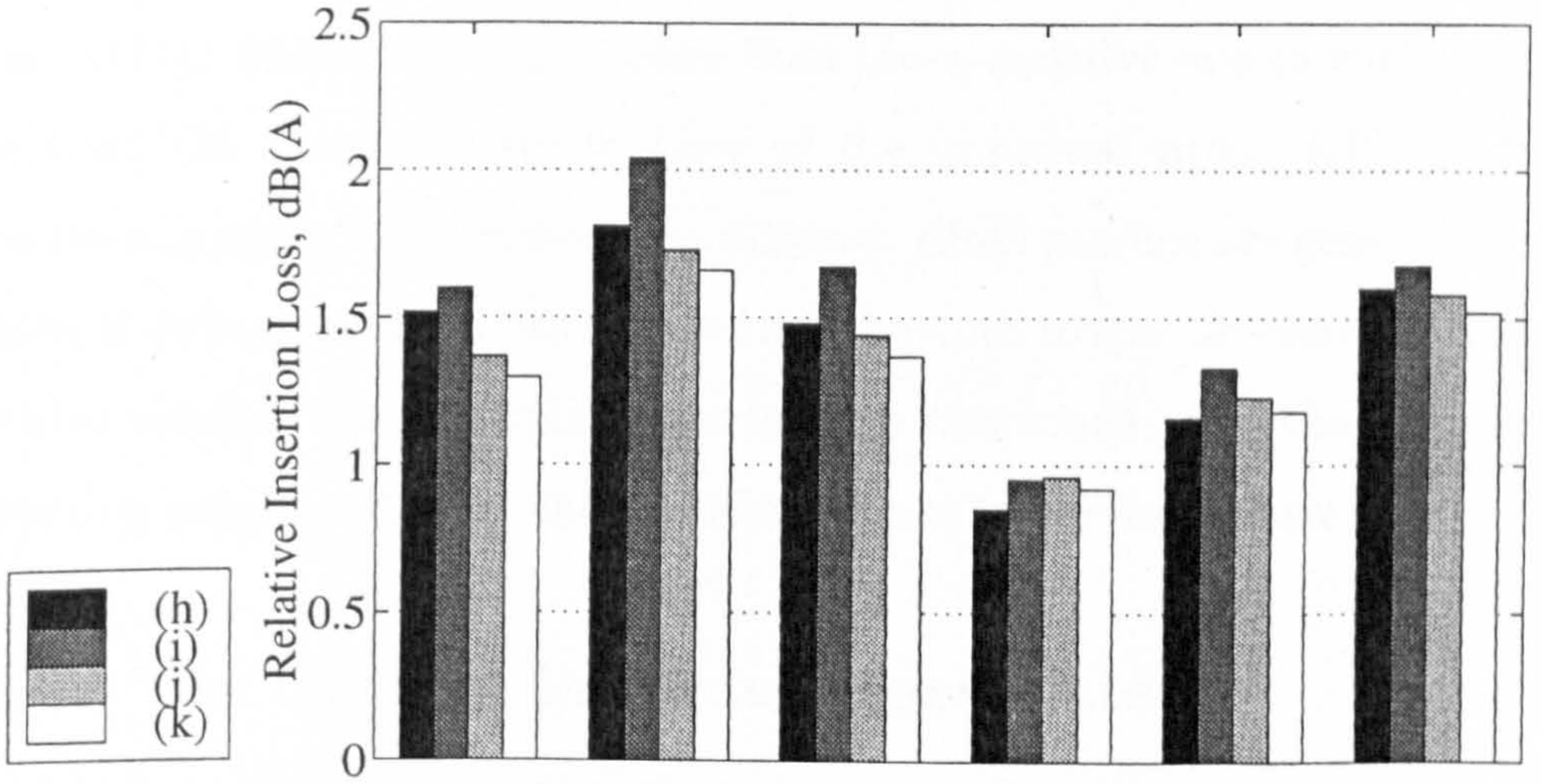

Receiver Position	-20.0, 1.5	-40.0, 1.5	-80.0, 1.5	-20.0, 4.5	-40.0, 4.5	-80.0, 4.5	Mean
Profile type (h)	1.52	1.81	1.48	0.85	1.16	1.60	1.40
Profile type (i)	1.60	2.04	1.67	0.95	1.33	1.68	1.55
Profile type (j)	1.37	1.73	1.44	0.96	1.23	1.58	1.39
Profile type (k)	1.30	1.66	1.37	0.92	1.18	1.52	1.33

Figure 5.8: Relative insertion losses, dB(A), for asymmetric multiple-edge barrier configurations - inclined panels.

receivers, at 40 and 80 m behind the barrier. The addition of absorptive treatment to these panels, as in design (f), does not significantly affect the performance. This would suggest that any improvement in screening potential is largely a result of the tilting action and the corresponding change in the position of the lower diffracting edges.

Further increasing the inclination of the panels, as in designs (g) and (h), causes no significant reduction in average screening, although the two designs produce higher insertion losses than design (e) at the (20.0, 1.5) receiver position. This would suggest that less sound is propagating through the bottom of the multiple-edge profile. Changing the position of the absorptive treatment from the receiver-facing to the source-facing sides of the panels, i.e. changing from design (h) to (i), has a small benefit. The type (i) profile is observed to provide similar insertion loss to design (d). The use of cranked panels in designs (j) and (k) is shown to be less efficient than simply using plane tilted panels.

The results indicate that the benefits of using inclined panels are small, providing lower average relative insertion losses than the absorptive design with the horizontal baseplate, (d) - unfortunate in view of the improved practicality of the design. Variations in noise level between the different tilted profiles are generally very small, making it difficult to attribute changes in behaviour to specific characteristics. Based on these results, the remaining tests will be concerned with the study of vertical diffracting panels, with any modifications made to the baseplates.

5.2.3 The effect of individual base-plates

The type (d) design has so far been shown to be on average the most effective multiple-edge profile. Although the introduction of small holes into the baseplate would permit drainage, also inclining the base will assist this. For example, such a change has been introduced in the development of the Calmzone device from that tested by Iida et al (see Chapter 3). The designs tested in the following section feature the additional diffracting panels with individual inclined baseplates, which

are unattached to the adjoining panels. Configurations (l) to (p) in Figure 5.9 use baseplates on the rear panel which do not extend below the level of the front panel (see detail in Figure 5.9). In all cases, the horizontal separation between the adjacent panel/upright has been fixed at 0.1 m. Baseplate inclinations are given in terms of the inclination to the horizontal. The details of the individual configurations are as follows: type (l), both base panels inclined at 37°; (m), front base panel inclined at $18\frac{1}{2}°$, rear base panel inclined at 37°; (n), front base panel inclined at $18\frac{1}{2}°$, rear base panel inclined at 37°, absorbent treatment on all panels and top section of upright; (o), front base panel inclined at $18\frac{1}{2}°$, rear base panel inclined at 37°, absorbent treatment on front faces of panels; (p), front base panel inclined at $18\frac{1}{2}°$, rear base panel inclined at 37°, absorbent treatment on inner faces of rear "channel". The insertion losses at the individual receiver positions, relative to the the basic type (a) configuration, are presented in Figure 5.10

All five of the profiles of Figure 5.9 give increased screening in comparison to the basic design, type (a), on average between 0.75 – 0.97 dB(A). The improvement relative to type (d) is less significant being in the range 0.02 – 0.24 dB(A). Type (l) is the most effective profile tested, which is unexpected since it is rigid. In comparison to type (d), similar relative insertion losses are observed at the low receivers, the improvements occurring at the 4.5 m height receivers. Reducing the angle of the front baseplate improves the performance relative to type (l) at the low receivers, although the performance at high level is degraded. One possibility is that the angle of the baseplate affects the amount of sound reflected out of the profile, whilst the position of the gaps at the bottom of the profile affects the diffraction of sound propagating through the device.

Designs (n) – (p) investigate how the positioning of the absorptive material on the vertical faces affects the behaviour of the profile. In all three cases, screening is reduced relative to the rigid equivalent, design (m), by approximately 0.14 dB(A), although the position of the absorptive treatment appears relatively unimportant.

Overall, the results suggest that decreasing the angle of tilt below 37° has a negative effect. Additionally, following the introduction of the inclined baseplates,

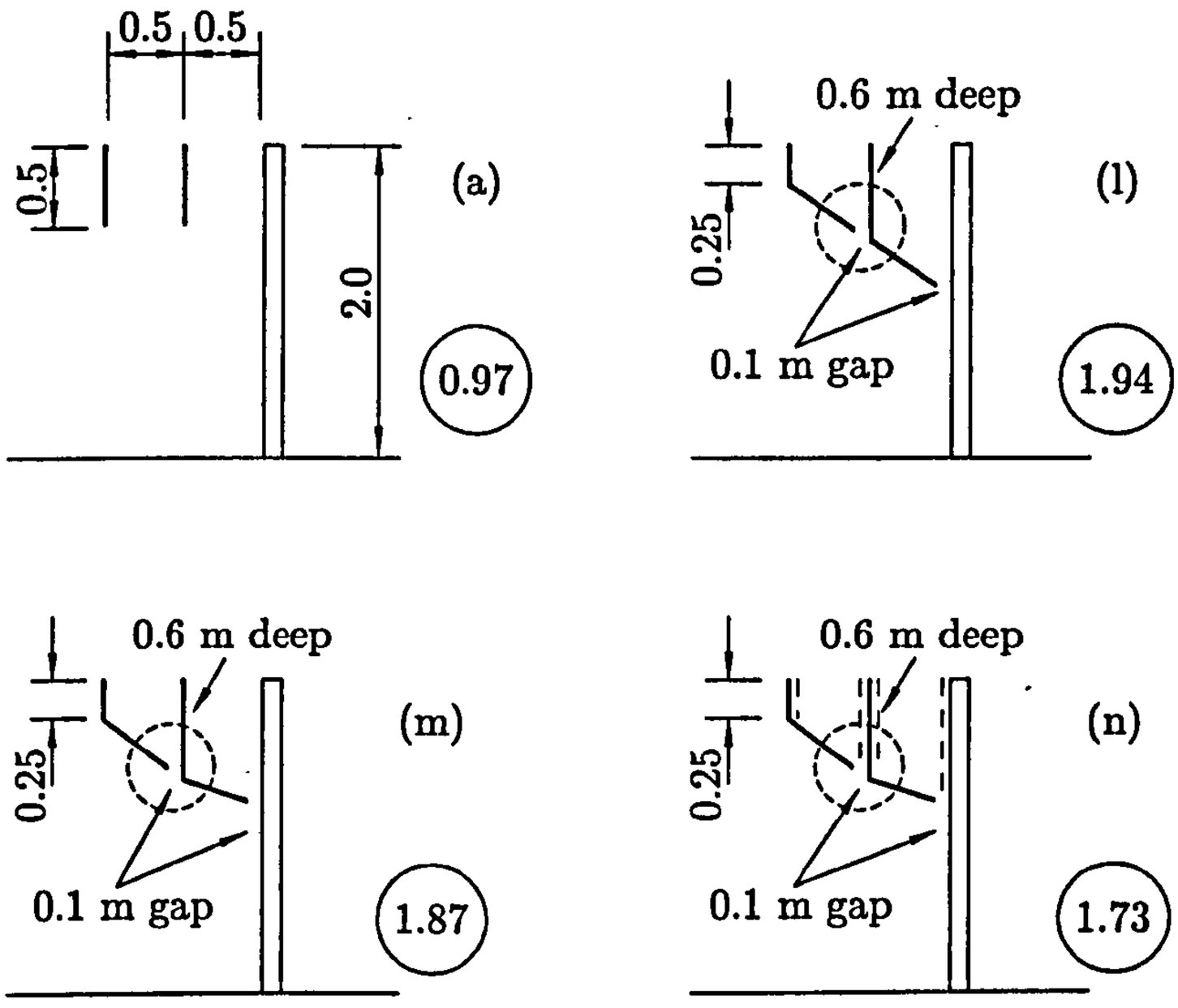

Figure 5.9: Relative mean insertion losses, dB(A), for asymmetric multiple-edge barrier configurations - distorted panels. Dashed lines denote absorptive surfaces. Basepanels inclined at 37° or $18\frac{1}{2}°$ from the horizontal.

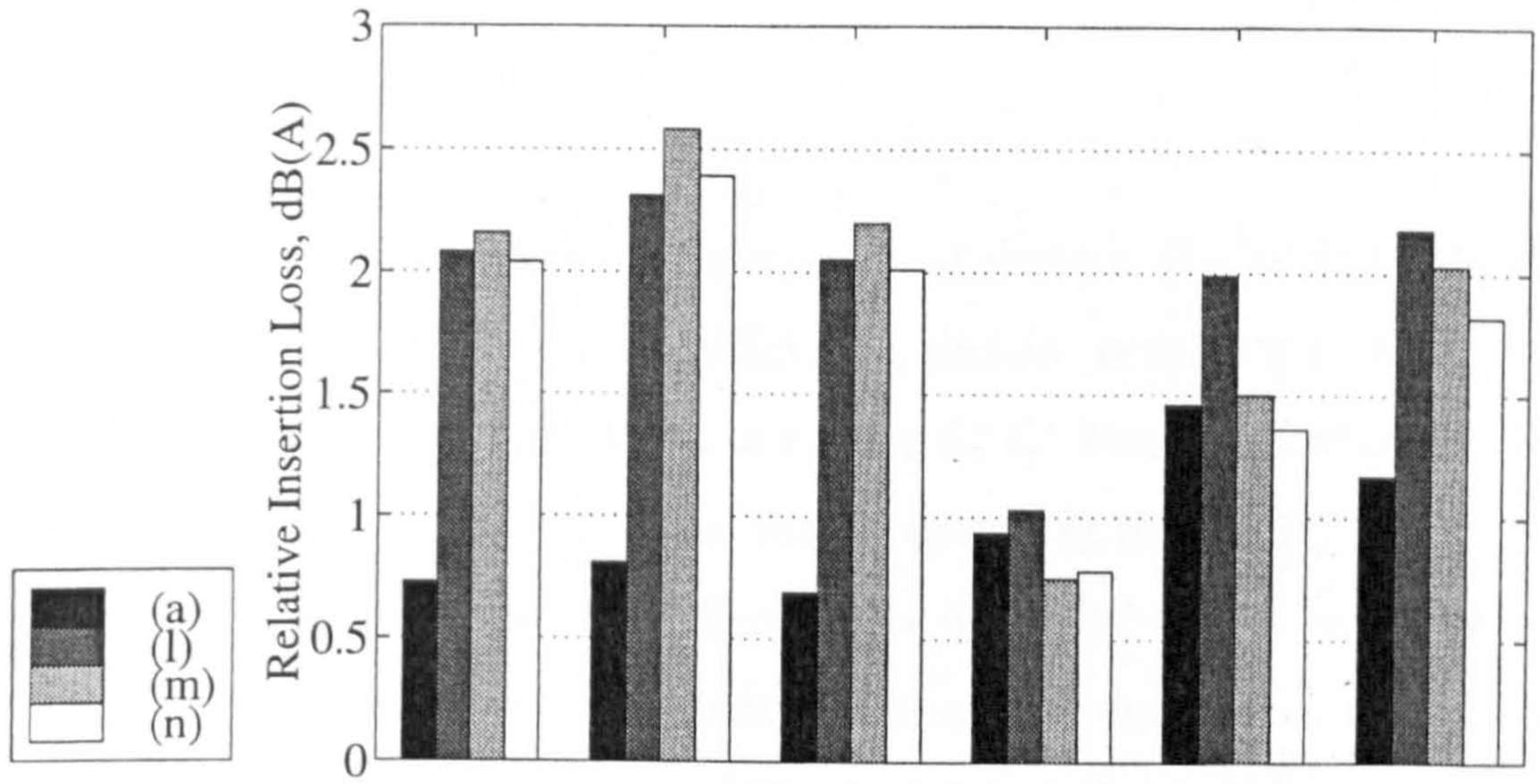

Receiver Position	-20.0, 1.5	-40.0, 1.5	-80.0, 1.5	-20.0, 4.5	-40.0, 4.5	-80.0, 4.5	Mean
Profile type (a)	0.73	0.81	0.69	0.94	1.46	1.17	0.97
Profile type (l)	2.08	2.31	2.05	1.03	1.99	2.18	1.94
Profile type (m)	2.16	2.58	2.20	0.75	1.50	2.03	1.87
Profile type (n)	2.04	2.39	2.01	0.78	1.36	1.82	1.73

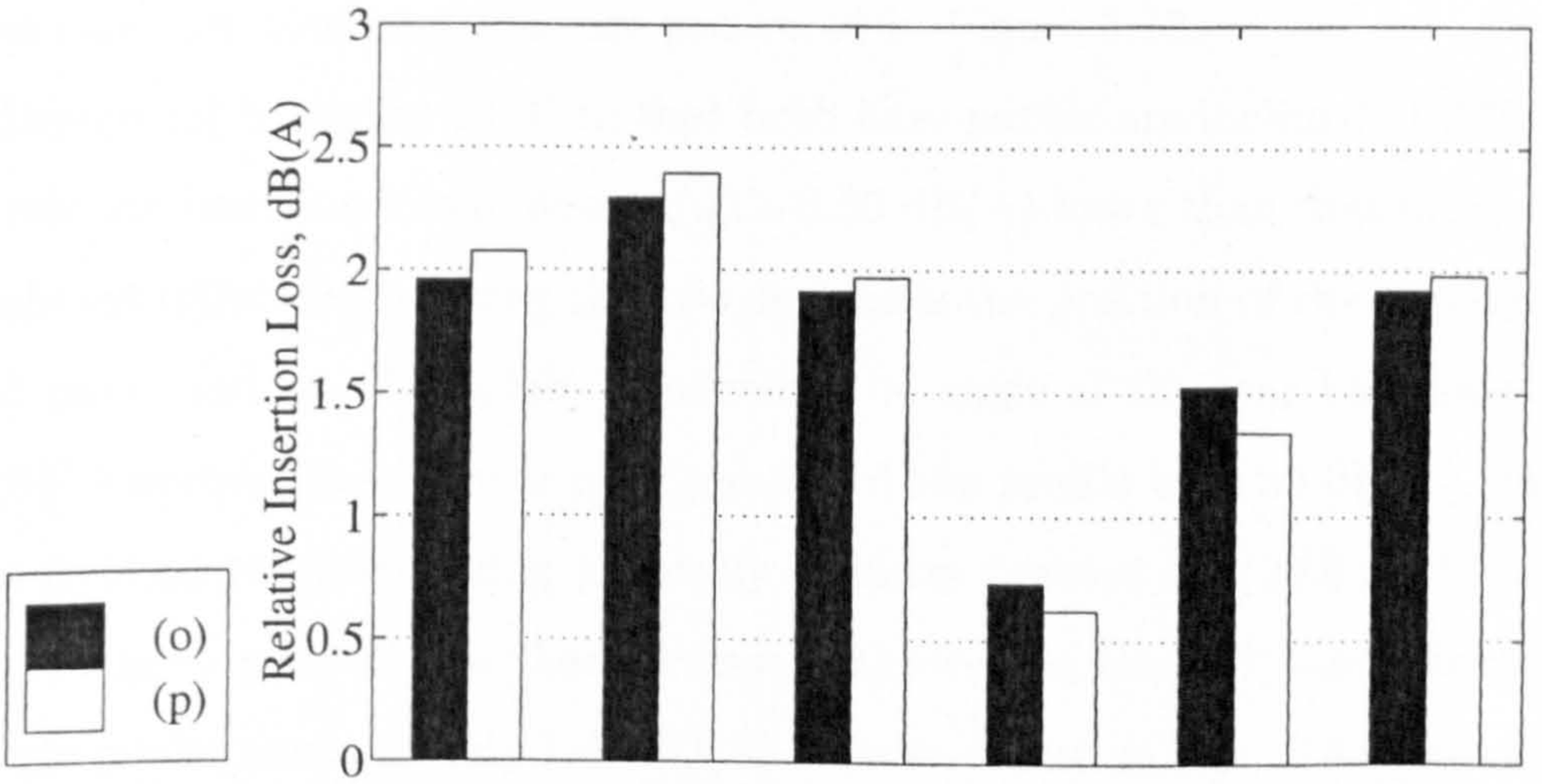

Receiver Position	-20.0, 1.5	-40.0, 1.5	-80.0, 1.5	-20.0, 4.5	-40.0, 4.5	-80.0, 4.5	Mean
Profile type (o)	1.96	2.29	1.91	0.73	1.53	1.92	1.72
Profile type (p)	2.07	2.39	1.97	0.62	1.34	1.98	1.73

Figure 5.10: Relative insertion losses, dB(A), for asymmetric multiple-edge barrier configurations - distorted panels.

performance has been observed to be degraded if absorptive treatment is applied. Consequently, the remaining test configurations will be largely restricted to construction from rigid surfaces.

An alternative to the basic configurations of designs (l)-(p) is to terminate the rear base panel beneath the front diffracting panels, resulting in a gap which lies more in the vertical plane (see detail in Figure 5.11). Examples of such a design are presented in Figure 5.11 where, with the exception of design (t), the gap between the front and rear base panels is fixed at a depth of 0.125 m. The horizontal separation between the front baseplate and the main upright is maintained, as in the previous set of tests, at 0.1 m. The details of the individual profiles are as follows: (q), both baseplates inclined at 37°; (r), front baseplate inclined at $18\frac{1}{2}°$, rear baseplate inclined at 37°; (s), front baseplate horizontal, rear baseplate inclined at 37°. Configuration (t) features baseplates inclined at 37° but with a gap between the panels of depth 0.38 m. This is achieved by reducing the depth of the first additional diffracting panel from 0.5 to 0.25 m. The relative insertion losses for these cases are configurations are presented in Figure 5.12.

Design (q) is similar to (l) in that both base panels are inclined at 37°. However the relative insertion loss of design (q) is 0.35 dB(A) lower than that of (l). The only significant difference between the two designs is the position of the gap between the front panel and rear baseplate. Reducing the angle of the rear baseplate from 37° to $18\frac{1}{2}°$ improves the average performance of the profile by 0.33 dB(A), the change at individual receivers being generally uniform (except at (20.0, 4.5), where the performance is poorer). Further decrease of the inclination to 0° sees a degradation in average performance to only 1.47 dB(A) relative insertion loss. The most significant differences in this case are observed at the close 1.5 m height receivers. It is suspected that the degree of diffraction from the gaps in the baseplates is likely to be affected by the angle of the front baseplate, particularly with regard to how sound propagated through the device is reflected from the underside of the profile. Within the profile, the angle of the baseplate will affect the way in which sound is reflected upwards.

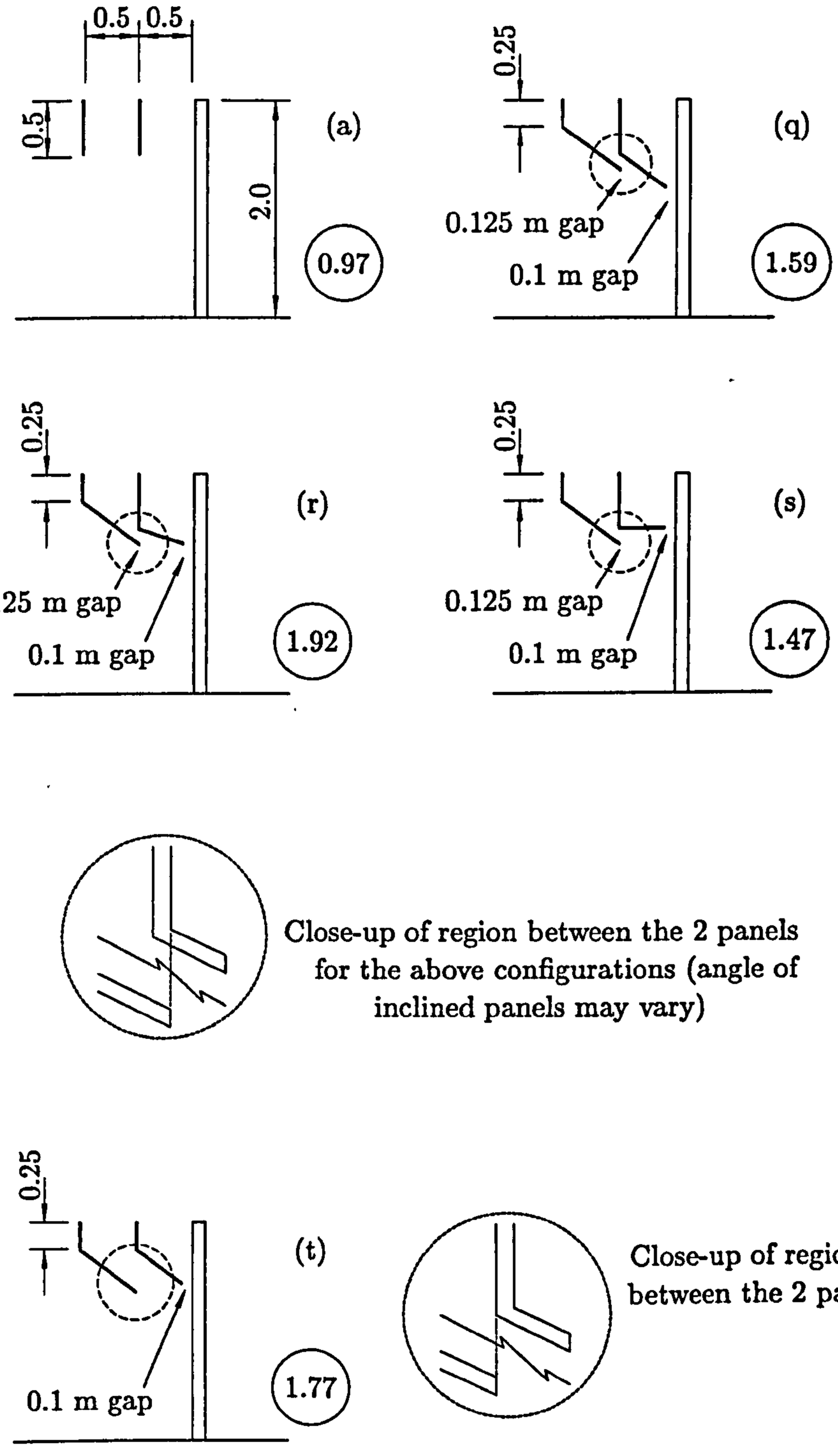

Figure 5.11: Relative mean insertion losses, dB(A), for asymmetric multiple-edge barrier configurations - distorted panels No.2. Dashed lines denote absorptive surfaces.

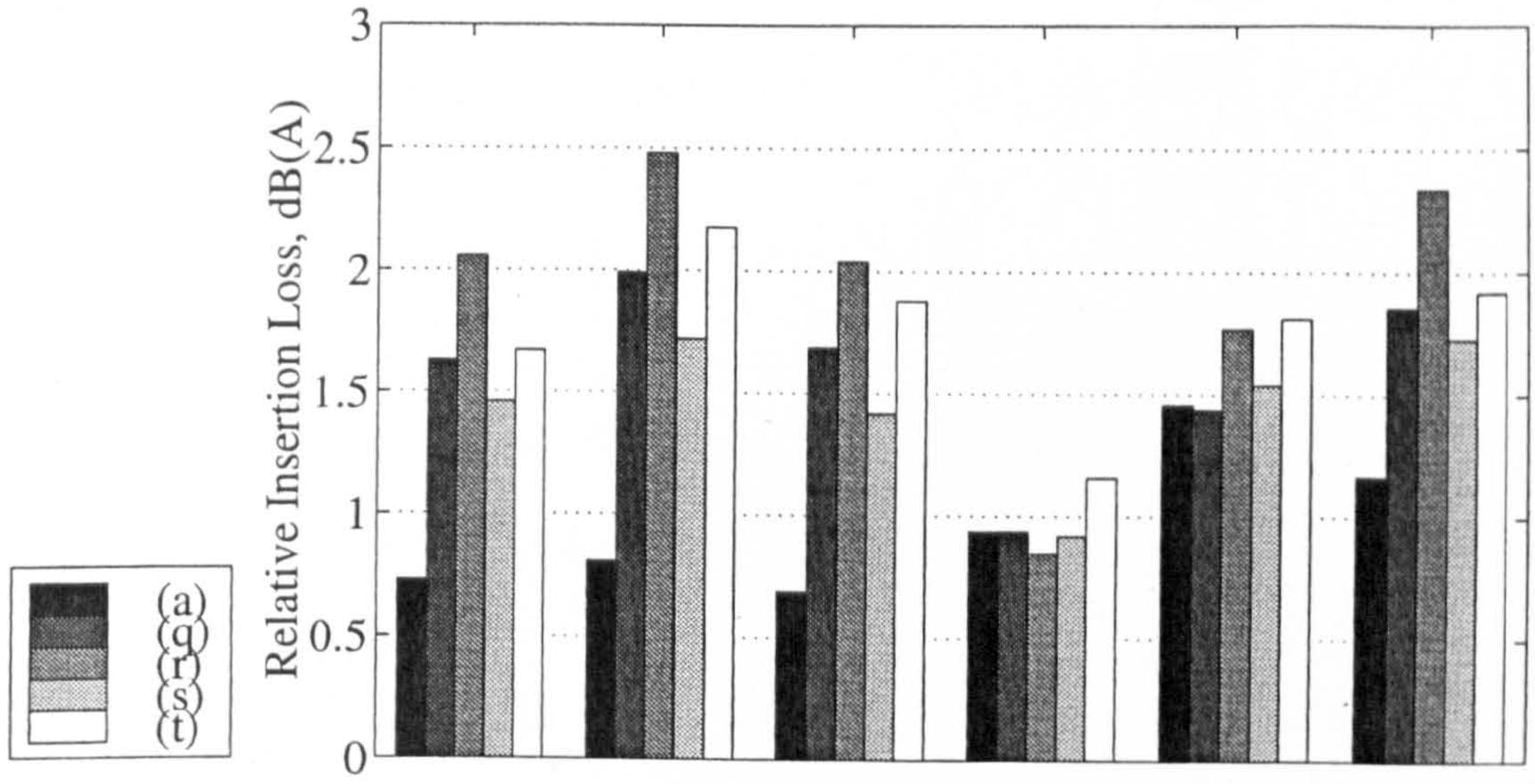

Receiver Position	-20.0, 1.5	-40.0, 1.5	-80.0, 1.5	-20.0, 4.5	-40.0, 4.5	-80.0, 4.5	Mean
Profile type (a)	0.73	0.81	0.69	0.94	1.46	1.17	0.97
Profile type (q)	1.63	1.99	1.69	0.94	1.44	1.86	1.59
Profile type (r)	2.06	2.48	2.04	0.85	1.77	2.34	1.92
Profile type (s)	1.46	1.72	1.42	0.92	1.54	1.73	1.47
Profile type (t)	1.67	2.18	1.88	1.16	1.81	1.92	1.77

Figure 5.12: Relative insertion losses, dB(A), for asymmetric multiple-edge barrier configurations - distorted panels.

The addition of design (t) to a plane screen leads to an improvement in screening of on average 1.77 dB(A), which is better than that achieved using designs (q), (s) or (m) – (p) by varying degrees. The depth of the gap between the base panels is such that leakage of diffracted sound is unavoidable. However, the length of the resultant channel combined with the 37° angle appears sufficient to redirect any reflected sound away from the receivers considered in this study.

5.2.4 The effect of a single inclined base-plate

A further possibility is the use of a single baseplate which is unconnected to the central diffracting plate, as in the different configurations presented in Figure 5.13. These profiles are all based around a baseplate inclined at 37° to the horizontal, changing only the horizontal separation of the upright and two diffracting panels.

The separation between the end of the baseplate and the main upright is fixed as in previous tests at 0.1 m.

It is observed from the dimensions shown in Figure 5.13 that for each configuration the depth of the gap between the bottom edge of the middle panel and the baseplate varies. This has been done to maintain the ratio between gap depth and panel separation, set from type (u) as 0.125/0.5 = 0.25, allowing the angle of the baseplate to be fixed, and the two baseplates to be aligned with one another. Consequently the depth of the middle panel varies according to this ratio, whilst the depth of the rear panel is fixed at 0.25 m. The designs, which are all rigid unless specified otherwise, are as follows: (u), panel separation = 0.5 m, middle panel height = 0.5 m, gap depth = 0.125 m; (v), panel separation = 0.5 m, middle panel height = 0.5 m, gap depth = 0.125 m, all internal surfaces being treated with absorbent material; (w), panel separation = 0.343 m, middle panel height = 0.422 m, gap depth = 0.086 m; (x), panel separation = 0.422 m, middle panel height = 0.462 m, gap depth = 0.106 m; (y), panel separation = 0.55 m, middle panel height = 0.526 m, gap depth = 0.138 m; (z), panel separation = 0.48 m, middle panel height = 0.491 m gap depth = 0.12 m; (aa), panel separation = 0.52 m, middle panel height = 0.512 m, gap depth = 0.13 m. The insertion losses predicted at the individual receiver positions are summarised in Figure 5.14.

The average insertion loss over the six receiver positions resulting from the introduction of the type (u) profile is 2.10 dB(A), the highest value observed over all of the tests and an improvement on the screening provided by the basic type (a) profile by approximately 1.1 dB(A). In comparison to other similar profiles, (l) and (q), with 37° angle baseplates and the same panel separations, there is also an improvement of ≈0.15 and 0.5 dB(A) respectively. Considering the levels at the individual receiver positions, the most noticeable improvement over type (a) (and also over (l) and (q)) is observed at the low height receivers, being in the range 1.5 - 1.9 dB(A). The poorest performance is observed at (-20.0, 4.5) where the level is approximately the same as that observed using (a). Again the introduction of absorptive treatment onto the internal faces of the device, as shown by type (v), has negligible benefit on the average screening, although a small improvement is

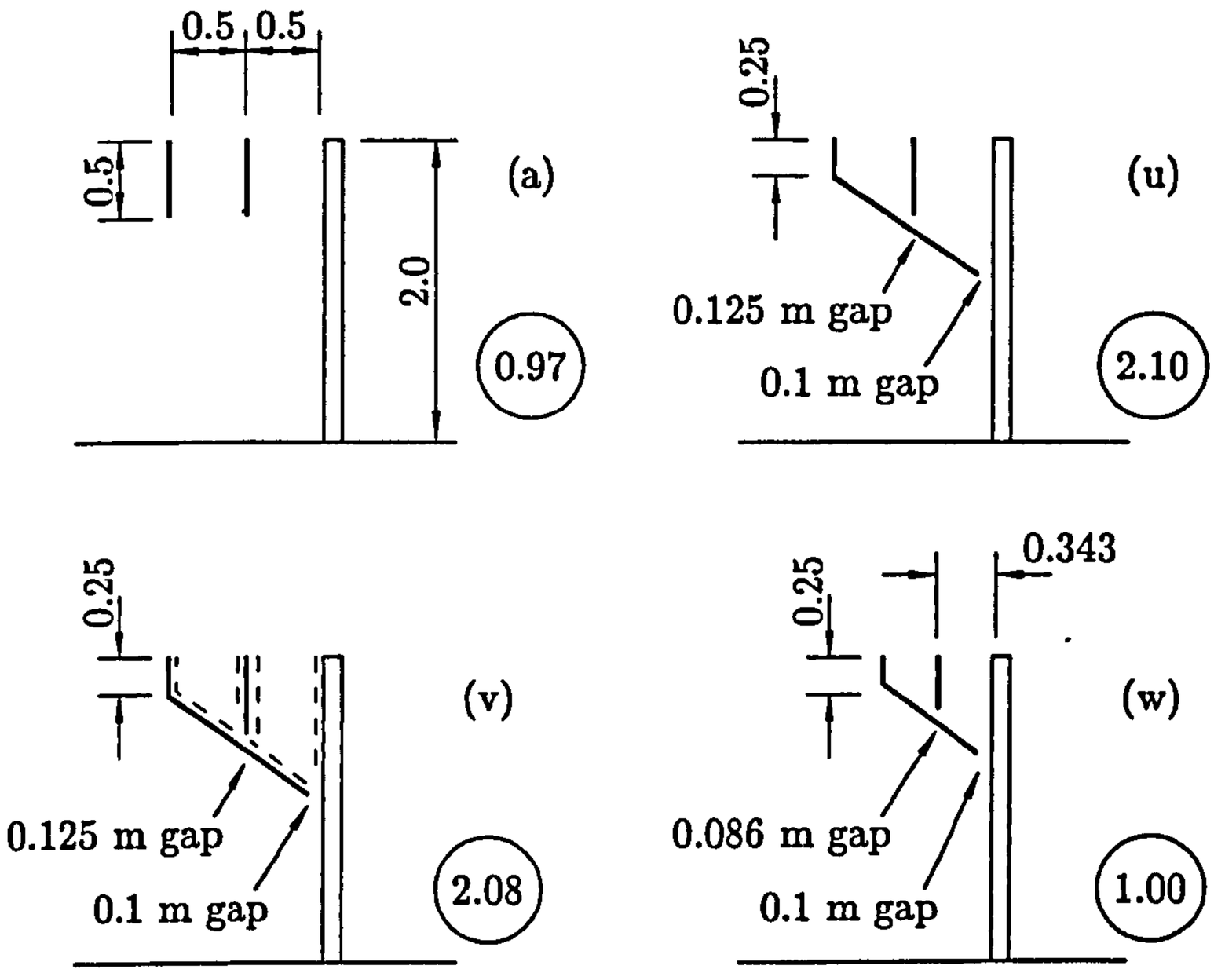

Figure 5.13: Relative mean insertion losses, dB(A), for asymmetric multiple-edge barrier configurations - inclined, open baseplates. Dashed lines denote absorptive surfaces. The panels and barrier are equally separated in each arrangement.

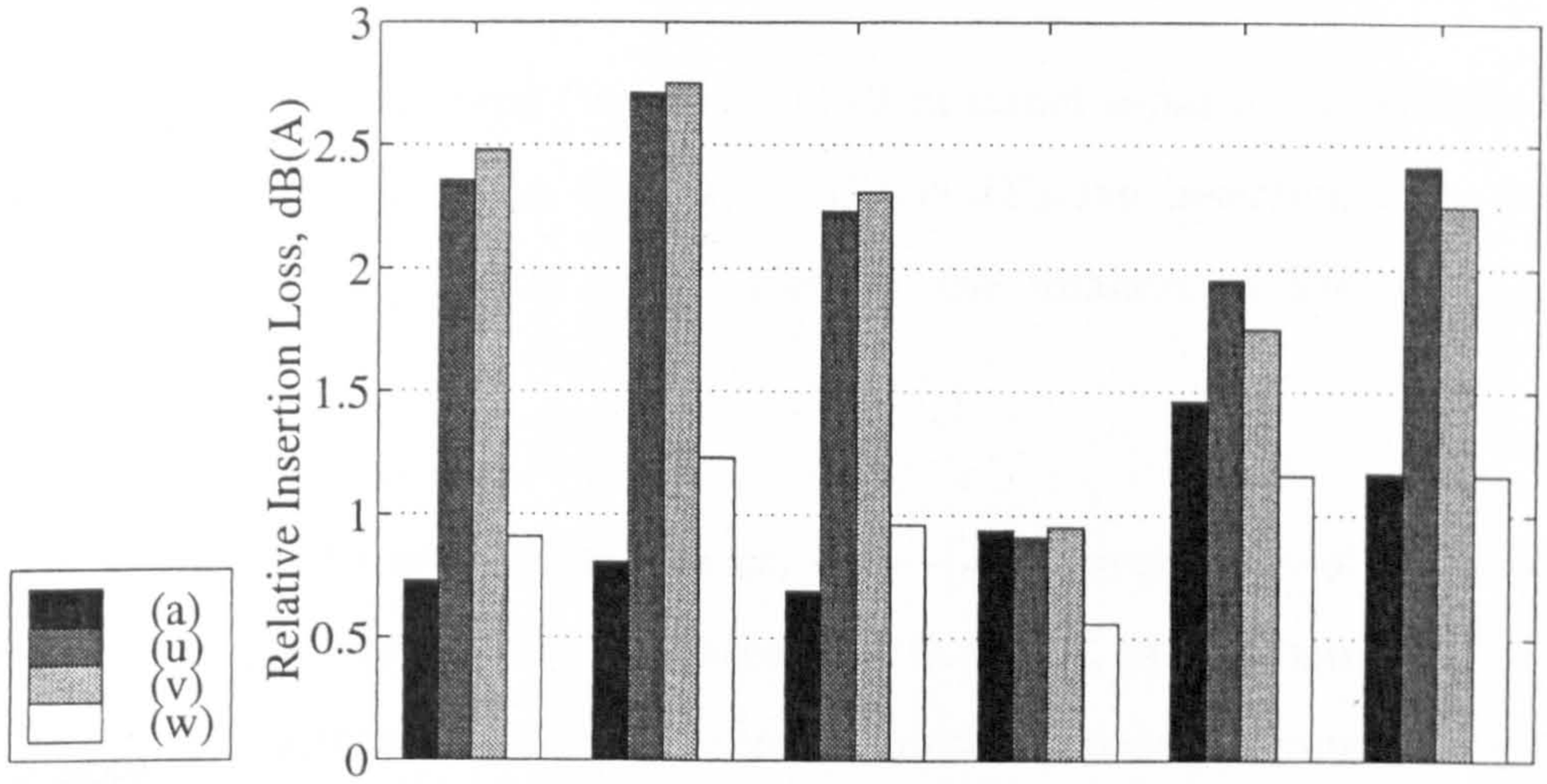

Receiver Position	-20.0, 1.5	-40.0, 1.5	-80.0, 1.5	-20.0, 4.5	-40.0, 4.5	-80.0, 4.5	Mean
Profile type (a)	0.73	0.81	0.69	0.94	1.46	1.17	0.97
Profile type (u)	2.36	2.71	2.23	0.91	1.95	2.41	2.10
Profile type (v)	2.48	2.75	2.31	0.95	1.75	2.25	2.08
Profile type (w)	0.91	1.23	0.96	0.56	1.16	1.16	1.00

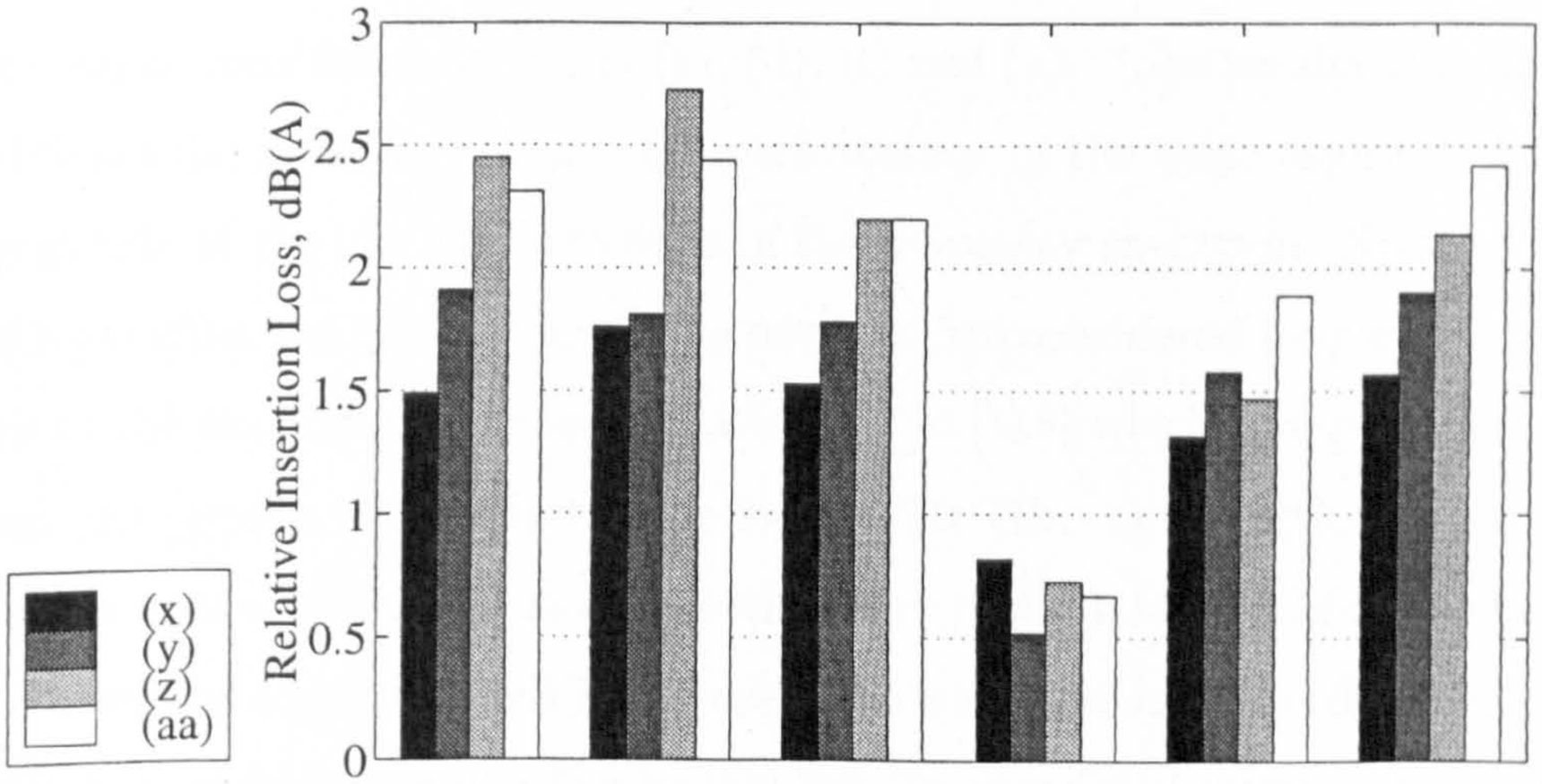

Receiver Position	-20.0, 1.5	-40.0, 1.5	-80.0, 1.5	-20.0, 4.5	-40.0, 4.5	-80.0, 4.5	Mean
Profile type (x)	1.49	1.76	1.53	0.82	1.32	1.57	1.42
Profile type (y)	1.91	1.81	1.78	0.52	1.58	1.90	1.58
Profile type (z)	2.45	2.73	2.20	0.73	1.47	2.14	1.95
Profile type (aa)	2.31	2.44	2.20	0.67	1.89	2.42	1.99

Figure 5.14: Relative insertion losses, dB(A), for asymmetric multiple-edge barrier configurations - inclined, open baseplates.

observed at the low receiver positions.

The smaller profile, type (w), with 0.343 m panel separation exhibits very poor screening in comparison, on average 1 dB(A) relative insertion loss, comparable to the basic type (a) profile and is thereby the weakest of the modified designs considered.

The tests on the remaining devices, (x) – (aa), investigate other panel separations. As the panel separation increases from 0.343 m, the average relative insertion loss gradually increases but then reaches a local maximum around a separation of 0.5 m (design (u)). It is noted that in maintaining the panel depth/separation ratio, the variation in performance cannot be attributed solely to the width the profile.

Figures 5.15 and 5.16 compare the insertion loss spectra relative to the plane rigid screen (i.e. insertion loss for the device - insertion loss for the screen) for several designs at the individual receiver positions for heights of 1.5 and 4.5 m respectively. The designs considered are types (a), (d), (l) and (u). The results indicate that the modifications generally enhance the performance of the basic asymmetric multiple-edge profile at the low and high ends of the frequency spectrum. No single modified profile provides the greatest screening over the full considered frequency range. Contrary to the experimental results of Watts et al [118] which observed that the basic symmetric profile was ineffective below 400 Hz (the wavelength at this frequency being approximately equal to the width of the profile), the BEM predictions of relative insertion loss presented in Figures 5.15 and 5.16 indicate the basic profile to be effective at frequencies as low as 200 Hz. The modified profiles exhibit improved screening at even lower frequencies.

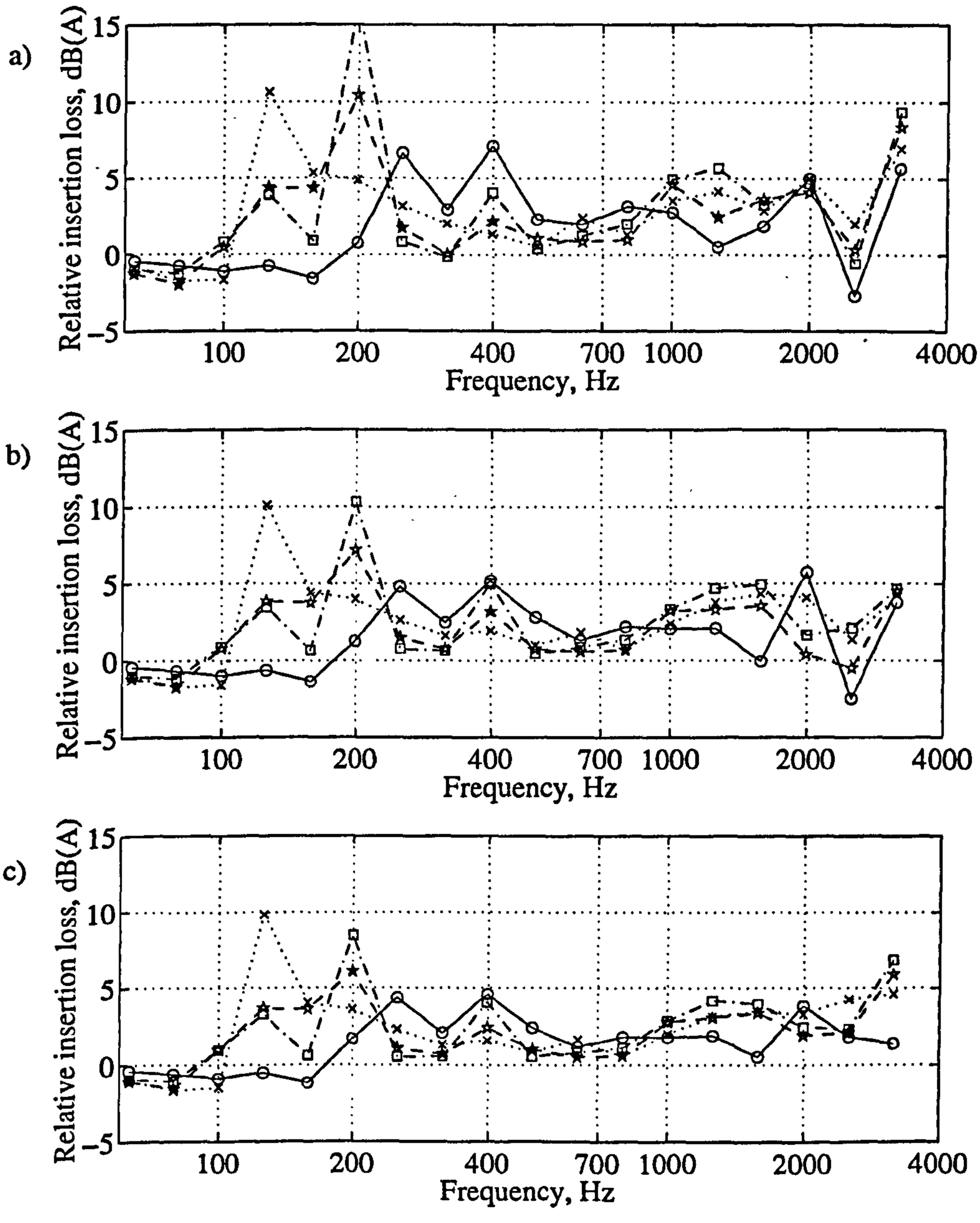

Figure 5.15: Comparison of relative insertion loss spectra at individual receiver positions for different multiple-edge profiles; a) Receiver position (20, 1.5); b) Receiver position (40, 1.5); c) Receiver position (80, 1.5); ∘, Type (a); ×, Type (d); ⋆, Type (l); □, Type (u).

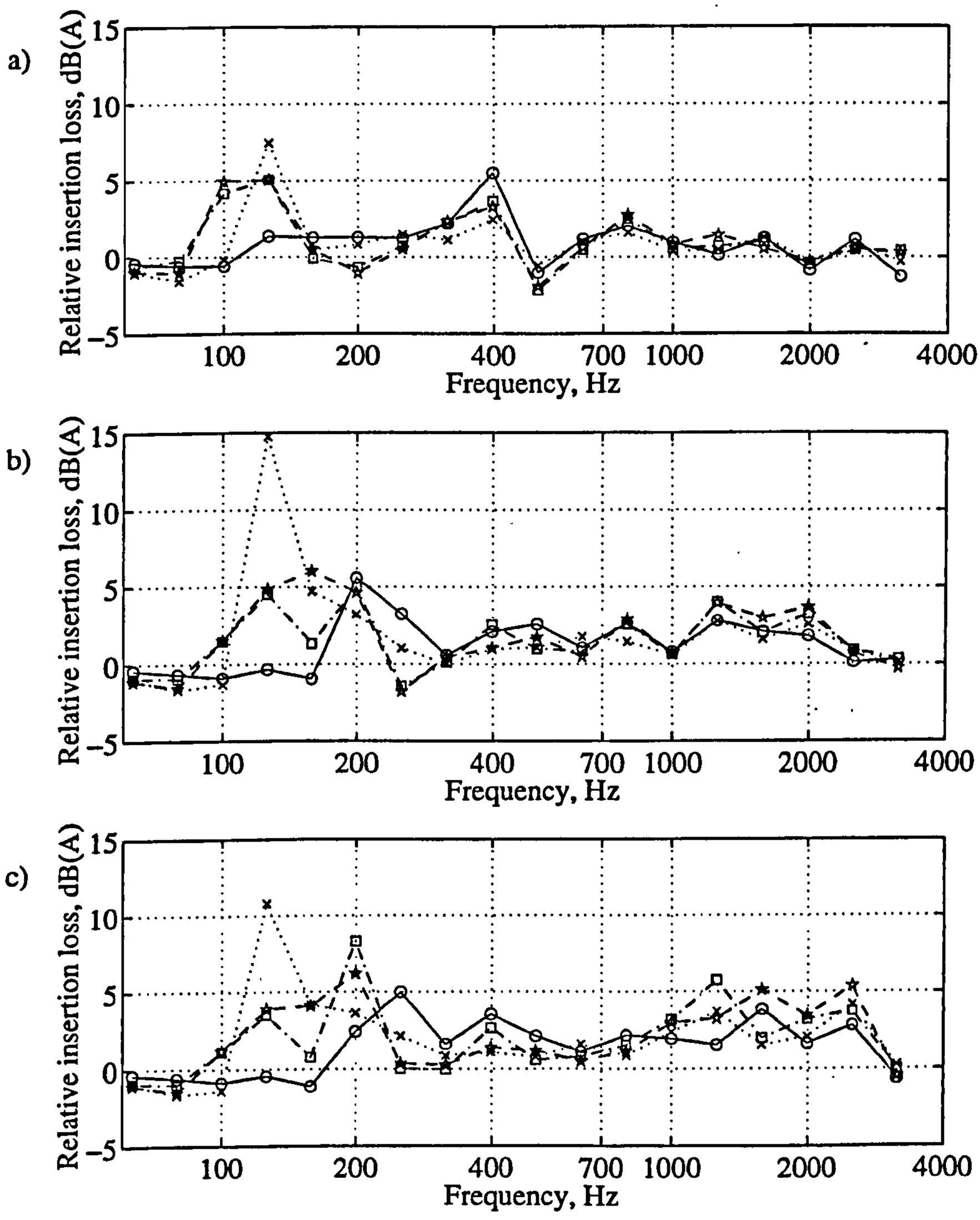

Figure 5.16: Comparison of relative insertion loss spectra at individual receiver positions for different multiple-edge profiles; a) Receiver position (20, 4.0); b) Receiver position (40, 4.5); c) Receiver position (80, 4.5); ∘, Type (a); ×, Type (d); ⋆, Type (l); □, Type (u).

5.3 Conclusions

The results predicted using the boundary element method have indicated that the most effective design is Type (u), that with a single inclined open baseplate, providing approximately 2.0 dB(A) additional average insertion loss relative to the basic plane screen. In comparison to the basic asymmetric RTB profile (type (a) in Figure 5.5), the improvement is approximately 1.0 dB(A). Comparison of this design of cross-section can be made with the Calmzone device tested in Chapter 3 which, in addition to a series of ducts, is comprised of an inclined baseplate and a single additional diffracting edge. Using the boundary element method for the same site geometry, the Calmzone was observed to provide an average improvement in insertion loss of 1.0 dB(A) with the interference ducts blocked (relative to a plane rigid screen of the same height, 2.225 m), and 1.5 dB(A) with the ducts open.

It is noted that these tests have been conducted on flat ground. Further simulations would be required to assess the performance of the optimised device on sites where the receiver is well below the top of the barrier. The in-situ tests [121] indicate that the performance of the basic device is influenced by site geometry, such that optimisation may be necessary for each individual site.

Additionally, although the type (u) device is the most effective, it is of sufficient size (particularly in terms of depth) to impose practical limitations upon its use. Although the Calmzone device is of a similar depth (0.7 m), it is only half the width, and constructed from lightweight plastics. Scale model tests on the multiple-edge profile [106] have indicated excessive wind loadings upon such a design to be problematic. The base panel would most likely require support from beneath, otherwise, structural modifications or foundation improvements would probably be required to support the suspended panels.

In view of the limited improvement in screening observed in this study compared to the probable cost of installation, the type (u) design appears unfeasible. In view of this, it seems reasonable to propose that the multiple edge design is best suited for use on relatively level sites where the standard design, i.e. vertical reflective panels and no baseplate, can be adopted, or sites where the height of the receivers

are similar to the height of the barrier. In other situations, other options should perhaps be considered first.

The boundary element method has been shown to be a useful tool for optimisation purposes, for situations where the cross-section of the barrier is constant along its length. However, its application is limited to modelling geometries where the ground is fairly flat (although geometries with cuttings can also be simulated efficiently - see Chapter 2).

Chapter 6

Trackside Noise Barriers For Railways

Noise nuisance from railways has become a major concern particularly near lines which carry heavy traffic at high speeds. Noise barriers are commonly used to alleviate the problem. A range of experimental and theoretical studies have been reported on the efficiency of plane screens and other forms of noise barrier in attenuating railway noise [53, 67, 105, 63, 21, 116].

In this chapter a study is presented of the performance of various forms of trackside noise barrier, determined using the two-dimensional boundary element numerical method discussed in Chapter 2. The method has been adapted to allow for the simulation of dipole-type sources.

A comparison is carried out of the performance of simple barriers and vehicle shapes, calculated using monopole and dipole sources, with results obtained using the standard UK prediction method, the Calculation of Railway Noise [33, 34]. Results are presented showing the effects of the cross-sectional profile of the rolling stock. Using a cross-section representative of high-speed trains, calculations have been carried out on a wide range of barrier profiles to establish the effect of barrier shape on screening performance. The barrier position relative to the track has been chosen using an appropriate structure gauge.

6.1 Selection of Source Characteristics

6.1.1 Source Position

Three main forms of noise generation occur on railway trains. Noise is generated from the interaction and vibration of the rails and wheels, sound is aerodynamically induced from the vehicle body and pantograph, and there is power unit noise (e.g. [110]).

Noise from locomotives is less dependent on movement than that from the other sources and the array of individual source components varies with the type of vehicle. For high speed trains, which are of primary concern, the power units are located at the ends of the train. Our aim will be to predict levels which could be expected when the centre of the train passes the observation point, when power unit sources will have little contribution to the overall level, particularly for receiver positions relatively close to the track.

King [70] observed that aerodynamic sound sources on a high speed train include pantographs and other roof-mounted equipment, bogie units and the "cut-out" areas of the body shell into which these are mounted, and detached flow at the head of the leading car. At high speeds, the latter often produces the strongest aerodynamic source, followed by vortex shedding from pantographs. For the most part, such sources have been shown [69] to be unimportant at speeds below 240 km/h although experimental results from studies of the French TGV-Atlantique [81] have suggested that this limit is actually as high as 300 km/h. Aerodynamic noise tends to increase more dramatically with speed than wheel/rail noise. Measurements performed by Holzl et al [55] indicated that for high-speed trains the noise levels resulting from pantograph noise and wheel/rail noise on the front and rear power cars are similar.

The sound propagating from the majority of aerodynamic sources on the upper half of the train body, the pantograph and also the locomotive exhaust outlets will be unobstructed by a typical low barrier of approximately 2 m in height. The direct propagation of sound from these sources should thus be considered separately. Barriers 5-6 m in height would be necessary to shield the surroundings from these sources. In the region of the rails and wheels noise arising from vibration and

interaction of these elements is significantly shielded by low barriers. The purpose of this investigation is to examine the attenuation of noise produced in this region.

Van Leeuwen [115] conducted a survey of various prediction methods used to determine the effects of track-side noise barriers and found that from the 14 methods studied, 9 different source positions were used. These were located predominantly above either the centreline of the nearest track or the nearside rail and all at heights of less than 1.0m above the trackbed. Theoretical calculations carried out by Ughi et al [113] used a source spectrum composed of wheel/rail noise, pantograph and aerodynamic noise but maintained the source position at the railhead. A source position at the railhead was used in this investigation.

6.1.2 Source Spectrum

There are considerable difficulties in establishing a typical source spectrum for a train. Apart from individual variations between vehicles, the distribution of the sources is diverse and the relative contributions to the overall noise levels vary with speed.

Hemsworth [52] presented wheel/rail noise spectra for several vehicle types, using different wheel diameters and either tread or disc-braked wheels. These included British Rail Mk II and Mk III carriages fitted with tread-brakes and disc-brakes respectively. The A-weighted spectra for the Mk III carriages is shown in Figure 6.1. The train speed for this particular data was 160 km/hr and the measurement position was 25m from the nearside track.

Figure 6.1 also shows bypass spectra established during other studies. These have all been adapted to values equivalent to a measurement position of 25 metres from the nearside track and are as follows.

- *Houtave*: [62], Measured data from studies of the TGV-Atlantique to investigate the performance of noise barrier systems (Rolling stock: TGV-Atlantique, train speed: 300 km/h, original measurement position was at 25 m).

- *Van Der Toorn*: [114], Measured data from studies of the TGV-Atlantique to identify the vertical distribution and strength of acoustic sources (Rolling

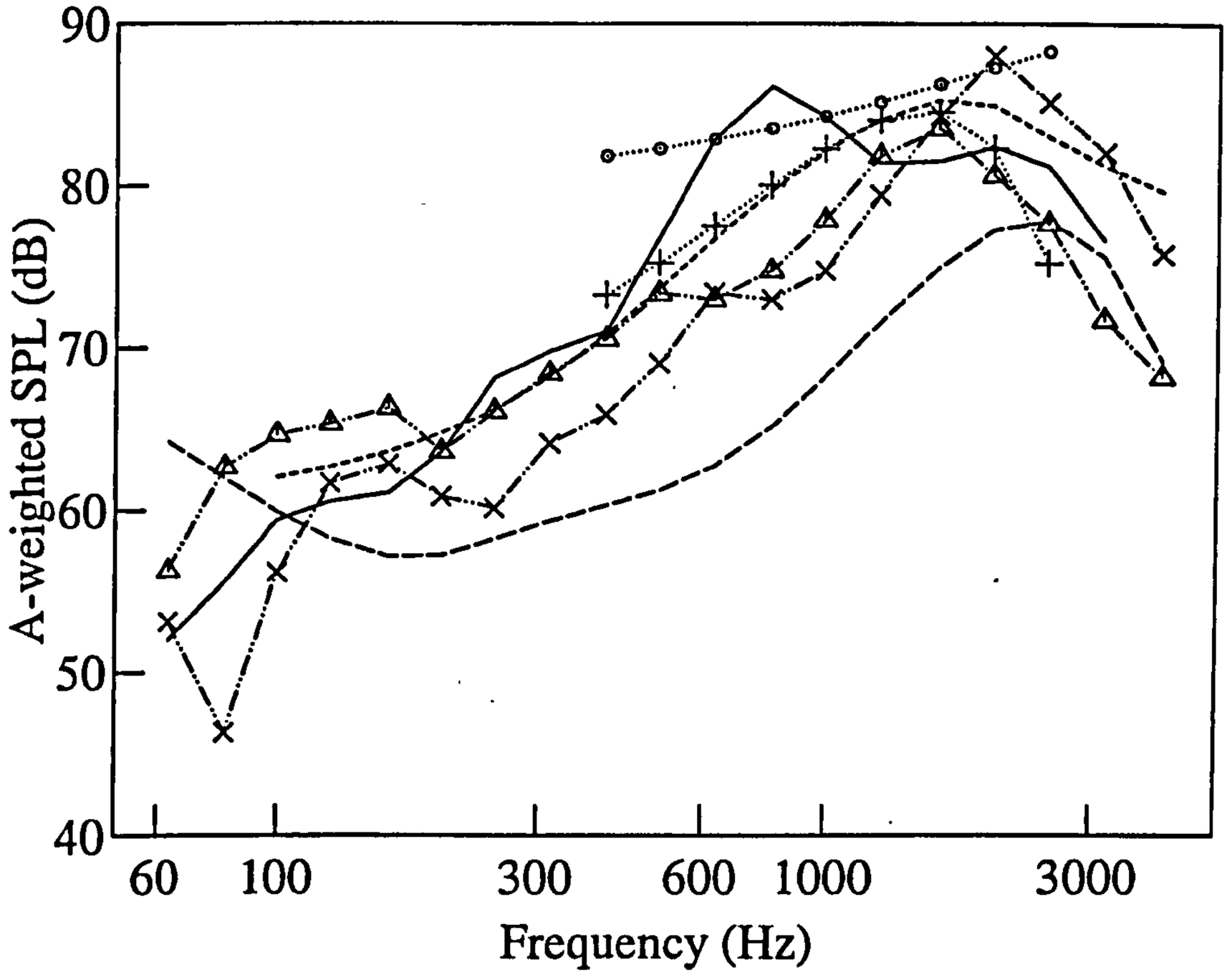

Figure 6.1: 1/3 octave band A-weighted bypass spectra for different rolling stock, adjusted for measurement position at 25m from the nearside track. ——, Hemsworth; - - - -, Houtave; +, Van Der Toorn (1); ∘, Van Der Toorn (2); ×, Feldmann (1); △, Feldmann (2); – – – , Ughi.

stock: TGV-Atlantique, train speeds: 200 km/hr (1) and 300 km/hr (2), original measurement position was at 25m).

- *Feldmann*: [42], Measured data for coaches with different wheel types from a study of the noise behaviour of wheel/rail-systems (Rolling stock: Carriages with absorber rim damping (1) and sandwich disk damping (2), train speed: 200 km/hr, original measurement position was at 3m).

- *Ughi*: [113], Measured data from a study into the combined effectiveness of different height noise barriers. This spectrum is a combination of wheel/rail, pantograph and aerodynamic noise (Rolling stock: ETR 500, Train speed: 250 km/h, original measurement position is not specified).

Although there is considerable variation in the results shown in Figure 6.1 the

general trend is similar, with a peak in the spectrum at approximately 1 to 2 kHz. The source spectrum used in the investigation was that of Hemsworth for British Rail Mk III disc-braked rolling stock.

6.1.3 Source Radiation Characteristics

Wheel/rail noise is commonly modelled by a line of incoherent dipole sources. This approximation gives good agreement with measured data [102]. Hohenwarter [54] conducted measurements at short distances for a selection of different trains and speeds and found that in most cases, electrically hauled trains radiate sound with dipole source characteristics. The ÖAL model [97] uses a combination of dipole and monopole sources, with the ratio 15% monopole and 85% dipole type radiation.

6.2 Modifications Required For The Boundary Element Method

For the purpose of this study, the standard boundary element method described in Chapter 2 is implemented using two sources for each track, located at the railhead and exhibiting either monopole or dipole type radiation characteristics. A separate simulation is made for each source position and the resulting predicted noise levels are added logarithmically.

For a monopole source located at $\mathbf{r}_0$, $p_0(\mathbf{r}) = G_{\beta_c}(\mathbf{r}, \mathbf{r}_0)$. A dipole source is two coincident monopole sources. That is, for a dipole source,

$$\begin{aligned} p_0(\mathbf{r}) &= \lim_{h\to 0}\left[\frac{G_{\beta_c}(\mathbf{r}, \mathbf{r}_0 + h\mathbf{u}) - G_{\beta_c}(\mathbf{r}, \mathbf{r}_0)}{h}\right] \\ &= \mathbf{u}\cdot\nabla_{\mathbf{r}_0} G_{\beta_c}(\mathbf{r}, \mathbf{r}_0) \\ &= u_x \frac{\partial G_{\beta_c}(\mathbf{r}, \mathbf{r}_0)}{\partial x_0} + u_y \frac{\partial G_{\beta_c}(\mathbf{r}, \mathbf{r}_0)}{\partial y_0} \end{aligned} \tag{6.1}$$

where $\mathbf{u} = (u_x, u_y)$ is a unit vector along the axis of the dipole (i.e. the axis of maximum emission). In the simulations we carry out we assume, as in [102], that $\mathbf{u} = (1, 0)$ is in the horizontal direction. Expressions and efficient numerical calculation procedures for $\partial G_{\beta_c}(\mathbf{r}, \mathbf{r}_0)/\partial x_0$ and $\partial G_{\beta_c}(\mathbf{r}, \mathbf{r}_0)/\partial y_0$ are given in [19].

6.3 Method and Comparison With Other Prediction Methods

The cross-section of the track, rolling stock, ballast and sound sources is shown in Figure 6.2, together with a noise barrier situated at one side of the track. This is a multiple edge barrier configuration [26], achieved by fitting two extra panels to a plane screen, which is discussed later.

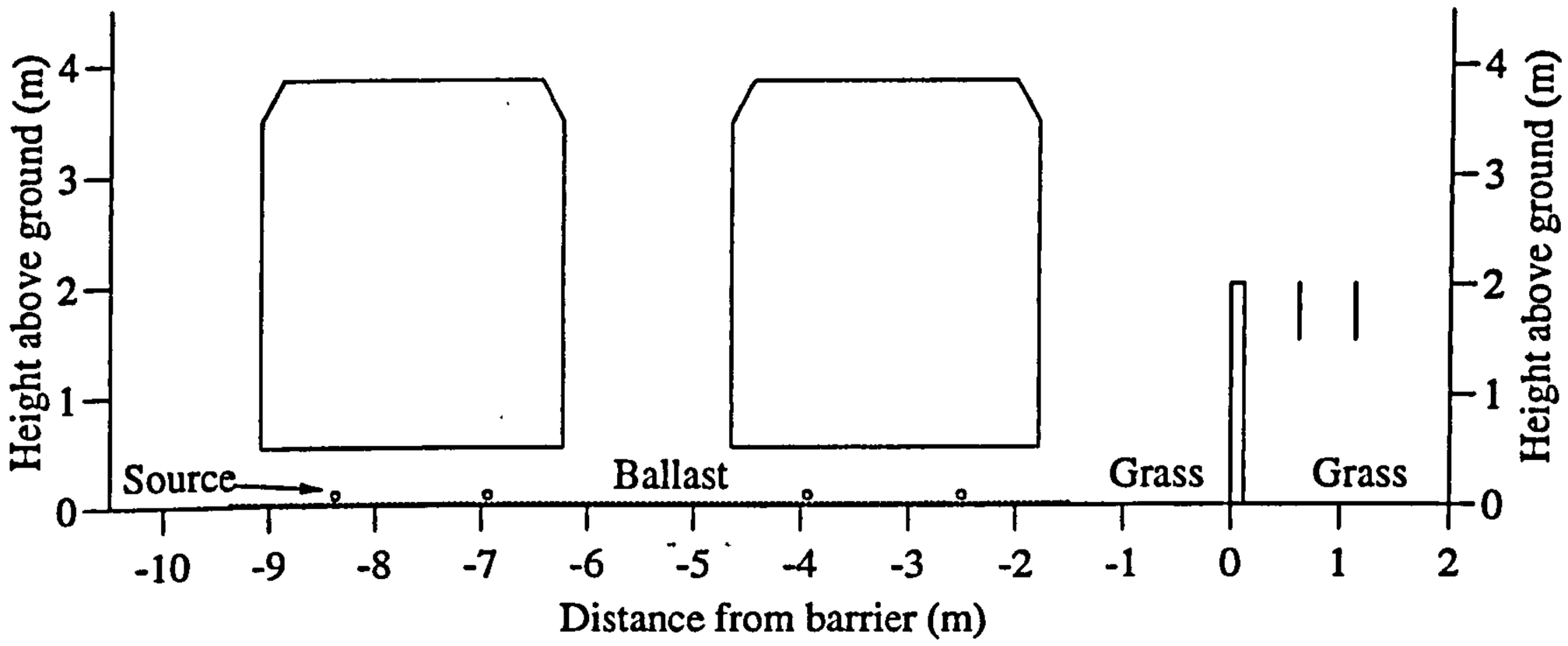

Figure 6.2: Basic railway cross-section

The ground is flat and the non-rigid surfaces, namely the ballast, grass and absorbing barrier faces, are assumed to consist of a homogeneous porous layer with a rigid backing. The acoustical properties of the porous layer are given by the four-parameter model of Attenborough [10, 11] using the parameter values given in Table 6.1. Type 1 ballast is equivalent to pea-gravel. Type 2 ballast is based upon measurements carried out as part of a study into noise barriers for the TGV [62]. For these preliminary tests, Type 1 ballast is assumed.

All other surfaces are assumed rigid, with zero admittance. Receiver positions are located at distances of 20, 40 and 80 m on the far side of the barrier and at heights of 1.5 and 4.5 m. A source is located at each railhead. The source spectrum used is that of Hemsworth for British Rail Mk III disc-braked rolling stock [52] as

Surface type	Flow resistivity σ, (Nsm^{-4})	Porosity Ω	Tortuosity q	Layer depth d, (m)	Pore shape factor s_p
Grass	125,000	0.50	1.67	∞	0.5
Ballast, Type 1	9,570	0.40	1.54	0.5	0.4
Ballast, Type 2	180,000	0.40	2.30	∞	0.5
Absorbing barrier	6,300	0.90	1.50	0.13	0.5

Table 6.1: Parameter values used in the impedance model.

shown in Figure 6.1.

Several different configurations of plane screen of different heights were considered which are described in Table 6.2. For the absorbing barrier case, only the traffic-facing side of the barrier was treated. Insertion losses were calculated at 1/9th octave band centre frequencies and the results combined to obtain a broad band insertion loss. Results for carriages on the nearside and farside tracks were considered separately. Results were calculated using the boundary element method, for both monopole and dipole sources, and the standard UK prediction method, The Calculation of Railway Noise (CRN) [33].

		Nearside track			Farside track		
Barrier type	Method	1.5 20.0 (m)	1.5 40.0 (m)	1.5 80.0 (m)	1.5 20.0 (m)	1.5 40.0 (m)	1.5 80.0 (m)
1.5m rigid	Monopole	3.7	0.0	-4.0	3.3	-0.7	-4.1
	Dipole	3.9	0.3	-3.8	3.4	-0.7	-4.1
	CRN	9.9	9.4	8.7	6.4	5.9	5.3
1.5m absorbing	Monopole	12.7	9.5	6.2	6.9	3.4	0.7
	Dipole	13.3	10.0	6.9	7.1	3.6	0.8
	CRN	14.3	13.8	13.1	9.6	9.2	8.5
2.0m absorbing	Monopole	15.6	11.7	8.0	9.6	6.3	2.6
	Dipole	16.2	12.5	8.7	10.0	6.4	2.6
	CRN	16.3	15.7	14.9	11.9	11.2	10.4

Table 6.2: Comparison of broad band insertion losses, dB(A).

The insertion losses for the rigid barrier as calculated using the boundary element method are small for both monopole and dipole sources, not exceeding 4 dB(A). The introduction of an absorbing surface onto the track-facing side of the barrier significantly improves performance by reducing multiple reflections. Increasing the height of the absorbing barrier further improves performance at all positions. The differences between the monopole and dipole results increases with increasing barrier height, as would be expected from consideration of the emission characteristics.

For the rigid barrier, the boundary element results are very much smaller than those predicted by CRN. This may be because the boundary element method overestimates the effect of multiple reflections between parallel surfaces due to the perfect geometry of the model and the exactly parallel faces of the rolling stock and barrier. There is good agreement between results from CRN and the boundary element method for the absorbing barriers and the close receiver positions. At larger distances the differences are attributable to ground attenuation which is always considered in the boundary element method. In CRN the ground effect can never exceed 4 dB(A) and is assumed zero when the barrier is present.

Table 6.3 presents the results from the numerical method using a dipole source for various plane barrier arrangements and the multiple edge barrier configuration shown in Figure 6.2. The results suggest that inclusion of the additional panels is equivalent to increasing the height of the plane absorbing barrier by at least 0.5 m.

6.4 The Effect of Carriage Shape Upon Barrier Performance

To investigate the effect of the carriage shape upon barrier performance, calculations were carried out using a complex cross-section characteristic of high speed trains as shown in Figure 6.3. This cross-section is based upon British Rail Mk IV carriages and is similar to the profile of TGV rolling stock which is also shown in Figure 6.3.

The barrier position was determined using standard structure gauges [103] and

Barrier type	Nearside track			Farside track		
	1.5 20.0 (m)	1.5 40.0 (m)	1.5 80.0 (m)	1.5 20.0 (m)	1.5 40.0 (m)	1.5 80.0 (m)
1.5m rigid	3.9	0.3	-3.8	3.4	-0.7	-4.1
1.5m absorbing	13.3	10.0	6.9	7.1	3.6	0.8
1.5m absorbing, & RTB panels	15.4	12.3	9.3	9.7	6.1	3.1
2.0m absorbing	16.2	12.5	8.7	10.0	6.4	2.6
2.0m absorbing & RTB panels	19.0	14.9	11.1	12.7	8.6	5.0
3.0m absorbing	18.9	16.3	10.4	13.2	8.3	4.6
3.0m absorbing & RTB panels	21.2	17.3	13.2	16.4	11.4	6.9

Table 6.3: Broad band insertion losses, dB(A), for various barrier configurations.

corresponded to the position of overhead cable masts. The impedance characteristics used for the ballast were those given for Type 2 in Table 6.1. Carriages on the nearside track were considered with a dipole source at each railhead. Results are presented in Table 6.4, in terms of the mean insertion loss over the 6 measurement positions described previously.

Cross-section type	Average insertion loss, dB(A)	
	Rigid barrier	Non-rigid barrier
Simple	4.1	18.5
Complex	11.4	17.4

Table 6.4: Comparison of average insertion losses, dB(A), for different carriage profiles.

For the case of the rigid barrier, there is a significant improvement in barrier screening when using the complex cross-section, an average of almost 7.5 dB(A). As already observed, the low values for the simple cross-section are due in part to the perfect geometry of the model. However, the angle of the lower surfaces on the complex cross-section suggests that reflected sound is directed back towards the ground between the train and the barrier, whilst the upper surfaces help direct sound above the receiver positions which have been used.

Introducing an absorbing surface onto the track-facing side of the barrier reduces

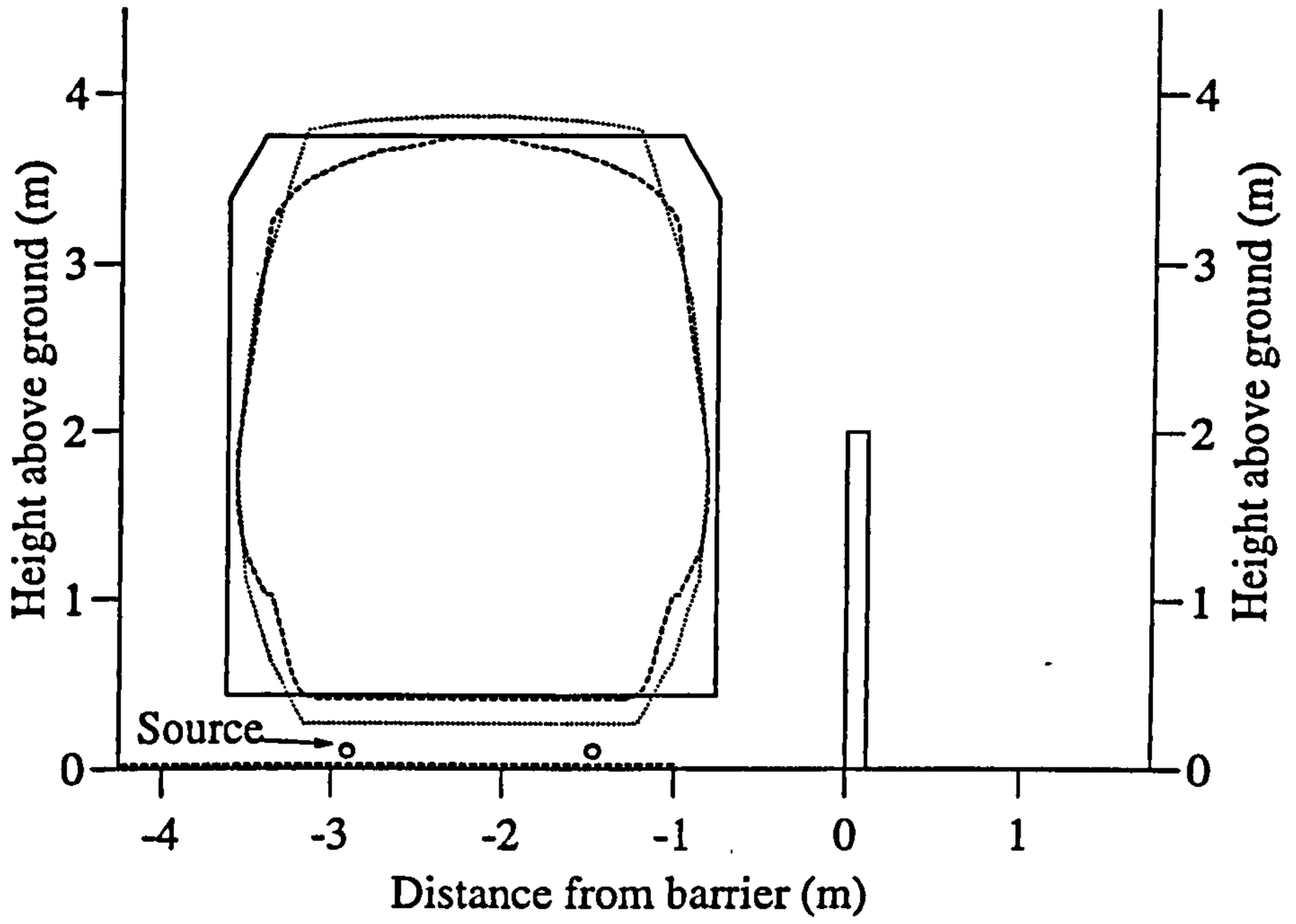

Figure 6.3: Cross-section for comparison of carriage shapes. ——, Simple; - - - -, BR Mk IV; ···, TGV

the benefits of these inclined rigid-surfaces, leading to a similar degree of screening for the two carriage cross-sections.

6.5 The Effect of Barrier Shape Upon Screening Performance

To investigate the effect of the shape of the noise barrier upon the screening performance, the same basic geometry and sources were adopted as in Section 6.4. The barrier height was 2.0 m. Figure 6.4 shows the position of five of the different barrier profiles which were studied. The positions were chosen such that no barrier surface fell within the structure gauge. The top edge of the vertical barriers and those inclined towards the track were coincident.

Figure 6.5 shows the individual barrier arrangements together with the corresponding mean insertion loss over the six measurement positions. In the case of absorbent barriers, the whole track-facing side was treated except in case d) where

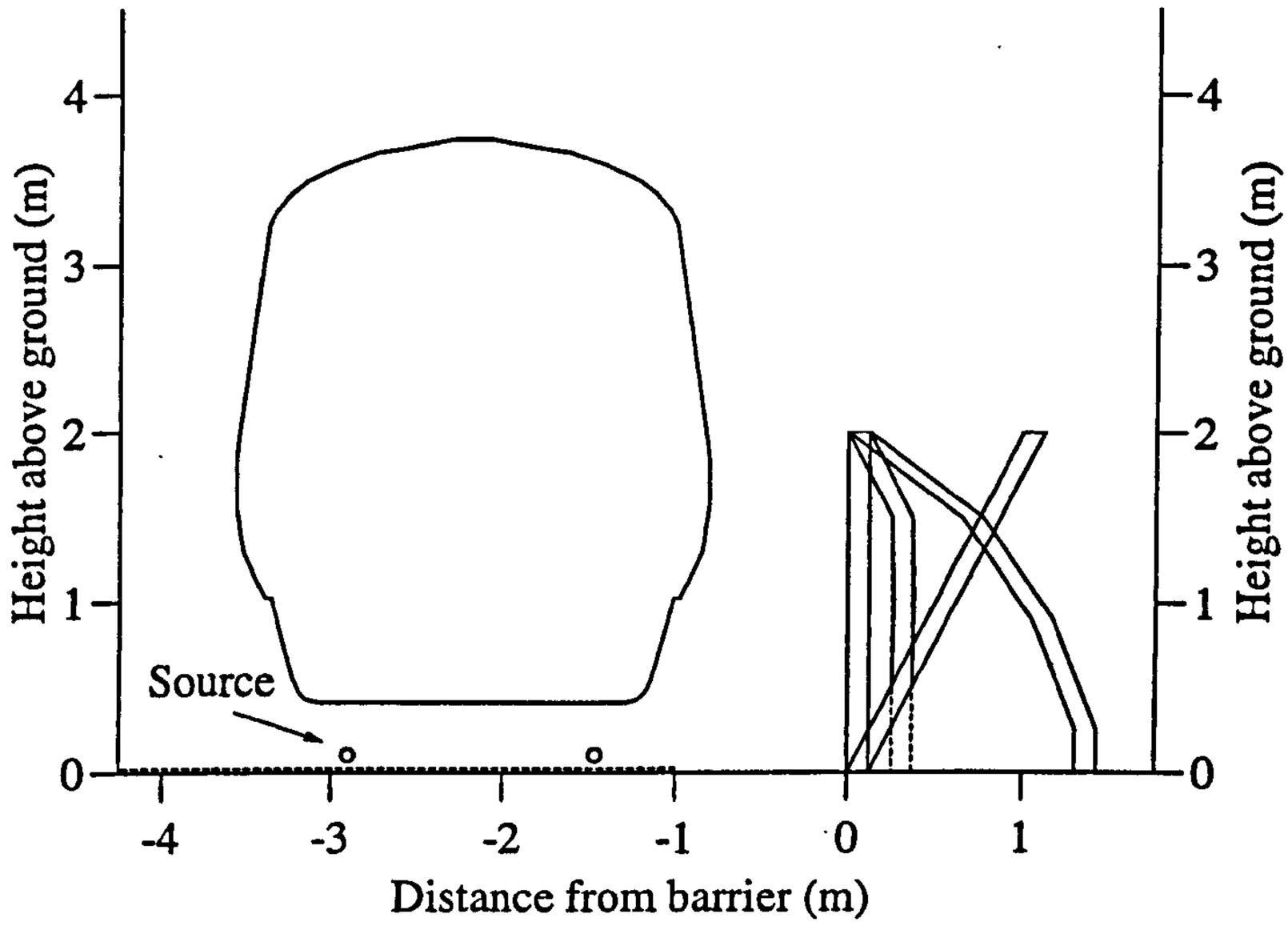

Figure 6.4: Cross-section for comparison of barrier shapes

the treatment was applied to the upper 0.75 m. "R" denotes the result for a rigid barrier and "A" the absorbing case.

Consider first the rigid barriers (Figure 6.5, designs (a), (c) and (f)). The mean insertion loss is in the range 7.1 – 13.5 dB(A). Of the three designs, the parabolic form, (c), is the least efficient. The reason for this may be that the outward sloping lower section of the parabolic profile is reflecting sound upwards and reducing the benefits of profiling the carriage sides. The screen sloping towards the carriage, (f), is more efficient than the plane screen when their upper edges are coincident.

For those barriers with absorbent surfaces, the mean insertion loss is in the range 11.8 – 17.9 dB(A). As for the rigid case, barrier (c) produces the lowest value of mean insertion loss. The most efficient single barrier is the plane screen (a). Other designs produce very similar mean insertion losses between these values, as was observed by Van Tol [116]. In assessing the relative efficiency in these cases it must be remembered that the performance will be affected by the criteria used for the relative positions of the upper edges. In this investigation the position of the upper

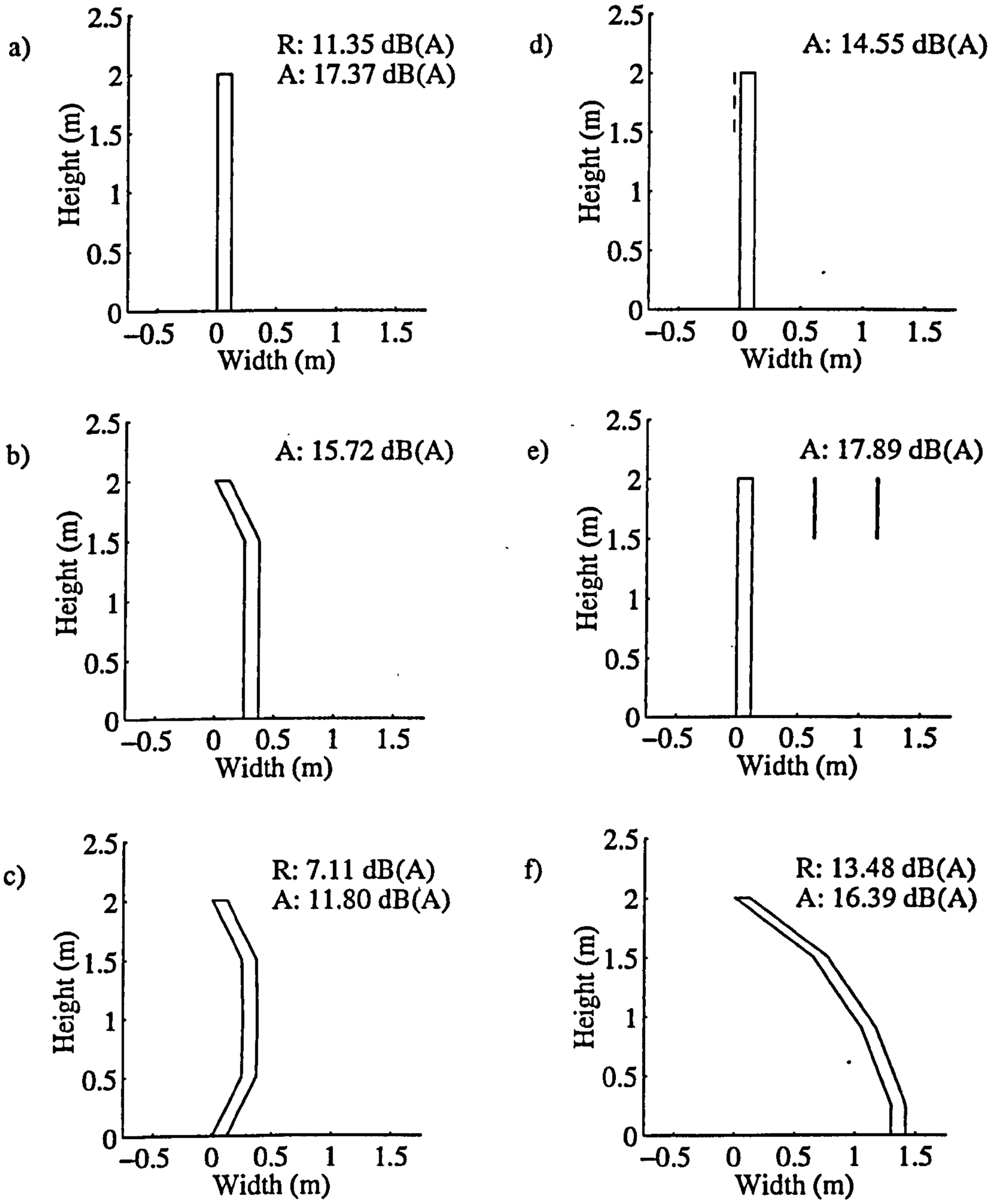

Figure 6.5: Average insertion losses, dB(A), for the barrier arrangements tested

edges are coincident. Other studies [63, 21], in which the feet of the barriers are coincident, report that screens inclined towards the track are the most effective. For the partially absorbing barrier, (e), the mean IL is midway between that achieved using either a fully rigid or fully absorbing barrier. In this instance, screening will be improved by increasing the proportion of the barrier surface which is absorbent.

Enhanced screening can be achieved by incorporating multiple edge devices, as was observed by Rudolphi and Akerlöf [105]. For the complex train cross-section, the insertion loss of the multiple edge device is approximately 0.5 dB(A) greater screening than that for the plane absorptive barrier. This is not as significant as was observed during the preliminary tests with a simple cross-section, where the improvement was equivalent to a 0.5 m increase in barrier height.

6.6 Conclusions

The boundary element numerical method is a useful tool for investigating the relative efficiency of various forms of track-side noise barrier for railways. The results of the two-dimensional method can be interpreted in three dimensions as equivalent to those for a coherent line source of sound. The results are expected to be representative of levels obtained when the centre of the train passes the observation point.

Sources at the railhead have been used which are appropriate for a variety of sources below the level of the upper edge of the noise barriers. Aerodynamic and power unit noise above the barrier will not be attenuated and have not been considered.

The difference in barrier insertion loss resulting from assuming monopole and dipole source characteristics is quite small, but becomes more important as the height of the barrier increases.

The results obtained using the numerical method suggest that for any particular shape, an absorbent barrier provides much better screening efficiency than the rigid

equivalent. The cross-section of the rolling stock significantly affects the performance of rigid barriers. The screening efficiency of such barriers is poor when the sides of the rolling stock are vertical. However an average improvement in insertion loss of up to 7.5 dB(A) for a 2 m high barrier results when the upper and lower surfaces of the vehicle sides are inclined; this helps to redirect reflected sound either towards the trackbed or upwards. Such profiles are commonly used, particularly on high speed trains.

If the position of the upper edge is fixed, the results suggest that vertical absorptive barriers provide more effective screening than those tilted towards the track, since the benefits of using profiled rolling stock are eliminated. The addition of multiple edges to a barrier provides additional insertion loss of up to 3.0 dB(A) without any increase in height for carriages with vertical sides. The average improvement is 0.5 dB(A) for profiled rolling stock.

Chapter 7

Conclusions

The performance of outdoor noise barriers has been investigated using both numerical modelling, through application of the 2-D boundary element method, and full scale testing.

The two-dimensional boundary element method is well proven for the study of road traffic noise barriers. However certain characteristics of the method place limitations upon its application. Providing that these limitations are realised, then the method is an effective prediction tool. Modifications have been made, and presented in Chapter 2, in order to improve its computational efficiency so as to extend the types of cross-section which can be modelled with this method.

The first improvement has been to adapt the method to allow for the efficient simulation of cross-sections in which the noise barrier or barriers sit on flat ground which consists of ground of two distinct impedance values, particularly parallel barrier cross-sections where the outlying ground is different to that between the barriers. The results obtained give reasonable agreement with those predicted using the existing method, although there is some suggestion that accuracy is reduced when the flow resistivity of the outlying ground is low. The reduction in computation time through using the modified procedure is considerable, being as much as 90%. Successful application of the procedure has been reported for the study of both parallel barrier arrangements and cases of single barriers where different ground types exist

on either side of the barrier.

The second modification to the method has been made to extend the efficient application of the method to cross-sections where a cutting lies below the level of the main ground plane. The revised method is a three-stage approach. Testing using an incident plane wave and comparison with results predicted using a coupled integral equation method indicate that the modified procedure is accurate in its calculations and that the approximations used are good. Comparisons with the existing boundary element method are generally very good although the predictions for cross-sections incorporating rigid ground either as the outlying ground plane or the cutting floor show some discrepancy. This has been shown to be largely due to the occurance of eigenfrequencies in either the existing method or the modified procedure. The reduction in CPU time has been shown from these tests to be commonly of the order of 70-80%, although this is dependant on the position of the receivers relative to the cutting. The approach also requires significantly less memory.

In Chapter 3, full scale measurements and boundary element simulations have been performed upon a commercially available interference device, Calmzone, which is known to improve the insertion loss of a plane screen. The measurements have shown that the device increases the average screening performance by 1.9 dB(A) when compared with a simple barrier of identical height. However, the improvement was not as significant as that observed during previously reported tests on multiple-edge barrier profiles [118], which when mounted on a plane reflective screen improved the average insertion loss of the screen by 2.5 dB(A). The boundary element predictions of the interference device showed less improvement, although the effect of blocking the ducts of the device was similar. The device produced consistent improvement in screening over a wide area, although some variation was observed depending upon the source position. It is considered that the primary reason for the noise reduction is the presence of the back panel which behaves as a second diffracting edge. The results obtained here suggest that approximately one third of the reduction produced is attributable to the interference effect produced by the

phase delay introduced by the stacked vent system. The results further validate the use of the boundary element method as a prediction method. The method would be an effective means of attempting to optimise the performance of such an interference device.

In Chapter 4, the boundary element method has been applied to the study of parallel barrier arrangements where the source is located between the barriers. A modification has been proposed which is intended to reduce the effects of over-estimation of multiple reflections in the model. Providing account is taken of the perfect geometry and any reflective surfaces within the cross-section, the method is an efficient tool for studying parallel barrier arrangements, particularly if the two-impedance ground modification of Chapter 2 is used. The development of a straightforward approximation has allowed the transformation of line source results to those of a point source. Whilst this adjustment procedure does not provide results detailing the absolute performance of the barrier, combining data from stages of this adjustment with data from the original boundary element method allows the insertion loss of such an arrangement using multiple point sources to be calculated. There was reasonable agreement with experimental data from full-scale measurements: errors between the two may be due to inadequately modelling the ground conditions.

Full scale measurements and boundary element simulations suggest that, for the geometries studied, the introduction of a reflective screen on the farside of the carriageway degrades the performance of a plane rigid screen by approximately 4 dB(A) for a line source. The introduction of absorptive treatment reduces the degradation loss by minimising reflections in the far barrier. Tests on a range of barrier configurations show that the use of absorptive, tilted and median barriers can significantly reduce the degradation loss.

A multiple-edge barrier configuration, the RTB profile, is known to offer improved screening performance over a plane screen. Reported in-situ measurements have suggested the behaviour to be influenced by site geometry. Boundary element

calculations have been used to optimise the design to minimise this influence. The results predict that the most effective design is that with a single inclined open baseplate, providing approximately 2 dB(A) additional average insertion loss relative to the basic plane screen. In comparison to the basic asymmetric RTB profile, the improvement is approximately 1dB(A). Boundary element predictions of the Calmzone interference profile, which includes an inclined baseplate and a single additional diffracting edge, have shown this device to provide approximately 1 dB(A) additional insertion loss relative to a plane screen of the same height when the interference ducts of the Calmzone are blocked.

It is noted that these tests have been conducted on flat ground. Further simulations would be required to assess the performance of the optimised device on sites where the receiver is well below the top of the barrier. Due to the large dimensions of the device, the design may not be particularly practical, and the cost of installation may outweigh the acoustic performance benefits. It appears from the previous roadside measurements that the basic RTB profile is best suited to site conditions where the height of the receiver positions are such that they lie close to the level of the top of the barrier. The boundary element method has been shown to be a particularly useful tool for optimisation, although less so if the ground being modelled is not level.

In Chapter 6, it has been demonstrated that the boundary element method is a useful tool for investigating the relative efficiency of various forms of track-side noise barrier for railways, particularly with a modification to allow for the simulation of dipole sources. The results obtained using the numerical method suggest that for any particular shape, an absorbent barrier provides much better screening efficiency than the rigid equivalent. The cross-section of the rolling stock significantly affects the performance of rigid barriers. The screening efficiency of such barriers is poor when the sides of the rolling stock are vertical. However an average improvement in insertion loss of up to 7.5 dB(A) for a 2 m high barrier results when the upper and lower surfaces of the vehicle sides are inclined; this helps to redirect reflected sound either towards the trackbed or upwards. Such profiles are commonly used,

particularly on high speed trains. If the position of the upper edge is fixed, the results suggest that vertical absorptive barriers provide more effective screening than those tilted towards the track, since the benefits of using profiled rolling stock are eliminated. The addition of multiple edges to a barrier provides additional insertion loss of up to 3.0 dB(A) without any increase in height for carriages with vertical sides. The average improvement is 0.5 dB(A) for profiled rolling stock.

7.1 Recommendations For Future Work

Although work has been reported on the development of 3-D boundary element methods [37, 38] for the prediction of propagation from a point source, the computation requirements are considerable. Furthermore, the 3-D boundary element method [37, 38] proceeds via a partial Fourier transform, by transforming the 3-D problem to a sequence of 2-D problems of the type studied in Chapter 2. Consequently, the 2-D boundary element method discussed in Chapter 2, whether in its original or modified form, is still a useful tool. The most immediate requirement is the modification of the 2-D method to eliminate the occurrence of eigenfrequencies (Note 3, page 16) which have been shown in Section 2.3.3 to reduce the accuracy of the modified approach for modelling cuttings. The proposed modification uses the equations derived in Section 2.3 for the partial derivatives of the integral equation.

The 2-D method described is currently being adapted by the author to model a 3-D incoherent line source (c.f. [37, 38]), rather than a coherent line source, but at the cost of greatly increased computation time.

The results obtained from the full scale measurements and simulations of the Calmzone device reported in Chapter 3 indicate the extent to which this interference device is effective in reducing A-weighted road traffic noise levels when installed on an existing noise barrier. Although the relative contributions of the different screening mechanisms have been identified, further study is required to establish if the dimensions of the ducts on Calmzone are such as to attenuate specific frequencies. The spectra presented in Chapters 3 and 6 illustrate how the dominant frequencies

differ between road traffic and railway noise. The studies of Calmzone using railway noise sources [48, 71] showed the introduction of the device providedup to 6 dB(A) additional insertion loss, far greater than observed by the author on the Noise Barrier Test facility. Whilst maintaining the overall form of the device, further investigation may allow the characteristic dimensions of the device to be successfully "tuned" to attenuate noise from specific forms of transport.

The investigations into parallel barrier arrangements reported in Chapter 4 have revealed the potential benefits of using low median barriers in conjunction with typical roadside noise barriers. Further experimental and theoretical work is required to investigate the effects of varying the height and geometry of such barriers. In view of the safety requirements which would need to be satisfied, the cross-sections necessary may be complex, e.g. Armco safety fences as currently installed on most motorways. Consequently, the use of the boundary element method in such studies would be advantageous.

The optimisation of the multiple-edge noise barrier configuration in Chapter 5 using the boundary element method was restricted to flat ground, although the modifications made during the optimisation process were in the light of poor experimental results on one M25 site, where the receiver positions were located well below the top edge of the barrier [121]. A consideration of mechanisms for the reduced performance in this case (see page 148) suggested closing the base of the device or treating the panels with sound absorbent material to minimise sound leakage. Further study using the boundary element method is necessary to identify if the optimised device offers improvements in such cases, or whether some other more efficient profile can be obtained. The continuing improvements in the speed and power of personal computers will allow this to be efficiently carried out. Furthermore, modifications to the boundary element method described in this thesis to allow the efficient simulation of cross-sections involving embankments are being carried out. Such advances may allow a far more detailed optimisation study to be performed.

With the increasing introduction of high speed railway lines, the abatement of railway noise is becoming more important. In comparison to road traffic noise and the use of porous road surfaces, the reduction of noise due to improvements in the track is limited. Consequently the development of efficient noise barriers, as reported in Chapter 6, is likely to continue. Further investigations are recommended to investigate the benefits of low noise barriers placed in close proximity to the track in addition to those positioned at the limit of the structure gauge as in this study. The barrier positions in Chapter 6 (not less than 2.08 m from the centre of the nearest track) have been chosen to correspond to structure gauges for existing UK railway lines (Appendix C of [103]). It is expected that new railway lines will comply with European regulations, in which the structure gauge limit is at a greater distance from the track (4.167 m, Appendix B of [103]). Additional work is required to establish if the conclusions drawn here are applicable to barriers complying with the new regulations.

References

[1] M. ABRAMOWITZ and I.A. STEGUN (editors)1965 *Handbook of mathematical functions.* New York: Dover.

[2] R.J. ALFREDSON and X. DU 1995 *Proceedings of Inter-Noise 95*, 381-384. Special shapes and treatment for noise barriers.

[3] M. AMRAM and R. STERN 1981 *Journal of The Acoustical Society of America* 70, 1463-1472. Refractive and other acoustic effects produced by a prism-shaped network of rigid strips.

[4] M. AMRAM, G.L. OSTIGUY and J. ROUSSELET 1983 *Journal of Sound and Vibration* 86 (2), 253-263. Optimum attenuation of low frequency noise by proper tuning of a prismatic array of waveguides.

[5] M. AMRAM and L. DROIN 1984 *Proceedings of Inter-Noise 84*, 291-294. Improved low frequency noise control with a phase reversal noise barrier on a large impedance ground.

[6] M. AMRAM and V.J. CHVOJKA 1985 *Journal of The Acoustical Society of America* 77 (2), 394-401. A slow-waveguide filter as an acoustic interference controlling device.

[7] M. AMRAM, V.J. CHVOJKA and L. DROIN 1987 *Noise Control Engineering Journal* 28 (1), 16-24. Phase reversal barriers for better noise control at low frequencies: Laboratory versus field measurements.

[8] M. AMRAM, L. P. SIMARD, V. J. CHVOJKA and G. OSTIGUY 1987 *Journal of The Acoustical Society of America* 81 (2), 215-221. Experimental study of forward scattering for a periodic arrangement of slotted waveguides.

[9] M. AMRAM and P. MASSON 1992 *Proceedings of Eurosymposium: Maitrise du Bruit Routier en Milieu Urbain*, 123-128. Système de contre-bruit passif pour améliorer la performance des ecrans acoustiques en milieu urbain.

[10] K. ATTENBOROUGH 1985 *Journal of Sound and Vibration* 99, 521-544. Acoustical impedance models for outdoor ground surfaces.

[11] K. ATTENBOROUGH and C. HOWARTH 1992 *Proceedings of Inter-Noise '92*, 223 -227. Prediction and measurement of the acoustical performance of porous road surfaces.

[12] L. BRILLOUIN 1948 *Journal of Applied Physics* 19, 1023-1041. Waveguides for slow waves.

[13] S.N. CHANDLER-WILDE and D.C. HOTHERSALL 1987 *Proceedings of The Institute of Acoustics* 9, 37-44. The boundary integral equation method in outdoor sound propagation.

[14] S.N. CHANDLER-WILDE 1988 *PhD thesis, University of Bradford, U.K.* Ground effects in environmental sound propagation.

[15] S.N. CHANDLER-WILDE and D.C. HOTHERSALL 1988 in *Computers in mathematical research* (N.M. Stephens and M.P. Thorne, editors). Oxford: Clarendon Press.

[16] S.N. CHANDLER-WILDE, D.C. HOTHERSALL, D.H. CROMBIE and A.T. PEPLOW 1991 *Recontres Scientifiques du Cinquintenaire: Ondes Acoustiques et Vibratoires, Interaction Fluide-Structures Vibrantes*, Publication du Laboratoire de Mécanique et d'Acoustique (CNRS Laboratoires, Marseille) (126), 73-90. Efficiency of an acoustic screen in the presence of an absorbing boundary.

[17] S.N. CHANDLER-WILDE and D.C. HOTHERSALL 1991 *Research Report, Department of Civil Engineering, University of Bradford, U.K.* On the Green function for two-dimensional acoustic propagation over a homogeneous impedance plane.

[18] S.N. CHANDLER-WILDE and K. HOROSHENKOV 1995 *Journal of the Acoustical Society of America* 98 (1), 1-12. Padé approximants for the acoustical characteristics of porous materials.

[19] S. N. CHANDLER-WILDE and D. C. HOTHERSALL 1995 *Journal of Sound and Vibration* 180, 705-724. Efficient calculation of the Green's function for acoustic propagation above a homogeneous impedance plane.

[20] V.J. CHVOJKA, L.P. SIMARD and M. AMRAM 1985 *Journal of The Acoustical Society of Canada* 13, 25-43. Etude par réflexion de l'impédance d'entrée, sous incidence oblique, d'un écran acoustique ajouré.

[21] J.-P. CLAIRBOIS, P. HOUTAVE and N.NICOLAS 1997 *Proceedings of Inter-Noise 97*, 425-428. Specific designs of noise barriers for trains. Part II: In-situ verification of effectiveness.

[22] S.B. COHN 1949 *Journal of Applied Physics* 19, 257-262. Analysis of the metal-strips delay structure for microwave lenses.

[23] D. H. CROMBIE 1993 PhD thesis, University of Bradford, UK. The acoustic performance of road traffic noise barriers.

[24] D.H. CROMBIE and D.C. HOTHERSALL 1994 *Journal of Sound and Vibration* 176 (4), 459-473. The performance of multiple noise barriers.

[25] D. H. CROMBIE and D. C. HOTHERSALL 1994 *Proceedings of Inter-Noise '94*. The acoustic performance of multiple edge noise barriers. 587-590.

[26] D.H. CROMBIE, D.C. HOTHERSALL and S.N. CHANDLER-WILDE 1995 *Applied Acoustics* 44, 353-367. Multiple-Edge Noise Barriers.

[27] D.H. CROMBIE, A.T.PEPLOW and D.C.HOTHERSALL 1992 *Proceedings of The Institute of Acoustics* **14** (4), 659-665. Efficiency of absorbing screens in the presence of high-sided vehicles.

[28] M.E. DAINES 1992 *Trials of porous asphalt and rolled asphalt on the A38 at Burton.* Report RR323, Transport Research Laboratory, Crowthorne, UK.

[29] A. DUMAS 1978 *Acustica* **40**, 213-?. Etude de la diffraction par un écran mince disposé sur le sol.

[30] B.A. DE JONG, A. MOERKERKEN and J.D. VAN DER TOORN 1983 *Journal of Sound and Vibration* **86** (1), 23-46. Propagation of sound over grassland and over an earth barrier.

[31] M.E. DELANY and E.N. BAZLEY 1970 *Applied Acoustics* **3**, 105-116. Acoustic properties of fibrous absorbent materials.

[32] DEPARTMENT OF TRANSPORT and WELSH OFFICE 1988 *Calculation of road traffic noise*, London: HMSO.

[33] DEPARTMENT OF TRANSPORT 1995 *Calculation of railway noise.* London: HMSO.

[34] DEPARTMENT OF TRANSPORT 1995 *Calculation of railway noise. Supplement no. 1: Procedure for the calculation of noise from Eurostar trains class 373.* London: HMSO.

[35] DEUTSCHES PATENTAMT 1980. Auslegeschrift 26 24 026.

[36] L. DROIN, M. AMRAM and V.J. CHVOJKA 1986 *Applied Acoustics* **19**, 285-303. Optimisation geometrique de guides d'ondes utilises comme filtre passe-bas pour le controle des bruits de basses frequences.

[37] D. DUHAMEL 1996 *Journal of Sound and Vibration* **197** (5), 547-571. Efficient calculation of the three-dimensional sound pressure field around a noise barrier.

[38] D. DUHAMEL and P. SERGENT 1998 *Journal of Sound and Vibration* **218** (5), 799-823. Sound propagation over noise barriers with absorbing ground.

[39] T.F.W. EMBLETON, J.E. PIERCY and G.A. DAIGLE 1983 *Journal of The Acoustical Society of America* **74** (4), 1239-1244. Effective flow resistivity of ground surfaces determined by acoustical measurements.

[40] A.L. ESPERANCE and J. NICOLAS 1989 *Journal of The Acoustical Society of America* **86** (3), 1060-1064. Insertion loss of absorbing barriers on the ground.

[41] T.W. FAMULOK and P. ROCH 1996. Proceedings of International Rubber Conference 1996. The tyre in the 21st Century.

[42] J. FELDMANN 1983 *Journal of Sound and Vibration* **87**, 179-187. The noise behaviour of the wheel/rail-system - Some supplementary results.

[43] K. FUJIWARA and N. FURUTA 1991 *Noise Control Engineering* **37** (1), 5-11. Sound shielding efficiency of a barrier with a cylinder at the edge.

[44] GETZNER-WERKSTOFFE 1993 Bludenz-Bürs, Austria. Private communication.

[45] D. HABAULT and P. FILIPPI 1980 *Acustica* **46**, 1-7. Diffraction d'une onde monochromatique par différents mod eles de sols plans.

[46] J.J. HAJEK 1980 *Performance of parallel noise barriers: Yonge St to Bayview Avenue.* Ottawa: Ontario Ministry of Transportation and Communication.

[47] J.J. HAJEK and C.T. BLANEY 1984 *Transportation Research Record* (983), 8-17. Evaluation of T-profile noise barriers.

[48] N. HAMPL, K.A.KOHLER and M. WENZL 1991 *Fortschritte der Akustik - DAGA 91*, 349-352. Interferenz-schallabsorber für schallschutzwände.

[49] S. I. HAYEK 1980 *Proceedings of Inter-Noise 80*, 585-690. Efficiency of double walled noise barriers.

[50] S. I. HAYEK 1985 *Proceedings of Inter-Noise 85*, 495-498. Noise reduction by absorbent double parallel barriers over hard ground.

[51] B. HEMSWORTH 1979 *Journal of Sound and Vibration* **66** (3), 297-310. Recent developments in wheel/rail noise research.

[52] B. HEMSWORTH 1987 in *Transportation Noise Reference Book* (P. M. Nelson, editor). London: Butterworth. Prediction of train noise.

[53] Y. HIDAKA, H. TACHIBANA, Y. MATSUI and R. KANEKO 1995 *Proceedings of Inter-Noise '85*, 215-218. Measurement of sound radiation from Shinkansen train by sound intensity method.

[54] D. HOHENWARTER 1990 *Journal of Sound and Vibration* **141**, 17-41. Railway noise propagation models.

[55] G. HOLZL, P. FODIMAN, K.-P. SCHMITZ, M. A. PALLAS and B. BARSIKOW 1994 *Proceedings of Inter-Noise '94*, 193-198. Deufrako-2: localised sound sources on the high-speed vehicles ICE, TGV-A and TR 07.

[56] E. HOLZMANN and H. VENHAUS 1989 *VDI report* (742), 429-438. Effects of low sound protection wall in the immediate neighbourhood of the track on a Federal Railways line.

[57] D.C. HOTHERSALL, S.N. CHANDLER-WILDE and N.M. HAJMIRZAE 1991 *Journal of Sound & Vibration* **146** (2), 303-322. Efficiency of single noise barriers.

[58] D.C. HOTHERSALL, D.H. CROMBIE and S.N. CHANDLER-WILDE 1991 *Applied Acoustics* **32**, 269-287. The performance of T-profile and associated noise barriers.

[59] D.C. HOTHERSALL and D.H. CROMBIE 1992 *Proceedings of The Institute of Acoustics* **14** (4), 673-676. Prediction and the effects of parallel road traffic noise barriers.

[60] D.C. HOTHERSALL and S.A. TOMLINSON 1995 *Proceedings of Inter-Noise 95*, 397-400. High sided vehicles and road traffic noise barriers.

[61] D.C. HOTHERSALL and S.A. TOMLINSON 1997 *Journal of The Acoustical Society of America* **102** (2), 998-1003. Effects of high-sided vehicles on the performance of noise barriers.

[62] P. HOUTAVE 1997 Acoustical Technologies, Brussels, Belgium, Private communication.

[63] P. HOUTAVE and J.-P. CLAIRBOIS 1997 *Proceedings of Inter-Noise 97*, 421-424. Specific designs of noise barriers for trains. Part I: Theoretical study of forms and materials.

[64] D.A. HUTCHINS, H.W. JONES and L.T. RUSSELL 1984 *Journal of The Acoustical Society of America*, **75**, (6), 1817-1826. Model studies of barrier performance in the presence of absorbing ground surfaces. Part II - different shapes.

[65] K. IIDA, Y. KONDOH and Y. OKADO 1984 *Transportation Research Record*, (983), 51-54. Research on a device for reducing noise.

[66] I. ISEI, T.F.W. EMBLETON and J.E. PIERCY 1980. *Journal of The Acoustical Society of America* **67**, 46-58. Noise reduction by screens on finite impedance ground.

[67] C. J. C. JONES, A. E. J. HARDY, R. R. K. JONES and A. WANG 1996 *Journal of Sound and Vibration* **193**, 427-431. Bogie shrouds and low track-side barriers for the control of railway vehicle rolling noise.

[68] T. KAWAI 1981 *Journal of Sound and Vibration* **79** (2), 229-242. Sound diffraction by a many sided barrier or pillar.

[69] W.F.KING III 1977 *Journal of Sound and Vibration*, **54**, 361-378. On the role of aerodynamically generated sound in determining the radiated noise levels of high speed trains.

[70] W.F.KING III 1996 *Journal of Sound and Vibration* **193**, 349-358. A precis of developments in the aeroacoustics of fast trains.

[71] K.A. KOHLER, N. HAMPL and M. HEIM *Fortschritte der Akustik - DAGA 92*, 349-352. Interferenzabsorber für schallschutzwände an eisenbahnstrecken.

[72] M. KOYASUTA and M. YAMASHITA 1973 *Applied Acoustics* **3**, 233-241. Scale model experiments on noise reduction by acoustic barrier of a straight line source.

[73] U.J. KURZE and G.S. ANDERSON 1971 *Applied Acoustics* **4**, 35-53. Sound attenuation by a barrier.

[74] R. LAHLOU, M. AMRAM and G.OSTIGUY 1989 *Journal of The Acoustical Society of America* **85** (4), 1449-1455. Oblique acoustic wave propagation through a slotted waveguide.

[75] K. M. LI and Q. WANG 1998 *Journal of Sound and Vibration* **211** (4), 663-681. A BEM approach to assess the acoustic performance of noise barriers in a refracting atmosphere.

[76] Y. L. LI, S. J. FRANKE and C. H. LIU 1993 *Journal of The Acoustical Society of America* **92** (2), 1067-1075. Wave scattering from a ground with a Gaussian bump or trough in an inhomogeneous medium.

[77] Z. MAEKAWA 1966 *Applied Acoustics* **1**, 157-173. Noise reduction by screens.

[78] Z. MAEKAWA and S. OSAKI 1985 *Applied Acoustics* **18**, 355-368. A simple chart for the estimation of the attenuation by wedge diffraction.

[79] P. MASSON, M. AMRAM and G. OSTIGUY 1995 *Journal of Sound & Vibration* **179** (2), 327-345. Theoretical and experimental study of plane wave propagation in asymmetrical rectangular waveguide filters.

[80] T. MATSUMOTO, K. YAMAMOTO, K. IIMURA and G. SAKAMOTO 1994 *Proceedings of Inter-Noise 94*, 579-582. Scale model studies of new type highway noise barriers.

[81] B. MAUCLAIRE 1990 *Proceedings of Inter-Noise '90*, 371-374. Noise generation by high speed trains. New information acquired by SNCF in the field of acoustics owing to the high speed test program.

[82] D.N. MAY and M.M. OSMAN 1980 *Journal of Sound & Vibration*, **71**, (1), 73-101. Highway noise barriers: New shapes.

[83] C.W. MENGE 1978 *Proceedings of Inter-Noise 78*, 509-512. Sloped barriers for highway noise control.

[84] K. MIZUNO, H. SEKIGUCHI and K.IIDA 1984 *Japan Soc. Mech Engrs*, **27** (229), 1499-1505. Research on a noise control device (First report, fundamental principles of the device).

[85] K. MIZUNO, H. SEKIGUCHI and K.IIDA 1985 *Japan Soc Mech Engrs*, **28** (245), 2737-2743. Research on a noise control device (Second report, fundamental design of the device (1)).

[86] L. MONGEAU, M. AMRAM and J. ROUSSELET 1986 *Journal of The Acoustical Society of America* **80** (2), 665-671. Scattering of sound waves by a periodic array of slotted waveguides

[87] P.A. MORGAN, S.N. CHANDLER-WILDE and D.C.HOTHERSALL 1994 *Proceedings of The Institute of Acoustics* **16** (2), 101-112. Numerical modelling of parallel noise barriers.

[88] P.A. MORGAN, C.R. ROSS and S.N. CHANDLER-WILDE 1995 *Proceedings of The Institute of Acoustics*, **17** (4), 465-477.An efficient boundary element model for the performance of parallel noise barriers.

[89] P.A.MORGAN, C.R. ROSS and S.N. CHANDLER-WILDE 1996 *Proceedings of Inter-Noise '96* **6**, 3011-3016. An efficient boundary element model for noise propagation from cuttings.

[90] P.A. MORGAN and D.C. HOTHERSALL 1997 *Proceedings of Inter-Noise '97*, **1**, 433-436. Numerical modelling of railway noise barriers.

[91] P.A. MORGAN, D.C. HOTHERSALL and S.N. CHANDLER-WILDE 1998 *Journal of Sound and Vibration* **217** (3), 405-417. Influence of shape and absorbing surface - A numerical study of railway noise barriers.

[92] P.M. MORSE and K.U. INGARD 1968 *Theoretical Acoustics.* New York: McGraw Hill Book Company.

[93] P.M. NELSON, P.G. ABBOTT and C. SAVIDGE 1976 *Acoustic performance of the M6 noise barriers.* Transport Research Laboratory Report LR 731, Crowthorne, UK.

[94] P.M. NELSON and P.G. ABBOTT 1990 *Transportation Research Record* (1265). Acoustical performance of pervious macadam surfaces for high speed roads.

[95] J. NICOLAS, T.F.W EMBLETON and J.E. PIERCY 1983 *Journal of The Acoustical Society of America* **73**, 44-54. Precise model measurements versus theoretical prediction of barrier insertion loss in presence of the ground.

[96] J. NICOLAS and G.A. DAIGLE 1986 *Journal of The Acoustical Society of America*, **80** (3), 869-876. Experimental study of a slow-waveguide barrier on finite impedance ground.

[97] *ÖAL-Richtlinie* Nr.30, 1990 *Calculation of the sound imission from rail traffic* (in German).

[98] A. OMOTO and K. FUJIWARA 1993 *Journal of The Acoustical Society of America* **94** (4), 2173-2180. A study of an actively controlled noise barrier.

[99] A.T. PEPLOW and S.N.CHANDLER-WILDE 1992 *Proceedings of The Institute of Acoustics* **14** (4), 667-672. Three dimensional numerical modelling of sound propagation over noise barriers of arbitrary uniform cross-section.

[100] A.T. PEPLOW 1995 *PhD Thesis, University of Bradford, U.K.* Integral equation methods for acoustic scattering by infinite obstacles and surfaces.

[101] A.T. PEPLOW and S.N. CHANDLER-WILDE 1999 to appear in *Journal of Sound and Vibration.* Noise propagation from a cutting of arbitrary cross-section and impedance.

[102] S. PETERS 1974 *Journal of Sound and Vibration*, **32**, 87-99. The prediction of railway noise profiles.

[103] RAILTRACK 1995 *Railway Group Standard GC/RT 5204, Structure gauging and clearances.*

[104] K.B. RASMUSSEN 1985 *Journal of Sound and Vibration* **98** (1), 35-44. On the effect of terrain profile on sound propagation outdoors.

[105] E. RUDOLPHI and L. AKERLÖF 1996. *Proceedings of Inter-Noise '96*, 799-802. Full scale tests on the design of railway noise barriers.

[106] SCOTT WILSON KIRKPATRICK & PARTNERS 1993, Private communication.

[107] H. SEKIGUCHI, K. MIZUNO and K. IIDA 1986 *Japan. Soc. Mech. Engrs*, **29** (253), 2260-2265. Research on a noise control device (Third report, Fundamental design of the device (2)).

[108] R. SEZNEC 1980 *Journal of Sound and Vibration* **73**, 195-209. Diffraction of sound around barriers: use of the boundary elements technique.

[109] S. SLUTSKY and H. L. BERTONI 1988 *Transportation Research Record* (1176). Analysis and programs for assessment of absorptive and tilted parallel barriers.

[110] C. STANWORTH 1987 in *Transportation Noise Reference Book* (P. M. Nelson, editor). London: Butterworth. Sources of railway noise.

[111] D. C. TOBUTT and P. M. NELSON 1990 *A model to calculate traffic noise levels from complex highway cross-sections.* Transport Research Laboratory Report RR 245, Crowthorne, UK.

[112] J.W. TYLER 1979 *TRRL quiet vehicle programme, quiet heavy vehicle (QHV).* TRRL Report SR 521, Dept. of Environment, Dept. of Transport.

[113] S. UGHI, F. ARTOM, S. CINGOLANI and L. ASTE 1995 *Proceedings of Inter-Noise '95*, 377-380. Behaviour of normal height sound barriers combined with low barriers at minimum distance from the railway tracks.

[114] J. D. VAN DER TOORN, H. HENDRIKS and T.C. VAN DEN DOOL 1996 *Journal of Sound and Vibration* **193**, 113-121. Measuring TGV source strength with Syntacan.

[115] J. J. A. VAN LEEUWEN 1996 *Journal of Sound and Vibration* **193**, 269-276. Noise prediction models to determine the effect of barriers placed alongside railway lines.

[116] P. F. VAN TOL 1997 *Proceedings of Inter-Noise '97*, 429-432. An array measurement technique applied to high speed train noise barriers.

[117] C.WASSILIEFF 1988 *Journal of The Acoustical Society of America*, 84 (2), 645-650. Improving the noise reduction of picket barriers.

[118] G.R.WATTS, D.H. CROMBIE and D.C. HOTHERSALL 1994 *Journal of Sound and Vibration* **177** (3), 289-305. Acoustic performance of new designs of traffic noise barriers: full scale tests.

[119] G.R. WATTS 1994 Proceedings of Inter-Noise 94, 583-586. Acoustic performance of parallel traffic noise barriers: full scale tests.

[120] G.R. WATTS 1996 *Applied Acoustics* **47** (2), 95-119. Acoustic performance of parallel traffic noise barriers.

[121] G.R. WATTS 1996 *Applied Acoustics* **47**, 47-66. Acoustic performance of a multiple edge noise barrier profile at motorway sites.

[122] G.R. WATTS and P.A. MORGAN 1996 *Applied Acoustics* **49** (1), 1-16. Acoustic performance of an interference type noise barrier.

[123] G.R. WATTS, S.N. CHANDLER-WILDE, P.A. MORGAN, I.D. RICHARDSON and C.R.ROSS 1996 *Proceedings of Inter-Noise '96* **6**, 3103-3108. The combined effects of porous asphalt surfacing and barriers on traffic noise.

[124] G.R.WATTS, S.N. CHANDLER-WILDE and P.A. MORGAN 1999 *Applied Acoustics* **58**, 351-377. The combined effects of porous asphalt surfacing and barriers on traffic noise.

[125] L.S. WIRT 1979 *Acustica*, **42** (2), 73-88. The control of diffracted sound by means of thnadners (shaped noise barriers).

Appendix A

FORTRAN BEM Model Input and Output Files

The operation of the FORTRAN encoded boundary element method requires two input files, TINPUT and TINPUTSP, to be created by the operator. These files contain the geometrical configuration of the cross-section under study (including the positions of all sources and receivers), the acoustic properties of the ground and barrier surfaces, and the spectral information related to the individual sources. The sample files included in this Appendix are used with the most recent version of the computer program, which incorporates the modifications described in Sections 2.2 and 2.3.

The output from the computer model is stored in a file, TOUTPT. In addition to a summary of the data provided in the TINPUT file, the results (Excess Attenuation (EA), Sound Pressure Level (SPL) and Insertion Loss (IL)) are listed by frequency as can be seen from the sample file included in this Appendix.

A.1 The TINPUT datafile

The TINPUT file contains the geometrical data necessary to define the cross-section in the boundary element method. From Chapter 2, that part of the cross-section to be discretized, γ, is defined as $\gamma = \Gamma_1 \cup \Gamma_2$, where Γ_2 includes only those surfaces where $y > 0$ and Γ_1 only those surfaces where both $y = 0$ and $\beta \neq \beta_c$. In the file

γ is described by a polygonal arc, the co-ordinates of the corners being specified in an anti-clockwise sequence to ensure that the unit normal is always directed out of the medium of propagation.

The required impedance model (either that of Delany and Bazley [31] or Attenborough [10, 11]) is selected and then the surface properties between adjacent corners specified. A class number of 1 denotes that a side is present between the corners, and 2 that no side is present. Each side present is assumed to have the acoustic properties appropriate to a homogeneous porous layer of thickness d, with an acoustically rigid backing. The parameters values required for the individual models are as follows:

- For the Delany and Bazley model: the effective flow resistivity of the layer, σ_E (in Nsm^{-4}), and the depth of the porous layer, d (in metres).

- For the Attenborough model: the effective flow resistivity of the layer, σ_e (in Nsm^{-4}), the effective depth of the porous layer, d_e, the porosity of the layer, Ω, the tortuosity of the layer, q (q^2 is referred to as the tortuosity in some references), and the dominant angle of incidence (specifying a zero value amounts to an assumption of a locally reactive surface). Here, $\sigma_e = (4s_p^2\sigma)/\Omega$, σ being the flow resistivity in Nsm^{-4}, s_p the pore shape factor ($s_p = 0.5$ for circular pores) and $d_e = dq$. The notation used here is that of [18].

Finally, the number and coordinates of the source and receiver positions are specified. The last 3 lines of the input file are related to the degree of detail contained in the TOUTPUT file and the number of receiver positions used to calculate the mean insertion loss at each frequency.

The sample TINPUT file listing on the following pages (Figure A.2) applies to the cross-section shown in Figure A.1 where β_c is defined as being that for the ground outside of the barrier arrangement. It should be noted that the cross-section is described so as not to use the two-impedance ground modification, i.e. the standard boundary element method will be used to perform the calculations. To use the modifications of Sections 2.2 and 2.3, the only changes to the input data are in the

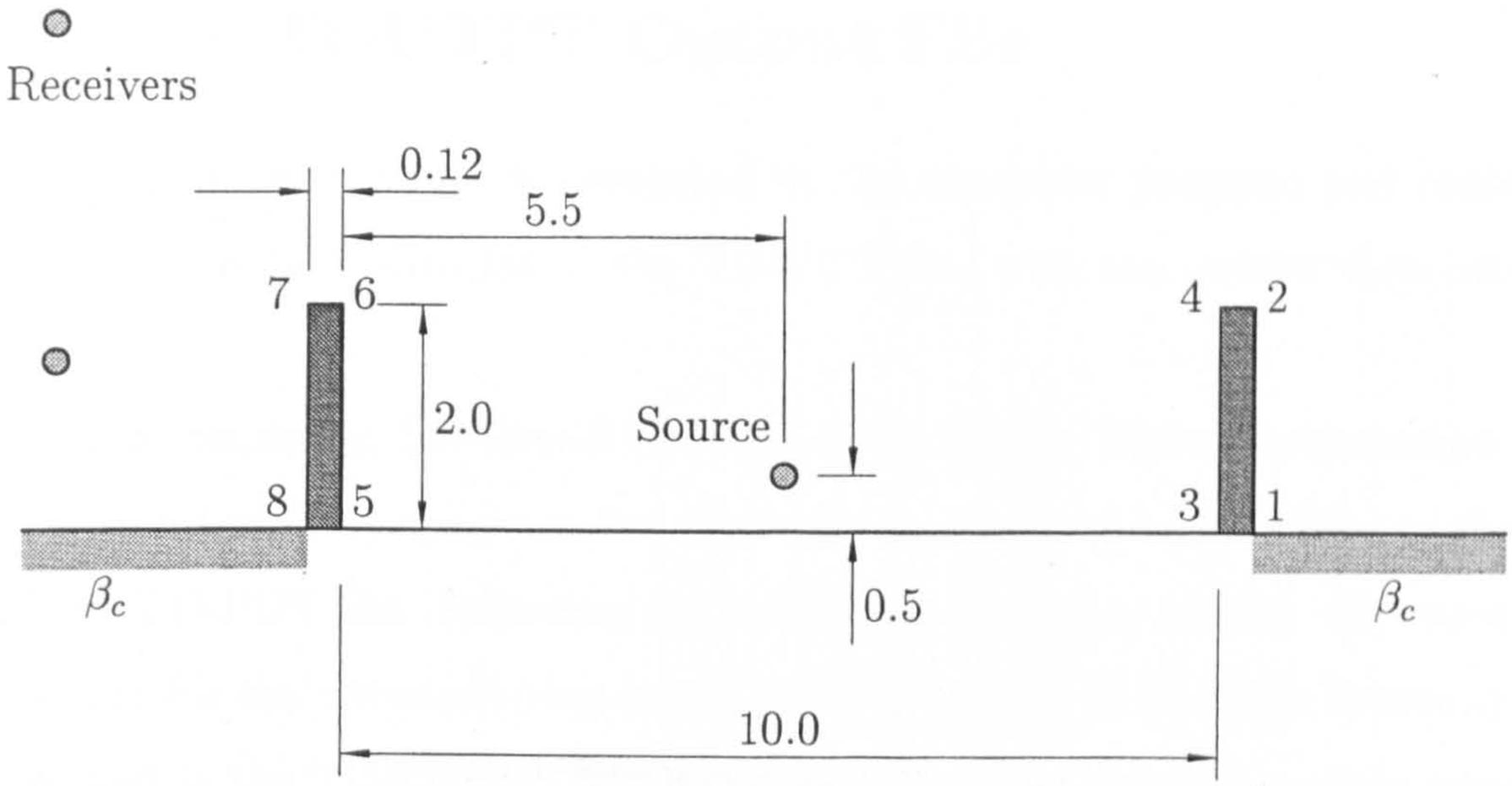

Figure A.1: Parallel barrier arrangement defined in sample TINPUT file. Dimensions in metres.

definitions of the class number and the need to use different parameter values for the Stage 1 and Stage 2 ground conditions.

A.2 The TINPUTSP file

This file contains the spectral data to be used within the computer program. Multiple source spectra can be specified within this file. At each frequency, the element length to be used in the discretization is specified as a fraction of a wavelength, together with the source strength in dB, measured at 1.0 m in free-field conditions, for each chosen spectrum. To calculate an A-weighted broad-band level within the computer program, it is necessary to include an A-weighted spectrum in this input file. Calculations are usually performed at either third-octave or ninth-octave band centre frequencies.

The sample TINPUTSP file included in this Appendix (Figure A.3) contains a single source spectrum.

A.3 The TOUTPT Output File

This is the primary output file generated by the computer program and contains a summary of the data provided in the TINPUT file, with the results then listed by frequency.

For each frequency, the Sound Pressure Level (SPL), Excess Attenuation (EA) and Insertion Loss (IL) are presented for each receiver position specified in the final line of the TINPUT file. Following the individual frequency results, the same data is presented for the corresponding broad band spectrum. If multiple source spectra are specified in the TINPUTSP file, individual frequency results are only presented for the first spectrum. The results for the other spectra are given only in broadband terms as above.

The sample TOUTPUT file included in this Appendix (Figure A.4) is based upon calculations performed using the included TINPUT and TINPUTSP files, corresponding to the cross-section of Figure A.1.

Figure A.2: Sample TINPUT file

```
10                                  |   No of corners
10.500  0.000                       \
10.000  0.000                        |
10.000  2.000                        | Coordinates
 9.880  2.000                        | of corners
 9.880  0.000                        | (in m)
 0.120  0.000                        |
 0.120  2.000                        |
 0.000  2.000                        |
 0.000  0.000                        |
-0.500  0.000                       /
1                                   |   Model selection
3 800000  -1.0   0.5   1.5   0.0    \
1   1E20   0.0   1.0   1.0   0.0     |
1   1E20   0.0   1.0   1.0   0.0     | Properties of
1   1E20   0.0   1.0   1.0   0.0     | surfaces
4   1E20   0.0   1.0   1.0   0.0     | connecting
1   1E20   0.0   1.0   1.0   0.0     | adjacent corners
1   1E20   0.0   1.0   1.0   0.0     |
1   1E20   0.0   1.0   1.0   0.0     |
3 800000  -1.0   0.5   1.5   0.0    /
  1E20   0.0   1.0   1.0   0.0      |   Ground stage 1
800000  -1.0   0.5   1.5   0.0      |   Ground stage 2
1                                   |   No of sources
  5.62  0.05                        |   Source coordinates
6                                   |   No of receivers
-20.0  1.500                         \
-40.0  1.500                          | Coordinates
-80.0  1.500                          | of receivers
-20.0  4.500                          |
-40.0  4.500                          |
-80.0  4.500                         /
TRUE                                | Cancel detailed output
6                                   | Mean over 6 receivers
6                                   | Output for 6 receivers
```

Figure A.3: Sample TINPUTSP file

```
 18 1                    | No of frequencies & spectra
100.000 0.0300  56.9  \
125.893 0.0350  56.3   | Frequency (in Hz), element
158.489 0.0400  57.5   | length as a fraction of a
199.526 0.0450  62.1   | wavelength, and SPL (dB) at
251.189 0.0500  63.3   | 1.0 m from the source
 316.228 0.0600  66.0   |
 398.107 0.0700  68.0   |
 501.187 0.0800  71.0   |
 630.957 0.0900  75.8   |
 794.328 0.1000  80.1   |
1000.000 0.1250  83.9   |
1258.925 0.1250  80.8   |
1584.893 0.1250  78.3   |
1995.262 0.1250  75.2   |
2511.886 0.1250  73.1   |
3162.278 0.1600  69.7   |
3981.072 0.2000  65.8   |
5011.872 0.2500  61.9  /
```

Figure A.4: Sample TOUTPT file

```
PROGRAM ILV10CM RUNNING SUBROUTINE BARI9E
-----------------------------------------

THE FOLLOWING ELEMENT LENGTHS ARE USED IN THE BOUNDARY
ELEMENT METHOD.

FREQUENCY (HZ)    ELEMENT LENGTH (WAVELENGTHS)
--------------    ----------------------------
     100.000                  0.0300
     125.893                  0.0350
     158.489                  0.0400
     199.526                  0.0450
     251.189                  0.0500
     316.228                  0.0600
     398.107                  0.0700
     501.187                  0.0800
     630.957                  0.0900
     794.328                  0.1000
    1000.000                  0.1250
    1258.925                  0.1250
    1584.893                  0.1250
    1995.262                  0.1250
    2511.886                  0.1250
    3162.278                  0.1600
    3981.072                  0.2000
    5011.872                  0.2500

SOURCE COORDINATES:

  SOURCE NO.     X/METRES    Y/METRES
  ----------     --------    --------
       1            5.62        0.05

GROUND AND BARRIER ELEMENTS ARE MODELLED USING THE
ATTENBOROUGH MODEL

THE TRUE GROUND SURFACE CHARACTERISTICS, USED AT
THE 2ND STAGE OF THE CALCULATION, ARE:
    EFFECTIVE FLOW RESISTIVITY   =   800000. SI UNITS
    POROUS LAYER DEPTH IS INFINITE
    POROSITY = 0.500
    TORTUOSITY = 1.500
    DOMINANT ANGLE OF INCIDENCE =  0.0 DEGREES


THE GROUND SURFACE CHARACTERISTICS, USED AT
THE 1ST STAGE OF THE CALCULATION, ARE:
    EFFECTIVE FLOW RESISTIVITY   =   800000. SI UNITS
    POROUS LAYER DEPTH IS INFINITE
    POROSITY = 0.500
    TORTUOSITY = 1.500
    DOMINANT ANGLE OF INCIDENCE =  0.0 DEGREES
```

COORDINATES OF BARRIER CORNERS:

CORNER NO.	X/METRES	Y/METRES
1	10.00	0.00
2	10.00	2.00
3	9.88	2.00
4	9.88	0.00
5	0.12	0.00
6	0.12	2.00
7	0.00	2.00
8	0.00	0.00

POSITIONS AND SURFACE PROPERTIES OF BARRIER SIDES:

CORNER NOS.	SIDE BETWEEN PAIR OF CORNERS	CLASS NO.	EFFECTIVE FLOW RESISTIVITY (SI UNITS)	POROUS LAYER DEPTH (M)	POROSITY	TORTUOSITY	DOMINANT ANGLE OF INCIDENCE
1 2	YES	1	1E20	0.00	1.000	1.000	0.0
2 3	YES	1	1E20	0.00	1.000	1.000	0.0
3 4	YES	1	1E20	0.00	1.000	1.000	0.0
4 5	YES	1	1E20	0.00	1.000	1.000	0.0
5 6	YES	1	1E20	0.00	1.000	1.000	0.0
6 7	YES	1	1E20	0.00	1.000	1.000	0.0
7 8	YES	1	1E20	0.00	1.000	1.000	0.0

SOURCE SPECTRUM NUMBER 1

THIS SPECTRUM IS THE SINGLE FREQUENCY 100 HZ.

RECEIVER NUMBER	X-COORD. OF RECEIVER/M	Y-COORD. OF RECEIVER/M	SPL/DB	EA/DB	IL/DB
1	-20.00	1.50	41.64	1.17	6.61
2	-40.00	1.50	39.84	0.46	5.77
3	-80.00	1.50	37.31	0.26	5.34
4	-20.00	4.50	39.45	3.30	8.59
5	-40.00	4.50	38.93	1.36	6.38
6	-80.00	4.50	36.69	0.88	5.52

THE MEAN INSERTION LOSS OVER THE FIRST 6
RECEIVER POSITIONS IS 6.37 DB.

SOURCE SPECTRUM NUMBER 2

THIS SPECTRUM IS THE SINGLE FREQUENCY 126 HZ.

RECEIVER NUMBER	X-COORD. OF RECEIVER/M	Y-COORD. OF RECEIVER/M	SPL/DB	EA/DB	IL/DB
1	-20.00	1.50	55.79	-13.58	-8.36
2	-40.00	1.50	53.97	-14.27	-9.26
3	-80.00	1.50	51.19	-14.22	-9.57
4	-20.00	4.50	49.28	-7.13	-2.04
5	-40.00	4.50	51.73	-12.04	-7.33
6	-80.00	4.50	50.14	-13.17	-9.03

THE MEAN INSERTION LOSS OVER THE FIRST 6
RECEIVER POSITIONS IS -7.60 DB.

SOURCE SPECTRUM NUMBER 3

THIS SPECTRUM IS THE SINGLE FREQUENCY 158 HZ.

RECEIVER NUMBER	X-COORD. OF RECEIVER/M	Y-COORD. OF RECEIVER/M	SPL/DB	EA/DB	IL/DB
1	-20.00	1.50	46.71	-3.31	1.60
2	-40.00	1.50	45.26	-4.35	0.22
3	-80.00	1.50	42.39	-4.21	-0.20
4	-20.00	4.50	41.69	1.66	6.52
5	-40.00	4.50	41.52	-0.63	3.70
6	-80.00	4.50	40.89	-2.72	0.78

THE MEAN INSERTION LOSS OVER THE FIRST 6
RECEIVER POSITIONS IS 2.10 DB.

:
:

SOURCE SPECTRUM NUMBER 18

THIS SPECTRUM IS THE SINGLE FREQUENCY 5012 HZ.

RECEIVER NUMBER	X-COORD. OF RECEIVER/M	Y-COORD. OF RECEIVER/M	SPL/DB	EA/DB	IL/DB
1	-20.00	1.50	42.87	4.94	-2.59
2	-40.00	1.50	39.87	5.43	-6.23
3	-80.00	1.50	34.53	8.04	-8.58
4	-20.00	4.50	50.17	-2.42	-4.66
5	-40.00	4.50	46.96	-1.67	-6.02
6	-80.00	4.50	42.37	0.20	-7.99

THE MEAN INSERTION LOSS OVER THE FIRST 6
RECEIVER POSITIONS IS -6.01 DB.

SOURCE SPECTRUM NUMBER 19

THIS SPECTRUM IS SPECTRUM NO. 1 AS SUPPLIED IN FILE TINPUTSP.

RECEIVER NUMBER	X-COORD. OF RECEIVER/M	Y-COORD. OF RECEIVER/M	SPL/DB	EA/DB	IL/DB
1	-20.00	1.50	68.40	5.77	2.72
2	-40.00	1.50	66.32	5.35	-1.29
3	-80.00	1.50	63.41	5.52	-5.44
4	-20.00	4.50	74.81	-0.70	0.60
5	-40.00	4.50	69.70	1.95	1.11
6	-80.00	4.50	65.16	3.77	-0.44

THE MEAN INSERTION LOSS OVER THE FIRST 6
RECEIVER POSITIONS IS -0.46 DB.